



Manuel Bernhard Winkler, BSc

KIM -

Investigation of spherical cavity expansion employing different
constitutive models

MASTER'S THESIS

to achieve the university degree of

Diplom-Ingenieur

submitted to

Graz University of Technology

Supervisor

Ass.Prof. Dipl.-Ing. Dr.techn., Franz Tschuchnigg

Institute of Soil Mechanics, Foundation Engineering and
Computational Geotechnics

Graz, October 2018

Affidavit

I declare that I have authored this thesis independently, that I have not used other than the declared sources/resources, and that I have explicitly indicated all material which has been quoted either literally or by content from the sources used. The text document uploaded to TUGRAZonline is identical to the present master's thesis.

.....
Date

.....
Signature

Acknowledgements

There are so many people I would like to thank for their support during the past years of my studies and especially the last eight months of writing this thesis. They have guided me, placed opportunities and showed me which doors might be useful to open.

First, I would like to express my sincere gratitude to the initiator of this thesis Robert Thurner, former Technical Director at KELLER Middle East, who gave me the unique opportunity to work on such an interesting topic and enabled me to visit the KELLER construction sites in Dubai.

I would also like to thank my supervisor from my university Franz Tschuchnigg, for his valuable guidance, his motivation and his interest in the topic. He always steered me into the right direction, whenever I needed it, and has always been willing to listen also to my point of view.

My sincere acknowledgement also goes to all of my friends and my colleagues from the “Wasserbauzeichensaal” who made the past years of studying a pleasure. I would particularly like to thank Verena Ratschiller for being such a good friend and for proofreading my thesis.

And finally, my deepest heartfelt appreciation goes to my parents and my sister for their endless love and unfailing support throughout my entire life. Thank you, for making me the person who I am.

Manuel Bernhard Winkler

Graz, Austria, October 2018

Abstract

Manuel Bernhard Winkler

KIM - Investigation of spherical cavity expansion employing different constitutive models

One of the most important steps to be taken in the process of land reclamation is the densification of the placed fill to ensure that the material's design criteria with respect to stiffness, strength and liquefaction-resistance are met. All of these criteria refer to a certain accomplished level of the relative density which can be measured indirectly by performing post-compaction cone penetration tests (CPT). With the aid of appropriate interpretation methods, the target values of the measured cone penetration resistance corresponding to a desired value of the relative density can be established.

The main material encountered within land reclamation works in the UAE (United Arab Emirates) is carbonate sand containing a high amount of shells and coral lumps. Due to the special granulometric properties (grain-shape, -size, -hardness) these sands are prone to extensive grain crushing which drastically lowers the measured cone penetration resistance compared to tests performed in silica sands under similar conditions. This specific material behaviour makes the use of standard correlations unsuitable and requires the application of interpretation methods which can take grain crushing into account. One suitable interpretation approach for carbonate sands is represented by the semi-empirical Karlsruhe Interpretation Method (KIM).

This thesis focuses on the numerical simulation of the spherical cavity expansion problem as part of the KIM. After a short introduction to land reclamation works, the theory behind this interpretation method is explained. A finite-difference solution to the spherical cavity expansion problem is introduced and a curve-fitting procedure is proposed which can be used for the determination of the KIM-parameters required for the approximation of the spherical cavity expansion limit pressures. A detailed description is given on how the spherical cavity expansion problem can be implemented into the finite-element software PLAXIS 2D and the performance of the FE-models is studied using different constitutive laws for the modelling of the surrounding soil continuum. Further, two full KIM-analysis on hypoplastic materials from land reclamation projects in Dubai are presented and a comparison between the sensitivity of the PLAXIS models and the traditional finite-difference code is made. Finally, an online tool for the automatic calibration of the hypoplastic constitutive law is tested and the PLAXIS SoilTest tool is used to check the influence of single hypoplastic parameters on the results of lab test simulations.

Kurzfassung

Manuel Bernhard Winkler

KIM – Betrachtung der sphärischen Hohlräume aufweitung unter Verwendung verschiedener Stoffgesetze

Einer der wichtigsten Schritte im Zuge von Landgewinnungsarbeiten ist die Verdichtung des Füllmaterials, um sicherzustellen, dass die Bemessungskriterien in Bezug auf Steifigkeit, Festigkeit und Widerstand gegen Bodenverflüssigung eingehalten werden. Alle diese Kriterien sind abhängig von der erreichten relativen Lagerungsdichte, welche über die Durchführung von Drucksondierungen (CPT) indirekt bestimmt werden kann. Mit Hilfe geeigneter Korrelationsmethoden lassen sich die gemessenen Werte des Spitzendruckes in eine relative Lagerungsdichte überführen, welche für den Verdichtungserfolg steht.

Das am häufigsten eingesetzte Füllmaterial bei Landgewinnungsprojekten in den Vereinigten Arabischen Emiraten ist Kalksand, welcher vom Meeresgrund bezogen wird. Aufgrund seiner Herkunft weist dieses Material einen hohen Muschelgehalt auf, wodurch die einzelnen Körner wesentlich leichter zum Kornbruch neigen, als in herkömmlichen Quarzsanden. Die gemessenen Spitzendrucke in Kalksanden sind bedeutend geringer als in Quarzsanden bei gleichem Druck- und Dichteniveau. Dadurch wird der Einsatz von Standardkorrelationen ungeeignet und die Anwendung von Interpretationsmethoden erforderlich, welche in der Lage sind, einen eventuellen Kornbruch abzubilden. Eine geeignete Interpretationsmethode für den Einsatz in Kalksanden ist die Karlsruhe Interpretation Method (KIM).

Diese Arbeit konzentriert sich auf die numerische Simulation des Problems der sphärischen Hohlräume aufweitung als Teil der KIM. Nach einer kurzen Einführung in Bezug auf Landgewinnungsarbeiten wird die allgemeine Theorie zur KIM erläutert. Es wird eine Finite-Differenzen-Lösung für das Problem der sphärischen Hohlräume aufweitung vorgestellt und ein Kurvenanpassungsverfahren vorgeschlagen, das zur Ermittlung der KIM-Parameter verwendet werden kann, welche zur Approximation der Grenzdrücke aus der Hohlräume aufweitung benötigt werden. Es wird gezeigt, wie ein Modell der sphärischen Hohlräume aufweitung in der Finiten-Elemente-Software PLAXIS 2D implementiert werden kann, und Performance-Studien mit den FE-Modellen werden durchgeführt unter Einsatz verschiedener Stoffgesetze. Weiters werden zwei vollständige KIM-Analysen von hypoplastischen Materialien durchgeführt und ein Sensitivitätsvergleich des PLAXIS-Modells mit dem traditionellen Finite-Differenzen-Code angestellt. Abschließend wird ein Online-Tool zur automatischen Kalibrierung des hypoplastischen Materialgesetzes getestet und das PLAXIS SoilTest-Tool wird verwendet, um den Einfluss einzelner hypoplastischer Parameter auf die Ergebnisse von Labortest-Simulationen zu überprüfen.

Contents

1	Introduction	1
1.1	Current Situation in the UAE	1
1.2	Problem Formulation	2
1.3	Approach to the Problem	3
2	Land Reclamation, Carbonate Sands and Compaction Works	4
2.1	Land Reclamation by Hydraulic Filling	4
2.1.1	Dredging Process	4
2.1.2	Transport and Placement of Dredged Material	7
2.2	Carbonate Sands	9
2.2.1	Origin and Definition of Carbonate Sands	9
2.2.2	Characteristics of Calcareous Sands	10
2.2.3	Interrelation Carbonate Content – Soil Properties	11
2.3	Vibro Compaction of Reclaimed Land	13
2.3.1	Equipment and Limits of Application	13
2.3.2	The Process of Vibro Compaction	15
3	Quality Control of Compaction Works	16
3.1	Cone Penetration Test (<i>CPT</i>)	16
3.1.1	Testing Equipment	17
3.1.2	Penetration of the CPT Rods	17
3.2	CPTs at the KELLER Project PLM (Dubai)	18
3.3	CPT Interpretation Methods used in Geotechnical Practice	19
3.3.1	Calibration Chamber Tests	19
3.3.2	Interpretation Method - German Standard DIN 4094	22
3.3.3	Interpretation Method - Schmertmann	23
3.3.4	Interpretation Method – Jamiolkowski	24
3.3.5	Comparison of different Interpretation Methods	24
4	The Karlsruhe Interpretation Method	26
4.1	Hypoplasticity Theory	26
4.2	Hypoplastic Modell by “von Wolffersdorff”	27
4.2.1	Determination of the Material Parameters	29
4.2.2	Hypoplastic Parameters of KELLER Materials	36
4.3	Cavity Expansion Theory	37

4.3.1	The Spherical Cavity Expansion	37
4.4	Modelling of the Cone Penetration Test	43
4.5	The final KIM Equation	45
5	The OSINOV Code	46
5.1	The Utilization of the OSINOV Code	46
5.1.1	The Input-File	46
5.1.2	Generation of the Initial Conditions	48
5.1.3	The Output Files	49
5.2	Curve-fitting Procedures	50
5.2.1	The Least Square Method	51
5.2.2	Gnuplot Curve-Fitting	57
5.2.3	Comparison of Curve-Fitting Approaches	59
5.2.4	Improving the Simulation Series	61
5.3	Sensitivity Study by Slawik	63
5.4	Automatic Diagram Generation using MATLAB	64
5.4.1	CODE “StressPaths_1ID_Allp.m”	64
5.4.2	CODE “StressPaths_1p_AllID.m”	67
6	PLAXIS FEM-Model	71
6.1	Model Implementation in PLAXIS	72
6.1.1	Used Soil Models	72
6.1.2	Mesh Set-up	73
6.1.3	Generation of Initial Stresses	74
6.1.4	Calculation Phases	75
6.1.5	Output	76
6.2	Closed-form Solution of the SCE	77
6.2.1	Construction of the Pressure-Expansion-Curve	77
6.2.2	CPT Interpretation Method acc. to Randolphs et al.	79
6.3	Improvements of the PLAXIS Model	80
6.3.1	Influence of the Domain Size and Boundary Conditions	81
6.3.2	Influence of E and ν of the Cavity Material	85
6.3.3	Influence of the Cavity Discretization	87
6.3.4	Influence of the Flow Rule	90
6.3.5	Influence of Different Selected Output Nodes	93
6.3.6	The Final Plaxis Model	96
6.3.7	Comparison with Curves found in Literature	98
6.4	Mohr-Coulomb Material Study – Final Model	99

6.4.1	Variation of E for Material 1 and Material 3	101
6.4.2	Variation of K_0 for Material 1 and Material 3	103
6.4.3	Variation of p_0 for Material 1 and Material 3	104
6.5	PLAXIS Calculations – Hardening Soil Model	106
6.6	PLAXIS Calculations – Hypoplastic Model	108
6.6.1	General Aspects – Hypoplastic Model in PLAXIS	108
6.6.2	Advantage of Hypoplasticity over Elasto-Plasticity	108
6.6.3	Automatic Model Generation for KIM-Analysis	110
6.6.4	KIM-Analysis using the PLAXIS Model	111
6.6.5	Sensitivity Study – PLAXIS Model (Hypoplasticity)	115
6.7	Calculation of the q_c -Curves over Depth	119
7	Studies on the Hypoplastic Parameter Calibration	122
7.1	ExCalibre – Automatic Calibration Tool	122
7.1.1	Input – Excel Template	123
7.1.2	Calibration - Material PLM AZ28	125
7.1.3	Calibration - Material PLM BC36	129
7.2	The Influence of single Parameters on Lab-Test Simulations	135
7.2.1	PLAXIS SoilTest Tool – General Information	135
7.2.2	Dobransy Sand	135
7.2.3	Rohatec Sand	142
7.2.4	Conclusions	143
7.3	Calibration Procedure acc. to Meier	143
8	Summary and Outlook	148
8.1	Summary	148
8.2	Outlook	150
9	Bibliography	152

List of Figures

Fig. 1:	The Palm Jumeirah project in Dubai [1].....	1
Fig. 2:	Sketch of the Plain Suction Dredger [1].....	5
Fig. 3:	Sketch of the Cutter Suction Dredger [1].....	5
Fig. 4:	Sketch of the Trailing Suction Hopper Dredger (a) and fill placement using rainbowing (b) [1].....	6
Fig.5:	Sketch of a backhoe dredger [1].....	6
Fig. 6:	Sketch of a grab dredger [1].....	7
Fig. 7:	Transition between floating and onshore pipeline [12].....	8
Fig. 8:	Underwater bund construction using a grab dredger [1].....	9
Fig. 9:	Crushing of Quiou sand during oedometer tests.....	11
Fig. 10:	Relation between the content of carbonates and the limit void ratios e_{min} and e_{max} [2].....	11
Fig. 11:	Relation between the content of carbonates and the critical friction angle φ_c [2].....	12
Fig. 12:	Relation between the content of carbonates and the grain density ρ_s [2].....	12
Fig. 13:	Compaction mechanism [16].....	13
Fig. 14:	Cross-section of a modern depth vibrator [15].....	14
Fig. 15:	Limits of application for deep vibro techniques [16].....	14
Fig. 16:	The process of vibro compaction [16].....	15
Fig. 17:	Different parts of a cone penetrometer with u_i depicting the positions of pore pressure measurement [17].....	16
Fig. 18:	Typical CPT pushing equipment.....	17
Fig. 19:	Triangular pattern of compaction points.....	18
Fig. 20:	q_c -profiles from pre- and post-compaction CPTs [2].....	19
Fig. 21:	Cross-section of the calibration chamber found at the University of Karlsruhe [6].....	20
Fig. 22:	(a) Macro-voids start to occur for $e > e_i$ (b) dry masonry forms in case of $e > e_d$	28
Fig. 23:	Pressure dependency of the limit void ratios [30].....	29
Fig. 24:	Limit void ratios e_d , e_c and e_i vs. C_u [2].....	30
Fig. 25:	Limit void ratios e_d , e_c and e_i vs. $CaCO_3$ – content [2].....	31
Fig. 26:	The angle of repose test [6].....	32
Fig. 27:	Relationship between φ_c and the mean grain size d_{50} [2].....	32
Fig. 28:	Determination of n from considered pressure range of the compression curve (adapted after [30]).....	34
Fig. 29:	Influence of the mean grain size d_{50} on h_s and n [2].....	35
Fig. 30:	Shearing of a dense sample - Peak friction angle φ_p [35].....	35
Fig. 31:	Influence of β on the calculated compression curves for an initially loose (a) and an an initially dense (b) specimen [34].....	36
Fig. 32:	The boundary value problem of the spherical cavity expansion (adapted after [38]).....	37

Fig. 33:	Progression of radial (a) and tangential (b) stresses during a spherical cavity expansion in Ticino sand [8].....	39
Fig. 34:	p/q -paths (a) for $p_0 = 400$ kPa and e-p-paths (b) for $p_0 = 100$ and 400 kPa at the cavity wall for a spherical cavity expansion in Ticino sand [8].....	40
Fig. 35:	Spatial distribution of p_r , p_θ and e at the end of the spherical cavity expansion from r_a^0 to $3.3 r_a^0$ in Ticino sand (adapted after [8]).....	41
Fig. 36:	Limit pressure p_{LS} vs. mean effective stress p_0 for different relative densities ID^* obtained for Ticino sand [8].....	41
Fig. 37:	Limit pressure p_{LS} vs. mean effective stress p_0 for different carbonate sands at $ID^* = 0.1$ (a) and $ID^* = 0.9$ (b) [8].....	42
Fig. 38:	Simulation results of the SCE (a) and the calibration chamber testing results (b) for Ticino sand [6].....	43
Fig. 39:	Shape factor k_q vs. relative density ID^* for four different pressure ranges [8]	44
Fig. 40:	qc-curves for material PLM AZ28 from the KELLER-database [41]	45
Fig. 41:	Structure of the main text-file from the OSINOV code.....	47
Fig. 42:	Generated *.ini-file containing the calculation parameters.....	48
Fig. 43:	First 10 lines from the *.dat-file.....	49
Fig. 44:	Structure and contents of the *.kp1 output-file.....	49
Fig. 45:	The limit pressure p_{LS} from the *.kp1-file.....	50
Fig. 46:	p_{LS} -curves for material PLM AZ28 from the KELLER-database.....	50
Fig. 47:	First step of the curve-fitting procedure - extract from the Excel-file	51
Fig. 48:	Approximated p_{LS} -curve (left) and errors ² at considered values of p_0 (right) before the solver was applied.....	52
Fig. 49:	Approximated p_{LS} -curve (left) and errors ² at considered values of p_0 (right) after the solver was applied.....	52
Fig. 50:	Determination of the a_i -parameters - extract from the Excel-file	54
Fig. 51:	Approximated a -curve (left) and errors ² at considered values of I_D (right) .	56
Fig. 52:	Approximated b -curve (left) and errors ² at considered values of I_D (right) .	56
Fig. 53:	Structure of the final.dat-file for the Gnuplot curve-fitting approach.....	57
Fig. 54:	Approximated p_{LS} -curves from Gnuplot.....	58
Fig. 55:	Final q_c -curves from Gnuplot.....	58
Fig. 56:	Approximated a-curves (a) and b-curves (b) from Gnuplot.....	58
Fig. 57:	q_c over depth: Influence of KIM-parameters on the final results (PLM BC36)	60
Fig. 58:	Addressing of the input-files within the MATLAB-script.....	64
Fig. 59:	$s - t$ - diagrams for PLM AZ28 for 5 different p_0 and $I_D = 0.0$ (left) and $I_D = 0.9$ (right)	65
Fig. 60:	$p - q$ - diagrams for PLM AZ28 for 5 different p_0 and $I_D = 0.0$ (left) and $I_D = 0.9$ (right)	65
Fig. 61:	$\log(p) - e$ - diagrams for PLM AZ28 for 5 different p_0 and $I_D = 0.0$ (left) and $I_D = 0.9$ (right)	66
Fig. 62:	$r_a/r_a^0 - p_r$ - diagrams for PLM AZ28 for 5 different p_0 and $I_D = 0.0$ (left) and $I_D = 0.9$ (right)	66

Fig. 63:	$r_a/r_a^0 - p_\theta$ - diagrams for PLM AZ28 for 5 different p_0 and $I_D = 0.0$ (left) and $I_D = 0.9$ (right).....	66
Fig. 64:	$r_a/r_a^0 - e$ - diagrams for PLM AZ28 for 5 different p_0 and $I_D = 0.0$ (left) and $I_D = 0.9$ (right).....	67
Fig. 65:	$s - t$ - diagrams for PLM AZ28 for 10 different I_D and $p_0 = 0.050$ MPa (left) or $p_0 = 0.300$ MPa (right)	68
Fig. 66:	$p - q$ - diagrams for PLM AZ28 for 10 different I_D and $p_0 = 0.050$ MPa (left) or $p_0 = 0.300$ MPa (right).....	68
Fig. 67:	$\log(p) - e$ - diagrams for PLM AZ28 for 10 different I_D and $p_0 = 0.050$ MPa (left) or $p_0 = 0.300$ MPa (right).....	69
Fig. 68:	$r_a/r_a^0 - p_r$ - diagrams for PLM AZ28 for 10 different I_D and $p_0 = 0.050$ MPa (left) or $p_0 = 0.300$ MPa (right).....	69
Fig. 69:	$r_a/r_a^0 - p_\theta$ - diagrams for PLM AZ28 for 10 different I_D and $p_0 = 0.050$ MPa (left) or $p_0 = 0.300$ MPa (right).....	69
Fig. 70:	$r_a/r_a^0 - e$ - diagrams for PLM AZ28 for 10 different I_D and $p_0 = 0.050$ MPa (left) or $p_0 = 0.300$ MPa (right).....	70
Fig. 71:	Basic parts of the PLAXIS FEM-model.....	72
Fig. 72:	Locations of nodes and stress (gauss) points for a triangular element [43]..	73
Fig. 73:	Typical mesh (right) and 4-element-dicretization of the cavity cluster (left)	73
Fig. 74:	Initial stress field p for a model with $p_0 = 50$ kPa	74
Fig. 75:	Typical phases of the FEM-model ($\text{VolStrain200} \triangleq \varepsilon_v = 200\%$).....	75
Fig. 76:	Pressure-expansion-curves from the PLAXIS Curves Manager as typically received for a MC-model with a non-associated flow rule.....	76
Fig. 77:	Example of an “averaged” pressure-expansion-curve	77
Fig. 78:	Generated pressure-expansion curve from the script (closed-form).....	79
Fig. 79:	Mesh around the cavity for the large domain model	81
Fig. 80:	Mesh quality for models with different domain sizes	82
Fig. 81:	Distribution of σ_l', p' and $ u $ across the cavity – Small model	82
Fig. 82:	Distribution of σ_l', p' and $ u $ across the cavity – Medium model	82
Fig. 83:	Distribution of σ_l', p' and $ u $ across the cavity – Large model	83
Fig. 84:	Distribution of σ_l', p' and $ u $ across the cavity – Very large model.....	83
Fig. 85:	Outlier curves (blue lines) from nodes A, I, K and T in PLAXIS	84
Fig. 86:	Final pressure-expansion-curves for different domain sizes ($y_{max} = \text{free}$).....	84
Fig. 87:	Final pressure-expansion-curves for different domain sizes ($y_{max} = \text{fixed}$)...	85
Fig. 88:	Final pressure-expansion-curves for different cavity E and v	86
Fig. 89:	Typical output from PLAXIS for the studies on changing cavity E and v (CavityE2000_ny0).....	87
Fig. 90:	Mesh graduation for the models with 33 elements within the cavity (left) and the selected nodes within these models (right)	88
Fig. 91:	Distribution of σ_l', p' and $ u $ across the cavity – 33CavityElem_Medium model	89
Fig. 92:	Distribution of σ_l', p' and $ u $ across the cavity – 33CavityElem_Large model	89

Fig. 93:	Pressure-expansion-curves for the models with 33 elements within the cavity	90
Fig. 94:	Distribution of σ'_l, p' and $ u $ across the cavity – Associated20 model	91
Fig. 95:	Associated flow rule models: Pressure-expansion-curves	92
Fig. 96:	Output PLAXIS Curves manager – Associated flow rule	93
Fig. 97:	Different node-configuration with stress points outside and inside the cavity	94
Fig. 98:	PLAXIS Curves manager results for stress points chosen outside the cavity	94
Fig. 99:	Pressure-expansion-curves – Influence of different nodes	95
Fig. 100:	Mesh of the final model.....	97
Fig. 101:	Pressure-expansion-curves for material MC1 from improved PLAXIS model (left) and from Xu [43] (right).....	99
Fig. 102:	Pressure-expansion-curves for material MC2 from improved PLAXIS model (left) and from Xu [43] (right).....	99
Fig. 103:	Pressure-expansion-curves for Material 1 – non-associated (left) vs. associated flow rule (right).....	100
Fig. 104:	Pressure-expansion-curves for Material 2 – non-associated (left) vs. associated flow rule (right).....	100
Fig. 105:	Pressure-expansion-curves for Material 3 – non-associated (left) vs. associated flow rule (right).....	101
Fig. 106:	Pressure-expansion-curves for changing E of Material 1 (above) and Material 3 (below).....	102
Fig. 107:	Pressure-expansion-curves for changing K_0 of Material 1 (above) and Material 3 (below)	104
Fig. 108:	Pressure-expansion-curves for changing p_0 of Material 1 (above) and Material 3 (below).....	105
Fig. 109:	Pressure-expansion-curves for materials HS1, HS2 and HS3	106
Fig. 110:	Pressure-expansion-curves for materials HS4, HS5, HS6 and HS7	107
Fig. 111:	Example of the curves from the PLAXIS Curves manager for the hypoplastic models.....	109
Fig. 112:	Typical pressure-expansion-curve as received from the hypoplastic model...	110
Fig. 113:	Pressure-expansion-curves PLM AZ28 for I_D 0.0 and 0.1 (Plaxis).....	111
Fig. 114:	Pressure-expansion-curves PLM AZ28 for I_D 0.2 and 0.3 (Plaxis).....	111
Fig. 115:	Pressure-expansion-curves PLM AZ28 for I_D 0.4 and 0.5 (Plaxis).....	112
Fig. 116:	Pressure-expansion-curves PLM AZ28 for I_D 0.6 and 0.7 (Plaxis).....	112
Fig. 117:	Pressure-expansion-curves PLM AZ28 for I_D 0.8 and 0.9 (Plaxis).....	112
Fig. 118:	Approximated p_{LS} -curves for material PLM AZ28 – PLAXIS calculation (left) and OSINOV calculation (right).....	114
Fig. 119:	Approximated p_{LS} -curves for material PLM BC36 – PLAXIS calculation (left) and OSINOV calculation (right).....	115
Fig. 120:	Sensitivity diagram p_{LS} -range – PLAXIS $I_D = 0.2$ (PLM AZ28).....	117
Fig. 121:	Sensitivity diagram Δp_{LS} -range – PLAXIS $I_D = 0.2$ (PLM AZ28)	117
Fig. 122:	Sensitivity diagram p_{LS} -range – OSINOV $I_D = 0.2$ (PLM AZ28)	118

Fig. 123:	Sensitivity diagram Δp_{LS} -range – OSINOV $I_D = 0.2$ (PLM AZ28)	118
Fig. 124:	q_c vs z for $I_D = 0.9$ and GW 2 m below ground surface (PLM AZ28)	121
Fig. 125:	ExCalibre input – grading curve	123
Fig. 126:	ExCalibre input – oedometric compression curve	124
Fig. 127:	ExCalibre input – triaxial testing curves	124
Fig. 128:	Curves from 2 triaxial tests on dense samples – PLM AZ28 (provided by KELLER-Grundbau GmbH)	125
Fig. 129:	Curves from oedometer test on loose sample – PLM AZ28 (provided by KELLER-Grundbau GmbH)	126
Fig. 130:	Simulated and measured compression curves from ExCalibre output (PLM AZ28)	127
Fig. 131:	Simulated and measured triaxial curves (100 kPa cell pressure) from ExCalibre output (PLM AZ28)	127
Fig. 132:	Simulated and measured triaxial curves (600 kPa cell pressure) from ExCalibre output (PLM AZ28)	128
Fig. 133:	Pressure-expansion-curves PLM AZ28 for $p_0 = 100$ kPa and $I_D = 0.5$ – ExCalibre parameters (red curve) and report parameters (blue curve)	128
Fig. 134:	Pressure-expansion-curves PLM AZ28 for $p_0 = 100$ kPa and $I_D = 0.5$ – ExCalibre parameters+ α -report (red curve) and report parameters (blue curve)	129
Fig. 135:	Curves from 2 triaxial tests on loose samples – PLM BC36 [41]	130
Fig. 136:	Curves from 2 triaxial tests on dense samples – PLM BC36 [41]	130
Fig. 137:	Curves from oedometer test on loose sample – PLM BC36 (provided by KELLER-Grundbau GmbH)	131
Fig. 138:	Simulated and measured compression curves from ExCalibre output (PLM BC36)	132
Fig. 139:	Simulated and measured triaxial curves (100 kPa cell pressure-loose) from ExCalibre output (PLM BC36)	132
Fig. 140:	Simulated and measured triaxial curves (600 kPa cell pressure-loose) from ExCalibre output (PLM BC36)	132
Fig. 141:	Simulated and measured triaxial curves (100 kPa cell pressure-dense) from ExCalibre output (PLM BC36)	133
Fig. 142:	Simulated and measured triaxial curves (600 kPa cell pressure-dense) from ExCalibre output (PLM BC36)	133
Fig. 143:	Pressure-expansion-curves PLM BC36 for $p_0 = 100$ kPa and $I_D = 0.5$ – ExCalibre parameters (red curve) and report parameters (blue curve)	134
Fig. 144:	Pressure-expansion-curves PLM BC36 for $p_0 = 100$ kPa and $I_D = 0.5$ – ExCalibre parameters+ α report (red curve) and report parameters (blue curve)	134
Fig. 145:	Influence of φ_c on compression curve – Dobrany sand	137
Fig. 146:	Influence of φ_c on triaxial curves (50 kPa cell pressure) – Dobrany sand	137
Fig. 147:	Influence of φ_c on triaxial curves (200 kPa cell pressure) – Dobrany sand	137

Fig. 148:	Influence of h_s on compression curve – Dobrany sand	138
Fig. 149:	Influence of h_s on triaxial curves (50 kPa cell pressure) – Dobrany sand	138
Fig. 150:	Influence of h_s on triaxial curves (200 kPa cell pressure) – Dobrany sand	138
Fig. 151:	Influence of n on compression curve – Dobrany sand	139
Fig. 152:	Influence of n on triaxial curves (50 kPa cell pressure) – Dobrany sand ..	139
Fig. 153:	Influence of n on triaxial curves (200 kPa cell pressure) – Dobrany sand	139
Fig. 154:	Influence of α on compression curve – Dobrany sand	140
Fig. 155:	Influence of α on triaxial curves (50 kPa cell pressure) – Dobrany sand ..	140
Fig. 156:	Influence of α on triaxial curves (200 kPa cell pressure) – Dobrany sand	140
Fig. 157:	Influence of β on compression curve – Dobrany sand	141
Fig. 158:	Influence of β on triaxial curves (50 kPa cell pressure) – Dobrany sand ..	141
Fig. 159:	Influence of β on triaxial curves (200 kPa cell pressure) – Dobrany sand	141
Fig. 160:	Manual calibration procedure acc. to Meier [6]	144
Fig. 161:	Calculation of e from the volumetric strains	146
Fig. 162:	Oedometer test (loose) simulation results for different parameter sets from PLAXIS – Manual calibration approach acc. to Meier [6].....	146
Fig. 163:	Oedometer test (dense) simulation results for different parameter sets from PLAXIS – Manual calibration approach acc. to Meier [6].....	147
Fig. 164:	Triaxial test simulation results for different parameter sets from PLAXIS – Manual calibration approach acc. to Meier [6].....	147

APPENDIX

A. Fig 1:	MATLAB-code from the StressPaths_1ID_Allp.m script	164
A. Fig 2:	s - t -diagrams for PLM BC36 for 5 different p_0 and $I_D = 0.0$ (left) and $I_D = 0.9$ (right).....	165
A. Fig 3:	p - q -diagrams for PLM BC36 for 5 different p_0 and $I_D = 0.0$ (left) and $I_D = 0.9$ (right).....	165
A. Fig 4:	$\log(p)$ - e -diagrams for PLM BC36 for 5 different p_0 and $I_D = 0.0$ (left) and $I_D = 0.9$ (right).....	165
A. Fig 5:	r_a/r_a^0 - p_r -diagrams for PLM BC36 for 5 different p_0 and $I_D = 0.0$ (left) and $I_D = 0.9$ (right).....	166
A. Fig 6:	r_a/r_a^0 - p_θ -diagrams for PLM BC36 for 5 different p_0 and $I_D = 0.0$ (left) and $I_D = 0.9$ (right).....	166
A. Fig 7:	r_a/r_a^0 - e -diagrams for PLM BC36 for 5 different p_0 and $I_D = 0.0$ (left) and $I_D = 0.9$ (right).....	166
A. Fig 8:	MATLAB-code from the StressPaths_1p_AllID.m script	169
A. Fig 9:	s - t -diagrams for PLM BC36 for 10 different I_D and $p_0 = 0.025$ MPa (left) and $p_0 = 0.300$ MPa (right)	169

A. Fig 10:	p - q -diagrams for PLM BC36 for 10 different I_D and $p_0 = 0.025$ MPa (left) and $p_0 = 0.300$ MPa (right).....	170
A. Fig 11:	$\log(p)$ - q -diagrams for PLM BC36 for 10 different I_D and $p_0 = 0.025$ MPa (left) and $p_0 = 0.300$ MPa (right).....	170
A. Fig 12:	r_a/r_a^0 - p_r -diagrams for PLM BC36 for 10 different I_D and $p_0 = 0.025$ MPa (left) and $p_0 = 0.300$ MPa (right).....	170
A. Fig 13:	r_a/r_a^0 - p_θ -diagrams for PLM BC36 for 10 different I_D and $p_0 = 0.025$ MPa (left) and $p_0 = 0.300$ MPa (right).....	171
A. Fig 14:	r_a/r_a^0 - e -diagrams for PLM BC36 for 10 different I_D and $p_0 = 0.025$ MPa (left) and $p_0 = 0.300$ MPa (right).....	171
A. Fig 15:	MATLAB-code for the closed-form solution by Yu and Houlsby [44] of the SCE within an infinite continuum.....	174
A. Fig 16:	Distribution of σ_I' , p' and $ u $ across the cavity – CavityE250 model.....	174
A. Fig 17:	Distribution of σ_I' , p' and $ u $ across the cavity – CavityE250_ny0 model	175
A. Fig 18:	Distribution of σ_I' , p' and $ u $ across the cavity – CavityE1000 model.....	175
A. Fig 19:	Distribution of σ_I' , p' and $ u $ across the cavity – CavityE1000_ny0 model...	175
A. Fig 20:	Distribution of σ_I' , p' and $ u $ across the cavity – CavityE2000 model.....	176
A. Fig 21:	Distribution of σ_I' , p' and $ u $ across the cavity – CavityE2000_ny0 model...	176
A. Fig 22:	Phyton script - Automatic model generation - KIM-analysis	177
A. Fig 23:	Pressure-expansion-curves PLM BC36 for I_D 0.0 and 0.1 (PLAXIS)	178
A. Fig 24:	Pressure-expansion-curves PLM BC36 for I_D 0.2 and 0.3 (PLAXIS)	178
A. Fig 25:	Pressure-expansion-curves PLM BC36 for I_D 0.4 and 0.5 (PLAXIS)	178
A. Fig 26:	Pressure-expansion-curves PLM BC36 for I_D 0.6 and 0.7 (PLAXIS)	179
A. Fig 27:	Pressure-expansion-curves PLM BC36 for I_D 0.8 and 0.9 (PLAXIS)	179
A. Fig 28:	Sensitivity diagram p_{LS} -range – PLAXIS and OSINOV $I_D = 0.2$ (PLM AZ28)	180
A. Fig 29:	Sensitivity diagram Δp_{LS} -range – PLAXIS and OSINOV $I_D = 0.2$ (PLM AZ28).....	181
A. Fig 30:	Sensitivity diagram p_{LS} -range – PLAXIS $I_D = 0.8$ (PLM AZ28)	181
A. Fig 31:	Sensitivity diagram Δp_{LS} -range – PLAXIS $I_D = 0.8$ (PLM AZ28).....	182
A. Fig 32:	Sensitivity diagram p_{LS} -range – OSINOV $I_D = 0.8$ (PLM AZ28)	182
A. Fig 33:	Sensitivity diagram Δp_{LS} -range – OSINOV $I_D = 0.8$ (PLM AZ28)	183
A. Fig 34:	Sensitivity diagram p_{LS} -range – PLAXIS and OSINOV $I_D = 0.8$ (PLM AZ28)	183
A. Fig 35:	Sensitivity diagram Δp_{LS} -range – PLAXIS and OSINOV $I_D = 0.8$ (PLM AZ28).....	184
A. Fig 36:	MATLAB code – Calculation of q_c over depth z	188
A. Fig 37:	q_c vs z for $I_D = 0.3$, $z_{GW} = 10$ m and $w = 20$ % (PLM AZ28).....	188
A. Fig 38:	q_c vs z for $I_D = 0.6$, $z_{GW} = 10$ m and $w = 20$ % (PLM AZ28).....	189
A. Fig 39:	q_c vs z for $I_D = 0.9$, $z_{GW} = 10$ m and $w = 20$ % (PLM AZ28).....	189
A. Fig 40:	q_c vs z for $I_D = 0.3$, $z_{GW} = 10$ m and $w = 20$ % (PLM BC36).....	190

A. Fig 41: q_c vs z for $I_D = 0.6$, $z_{GW} = 10$ m and $w = 20$ % (PLM BC36)	190
A. Fig 42: q_c vs z for $I_D = 0.9$, $z_{GW} = 10$ m and $w = 20$ % (PLM BC36)	191
A. Fig 43: Influence of φ_c on compression curve – Rohatec sand.....	192
A. Fig 44: Influence of φ_c on triaxial curves (50 kPa cell pressure) – Rohatec sand .	192
A. Fig 45: Influence of φ_c on triaxial curves (200 kPa cell pressure) – Rohatec sand	192
A. Fig 46: Influence of h_s on compression curve – Rohatec sand	193
A. Fig 47: Influence of h_s on triaxial curves (50 kPa cell pressure) – Rohatec sand..	193
A. Fig 48: Influence of h_s on triaxial curves (200 kPa cell pressure) – Rohatec sand	193
A. Fig 49: Influence of n on compression curve – Rohatec sand	194
A. Fig 50: Influence of n on triaxial curves (50 kPa cell pressure) – Rohatec sand..	194
A. Fig 51: Influence of n on triaxial curves (200 kPa cell pressure) – Rohatec sand.	194
A. Fig 52: Influence of α on compression curve – Rohatec sand	195
A. Fig 53: Influence of α on triaxial curves (50 kPa cell pressure) – Rohatec sand..	195
A. Fig 54: Influence of α on triaxial curves (200 kPa cell pressure) – Rohatec sand.	195
A. Fig 55: Influence of β on compression curve – Rohatec sand	196
A. Fig 56: Influence of β on triaxial curves (50 kPa cell pressure) – Rohatec sand...	196
A. Fig 57: Influence of β on triaxial curves (200 kPa cell pressure) – Rohatec sand.	196
A. Fig 58: Flow chart of the calibration procedure acc. to Meier [6] – Influence of different parameter sets on the simulation results	197

List of Tables

Tab. 1:	B-values from Meier's studies on different materials [6]	21
Tab. 2:	B from k_c provided by Meier vs. B from accurate k_c for CCT M100-1	22
Tab. 3:	C_i -constants for the CPT interpretation method acc. to Schmertmann	23
Tab. 4:	C_i -constants for the CPT interpretation acc. to Jamiolkowski	24
Tab. 5:	Hypoplastic parameters required for the model by "von Wolffersdorff"	27
Tab. 6:	Values for a and b from the first step of the curve-fitting (PLM AZ28)	53
Tab. 7:	Values for a and b from the first step of the curve-fitting (PLM BC36)	53
Tab. 8:	KIM-parameters from OSINOV code calculations for material PLM AZ28	57
Tab. 9:	Comparison of KIM-parameters – Material PLM AZ28	59
Tab. 10:	Comparison of KIM-parameters – Material PLM BC36	59
Tab. 11:	KIM-parameters - 25 vs. 50 simulations	61
Tab. 12:	Values for a and b - 25 vs. 50 simulations	62
Tab. 13:	PLM AZ28 – Sensitivity of p_{LS} on the numerical parameters (OSINOV) for $p_0=0.05$ MPa	63
Tab. 14:	PLM AZ28 – Sensitivity of p_{LS} on the numerical parameters (OSINOV) for $p_0=0.30$ MPa	63
Tab. 15:	Initial material parameters used for the improvement of the FEM-model	80
Tab. 16:	Initial material parameters used for the improvement of the FEM-model	97
Tab. 17:	Continuum materials found from literature [43]	98
Tab. 18:	Investigated MC-materials assigned to the continuum	100
Tab. 19:	Used material sets – Variation of E for Material 1 and Material 3	102
Tab. 20:	Used material sets – Variation of K_0 for Material 1 and Material 3	103
Tab. 21:	Material parameters – HS-materials	106
Tab. 22:	Limit Pressures – PLAXIS vs. OSINOV (PLM AZ28)	113
Tab. 23:	Comparison of KIM-parameters – PLAXIS vs. OSINOV (PLM AZ28)	114
Tab. 24:	Comparison of KIM-parameters – PLAXIS vs. OSINOV (PLM BC36)	114
Tab. 25:	Received limit pressures p_{LS} from the sensitivity study in PLAXIS	116
Tab. 26:	Hypoplastic parameters from report – PLM AZ28	125
Tab. 27:	Hypoplastic parameters from ExCalibre – PLM AZ28	126
Tab. 28:	Hypoplastic parameters from report – PLM BC36	129
Tab. 29:	Hypoplastic parameters from ExCalibre – PLM BC36	131
Tab. 30:	Hypoplastic parameters from materials of the „soilmodel.com“-database	135
Tab. 31:	Investigated values of 5 different hypoplastic parameters – Dobrany sand	136
Tab. 32:	Initial void ratios used in PLAXIS – Dobrany sand	136
Tab. 33:	Investigated values of 5 different hypoplastic parameters – Rohatec sand	142
Tab. 34:	Initial void ratios used in PLAXIS – Rohatec sand	142
Tab. 35:	Final hypoplastic parameters for Dubai sand [6]	143
Tab. 36:	Iterative adjustments of parameters within each calibration step [6]	145
Tab. 37:	Initial void ratios used for the manual calibration procedure in PLAXIS – Dubai sand	145

APPENDIX

A. Tab. 1: Investigated materials by Reinisch [2]	156
A. Tab. 2: Index properties of Dubai sand and Karlsruhe sand [6]	157
A. Tab. 3: Results of calibration chamber tests performed by Meier [6]	157
A. Tab. 4: B from k_c provided by Meier vs. B from accurate k_c for all performed CCTs by Meier [6]	158
A. Tab. 5: Hypoplastic parameters of the materials within the KELLER-database [2]	160
A. Tab. 6: Comparison of KIM-parameters – Palm Jumeirah (values from [9]).....	161
A. Tab. 7: Limit Pressures – PLAXIS vs. OSINOV (PLM BC36)	179

List of Abbreviations

UAE	United Arab Emirates
MDD	Maximum Dry Density
SCF	Shell Correction Factor
KIM	Karlsruhe Interpretation Method
SCE	Spherical Cavity Expansion
CCT	Calibration Chamber Test
CC	Calibration Chamber
PSD	Plain Suction Dredger
CSD	Cutter Suction Dredger
TSHD	Trailing Suction Hopper Dredger
OCT	Oedometric Compression Test
CPT	Cone Penetration Test
CPTU	Cone Penetration Test with pore water measurement
TXC	Triaxial Compression Test

List of Notations

q_c	cone penetration resistance	[MPa]
Q_c	total force acting on the cone	[kN]
A_c	projected area of the cone	[m ²]
I_D	relative density	[-]
F_s	total force acting on the friction sleeve	[kN]
A_s	surface area of the friction sleeve	[m ²]
p_{LS}	limit pressure	[kPa]
d_{50}	mean grain size	[mm]
D_s	sample diameter (calibration chamber)	[cm]
d_c	cone diameter (calibration chamber)	[cm]
$q_{c,m}$	cone penetration resistance measured in CCTs	[MPa]
$q_{c,c}$	corrected cone penetration resistance	[MPa]
e	void ratio	[-]
e_{max}	Maximum void ratio from index test	[-]
e_{min}	Minimum void ratio from index test	[-]
p_a	atmospheric pressure	[kPa]
K_0	coefficient of lateral earth pressure	[-]
C_u	coefficient of non-uniformity	[-]
\mathbf{T}	stress tensor	[kPa]
\mathbf{D}	strain tensor	[-]

1 Introduction

This chapter aims at giving the readers a short background about the motivation of this study and highlights the key issues involved in the execution of extensive land reclamation works. Furthermore, the importance of the findings of this master's thesis to the KELLER Grundbau GmbH will be clarified and a promising CPT interpretation approach intended to close the gap between theory and practice will be presented.

1.1 Current Situation in the UAE

Since the discovery of oil in the United Arab Emirates (UAE) back in the 1970s, the country has started its way into a new era of fortune. Especially the Emirate of Dubai has from then on turned into one of the world's fastest growing economies. Having in mind that one day soon the oil deposits will dry up, Dubai is unswervingly trying to establish new sustainable sources of income. One of the government's plans to maintain the flow of foreign cash into the emirate is to focus upon the field of tourism. Dubai's efforts in attracting an increasing number of people to visit the UAE have led to the situation that some of the world's largest and most spectacular projects are currently being realized in the City of Dubai.

To meet the demand for high-class beachfront properties as well as new residential and recreational areas, Dubai was forced to find a way out of the ever more limited development areas along its coast. The creation of artificial islands in the sea close to the shoreline, referred to as land reclamation, is one attempt to escape this problem. Over the past few years, some of the world's largest land reclamation projects such as Palm Jumeirah and Palm Jebel Ali have been finished in the UAE, significantly changing the appearance of the country's coastline.



Fig. 1: The Palm Jumeirah project in Dubai [1]

1.2 Problem Formulation

One of the key issues for contractors commissioned with the execution of land reclamation works is the compaction of the backfilled material. A sufficient densification of the soil is required to meet the design criteria regarding strength and stiffness. As the reclaimed areas are located off-shore, they are continually exposed to high ground water tables and marine currents. Thus, the compaction also aims at reducing the liquefaction potential of the subsoil, which is of major importance for the provision of stable building land.

The quality of compaction measures such as vibro compaction is related to a certain accomplished level of density. In order to make the densification requirements tangible for the contractors, they are converted into technical parameters [2] such as the relative density I_D or the maximum dry density MDD which are directly measured using the sand replacement or the cutter cylinder method. A way of indirectly determining the density state of a compacted soil mass is to perform CPT tests and use appropriate correlations between the measured cone penetration resistance q_c and the relative density I_D .

Some of the most frequently used interpretation methods in this context are the ones developed by Schmertmann [3] and Jamiolkowski [4]. They both have in common to incorporate empirically determined coefficients derived from calibration chamber tests (CCT) performed on a wide range of different silica sands. The fact that these correlations assign empirical findings to other materials without any additional experimental investigations makes them rather inappropriate for describing a site-specific soil behaviour, especially when the granulometric material properties (grain hardness, grain shape, grain size distribution) vary substantially from those of silica sands [5]. Due to the origin of the used materials for the land reclamation projects in the UAE they are at least partially consisting of carbonate minerals. This suggests that the use of interpretation methods like the ones from Schmertmann [3] or Jamiolkowski [4] might not be the best choice to reflect the real behaviour of these special types of sands, referred to as “Carbonate Sands”.

Carbonate sands are made up of a varying amount of shells and skeletal remains of marine organisms. Their grains are much softer than regular quartz grains [6] (calcite: Mohs' hardness 3; quartz: Mohs' hardness 7) which increases the material's tendency towards grain crushing when subjected to pressure. Almeida et al. [7] was able to show that the values for the measured cone penetration resistance q_c from carbonate-rich sands tend to be considerably smaller, compared to the ones obtained from silica sands. This even applies for a comparable state of the material in terms of effective mean pressure p_0 and relative density I_D which again brings into question the applicability of the aforementioned CPT interpretation methods on carbonate sands.

1.3 Approach to the Problem

One attempt to accommodate for the effect of grain crushing when performing CPT tests in calcareous sands is the introduction of a so-called shell correction factor (SCF). The SCF transfers the lower q_c -value obtained for carbonate sand into a q_c -value of a reference silica material which can then be used in connection with the common empirical correlations. However, the value of the SCF has over time become a matter of negotiations between the client and the contractor without being justified on a proper physical basis. While the contractor aims at negotiating for the highest SCF-value, to keep the requirements on the cone resistance small, the client aims for a relatively low value to keep the compaction criterion high.

A more reliable way of narrowing the grain crushing problem, with the additional advantage of accounting for the site-specific material behaviour, is promised by the application of a semi-empirical interpretation method developed by Cudmani in 2000 [8], known as the Karlsruhe Interpretation Method (KIM). The key point of this method involves the numerical solution of a spherical or cylindrical cavity expansion problem under the employment of a hypoplastic constitutive equation. The hypoplastic equation can be calibrated to the site-specific material via “simple” lab tests without the need of performing costly and time-consuming calibration chamber tests for the evaluation of certain coefficients. On the condition of a careful model calibration, Meier [6] was able to show that using the KIM can yield a good representation of the actual material on site, coming at a relatively small effort for the parameter determination. A more detailed description of the Karlsruhe Interpretation Method will be given in chapter 4.

The KELLER Grundbau GmbH recognized the value of the KIM on their projects in the United Arab Emirates. Therefore, they started to establish a database containing all the parameters related to the KIM for some samples retrieved from their projects. Up to the present day the database is containing a number of 13 different materials. They further launched an investigation program to assess the advantages and the drawbacks of this new method. First findings could already be gained by the studies of Meier [6], Reinisch [2] and Slawik [9].

The aim of the present thesis is to provide a finite element model of the spherical cavity expansion (SCE) problem and to study the influence of different constitutive models on the results of the obtained limit pressures p_{LS} . Furthermore, the sensitivity of the model is investigated, the influence of single parameters on the calibration of the hypoplastic constitutive model is studied and a relatively new online tool for the calibration of the hypoplastic model is examined towards its suitability for the use on carbonate sands.

2 Land Reclamation, Carbonate Sands and Compaction Works

The objective of this chapter is to provide a basic knowledge about the process of land reclamation by hydraulic filling and to explain the method of deep vibratory compaction for the densification of backfilled material. In addition, the equipment used for vibro compaction and the special characteristics of carbonate sands will be presented.

2.1 Land Reclamation by Hydraulic Filling

According to van't Hoff et al. [1] land reclamation can generally be described as the process of creating new land by raising the elevation of a seabed or other low-lying land (filling) or by pumping out water from a watery area that is enclosed by dikes (polder-construction). In contrast to carrying out filling by dry earth movement, hydraulic filling uses a mixture of soil and water to facilitate dredging, transport and placement of the filling material [10].

The right choice of the dredging equipment is substantial for the feasibility and the cost-efficiency of a land reclamation project. The following consecutive activities [1] are governed by the selected equipment:

- *Dredging* of the fill material in a borrow area by floating equipment
- *Transport* of the fill material from the borrow area to the reclamation site
- *Placement* of the fill material in the reclamation area

Since hydraulic filling is the main method involved in the creation of new land in the UAE, the subsequent chapters will solely focus on this type of filling procedure.

2.1.1 Dredging Process

Dredging is the process of retrieving fill material from one part of a water environment and relocating it to another. It can be carried out for many different purposes. Capital dredging, e.g., is used to enlarge existing channels, ports, marinas and boat harbours. In contrast, the objective of the so-called maintenance dredging is the conservation of the functionality of channels and waterways by maintaining the designated water depth [11].

Dredging can either be done mechanically, referred to as cutting, or with the aid of pumps, known as suction dredging. A combination of these two dredging techniques is also possible. The subsequent sections will give a more detailed description of the most commonly used types of dredgers [1].

SUCTION DREDGING:**Plain Suction Dredger (PSD)**

Suction dredgers use big suction pipes for the intake of eroded material which often gets loosened with the aid of attached jets to the suction mouth. The retrieved material can then either be pumped towards the reclamation side utilizing pipelines or it can be pumped onto a barge alongside the dredger. The plain suction dredger is mainly used for the extraction of sandy material. [1]

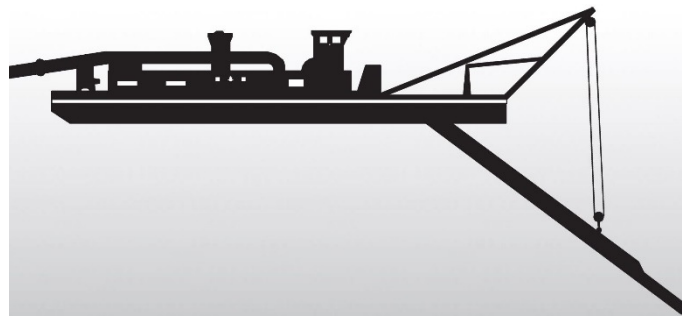


Fig. 2: Sketch of the Plain Suction Dredger [1]

Cutter Suction Dredger (CSD)

This type of equipment uses a combination of mechanical and suction dredging. Thereby, the material to be retrieved is cut with a cutter head and loosened up by the water flowing towards the suction mouth. In addition, jets attached to the cutter head can be used to increase its erosive power. The transportation of the material can either be carried out via pipelines or with the help of barges, on which the dredged material gets pumped. Depending on their installed power, the field of application for CSDs can range from dredging silt and soft clay up to moderately strong rock. [1]

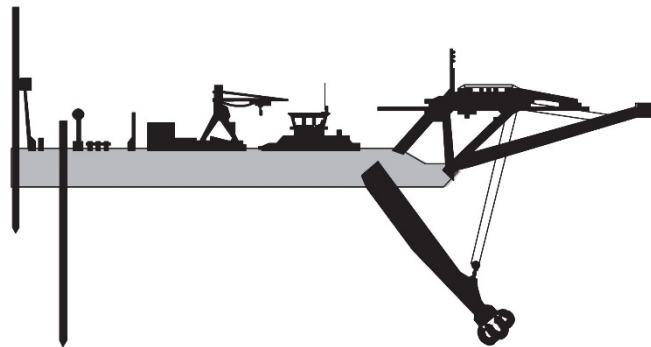


Fig. 3: Sketch of the Cutter Suction Dredger [1]

Trailing Suction Hopper Dredger (TSHD)

The TSHD can as well be assigned to the field of hybrid dredging equipment, combining mechanical cutting and suction dredging. During operation, one or two suction pipes get lowered to the seabed. The material gets loosened by a combination of cutting with the draghead, attached to the lower end of the suction pipe, and the waterflow towards the suction mouth with additional support of jetting streams. The eroded material is then pumped into the vessel's hopper and an overflow system is used to discharge excessive process water overboard. When the hopper has reached its maximum capacity, the vessel transports the fill towards the reclamation area. The filling material is then discharged by opening valves at the vessel's bottom, via pipelines, or by so-called rainbowing. A variety of materials, including clay, silt, sand and even weak rock can be dredged by the TSHD. [1]

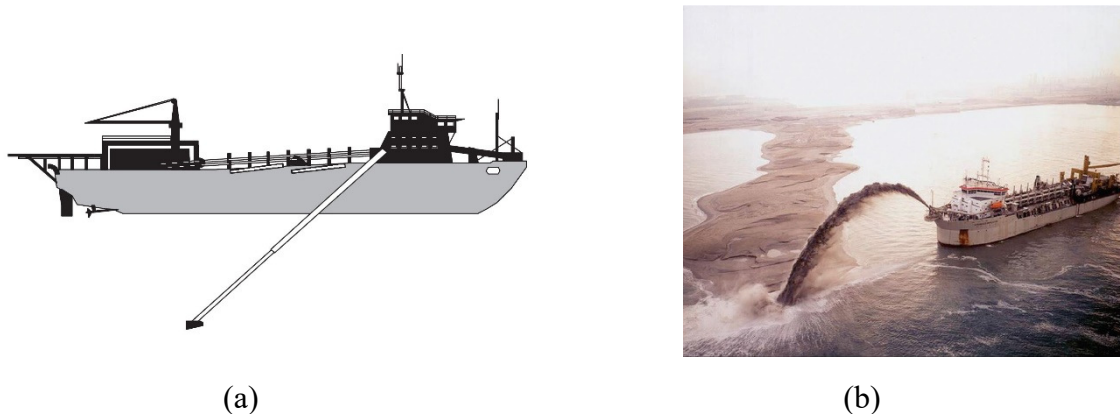


Fig. 4: Sketch of the Trailing Suction Hopper Dredger (a) and fill placement using rainbowing (b) [1]

MECHANICAL DREDGING:

Backhoe dredger

The Backhoe dredger consists of a hydraulic excavator attached to a swimming pontoon, which places the material either in a barge, in its own hopper or on land next to it. During dredging the pontoon can be secured in position using spuds (vertical elements which can be raised and lowered). With this type of mechanical dredger, materials such as compacted sand, stiff clay and weak rock may be dredged. [1]

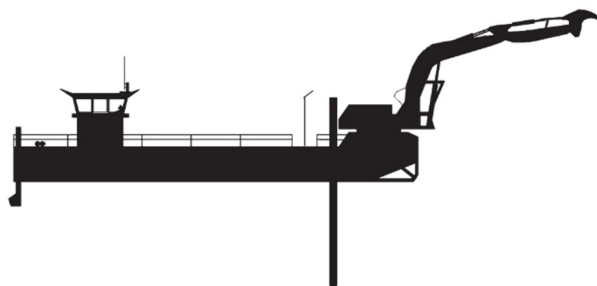


Fig.5: Sketch of a backhoe dredger [1]

Grab dredger

The equipment uses a wire crane installed on a pontoon for the extraction of material. Thereby, securing against movement is facilitated with the aid of wire anchors or spuds. The excavation forces are only determined by the shape and the weight of the grab, which is why this dredger's operation is limited to materials with a low strength. One of the biggest advantages of the grab dredger is its capability of reaching great depths (only limited by the length of the wire). [1]

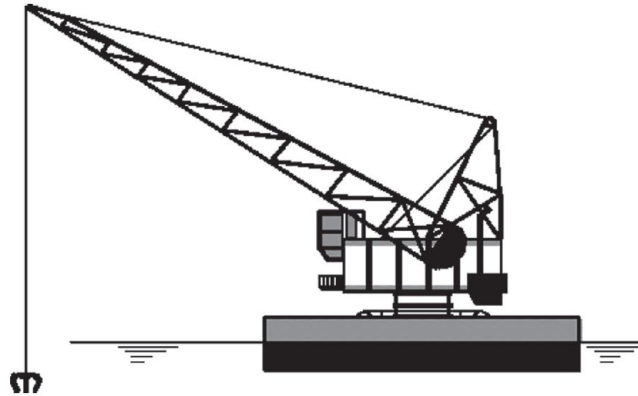


Fig. 6: Sketch of a grab dredger [1]

2.1.2 Transport and Placement of Dredged Material

There are two main methods available for the transport of dredged fill material. The hydraulic transport via pipelines allows for a maximum pumping distance for crushed rock and gravel of up to 4 to 5 km and up to 15 km for fine sands and silt. For projects in which hydraulic transport can't be efficiently used, hopper dredgers or barges may be utilized to carry the fill material towards the reclamation area. [1]

Hydraulic Transport through a Pipeline

After the soil mixes up with large amounts of water during the dredging process, the formed "slurry" is pumped through a pipeline from the borrow area to the designated location. Thereby, the water acts as a medium to facilitate the transportation process. Once the sand-water-mixture reaches the reclamation area, the solid grains will settle, and the discharge water gets drained off. [1]

The pipelines can either be installed onto swimming pontoons or floating jackets or can be laid onshore. Depending on the situation at the reclamation area the discharge of the material may either take place on land, from a spreader pontoon, a diffuser or another floating discharge device. [1]



Fig. 7: Transition between floating and onshore pipeline [12]

Transport by Barge or TSHD

Barges and TSHDs are equipped with storage hoppers. Once the hoppers are filled with material, the vessels start sailing towards the discharging point. There are several options for the discharge available [1]:

- Material discharge via bottom valves
- Material discharge through pipelines
- Material discharge through a nozzle attached to the vessel's bow (rainbowing)

The material can either be dropped-off at the desired fill area or at a so-called re-handling (interim) pit, from which the material gets dredged again, e.g., by suction dredgers. The second option has the advantage of reducing discharging times of TSHDs and waiting times, when several dredgers want to simultaneously connect to the same floating pipeline. The use of interim pits can also encourage a more continuous fill supply to the location of reclamation. [1]

The transportation by barges and TSHDs is preferred especially when long haulage distances must be dealt with and too few long pipelines are available. [1]

Placement of the Fill Material

The different methods for the fill placement have already been discussed in chapter 2.1.2.

The placement of fill material usually starts under water. Once the filled layers reach the water level, the filling can continue in a dry environment. The chosen placement method depends on various factors, such as the nature of the fill material, the desired placement accuracy or the environmental requirements. To increase the horizontal spreading

resistance and stability of the filled material, or to control the water table within the reclamation area, the fill is often bounded by containment bunds. [1]

Fig. 8 shows the construction of such bunds for the situation below the water table using a grab dredger.

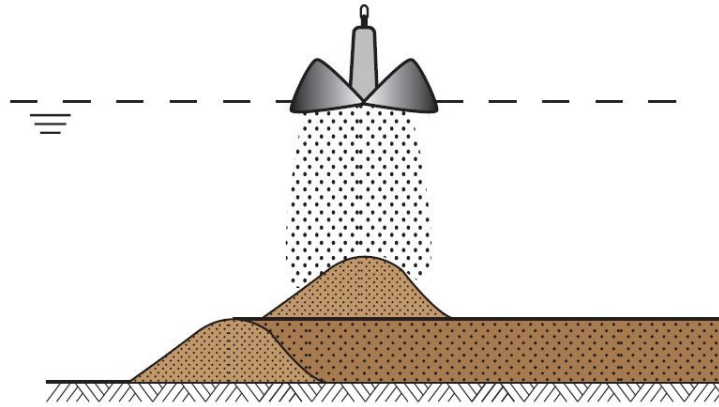


Fig. 8: Underwater bund construction using a grab dredger [1]

In general, placing the fill underwater results in a lower density than above water. The higher values for the density above the water table are in most cases attributed to the usage of bulldozer compaction. Another contributing factor is the segregation of particles for the underwater placement, resulting in a higher compressibility of the fill. [1]

2.2 Carbonate Sands

The acquisition of large quantities of the preferred well graded quartz sand as a filling material [1] for land reclamation projects in the UAE is, economically speaking, not possible. Therefore, soil with an inferior quality must be made use of, which gets dredged from the seabed. The most frequently encountered material in the UAE is sand with a varying amount of carbonate content, having a large influence on the materials' properties and its mechanical behaviour. The following paragraphs in this chapter will briefly explain the origin and definition of the carbonate sands, the main characteristics of calcareous sands and the influence of the carbonate content on the material properties.

2.2.1 Origin and Definition of Carbonate Sands

Carbonate soils are defined as soils made up of a varying amount of different types of carbonate minerals. Their natural deposits are distributed widely over the warm and shallow seas and oceans within latitude 30° north and 30° south. These areas are known as the world's tropical and subtropical regions. [1]

The formation of carbonate soils can occur in different ways. The most important formation process is the accumulation of skeletal remains of marine organisms, e.g., shells or coral lumps. Another noteworthy process is the formation through the chemical precipitation of a carbonate-rich water solution. [13]

One of the most frequently entailed type of carbonates within carbonate sediments is known to be Calcium Carbonate ($CaCO_3$). The adjective “calcareous” sand has often been used to describe sands consisting predominantly of carbonates, however, the term “carbonate sand” is to be preferred as it doesn’t preclude other types of carbonate minerals than $CaCO_3$ [13].

To prevent general confusion regarding the designation of sediments containing carbonate minerals Clark and Walker [14] proposed the following classification nomenclature for carbonate sands:

- Carbonate content > 90 % → “carbonate” sand
- Carbonate content 50 – 90 % → “siliceous carbonate” sand
- Carbonate content 10 – 50 % → “calcareous” sand

To simplify terminology throughout the entire scope of this thesis, the designation of soils, containing carbonate minerals, is kept more general and the terms “carbonate” and “calcareous” are used equally.

2.2.2 Characteristics of Calcareous Sands

In contrast to the rounded grains of silica sands, the grain shape of bioclastic carbonate sand is rather flaky with a high angularity. In combination with poor grading and intra-particle porosity, the high angularity leads to higher initial void ratios than for quartz sands at a comparable material state. [1]

Another very typical property of the mineral Calcium Carbonate ($CaCO_3$) is its softness. Classified by the Moh’s hardness scale, $CaCO_3$ only reaches a value of 3, compared to quartz sand with a value of 7. This has a distinct impact on the material’s crushability behaviour and therefore also results in a high compressibility. High stress concentrations at grain contacts due to the grains’ pronounced angularity are also encouraging particle breakage.

Almeida et. al [7] performed a crushability study on calcareous Quiou sand with a carbonate content of more than 80 %. A number of 4 oedometric compression tests (OCT) were conducted on saturated specimens, which were subjected to different maximum stress levels. After each test, the grading curves were determined and the mean grain size D_{50} was calculated. Fig. 9, in which the D_{50} -values are plotted against the effective mean pressures p' (logarithmic scale), clearly depicts the influence of the particle breakage on the grading curves. With increasing stress level, grain crushing results in a bigger content of fines, and therefore a smaller value of D_{50} .

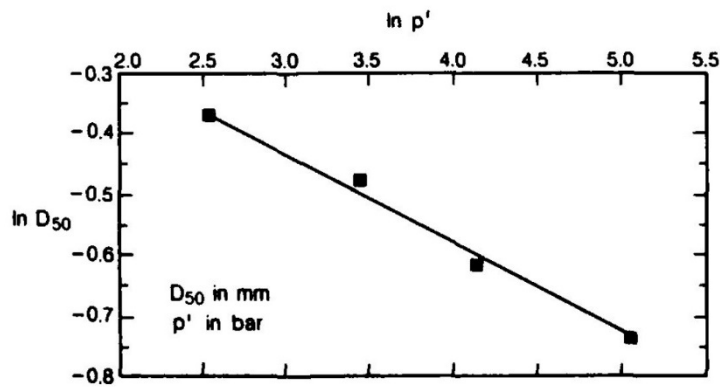


Fig. 9: Crushing of Quiou sand during oedometer tests.

The effect of precipitation of carbonates, or other salts, from saturated pore water often leads to the phenomenon of cementation of the grains. This generally increases the shear strength and stiffness of the placed fill but reduces the production rate of a dredger. [1]

2.2.3 Interrelation Carbonate Content – Soil Properties

In his studies, Reinisch [2] was able to show that the carbonate content of a sand is primarily influencing three basic geotechnical parameters, namely the limit void ratios e_{min} and e_{max} (counted as one parameter), the friction angle φ_c and the grain density ρ_s . In total Reinisch investigated 23 different materials, either found in literature or within the database of KELLER, incorporating a carbonate content ranging from 0 to 100 %. The materials under investigation can be found within A. Tab. 1: .

Limit Void Ratios e_{min} and e_{max}

Both parameters, e_{min} and e_{max} , tend to increase with increasing content of $CaCO_3$. This behaviour is believed to be attributed to the high angularity of the single grains forming a strong interlocking skeleton with a high number of voids. The occurrence of intra-particle porosity in contained coral lumps is another contributing factor. [2] Fig. 10 depicts the relation between the carbonate content and the void ratios e_{min} and e_{max} .

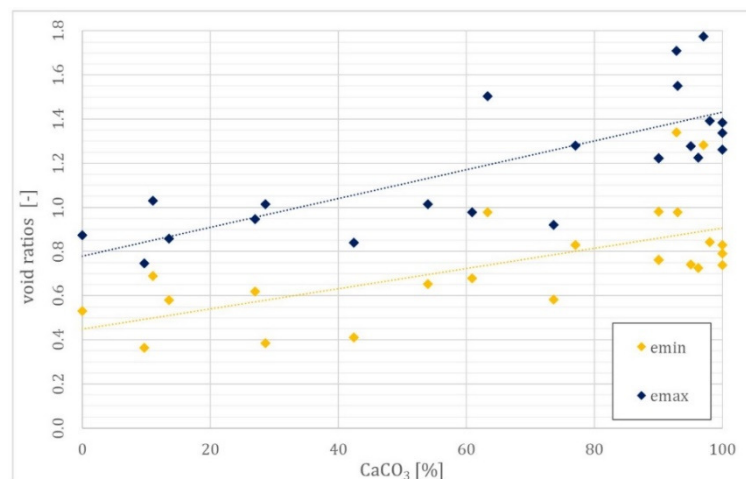


Fig. 10: Relation between the content of carbonates and the limit void ratios e_{min} and e_{max} [2]

Critical Friction Angle φ_c

Also, the friction angle shows a distinct rise with increasing carbonate content. Again, the interlocking particles are supposed to be the main contributing factor. Being exposed to different environmental influences, the grains of calcareous sands tend to break into smaller angular particles rather than getting rounded through grinding over time, like it is the case for the harder quartz grains. This fact maintains the high angularity of the grains which confirms the above mentioned hypothesis. [2] In Fig. 11, the relationship between an increasing carbonate content and the friction angle φ_c is shown.

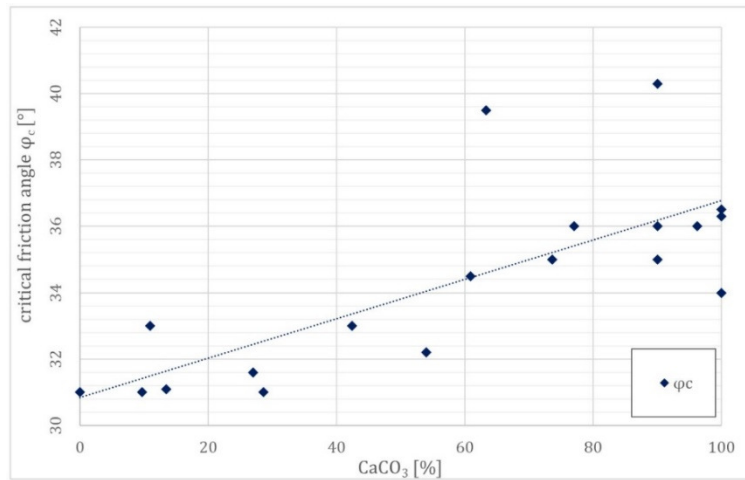


Fig. 11: Relation between the content of carbonates and the critical friction angle φ_c [2]

Grain Density ρ_s

Fig. 12 shows a rising grain density for an increasing content of $CaCO_3$. The reason therefore lies in the different types of minerals occurring either in silica sands or calcareous sands. While silica sands are mainly composed of silicon dioxide (SiO_2), with a density of 2.6 – 2.7 g/cm³, carbonate sands are made up primarily of calcite, with a density of 2.7 g/cm³, or even seashells and corals, containing the mineral aragonite, which has an even higher density of up to 3.0 g/cm³. [2]

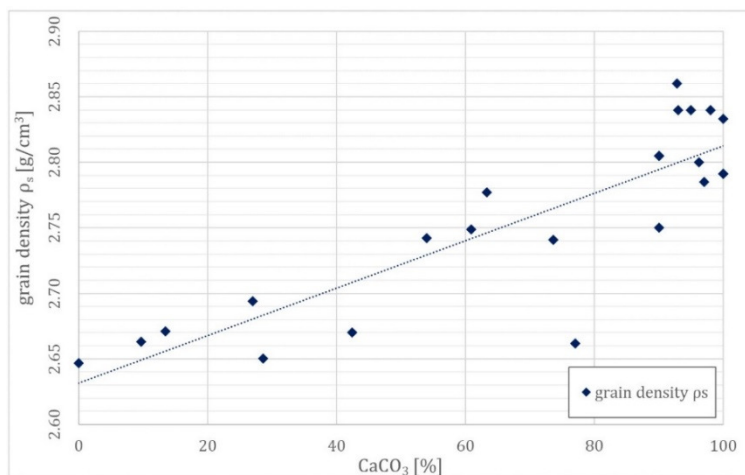


Fig. 12: Relation between the content of carbonates and the grain density ρ_s [2]

2.3 Vibro Compaction of Reclaimed Land

One of the most important steps to be taken in land reclamation works is the compaction of the placed fill by the application of different ground improving techniques. A proper compaction is necessary for the fill to reach the desired properties regarding its stiffness, shear strength and liquefaction resistance.

The aim of contractors commissioned with ground improvement works on reclaimed land is to transfer the fill, with an initial density right after the placement, into a denser state which relates to the aforementioned requirements. The denser state is defined by a contractually agreed minimum value for the relative density I_D . The difficult task is to compact the material up to the point, when a sufficient compaction is reached. Should the density after compaction be below the requirements, the contractors are forced to recompact the areas with the insufficient density which means that their economical effort is increasing rapidly. A compaction far beyond the criterion basically has the same effect. The key lies in finding the sweet spot.

As vibratory-compaction is the main ground improvement technique used for the KELLER projects within the UAE, the subsequent sections will solely focus on this method and explain it in more detail.

2.3.1 Equipment and Limits of Application

Loose to medium dense clean sands are generally densified as the particles become rearranged more closely under the presence of vibrations. The range of influence for surface compaction using vibratory rollers is limited to a depth of around 1.5 m. For deeper sand deposits deep compaction methods such as vibro compaction must be applied. Thereby, generated horizontal vibrations break the frictional contact between the soil particles to allow them to rearrange themselves to a state of lower potential energy (from loose to dense). [15]

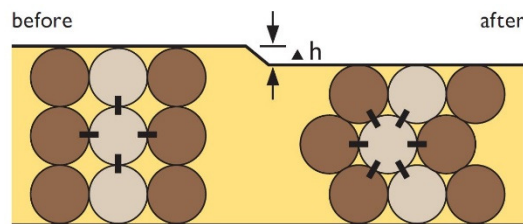


Fig. 13: Compaction mechanism [16]

The vibrations are caused by depth vibrators, consisting of a cylindrical steel tube (external diameter 300 to about 500 mm) containing a rotating vertical shaft, with an eccentric weight attached to it, which is linked to an electric motor. The vibrators are usually between 3 to 4.5 m long and weigh in between 1500 to 4500 kg [15]. In most cases they are installed on huge crawler cranes which facilitates the working process and

allows for a fast relocation of the vibrators according to the spacing of the compaction grid. Fig. 14 displays the cross-section of a typical modern depth vibrator.

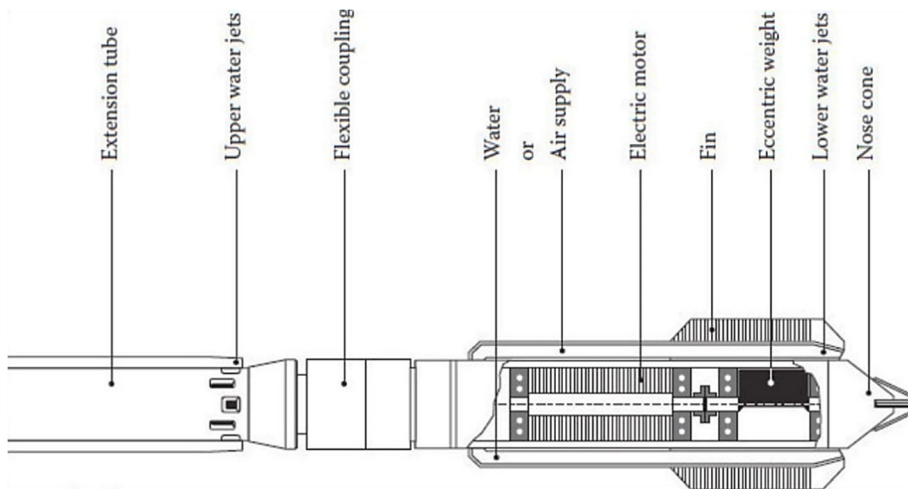


Fig. 14: Cross-section of a modern depth vibrator [15]

The grain size distribution of a fill material is the main decisive factor in choosing an appropriate compaction technique. Vibro compaction can only be applied to granular materials, such as sands and gravels, incorporating a fines content below 10 %. Larger percentages of fines will considerably obstruct the densification process, if not prevent it totally. [15]

Fig. 15 displays the limits of application, with respect to the grain size distribution of a fill material, for two deep compaction methods, namely the vibro compaction and the vibro replacement method. The latter method is based on the introduction of aggregate columns into the ground to increase the bearing capacity and can be applied to soils with a fines content higher than 10 %.

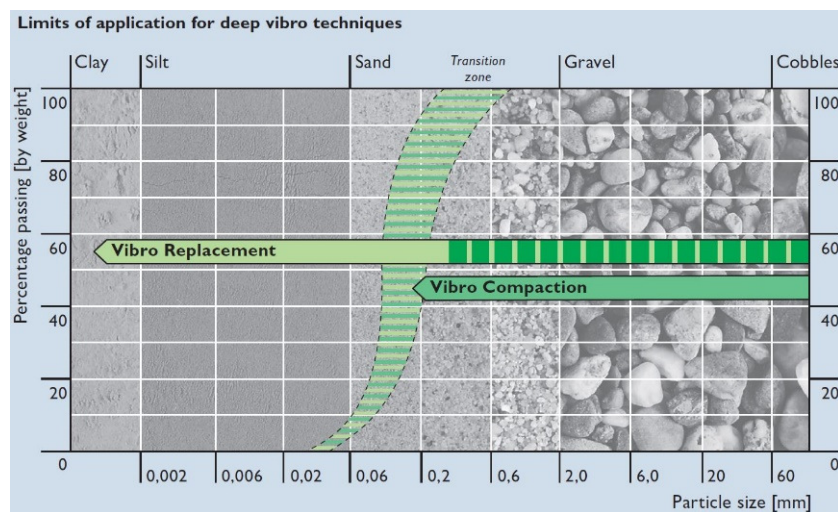


Fig. 15: Limits of application for deep vibro techniques [16]

2.3.2 The Process of Vibro Compaction

The vibro compaction process includes 4 different steps to be carried out one after the other. For each point in the compaction grid, these 4 steps are repeated.

During step 1, referred to as the penetration stage, the running vibrator is lowered down to the designated penetration depth. This is done under the presence of a water flush, which helps to remove fines and to form an annular gap around the vibrator to ease the penetration process. Once the desired depth is reached, the water flush is reduced or switched off completely. [16]

Step 2 is the so-called compaction phase. Thereby, the oscillating vibrator is withdrawn in sections of up to 1 m and kept at a certain level for at least 30 s to provide a proper densification of the surrounding soil body [15] (up to 5 m in diameter [16]). The amount of densification can be concluded from an increased power consumption of the vibrator [16].

In step 3 material has to be backfilled as the soil is collapsing wedge-shaped around the vibrator during the compaction phase. In total a volume of up to 15 % of the treated soil is required to fill up the produced craters. [16] In other words, the backfill material is needed to compensate the reduction of the pore volume due to the densification.

Step 4 involves the final treatment of the surface of compacted fill material. The surface gets re-levelled and compacted by vibratory rollers, if necessary. [16]

Fig. 16 pictures the 4 steps involved in the process of vibro compaction. Step 1 (penetration) can be found on the very left, step 2 (compaction) in the middle and step 3 and 4 (backfilling and finishing) both on the right-hand side.

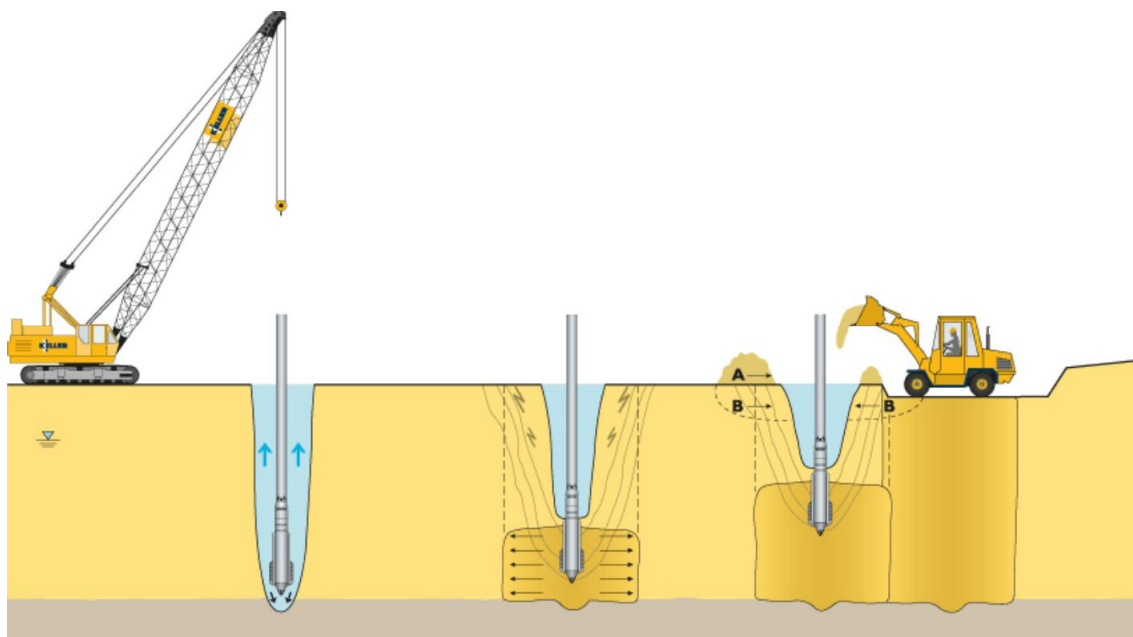


Fig. 16: The process of vibro compaction [16]

3 Quality Control of Compaction Works

The most sophisticated tool to control the quality of soil compaction measures is the cone penetration test (CPT). By using appropriate correlations between the measured cone resistance q_c and the technical formulation of the density state, the relative density I_D , it can indirectly be implied, whether the minimum requirements regarding strength and stiffness of the soil have already been attained through the employed compaction measures.

In this chapter the CPT testing procedure, the used equipment and a specific testing program for one project of the KELLER Grundbau GmbH will be presented. Further, the most commonly applied CPT interpretation methods and their derivation from calibration chamber tests (CCT) will be demonstrated, as well as the reason will be mentioned, why their use on carbonate sands might not be the first choice.

3.1 Cone Penetration Test (CPT)

The cone penetration test is a well-established in-situ testing method to derive information on the geotechnical properties of a soil material and to depict the present stratigraphy.

In cone penetration testing a cone attached to the end of a series of rods is pushed into the ground at a constant rate. The nature of the instrumentation allows for a continuous measurement of the penetration resistance of the cone during the penetration, as well as the resistance on the outer sleeve of the cone. The cone resistance q_c can be determined by dividing the total force Q_c acting on the cone by the projected area of the cone A_c . The sleeve friction f_s is obtained in the same manner by dividing the force F_s acting on the friction sleeve by the surface area of the friction sleeve A_s . Additionally, the developing pore pressures during the penetration process can be measured by the application of so-called piezocones. [17]

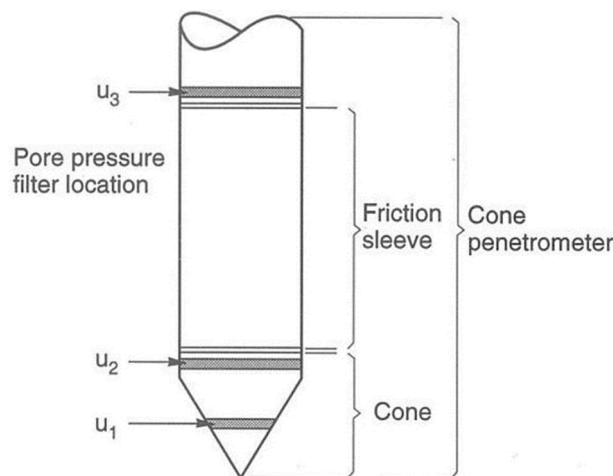


Fig. 17: Different parts of a cone penetrometer with u_i depicting the positions of pore pressure measurement [17]

3.1.1 Testing Equipment

In its standard form the CPT equipment consists of a cone penetrometer, with or without pore water measurement (CPTU or CPT), the pushing equipment and the data acquisition system. [17]

In most cases a 60° cone penetrometer with a 10 cm² base area (35.7 mm diameter) and a 150 cm² friction sleeve area is used. However, an increasing number of inbuilt sensors results in larger diameters of the cone and 15 cm² cones are more and more commonly applied. [17]

In general, the rod system with the attached penetrometers are pushed into the ground using either specially build CPT trucks with a high dead load or smaller CPT rigs, which incorporate an anchoring system to secure the unit against off-lifting when pushing.



(a)



(b)

Fig. 18: Typical CPT pushing equipment
(a) CPT truck with crawling aid, (b) small rig [18]

3.1.2 Penetration of the CPT Rods

The testing rods are pushed into the ground at a rate of 20 ± 5 mm/s and a maximum thrust on the standard 35.7 diameter cone of up to 200 kN. When this value for the thrust is exceeded it may result in a damage of the steel rods due to buckling at the rig or the upper soft layers of soil. The penetration resistance, and therefore the axial force within the rods can be reduce by the application of a so-called friction reducer. It gets installed at a distance between 0.3 and 1 m behind the cone with the idea to expand the diameter of the hole and reduce the friction between the rods and the soil. Another way to increase the penetration depth would be the usage of drilling mud acting as a lubricant to reduce the friction. [17]

Robertson et al. [19] reported penetration depth exceeding 100 m in soft soils when using appropriate methods for the reduction of the frictional forces acting between the pushing rods and the surrounding soil.

3.2 CPTs at the KELLER Project PLM (Dubai)

This section focuses on the carried-out cone penetration tests in the course of quality control of the vibro compaction works for the Keller project Port de la Mer (PLM) in Dubai.

Generally, the quality of compaction measures can be assessed by comparing the results for the cone penetration resistance q_c of pre- and post-compaction CPTs. For the specific project the pre-compaction CPTs were carried out on a grid of 100 x 100 m, whereas the grid for the post-compaction CPTs was chosen with 25 x 25 m. [2]

The vibro-compaction points (black dots) were arranged in a triangular pattern as can be seen in Fig. 19. Additionally, the locations of possible CPT points (red dots) are depicted.

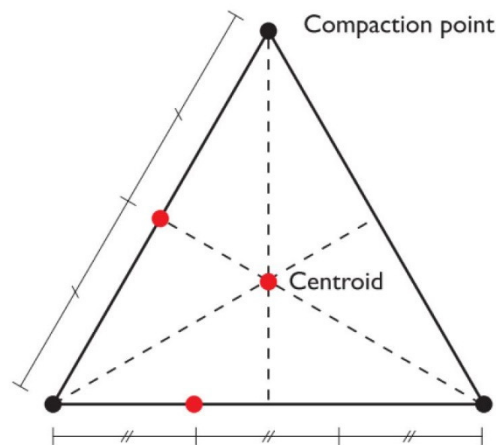


Fig. 19: Triangular pattern of compaction points and possible CPT points (red dots) [2]

In every box of 25 x 25 m two post-compaction CPTs were performed at the location in the centre of one compaction triangle, depicting the point with the least amount of densification, and additionally at 1/3 of the distance between two compaction points. The results of both cone penetration tests were then averaged using a rolling mean over a depth increment of 40 cm (20 cm above and 20 cm below) to minimize the influence of existing thin layers of less compacted fill. [2]

Fig. 20 shows such averaged q_c -profiles received from pre- and post-compaction CPTs for the PLM project in Dubai. The increase in the cone penetration resistance q_c indicates the desired effect of densification, especially for the layers deeper than 4 m.

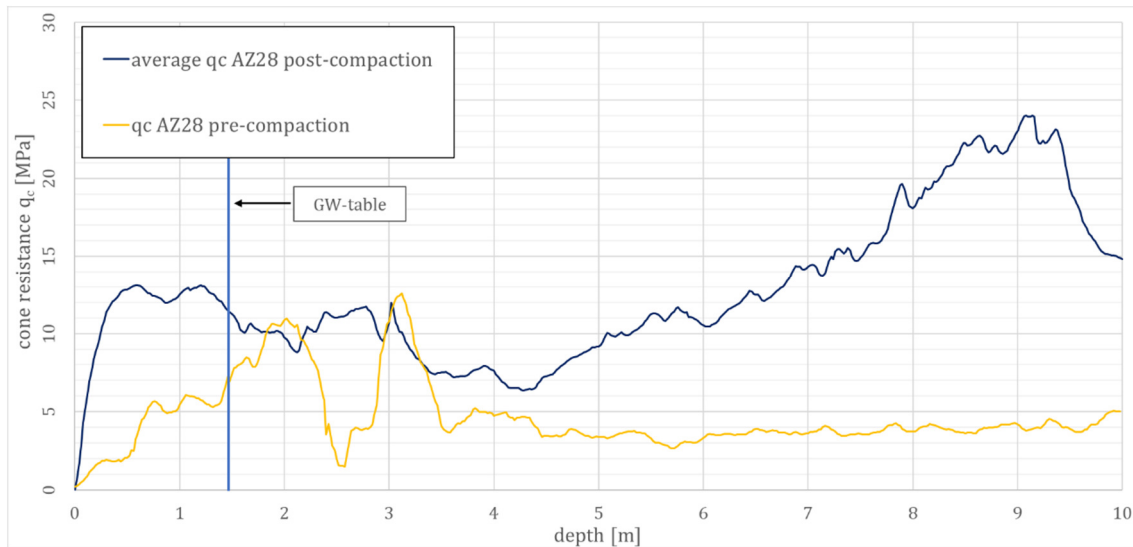


Fig. 20: q_c -profiles from pre- and post-compaction CPTs [2]

The contractually-agreed compaction requirements are in most cases formulated in terms of the relative density I_D . Various CPT interpretation methods have been developed which can be used to come up with a reference curve for the cone resistance q_c over the depth, relating to exactly this defined value of I_D . The measured curves after compaction can then be compared to the reference curves to see if the requirements over the whole depth are met.

3.3 CPT Interpretation Methods used in Geotechnical Practice

To receive a better understanding of the purpose of this master's thesis and the need for a specific CPT interpretation method for the carbonate materials encountered at the land reclamation projects in the UAE, the following paragraphs will explain the most commonly used interpretation methods, which are generally derived from performing a series of calibration chamber tests and point out their limitations.

3.3.1 Calibration Chamber Tests

In calibration chambers, CPTs can be performed under controlled boundary conditions. The radial and vertical stresses (σ_r and σ_v) can be imposed independently to the sample with the aid of air cushions [6]. This feature enables the intensive study of the relationship between the measured cone penetration resistance q_c and the relative density I_D [2]. The findings from such studies are the basis for the development of CPT interpretation methods which can further be applied to the correlation of q_c and I_D with respect to site-specific materials and soil conditions.

Calibration chambers (CC) are large cylindrical containers in which the testing material is placed at a known relative density I_D . With the aid of the air cushions the sample can

be consolidated to each desired stress state. A CPT is performed and the value for q_c can be determined for a certain material state, in terms of the relative density I_D and the stresses σ_1 and σ_3 . [2]

Fig. 21 illustrates the cross-section of the calibration chamber as can be found at the University of Karlsruhe. It features a diameter of $d = 92$ cm and a height of $h = 150$ cm and uses a standard 10 cm^2 cone for the conduction of the cone penetration tests. The sampling rate, at which the values for the cone resistance, the radial and vertical boundary pressures and the penetration depth are collected, comes at 10 Hz. [6]

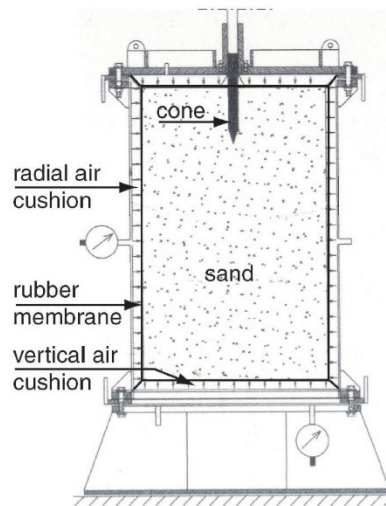


Fig. 21: Cross-section of the calibration chamber found at the University of Karlsruhe [6]

INFLUENCE OF BOUNDARY CONDITIONS:

The q_c -values obtained from calibration chamber testing cannot be directly compared to the actual values measured in the free field for the same material state due to the influence of boundary effects of the calibration chamber. With decreasing diameter of the chamber and increasing density of the placed sample the influence of the boundary conditions increases. [6]

Mayne and Kulhawy [20] stated that at a ratio of $\eta = D_s / d_c \geq 70$ (D_s sample diameter, d_c cone diameter) the free field conditions can be achieved and therefore no correction is needed. For the CC at Karlsruhe University η amounts to 26, which means that the measured values for q_c should be corrected acc. to the correction factor proposed by Mayne and Kulhawy [20],

$$k_c = \frac{q_{c,corrected}}{q_{c,measured}} = \left(\frac{\eta - A}{\eta_0} \right)^{-\frac{I_d}{B}} \quad (3.1)$$

where $A = 1$, $B = 200$ and $\eta_0 = 70 = \eta$ for which the influence of the boundary effects is negligible. It is suggested by Cudmani [8] to use $A = 0$ and calculate B separately for different Materials based on calibration chamber test results to allow for different granulometric properties to be considered by the correction.

STUDIES PERFORMED AT THE UNIVERSITY OF KARLSRUHE:

Meier [6] performed a series of calibration chamber tests with the apparatus encountered at Karlsruhe University on carbonate Dubai sand which he mixed up with different amounts of Karlsruhe silica sand to study the effect of particle breakage on the measured values for q_c . He used 5 different mixtures M0, M15, M30, M60, M100 with the label Mxx specifying the content of Dubai sand of xx%. The index properties of both materials can be found in A. Tab. 2.

Meier [6] used $A = 0$ and assumed $\eta_0 = 100$. To come up with the B parameters for the different mixtures, needed for the calculation of the correction factor k_c , he simulated 2 CPTs for each material with $\eta = 26$ (CC in Karlsruhe) and 100 (free field conditions) respectively using FE-modelling and incorporating a hypoplastic constitutive equation. He then received a value $q_{c,m,simulated}$ (q_c corresponding to the CC in Karlsruhe) and a value $q_{c,c,simulated}$ (q_c corresponding for the free field) and was able to calculate B from Eqn. (3.1). Tab. 1 shows the derived values for B of the different mixtures.

Tab. 1: B-values from Meier's studies on different materials [6]

	M0	M15	M30	M60	M100
B	3.882	4.830	5.911	7.261	6.511

In general, it can be observed that the values for B increase with an increasing shell content. The outlier for B of material M60 can be justified by problems with the calibration of the hypoplastic constitutive model used for the CPT simulation of this material. [6]

The results from the performed calibration chamber tests by Meier [6] can be found in A. Tab. 3. Therein, the mean pressures p_0 , the coefficients of lateral earth pressure K , the initial void ratios e , the relative density I_D , the measured values for the cone resistance $q_{c,m}$, the correction factor k_c and the corrected value for the cone resistance $q_{c,c}$ for all performed tests are given. Negative values for I_D are received from a very loose sample placement with $e > e_{max}$ as obtained from standard laboratory tests. For one material Meier performed up to 12 CCTs.

For the given values of k_c and I_D in A. Tab. 3 it was now tried to back-calculate the values for B stated in Tab. 1 using Eqn. (3.1). The results of this procedure suggested that it is not sufficient to provide the values for k_c only with two digits after the comma, as the stated values for B (Tab. 1) could not exactly be reproduced.

Tab. 2 depicts the back-calculated B -value $B_{calculated}$ from the k_c -value $k_{c,table}$, given in A. Tab. 3, with only two digits after the comma for test 1 on material M100. Additionally the k_c -value $k_{c,calculated}$ received from Meier's value for B for M100 using Eqn. (3.1) is represented in Tab. 2. It was found that it is necessary to provide the value for k_c with at least 5 digits after the comma to obtain the exact same value for B (B_{M100}) as Meier, when B is back-calculated from Eqn. (3.1). The values for the other parameters within Eqn. (3.1) were chosen in agreement with the ones used by Meier, this is $A = 0$, $\eta_0 = 100$ and $\eta = 26$. The calculations for all other tests and materials can be found in A. Tab. 4.

Tab. 2: B from k_c provided by Meier vs. B from accurate k_c for CCT M100-1

Test	$k_{c,table}$ [-]	$B_{calculated}$ [-]	$k_{c,calculated}$ [-]	B_{M100} [-]
M100-1	1.03	5.924	1.02726	6.511

At this point it is stated that the calculations for test M100-1 produced the smallest B -value from all tests conducted on material M100 with $B_{calculated} = 5.924$, whereas the highest value was received for test M100-3 with $B_{calculated} = 6.902$.

What we can learn from this small study is that for the determination of the B -value for a specific material from FE-simulations of the calibration chamber test the correction factor $k_c = q_{c,c,simulated}/q_{c,m,simulated}$ has to be provided with sufficient accuracy in order to end up with accurate values of B .

3.3.2 Interpretation Method - German Standard DIN 4094

The German standard DIN 4094-1:2002 provides two purely empirical equations for the calculation of the relative density I_D from the measured cone penetration resistance q_c . The equations are based on tests performed in the 1950s and 1960s on Berlin sand, which is a mixture of quartz and feldspar. The coefficient of uniformity $C_u = d_{60}/d_{10}$ of the material to be correlated decides which one of the two equations has to be applied. [6]

$$I_D = -0.33 + 0.73 \cdot \log(q_c) \quad C_u \leq 3 \text{ and } 3 \leq q_c \leq 30 \quad (3.2)$$

$$I_D = -0.25 + 0.31 \cdot \log(q_c) \quad C_u \geq 6 \text{ and } 3 \leq q_c \leq 30$$

A value of $C_u = 1$ means that the soil consists of grains which are all the same size, whereas a higher value is indicative of a grain size distribution that describes a balanced amount of coarse and fine grains [21]. Hence, the value of $C_u = 3$ can be associated to a poorly graded material, whereas a value above 6 is characteristic for a well graded soil. The Eqns. (3.2) are not applicable to any materials with a coefficient of uniformity in between 3 and 6.

This interpretation method has the big disadvantage that it doesn't consider important granulometric properties, such as the compressibility and the hardness of the grains. It also doesn't offer the opportunity to account for the stress state of the investigated

material, which are the reasons why this method should be withdrawn these days and more sophisticated interpretation methods should be given priority.

3.3.3 Interpretation Method - Schmertmann

The following empirical relationship for the interpretation of cone penetration tests performed in normally consolidated (NC) quartz sands was proposed by Schmertmann [3]:

$$q_c = C_0 \cdot \sigma'_v{}^{C_1} \cdot \exp(C_2 \cdot D_r) \quad (3.3)$$

$$I_D = \frac{1}{C_2} \cdot [\ln(q_c) - \ln(C_0 \cdot \sigma'_v{}^{C_1})] \quad (3.4)$$

Schmertmann recognised the importance of covering the stress state of a material within the relationship between the measured cone penetration resistance q_c and the relative density I_D and included the effective vertical stress σ'_v in his formulation of this relation. The C_i constants in Eqn. (3.3) and Eqn. (3.4) take into account the characteristics of a specific material. Throughout the years a few researchers came up with different sets of C_i - values which are derived from calibration chamber testing on different materials [2]. Tab. 3 lists some of these sets.

Tab. 3: C_i -constants for the CPT interpretation method acc. to Schmertmann

Correlation	Sand type	C_0	C_1	C_2
Schmertmann (1976)	quartz	12.31	0.71	2.91
Baldi et al. (1986)	quartz	157	0.55	2.41
Meier (2007) [6]	quartz	9.39	0.85	3.89
	carbonate	14.23	0.67	2.90

Schmertmann performed 80 different calibration chamber tests on different materials (with and without a tendency to grain fracturing) to come up with his set of constants C_i , which he proposed for general use. [6]

The C_i -values provided by Baldi [22] were obtained from performing numerous calibration chamber tests on Ticino sand.

In the scope of his PhD thesis, Meier [6] determined the specific values for C_i of the materials under investigation, namely Karlsruhe quartz sand and carbonate Dubai sand. Using these sets of C_i -values for the CPT interpretation acc. to Schmertmann he was able to show that Eqn. (3.4) can yield good results, when the constants are calibrated for a specific material.

Baldis values for C_i can be entered directly into Eqn. (3.3) and Eqn. (3.4) together with q_c and σ'_v provided in kPa [2], whereas for the usage of the constants of Schmertmann and Meier, q_c and σ'_v have to be converted from kPa to kgf/cm² (1 kPa = 0.01019716 kgf/cm²) [6].

3.3.4 Interpretation Method – Jamiolkowski

Jamiolkowski et al. [4] adapted the correlation method acc. to Schmertmann [3] by incorporating the atmospheric pressure p_a (98.1 kPa) and evaluated the set of C_i -values having recourse to a total number of 484 calibration chamber CPTs performed on three different silica sands. The cone resistance q_c and the vertical effective stress σ'_v in Eqn. (3.5) and Eqn. (3.6) can be entered in kPa.

$$q_c = C_0 \cdot p_a \cdot \left(\frac{\sigma'_v}{p_a}\right)^{C_1} \cdot \exp(C_2 \cdot D_r) \quad (3.5)$$

$$I_D = \frac{1}{C_2} \cdot \left[\ln(q_c) - \ln\left(C_0 \cdot p_a \cdot \left(\frac{\sigma'_v}{p_a}\right)^{C_1}\right) \right] \quad (3.6)$$

The values for the constants to be used with the interpretation method proposed by Jamiolkowski et al. [4] are listed in Tab. 4.

Tab. 4: C_i -constants for the CPT interpretation acc. to Jamiolkowski

Correlation	Sand type	C_0	C_1	C_2
Jamiolkowski [4]	quartz	17.68	0.50	3.10

3.3.5 Comparison of different Interpretation Methods

The most commonly used interpretation methods applied in geotechnical practice are almost solely based on empirical relations derived for silica sands, containing solid grains which feature only a slight up to no tendency towards grain crushing when exposed to a certain mean pressure level. This makes them indeed suitable for describing the characteristic behaviour of this type of sands, but raises the question if their application on materials with a greater likelihood of the grains towards crushing can also yield realistic results.

Meier [6] performed calibration chamber tests on both, carbonate and silica sands, and compared the results for the relative density I_D , calculated from the different interpretation methods, to the measured results from the tests.

He could prove that the purely empirical method after German standard DIN 4092 is not able to yield satisfying results even for Karlsruhe sand, a pure silica sand. The same applies to the correlation of a 100 % carbonate material (Dubai sand), which can be

justified by the fact that the relation was derived from tests performed on Berlin sand (silica sand). Good results obtained for mixtures of Dubai sand and Karlsruhe sand were rather a coincidence than an evidence for the capability of this method to account for the characteristics of different types of sands.

The also purely empirical relationship acc. to Schmertmann [3] performed quite well in the studies of Meier [6], when the calibrated values for C_i were considered. However, in practice the calibration of the C_i -values for each material encountered at a specific site is rather impractical. The interpretation using the constants suggested by Schmertmann for the general use also ended up in a good agreement of the compared I_D -values in case of all investigated materials. This was unexpected as Schmertmann's correlation is not based on any tests on carbonate sands.

Meier also made use of the semi-empirical interpretation method by Cudmani [8] which gave good results for both investigated pure materials. The advantage of this method is the possibility to account for the actual material properties found in-situ. The method didn't work satisfactorily on the mixtures of both sands which he explained with difficulties in the calibration of the involved hypoplastic constitutive equation. Meier [6] stated that up to now no sufficient data base is available for a final judgement of the applicability of the hypoplastic constitutive equation on materials with a tendency towards grain fracturing and further research is necessary. Then again, the results of Dubai sand demonstrated that a good representation of the mechanical behaviour of materials containing breakable grains is possible, in case of an accurate calibration.

4 The Karlsruhe Interpretation Method

Chapter 4 introduces the readers to the Karlsruhe Interpretation Method (KIM) which can be used for the interpretation of cone penetration tests. To understand this method in principle, a basic knowledge about hypoplasticity and the cavity expansion theory is required. Therefore, an introduction to the basic concepts of hypoplasticity and the hypoplastic model by “von Wolffersdorff” [23], as used within the KIM, will be given. The cavity expansion theory, especially focusing on the spherical cavity expansion, will be presented and the main structure of the Karlsruhe Interpretation Method will be explained.

4.1 Hypoplasticity Theory

Constitutive laws such as the hypoplastic constitutive law can generally be used to describe the mechanical behaviour of materials. Hence, they are mathematical formulations of the stress-strain relationship. [24]

When Kolymbas [25] came up with the first version of a rate-dependent hypoplastic constitutive equation, his main aim was to develop a mathematical relationship to describe irreversible deformations of solids without the need of additional formulations used in traditional elasto-plasticity, such as a yield surface, flow and hardening rules and a plastic potential. Kolymbas didn't distinguish between an elastic and a plastic regime as he was aware of the fact that in reality plastic deformations in soils develop from the beginning on [2]. In contrast to elasto-plasticity he used one single, but complex, equation for the description of the mechanical material behaviour. This equation holds equally for loading and unloading as the distinction between both situations is automatically accomplished by the equation itself [26].

To overcome shortcomings of the original formulation of the hypoplastic constitutive equation, improved versions have been introduced by several authors throughout the years. As there are more than just one constitutive equation based on the fundamentals of hypoplasticity, the term hypoplasticity should rather be conceived as a frame of constitutive equation than a particular one. [26]

The intergranular strain model proposed by Niemunis and Herle [27] in 1997 led to major improvements in hypoplasticity theory. The intergranular strain extension allows to model the effect of a small strain stiffness, to take into account the most recent deformation history and to get a better representation of the material stiffness in case of cyclic loading.

In 2005, Mašin [28] developed a constitutive equation for clay materials. This constitutive law is based on the generalised hypoplasticity principles which he combined with the concepts of traditional critical state soil mechanics. The model requires five input parameters, corresponding to the well-established Modified Cam clay model and it is

relatively simple to calibrate based on standard laboratory tests. Also, it may be combined with the intergranular strain concept.

A lot of research is currently going on in the field of hypoplasticity. Improvements towards a more sophisticated modelling of the non-linearity of soils are targeted. Especially the dependence of the mechanical material behaviour on the density (pyknotropy) and the stresses (barotropy) is part of this research. For example, the friction angle is not a material constant but dependent on the stress state and the stiffness, as well as the volumetric behaviour of the soil, is governed by the density state. All good constitutive models should incorporate these two mechanisms [29].

4.2 Hypoplastic Modell by “von Wolffersdorff”

The hypoplastic model by “von Wolffersdorff” [23] was proposed in 1996. It can be used for the description of the mechanical behaviour of granular materials such as sand and gravel and is the constitutive law of choice [8] to be used in connection with the KIM.

The model requires 8 different input parameters from which 4 are pure material constants obtained from standard testing procedures. The remaining 4 are invariant parameters obtained from the model calibration [23]. Important boundary conditions are the initial stresses and the initial void ratio e_{init} , having a huge influence on the calculation results. Tab. 5 lists the required hypoplastic parameters for the present constitutive equation.

Tab. 5: Hypoplastic parameters required for the model by “von Wolffersdorff”

Parameter		Determination	
critical friction angle	φ_c	angle of repose test	material parameters
limit void ratios	e_{d0}	standard index tests (ASTM D4254/D4253)	
	e_{c0} e_{i0}		
granulate hardness	h_s	high-pressure oedometer test	calibration parameters
exponent	n		
exponent	α	drained triaxial test	
exponent	β		

The general formulation of the constitutive law is a tensorial function of the rate-form, as follows

$$\dot{\mathbf{T}} = \mathbf{f}(\mathbf{T}, e, \mathbf{D}) \quad (4.1)$$

where \mathbf{f} is a function for the stress rate $\dot{\mathbf{T}}$ which is dependent on the stress state \mathbf{T} , the density (void ratio e) and the strain rate \mathbf{D} . Function \mathbf{f} is able to account for pyknotropy and barotropy in terms of factors calculated from scalar functions [23] and is homogenous of first order with respect to the strain rate, this is $\mathbf{f}(\lambda\mathbf{D}) = \lambda\mathbf{f}(\mathbf{D})$, describing a strain rate independent material behaviour [8]. For a more detailed description of the hypoplastic constitutive equation reference is made to [23], [30], [27] and [31].

The model by “von Wolffersdorff”, just like other hypoplastic constitutive models, is only valid under the assumption of a so-called simple grain skeleton. A simple grain skeleton is characterized by the following material properties [30]:

- The state of the simple grain skeleton is sufficiently described by the stress tensor σ and the void ratio e .
- The behaviour of grain skeletons is rate-independent (stress-strain curves do not change with strain or stress rate).
- The corresponding stress paths will become proportional, in case of proportional strain paths, independent of the initial state. This feature is called a SOM (Swept Out of Memory) behaviour and is an important asymptotic property of granular soils.
- In case of fully saturated voids, the mechanical behaviour is only dependent on the effective stress tensor, acc. to Terzaghi’s principle of effective stresses.
- There is an upper (e_i) and a lower limit (e_d) of the void ratio which both decrease with increasing mean skeleton pressure p' . The upper limit void ratio e_i describes the density state of a sample just at the point where grain contacts are still present, but would get lost in case of $e > e_i$. The lower limit void ratio e_d can be reached asymptotically by cyclic shearing. A void ratio of $e < e_d$ would describe a kind of dry masonry, and not a granular material any more, which could sustain vertical loads without a horizontal support. A third limit void ratio, the critical void ratio e_c , exists which is reached after large monotonic shearing.

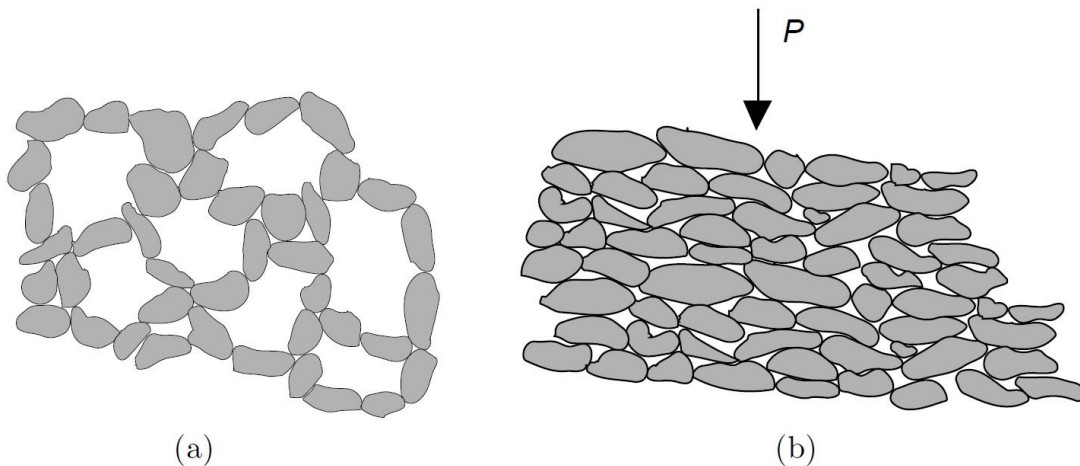


Fig. 22: (a) Macro-voids start to occur for $e > e_i$
 (b) dry masonry forms in case of $e > e_d$

- The grains of a simple grain skeleton are considered as granulometrically permanent (no abrasion or crushing).
- No attractive forces, this are physico-chemical forces or a cementation of grain contacts, are considered.

4.2.1 Determination of the Material Parameters

The reproduction of the mechanical behaviour of a granular material within a simulation is governed by the applied constitutive model. An accurate calibration of the material model, with respect to the material parameters, is an unconditional requirement in order to describe the stress-strain relationship of the sample in the best way possible. The subsequent paragraphs will therefore focus upon the process of hypoplastic parameter determination and explain the effects of changing single parameters.

Limit Void Ratios e_{d0} , e_{c0} , e_{i0}

As already stated in chapter 4.2 certain limiting values for the void ratio exist, which all decrease for an increasing effective mean pressure p' , acc. to the so-called compression law developed by E. Bauer [32],

$$\frac{e_c}{e_{c0}} = \frac{e_d}{e_{d0}} = \frac{e_i}{e_{i0}} = \exp \left[- \left(\frac{3p'}{h_s} \right)^n \right] \quad (4.2)$$

where e_c , e_d and e_i depict the void ratios at a certain pressure level p' and the additional index 0 denotes the limiting void ratios at zero mean pressure. A graphical representation of Eqn. (4.2) is given in Fig. 23,

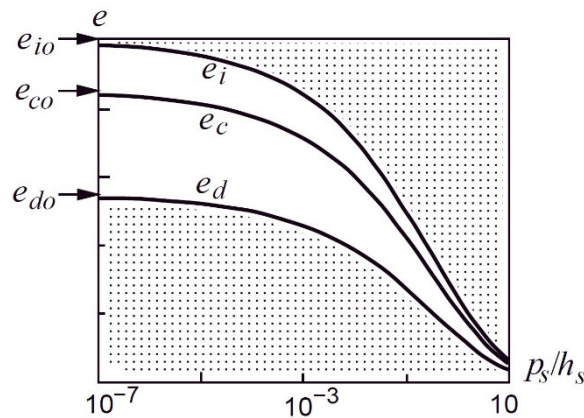


Fig. 23: Pressure dependency of the limit void ratios [30]

where the increasing pressure level is described by the ratio of the effective mean pressure p' and the hypoplastic parameter h_s (granulate hardness).

The maximum void ratio at zero pressure is denoted by e_{i0} which is theoretically reached during isotropic consolidation of a grain suspension in a gravity free space. It can be obtained from standard index tests (loosest packing) but due to the stress conditions during the experiment, e_{max} is always lower than the theoretical value of e_{i0} . For well-graded materials a ratio $e_{i0}/e_{max} \approx 1.15$ can be assumed and the upper bound limit void ratio can be calculated from $e_{i0} \approx 1.15e_{max}$. [33]

The pressure dependent limit void ratio e_d is a lower bound of allowable states for hypoplastic materials. The value of e_{min} obtained from the index test “densest packing” is very close, but not equal, to the defined lower bound limit void ratio at zero pressure e_{d0} . This is a result of limited densification during the test. However, the assumption $e_{d0} \approx e_{min}$ can be considered accurate enough to use for the model calibration. [33].

The third limiting void ratio is the critical void ratio e_{c0} which is related to the critical state. From many experimental studies it was observed that $e_{c0} \approx e_{max}$ is a good correlation, as within the standard index test for e_{max} the material undergoes large shear deformations at low pressures until a critical state is reached [33]. Acc. to Herle and Gudehus [30] the void ratio at critical state is heavily dependent on granulometric properties, like the angularity of the grains and the nonuniformity C_u of the grain size distribution. It is stated that e_{max} , and therefore e_c , increases with increasing angularity and decreasing C_u . The same behaviour applies to the upper (e_i) and the lower limit (e_d) of the void ratios.

Reinisch [2] investigated this statement in the course of his thesis and plotted the limit void ratios against C_u as well as the carbonate content, for the materials of the KELLER-database found within A. Tab. 1. Thereby, the $CaCO_3$ - content acted as an indirect measure for the angularity of the soil particles, assuming that shells tend to be more angular than silica grains. His studies revealed a strong correlation of the limit void ratios e_c and e_i on both, C_u and the carbonate content, whereas the lower bound void ratio e_d showed this dependency only for the $CaCO_3$ – content, but not for the nonuniformity C_u .

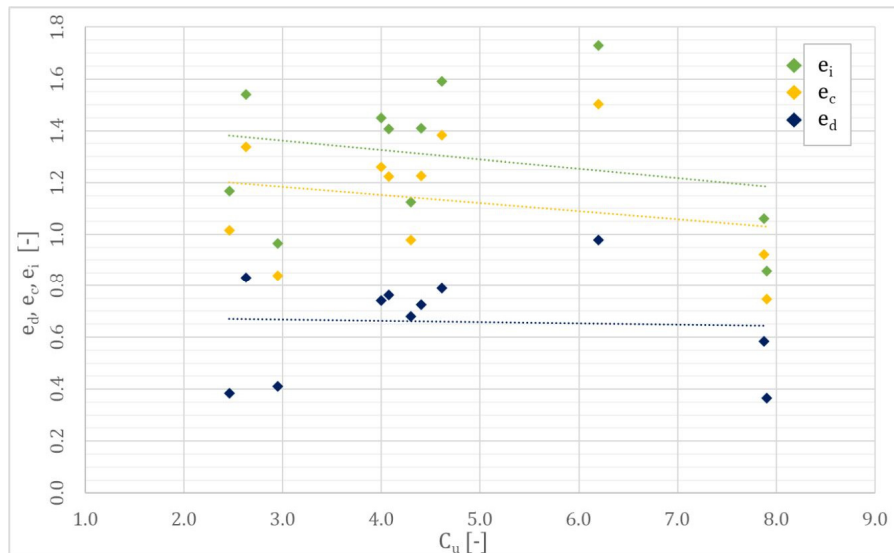


Fig. 24: Limit void ratios e_d , e_c and e_i vs. C_u [2]

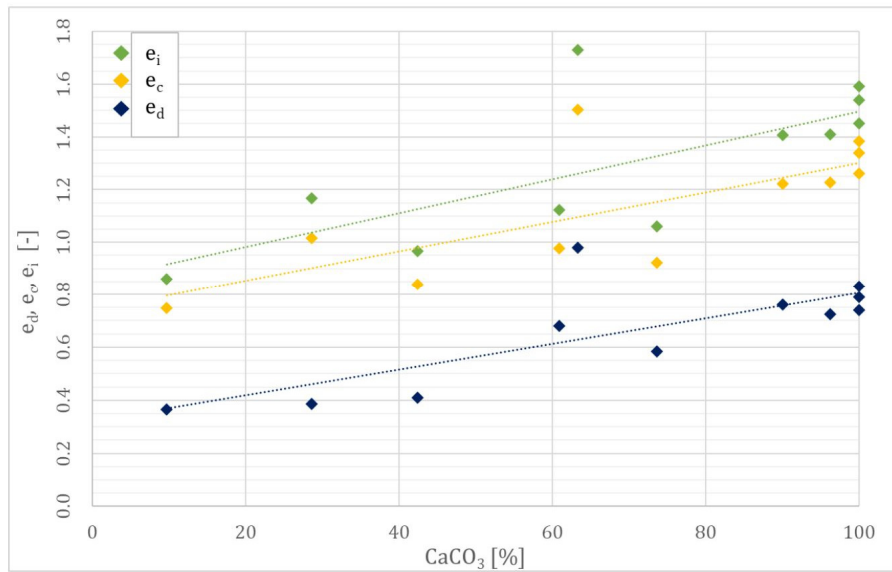


Fig. 25: Limit void ratios e_d , e_c and e_i vs. $CaCO_3$ – content [2]

Critical Friction Angle φ_c

The critical friction angle φ_c is responsible for the resistance of a granulate subjected to monotonic shearing in critical state. This is, when the stress rate $\dot{\sigma}$ and the volumetric strain rate $\dot{\epsilon}_v = \text{tr}(\dot{\epsilon})$ turn to zero. [6]

The critical friction angle φ_c can be determined from triaxial tests on very loose specimens, simple- or direct-shear tests or the angle of repose test [8]. However, some restrictive difficulties arise in connection with direct-shear testing or triaxial testing as homogeneous deformations can hardly be achieved due to the evolution of shear bands within the sample. This behavior becomes even more distinct for an increasing density [34]. Herle and Gudehus [30] pointed out that in some cases the published results for the critical friction angle φ_c for one type of sand, tested with the same kind of shear test but in different laboratories, yielded a greater scatter than φ_c determined from the angle of repose test.

The angle of repose test is the fastest and yet simplest method to derive the critical friction angle φ_c for a granular material [6]. Fig. 26 depicts the test setup for this kind of test.

During this test sand is poured into a funnel which then gets lifted vertically but without losing contact with the forming cone of dried granular material. The steady flow of the grains out of the funnel simulates a quasi-critical state to be reached, as the granulate on the surface is subjected to large monotonic shearing. The actual critical friction angle can then be obtained from measuring the height and the diameter of the cone ($\tan \varphi_c = 2h/d$) or can be measured with the aid of stencils (increments of 0.5° are considered sufficient).

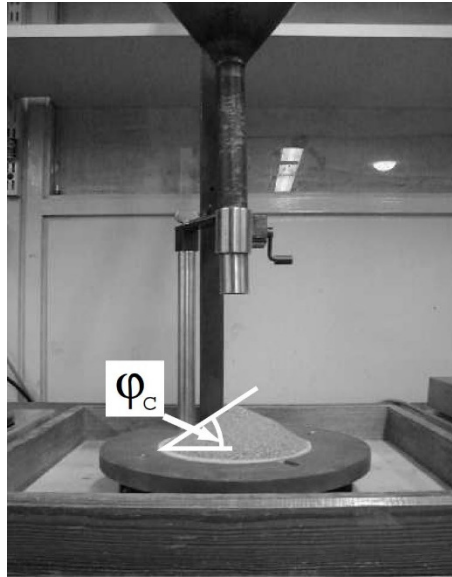


Fig. 26: The angle of repose test [6]

Herle and Gudehus [30] performed studies on soils with different grain-sizes and nonuniformity C_u of the grain size distribution to figure out the influence of d_{50} and C_u on the critical friction angle φ_c . They concluded that an increase in d_{50} causes an increase of the observed friction angles, whereas the nonuniformity C_u seems to play a less important role.

Reinisch [2] obtained the same dependency of φ_c on d_{50} for the materials of the KELLER-database, except for one. That's exactly the reason why the trendline in Fig. 27 shows a horizontal progression, rather than an increase of φ_c with increasing mean grain size d_{50} . When the outlier gets ignored, the findings of Herle and Gudehus can be confirmed.

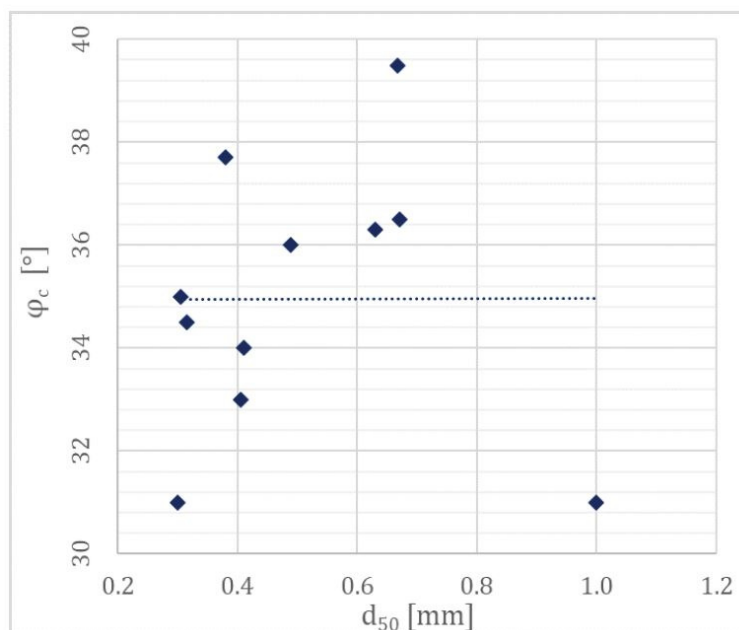


Fig. 27: Relationship between φ_c and the mean grain size d_{50} [2]

Granulate Hardness h_s and Exponent n

The granulate hardness h_s is a term that is predestined of causing general confusion as it doesn't describe the hardness of single grains but rather gets used as a kind of reference pressure which is independent from the density state [34] and has a dimension of stress [33]. According to Herle [34] h_s is mainly influenced by the grain-size, grain-shape and the grain-size distribution: An increasing angularity of the grains and a decreasing nonuniformity C_u result in a smaller value for h_s and therefore in a higher compressibility of the material. Further an increasing grain size can yield a decrease of the granulate hardness as the probability of possible grain defects is significantly higher [34].

In case of isotropic compression of a very loose sample with $e_0 = e_{max}$ the hypoplastic constitutive law reduces to the compression law acc. to Bauer [32]:

$$e = e_0 \cdot \exp \left[- \left(\frac{3p'}{h_s} \right)^n \right] \quad (4.3)$$

The exponent n is used to take into account the pressure sensitivity of a grain skeleton and reflects the curvature of the compression curve. [30]

The granulate hardness h_s together with the exponent n can be obtained from conducting oedometric compression tests (OCT) on initially very loose specimens for comparable pressure ranges as obtained in the actual CPT tests [6]. For carbonate sands the tests are performed at very high vertical pressures of up to 25 MPa in order to make sure that the effect of particle breakage occurs and that it can be sufficiently considered within the calibration process. Meier [6], however, stated that for his studies on different materials and mixtures, a maximum vertical pressure of $\sigma_{v,max} \approx 1/4 q_{c,max}$ was sufficient to get satisfying results. He justified this assumption with the fact that the pressure in the near field of the cone tip decreases quite rapidly and the maximum pressure applied in the oedometric compression test therefore only has to be a fraction of $q_{c,max}$.

It is not recommended to derive h_s and n directly from regression of the measured data, using Eqn. (4.3), due to a strong nonlinearity of the equation resulting in a very big scatter of the parameters in case of small changes in the measurements. [30]

It is more convenient to express the bulk modulus $K = -\dot{p}'/[\dot{e}/(1+e)]$ with the aid of Eqn. (4.3) as follows [30]:

$$K = \frac{1}{3} \frac{h_s}{n} \left(1 + \frac{1}{e} \right) \left(\frac{3p'}{h_s} \right)^{1-n} \quad (4.4)$$

By comparing this formulation of the bulk modulus with the conventional equation of K ,

$$K = \frac{p'^{(1+e)}}{C_c} \quad (4.5)$$

where C_c equals the compression index, the following expression for the granulate hardness h_s is received [30]:

$$h_s = 3 p' \left(\frac{n \cdot e}{C_c} \right)^{\frac{1}{n}} \quad (4.6)$$

Now considering a range from p'_1 to p'_2 with corresponding void ratios e_1 and e_2 and compression indices C_{c1} and C_{c2} (Fig. 28), the value of n can be calculated without the knowledge of the granulate hardness h_s .

$$n = \frac{\ln \left(\frac{e_1 \cdot C_{c2}}{e_2 \cdot C_{c1}} \right)}{\ln \left(\frac{p'_2}{p'_1} \right)} \quad (4.7)$$

After n is calculated, the granulate hardness h_s can simply be received from Eqn. (4.6). Unlike n , which effects the curvature of the compression curve, h_s governs the overall slope of it. [30]

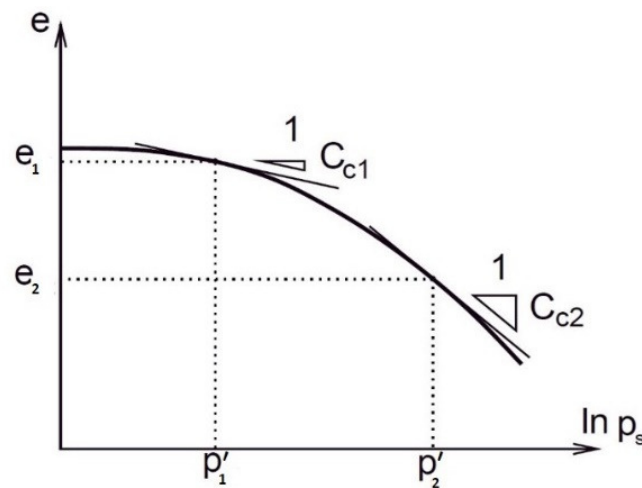


Fig. 28: Determination of n from considered pressure range of the compression curve (adapted after [30])

Reinisch [2] compared the values for the granulate hardness h_s and the exponent n for materials from the KELLER-database incorporating different values of the mean grain size d_{50} . Increasing values for d_{50} resulted in lower values for h_s , indicating a more pronounced compressibility. The values for n showed the opposite relation with respect to the mean grain size (n increasing with increasing d_{50}). The higher compressibility is believed to be a result of a higher tendency of bigger grains to crushing and the low hardness of the carbonate grains, whereby materials with a higher d_{50} contained a higher amount of these soft grains. Fig. 29 illustrates the mentioned relationships.

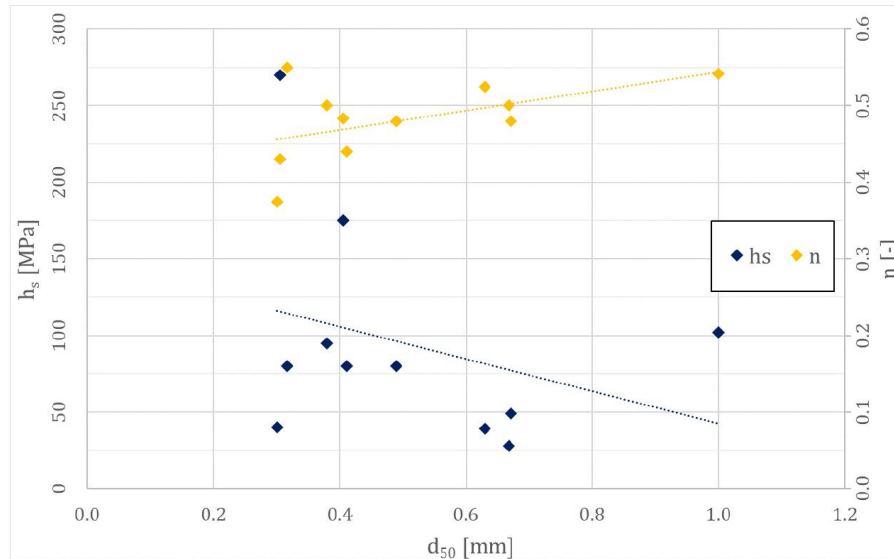


Fig. 29: Influence of the mean grain size d_{50} on h_s and n [2]

Exponent α

The exponent α is capable of controlling the material's peak friction angle, and hence the dilatancy behaviour of the sample [6]. The peak friction angle $\varphi_p > \varphi_c$ evolves when a dense sand sample gets sheared [33].

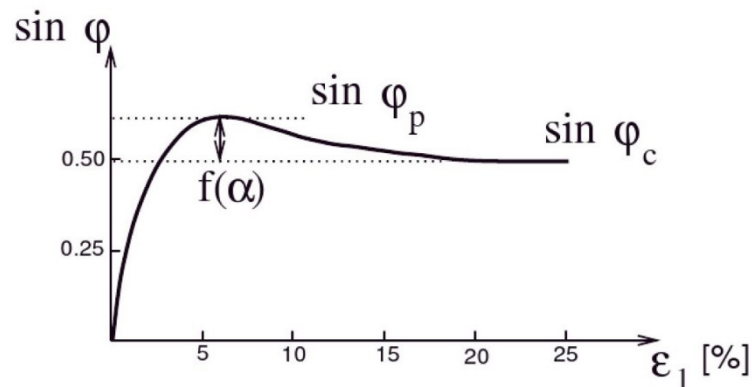


Fig. 30: Shearing of a dense sample - Peak friction angle φ_p [35]

Exponent α can be calibrated by performing drained triaxial tests on initially dense samples and fitting the results of test simulations, calculated with the hypoplastic constitutive equation, to the measured curves. It is not sufficient to consider α as an independent parameter for the calibration, as h_s and n also influence the results of the simulated triaxial tests. [6]

Exponent β

The stiffness of a dense grain skeleton with $e < e_c$ can be adjusted by the exponent β [6]. Increasing values of β increase the calculated incremental stiffness moduli $E = \dot{T}'_1 / D$, where \dot{T}'_1 denotes the effective vertical stress rate in case of oedometric compression [30].

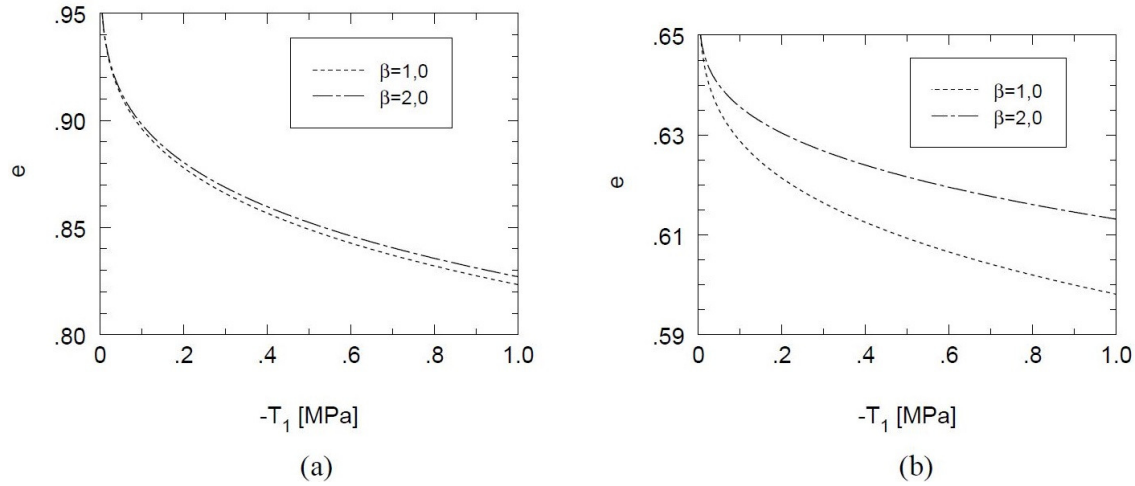


Fig. 31: Influence of β on the calculated compression curves for an initially loose (a) and an initially dense (b) specimen [34]

The influence of β on the compression curves is much greater for higher initial densities and an increasing pressure level [34]. Fig. 31 depicts the calculated compression curves for different values of β and different initial densities. The curves within the left diagram (low initial density) with different values for β are almost identical, whereas the curves in the right diagram (high initial density) are very different. T_1 denotes the vertical stress component within the oedometric test.

When the stiffness moduli E_1 and E_2 from oedometric compression tests at two different densities, described by the void ratios e_1 and e_2 , but at the same pressure T_1 are known, the exponent β can be calculated as follows [33]:

$$\beta = \frac{\ln\left(\beta_0 \frac{E_2}{E_1}\right)}{\ln\left(\frac{e_1}{e_2}\right)} \quad (4.8)$$

where β_0 incorporates several factors defined within the hypoplastic constitutive law. At this point reference is made to [33] for the calculation of β_0 .

Herle [34] evaluated the values of the exponent β for typical values of the void ratios and the ratio $E_2/E_1 \approx 2:1$ for sands and found that $\beta \approx 1.0$ is a good first approximation.

4.2.2 Hypoplastic Parameters of KELLER Materials

KELLER Grundbau had all the hypoplastic parameters of the materials, contained within their database, determined. An overview of these parameters can be found within A. Tab. 5. Note that this table only shows the parameters for materials which were contained within the database at the time when Reinisch [2] finished his thesis. Some more materials have been added since.

4.3 Cavity Expansion Theory

The cavity expansion theory deals with the theoretical study of changes in stresses, pore water pressures and displacements caused by the expansion and contraction of cylindrical or spherical cavities. The cavity expansion represents a useful tool for the modelling of many complex geotechnical problems. These problems include the investigation of the bearing capacity of pile foundations and earth anchors, the design of rock support in underground excavations and tunnelling, the prediction of the wellbore instability encountered in petroleum engineering or the interpretation of in-situ soil tests [36], such as the cone penetration test.

Over time, numerous analytical and numerical solutions using different constitutive models for the cavity expansion in soils and rock have been developed. Most of the used constitutive models are either based on the fundamentals of elasticity, plasticity or viscoelasticity [36]. However, there are also hypoplastic solutions of the cavity expansion problem available [37].

4.3.1 The Spherical Cavity Expansion

Due to the analogy of the deformations and stress changes caused by the penetration of a cone in sand and the expansion of a spherical cavity within a soil continuum, the spherical cavity expansion is one of the main tools to model any kind of penetration processes.

The cavity expansion in soils and rock is a one-dimensional boundary value problem [36]. Osinov and Cudmani [37] were able to develop a numerical solution to this problem for granular materials using the hypoplastic constitutive equation proposed by “von Wolffersdorff” [23]. Cudmani used this solution as part of his CPT interpretation method – The KIM.

The considered boundary value problem consists of a spherical cavity with an initial radius r_a^0 inside a drained body with finite or infinite dimensions. In the case of finite dimensions the body is a sphere (initial radius = r_b^0) that is concentrically arranged to the cavity. [8]

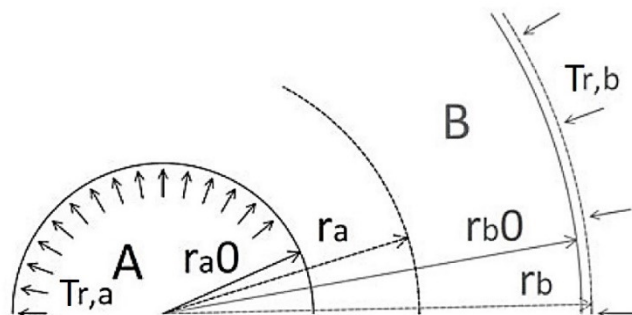


Fig. 32: The boundary value problem of the spherical cavity expansion (adapted after [38])

The problem can be mathematically described by four different differential equations whose results provide the temporal progression of the velocity component v_r , the stress components T_r (radial stress) and T_θ (tangential stress) and the void ratio e . These 4 variables are the unknowns within the system of equations. [8]

$$\frac{\partial T_r}{\partial r} + \frac{2}{r} (T_r - T_\theta) = 0 \quad (4.9)$$

$$\frac{\partial T_r}{\partial t} + v \frac{\partial T_r}{\partial r} = H_r \left(T_r, T_\theta, \frac{\partial v}{\partial r}, \frac{v}{r}, e \right) \quad (4.10)$$

$$\frac{\partial T_\theta}{\partial t} + v \frac{\partial T_\theta}{\partial r} = H_\theta \left(T_r, T_\theta, \frac{\partial v}{\partial r}, \frac{v}{r}, e \right) \quad (4.11)$$

$$\frac{\partial e}{\partial t} + v \frac{\partial e}{\partial r} = (1 + e) \left(\frac{\partial v}{\partial r} + 2 \frac{v}{r} \right) \quad (4.12)$$

Eqn. (4.9) depicts the equilibrium condition, Eqn. (4.10) and Eqn. (4.11) consider the hypoplastic constitutive model and Eqn. (4.12) is known as the mass-balance equation.[8]

The initial conditions of the boundary value problem include prescribed values for $T_r^0(r)$, $T_\theta^0(r)$ and $e^0(r)$ for time $t = 0$. $T_r^0(r)$ and $T_\theta^0(r)$ must satisfy the equilibrium condition. At the beginning of the cavity expansion a hydrostatic stress field and a homogeneous density is assumed.[8]

The objective of the problem is to find the solutions for $v(r,t)$, $T_r(r,t)$, $T_\theta(r,t)$ and $e(r,t)$ for $t \geq 0$ which fulfil the conditions of $\dot{r}_a(t) = v_0 > 0$ at radius r_a and $\dot{T}_r(r_b,t) = 0$ at radius r_b . As the hypoplastic constitutive equation describes a rate-independent material behaviour, any value can be chosen for v_0 . In case infinite dimensions of the models are assumed, the second condition can be replaced by the condition $v(r_b,t) = 0$. Both boundary conditions at r_b lead to the same results.[8]

A more detailed description of the present boundary value problem using a hypoplastic constitutive law and the numerical algorithm to solve it can be found in the paper “*Theoretical investigation of the cavity expansion problem based on a hypoplasticity model*” by Osinov und Cudmani [39]. Some studies on the spherical cavity expansion problem in the present thesis were performed with a finite difference code written by Osinov which uses the numerical algorithm stated in [39]. This code will later on be referred to as the “OSINOV code”.

Numerical Solution of the Spherical Problem

In order to receive sufficiently accurate results for the spherical cavity expansion (SCE) problem, the radius r_b^0 has to be chosen large enough to make sure that $\dot{T}_\theta(r_b,t)$ approaches 0 (no changes of tangential stresses at r_b). [8]

Results of the numerical evaluation for different kind of cohesionless soils [8] showed that the changes in circumferential stresses at radius r_b for an expansion of $r_a(t) \leq 3r_a^0$ can be expected smaller than 0.1 % if $r_b^0 / r_a^0 \geq 30$ for loose soils and $r_b^0 / r_a^0 \geq 90$ for dense soils.

Definition of the Limit Pressure p_{LS}

During the simulation of the spherical cavity expansion the radius r_a of the cavity is increasing. Sphere B is loaded with the initial mean effective pressure p_0 (depicted in Fig. 32 as $T_{r,b}$) which, acc. to the defined boundary conditions, remains the same throughout the entire simulation. With ongoing expansion the cavity pressure (depicted in Fig. 32 as $T_{r,a}$) is increasing, however not to infinity, but it is approaching a certain limiting value designated as the limit pressure p_{LS} . After reaching this value the cavity pressure remains stationary, also for a continuing expansion.

Not only does the radial component $T_{r,a}$ increase during the simulation but also the tangential stress component $T_{\theta,a}$ at the cavity wall (r_a). It, as well, monotonically approaches a limiting value.

The limiting values are dependent on the initial state of the soil defined by the initial void ratio e_0 (or the pressure-dependent relative density I_D^*) and the initial effective mean pressure p_0 . In hypoplasticity theory it is quite common to replace the definition of the relative density I_D [8]

$$I_D = \frac{e_{max} - e}{e_{max} - e_{min}} \quad (4.13)$$

by a more general expression which incorporates the pressure-dependent limit void ratios e_c and e_d [8]:

$$I_D^* = \frac{e_c - e}{e_c - e_d} \quad (4.14)$$

In case of $p \approx 0$ kPa the limit void ratios e_c and e_d are replaced by $e_{c0} \approx e_{max}$ and $e_{d0} \approx e_{min}$, the limit void ratios at zero pressure, and Eqn. (4.13) equals Eqn. (4.14).

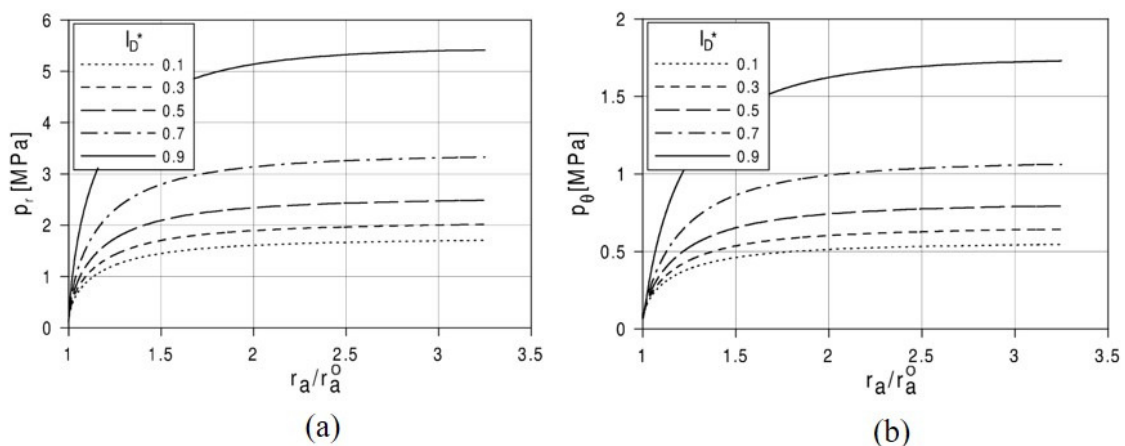


Fig. 33: Progression of radial (a) and tangential (b) stresses during a spherical cavity expansion in Ticino sand [8]

Fig. 33 shows the pressure-expansion curves obtained from the simulation of the spherical cavity expansion in Ticino sand at an initial effective mean stress $p_0 = 100$ kPa and for different relative densities I_D^* [8]. The variable p_r denotes the radial pressure at the cavity wall, whereas p_θ is representative for the tangential stress component. The results show that the limiting values are reached at around $r_a \approx 2r_a^0$ for loose samples ($I_D^* \approx 0.1$) and $r_a \approx 3r_a^0$ for dense samples ($I_D^* \approx 0.9$).

It is pointed out that different authors use different designations for the same mechanical quantities, which is the reason why in this thesis different notations for the radial and tangential stresses are taken into account.

Stress Paths and Void Ratios during the Expansion of a Spherical Cavity

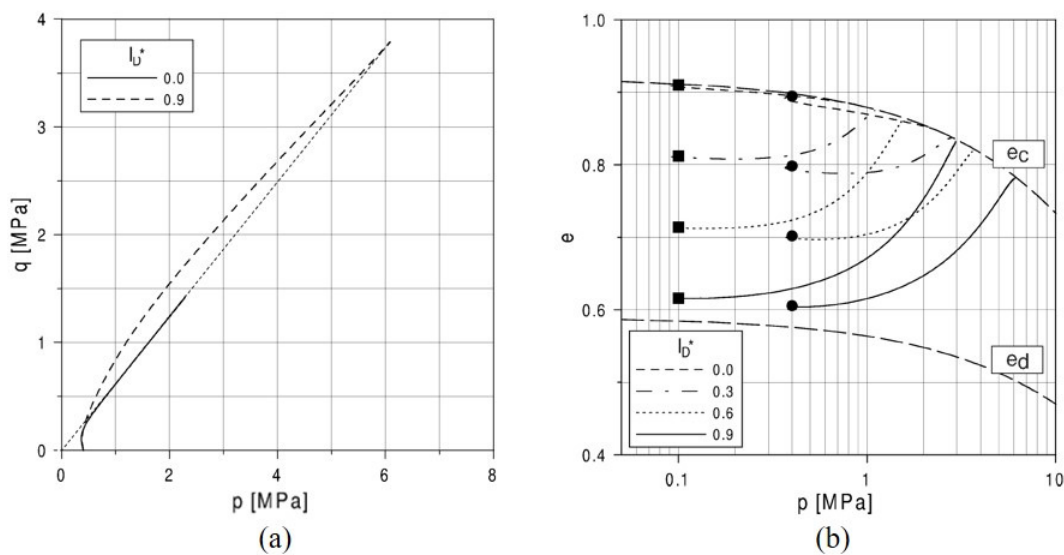


Fig. 34: p/q -paths (a) for $p_0 = 400$ kPa and e - p -paths (b) for $p_0 = 100$ and 400 kPa at the cavity wall for a spherical cavity expansion in Ticino sand [8]

Fig. 34 shows the deviatoric stress $q = (p_r - p_\theta)/2$ and the void ratio e in dependence of the mean pressure $p = (p_r + 2p_\theta)/3$ for the expansion of a spherical cavity in Ticino sand.

One can see that the curves within the p - q -diagram are asymptotically approaching the critical state which is depicted as a straight line. Hence, the ratio p/q for the limiting state is independent from the initial state of the soil, as the curves will approach the same critical state line, regardless of the initial density I_D^* . It is pointed out though that the critical state is reached only at higher pressures p when the soil is in a denser initial state.

The e - p -curves in Fig. 34 (b) also approach their critical state values (e_c -line acc. to Eqn. (4.2)) with increasing p . Loose soil will experience slight contraction during the expansion while dense soil will be loosened, because of dilatancy.

Spatial Distribution of p_r , p_θ and e around the Cavity

Fig. 35 below represents the spatial distribution of the radial and tangential stresses, as well as the void ratio e , at the end of a spherical cavity expansion from radius r_a^0 to $3.3r_a^0$. The diagram has to be considered as a cross section. For small deformations ($\Delta r \approx 2-3\%$) the soil experiences slight compression and the tangential stresses, as well as the void ratio, tend to decrease [8]. Therefore, p_θ and e are lying below its initial values at $r > 10r_a^0$. At a distance of 40 to $50r_a^0$ the effects of the cavity expansions are negligible and the values for p_r , p_θ and e do not change from the initial values.

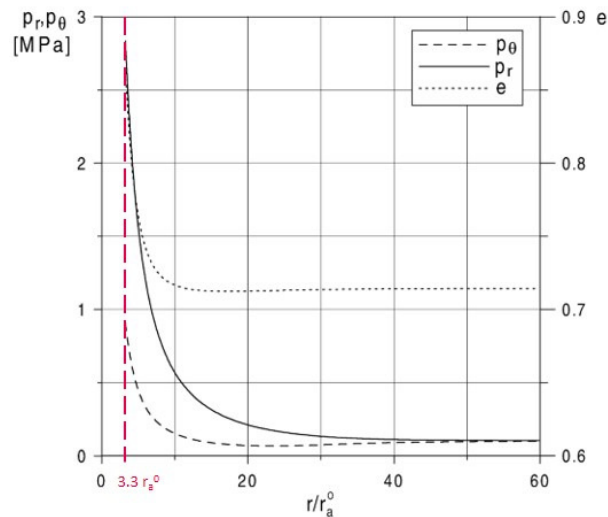


Fig. 35: Spatial distribution of p_r , p_θ and e at the end of the spherical cavity expansion from r_a^0 to $3.3 r_a^0$ in Ticino sand (adapted after [8])

Dependency of the Limit Pressure p_{LS} on the Initial State and Material Properties

The value of the received limit pressures p_{LS} are strongly connected to the initial values for the relative density I_D^* and the initial effective mean pressures p_0 . For increasing values of I_D^* and p_0 higher values for the limit pressure p_{LS} are received. [8] This relationship for Ticino sand can be seen in Fig. 36.

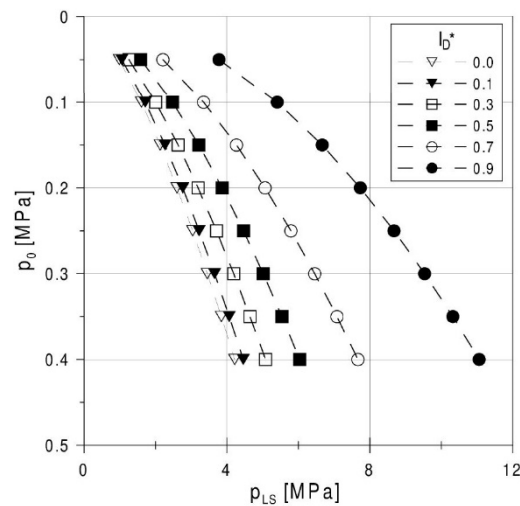


Fig. 36: Limit pressure p_{LS} vs. mean effective stress p_0 for different relative densities I_D^* obtained for Ticino sand [8]

The limit pressures p_{LS} for carbonate sands with different granulometric properties obtained for two different relative densities I_D^* are compared in Fig. 37. It is shown that p_{LS} for different carbonate materials can vary by a factor of almost 2 at the same initial state (I_D^*, p_0).

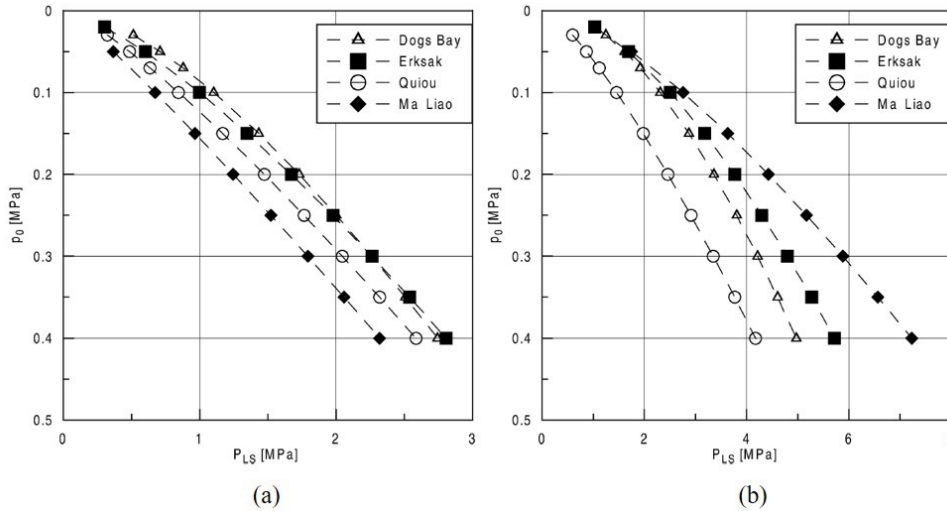


Fig. 37: Limit pressure p_{LS} vs. mean effective stress p_0 for different carbonate sands at $I_D^* = 0.1$ (a) and $I_D^* = 0.9$ (b) [8]

Approximation of Explicit Values for p_{LS} obtained from the Numerical Solution

Acc. to Cudmani [8] the limit pressures p_{LS} obtained from the spherical cavity expansion can be approximated by Eqn. (4.15) which represents a function dependent on the initial material state:

$$p_{LS} = a \cdot p_0^b \quad (4.15)$$

where p_0 is the initial effective mean pressure. Factor a and exponent b are further given by

$$a = a_1 + \frac{a_2}{a_3 + I_D^*} \quad b = b_1 + \frac{b_2}{b_3 + I_D^*} \quad (4.16)$$

The a_i and b_i parameters are known as the so-called KIM-parameters and can be received from curve-fitting for each material specifically. The detailed curve fitting procedure is presented in chapter 5.2. Once the KIM-parameters for the investigated material are known the limit pressure p_{LS} can be calculated for each value of I_D^* and p_0 with the aid of Eqns. (4.15) and (4.16).

4.4 Modelling of the Cone Penetration Test

The penetration of a cone cannot be directly modelled as a cylindrical or spherical cavity expansion [8]. However, the qualitative similarity between the limit pressures p_{LS} and the values for the cone resistance q_c measured in calibration chamber tests is obvious [6]. Fig. 38 depicts the simulation results of the SCE and the calibration chamber testing results for Ticino sand and different initial relative densities I_D . The same dependencies of p_{LS} and q_c on the effective mean pressures p_0 and relative densities I_D can be observed.

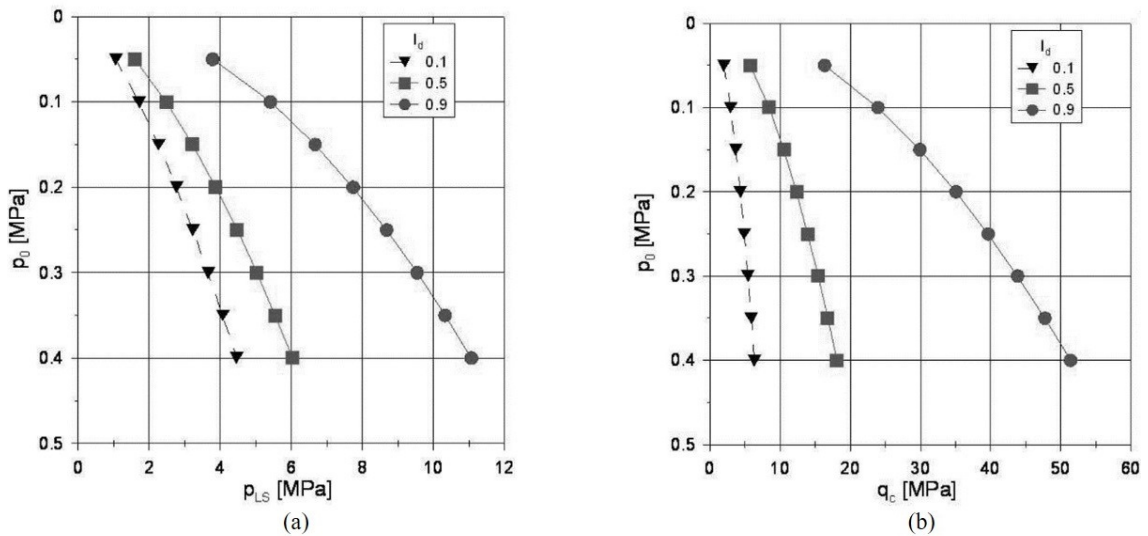


Fig. 38: Simulation results of the SCE (a) and the calibration chamber testing results (b) for Ticino sand [6]

Cudmani [8] introduced a shape factor k_q to quantitatively correlate p_{LS} with the cone resistance q_c and proposed the equation

$$q_c = k_q \cdot p_{LS} \quad (4.17)$$

The cone penetration resistance q_c depends on both, the horizontal stress σ_h and the vertical stress σ_v , and therefore also on the coefficient of lateral earth pressure K [8]. As for the simulation of the spherical cavity expansion an initial hydrostatic stress state is assumed, the influence of K cannot be accounted for. Nevertheless, the model can still provide sufficient results as the influence of the mean effective stress p_0 on q_c is much more pronounced than the influence of K [40].

Cudmani [8] evaluated the limit pressures p_{LS} and the calibration chamber cone resistances q_c for different materials with different initial relative densities and for different pressure ranges. From Eqn. (4.17) he calculated the values for the shape factor k_q and plotted them against the relative density I_D^* . Diagram (a) in Fig. 39 corresponds to a pressure range of $p_0 < 0.05$ MPa, diagram (b) to $0.05 < p_0 < 0.15$ MPa, diagram (c) to $0.15 < p_0 < 0.25$ MPa and diagram (d) to a pressure range $0.25 < p_0 < 0.5$ MPa.

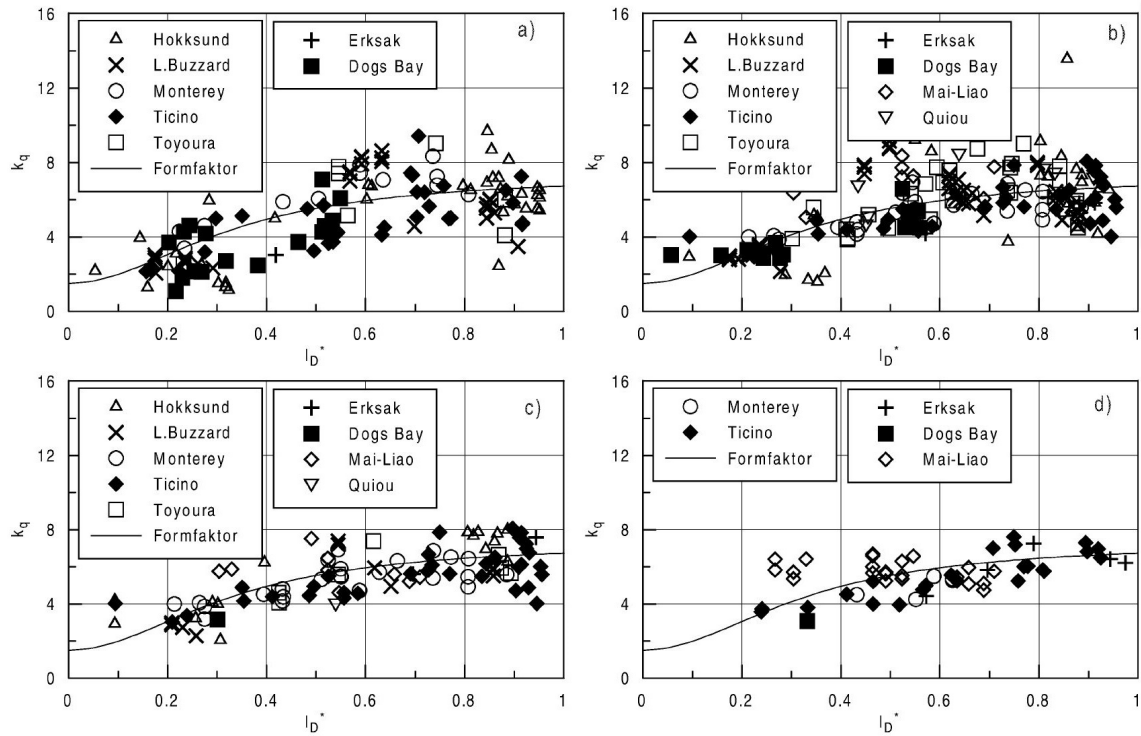


Fig. 39: Shape factor k_q vs. relative density I_D^* for four different pressure ranges [8]

The mean value of k_q (continuous lines) within Fig. 39 varies between 2 and 6 and shows no dependency on p_0 . Cudmani [8] suggested to use Eqn. (4.18) for the approximation of the shape factor in carbonate and silica sands in the ranges of $0.03 < p_0 < 0.5$ MPa, $0 < I_D^* < 1$ and $50 < h_s < 10000$ MPa. This equation represents the continuous lines within the diagrams above.

$$k_q(I_D^*) = 1.5 + \frac{5.8 (I_D^*)^2}{(I_D^*)^2 + 0.11} \quad (4.18)$$

Despite the suggested ranges for the application of Eqn. (4.18) Cudmani [8] showed that this expression for the shape factor might also provide “satisfying” results for materials with a lower granulate hardness than 50 kPa.

The stated formulation of the shape factor, though, is very general and doesn’t necessarily represent the actual values of k_q for different materials and different mean effective pressures p_0 . Although Cudmani [8] wasn’t able to recognize any big effect of p_0 on k_q , the influence of the mean effective stress p_0 may not be disregarded in improved future formulations of the shape factor, especially when pressure ranges, different from the ones by Cudmani, are considered. The shape factor might be the element within the KIM containing the biggest uncertainties and is therefore affecting the accuracy of this method.

The most reliable way of determining the value for k_q would be to perform calibration chamber tests for each material under investigation. This approach, though, is very time-consuming and expensive. To overcome this problem the calibration chamber tests could

be simulated by means of finite element modelling and solving the general boundary value problem of the cone penetration test. However, this is not a straight forward task as Cudmani [8] could prove and further research w.r.t the shape factor k_q is needed.

4.5 The final KIM Equation

The final KIM equation is build-up from Eqn. (4.15), Eqn. (4.16), Eqn. (4.17), Eqn. (4.18) and the following formulation of the mean effective stress p_0 ,

$$p_0 = \frac{1}{3} \cdot \sigma'_v \cdot (1 + 2 \cdot K_0) \quad (4.19)$$

where σ'_v represents the effective vertical stress. The cone penetration resistance q_c can be expressed with

$$q_c = \left(1.5 + \frac{5.8 \cdot I_D^{*2}}{I_D^{*2} + 0.11}\right) \cdot \left(a_1 + \frac{a_2}{a_3 + I_D^*}\right) \cdot \left(\frac{1}{3} \cdot \sigma'_v \cdot (1 + 2 \cdot K_0)\right)^{\left(b_1 + \frac{b_2}{b_3 + I_D^*}\right)} \quad (4.20)$$

In case the a_i and b_i parameters for a specific material are known, the cone penetration resistance q_c can be determined for each desired relative density I_D^* and each value for the effective mean pressure p_0 . A graphical representation of the q_c -curves obtained from the KIM-analysis for material PLM AZ28 from the KELLER-database can be found in Fig. 40.

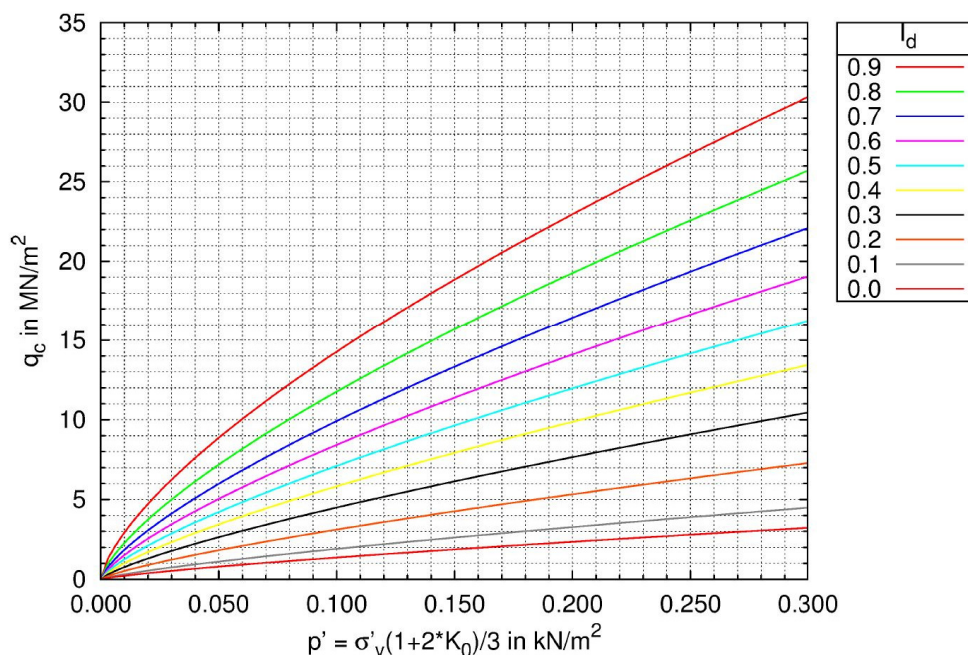


Fig. 40: q_c -curves for material PLM AZ28 from the KELLER-database [41]

5 The OSINOV Code

The OSINOV code is a finite difference computer code written by V.A. Osinov [42]. It can be used for the calculation of the spherical cavity expansion limit pressures p_{LS} and comprises the numerical solution obtained by Osinov and Cudmani [39] which is based on the hypoplastic constitutive law by “von Wolffersdorff” [23]. In the course of the investigation program on the KIM launched by KELLER Grundbau the program has been thankfully provided by Dr. Thomas Meier from Baugrund Dresden for the purpose of academic research.

Chapter 5 deals with the appropriate usage of the OSINOV code and explains the steps to be taken to receive proper values for the limit pressures p_{LS} . Further, a detailed description of the curve fitting method, required for the approximation of the p_{LS} -values, will be given and some of the calculation results from a sensitivity study [9] performed on materials from the KELLER-database will be presented. Finally, a MATLAB script for the automatic generation of stress-path-diagrams and pressure-expansion-curves from the output-files of the OSINOV code will be introduced to the readers.

5.1 The Utilization of the OSINOV Code

As the OSINOV code is not a commercially available software tool, the users of the program are not provided with any kind of instructions or user manuals. Hence, most of the information on the utilization of this code given in Chapter 5.1 is solely based on the studies of Slawik [9] and the author of this thesis.

The program comprises 3 different main files two of which are application-files (.exe). The third file is a simple text-file containing the input data which can be opened and modified with the aid of any text-editor program.

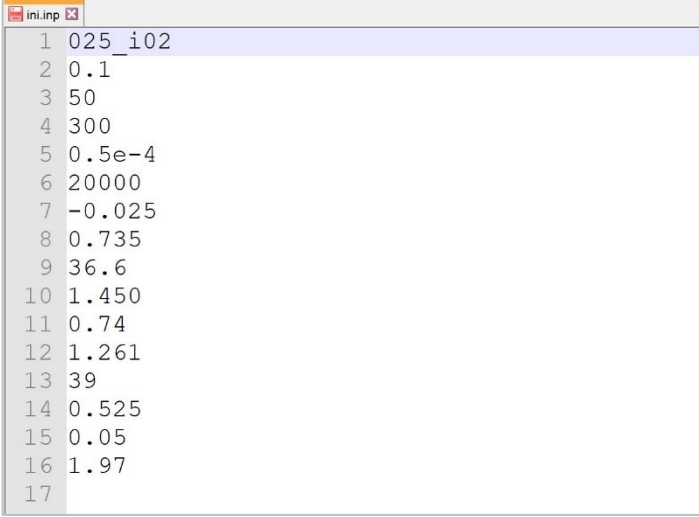
5.1.1 The Input-File

For each calculation of the limit pressure p_{LS} for a desired initial state the content of the text-file (named ini.inp) has to be adapted. Fig. 41 shows the structure of this text-file.

The different lines within ini.inp have the following meaning:

- 1) **025_i02** name of the calculation (025: $p_0 = 0.025$ MPa, i04: $I_D = 0.2$)
- 2) **0.1** initial radius in [m].
- 3) **50** boundary radius in [m]
- 4) **300** number of discretization points between 2) and 3).
- 5) **0.5e-4** pseudo-time step
- 6) **20000** number of calculation steps

- 7) **-0.025** initial isotropic pressure in [MPa] (pressure is negative)
- 8) **0.735** initial void ratio e at pressure p_0 (example corresponds to $I_D = 0.2$)
- 9) **36.6** critical friction angle φ_c in $[\circ]$
- 10) **1.450** upper bound limit void ratio e_{i0} at zero pressure
- 11) **0.74** lower bound limit void ratio e_{d0} at zero pressure
- 12) **1.261** critical void ratio e_{c0} at zero pressure
- 13) **39** granulate hardness h_s in [MPa]
- 14) **0.525** exponent n
- 15) **0.05** exponent α
- 16) **1.97** exponent β



```

ini.inp
1 025_i02
2 0.1
3 50
4 300
5 0.5e-4
6 20000
7 -0.025
8 0.735
9 36.6
10 1.450
11 0.74
12 1.261
13 39
14 0.525
15 0.05
16 1.97
17

```

Fig. 41: Structure of the main text-file from the OSINOV code

The parameters provided in line 2 to 6 govern the calculation process and are therefore referred to as the calculation parameters. The values for these parameters stated in Fig. 41 are suggested for the general use (Dr. Thomas Meier/Baugrund Dresden) and should only be changed by experienced users.

Within the code the initial relative density I_D is considered in terms of the initial void ratio e at the given effective mean pressure p_0 in line 7. It should not be confused with the value for the initial void ratio e_0 at zero pressure as with an increasing pressure level the void ratio tends to decrease [32]. The void ratio e can be calculated from the following equation, already stated in chapter 4.3.1. Instead of using I_D^* for the notation of the pressure-dependent relative density the notation I_D is used subsequently as both formulations represent the same value and only differ by the incorporated kind of void ratios.

$$I_D = \frac{e_c - e}{e_c - e_d} \quad (5.1)$$

The pressure-dependent critical void ratio e_c and the pressure-dependent lower bound limit void ratio e_d can be obtained from the compression law acc. to Bauer [32], with

$$e_c = e_{c0} \cdot \exp \left[- \left(\frac{3p_0}{h_s} \right)^n \right] \quad e_d = e_{d0} \cdot \exp \left[- \left(\frac{3p_0}{h_s} \right)^n \right] \quad (5.2)$$

By combining Eqn. (5.1) and Eqn. (5.2) the initial void ratio e at pressure p_0 for a given value of the relative density I_D can be calculated with

$$e = e_{c0} \cdot \exp \left[- \left(\frac{3p_0}{h_s} \right)^n \right] - I_D \cdot \exp \left[- \left(\frac{3p_0}{h_s} \right)^n \right] \cdot (e_{c0} - e_{d0}) \quad (5.3)$$

5.1.2 Generation of the Initial Conditions

Once the text-file `ini.inp` is filled in with the desired information the initial conditions for the cavity expansion process can be generated by running the `ini.exe` file. This execution-file extracts data from the text-file and creates 3 additional files. Subsequently the symbol `*` will be used as a placeholder for the calculation name defined in line 1 in the initial text-file.

The generated `*.hyp`-file contains the hypoplastic parameters provided within the file `ini.inp`.

The second `*.ini`-file holds the numerical parameters for the calculation and contains 3 different point numbers from material points between the initial radius and the boundary radius for which the stresses, displacements and void ratios will be evaluated during the cavity expansion. For a given number of 300 discretization points the first point number `kp1` is automatically chosen with 1 (point at the cavity wall), the second point number `kp2` with 10 (point close to the cavity) and the third point number `kp3` with 300 (point at the boundary). Fig. 42 shows an example for 300 discretization points.

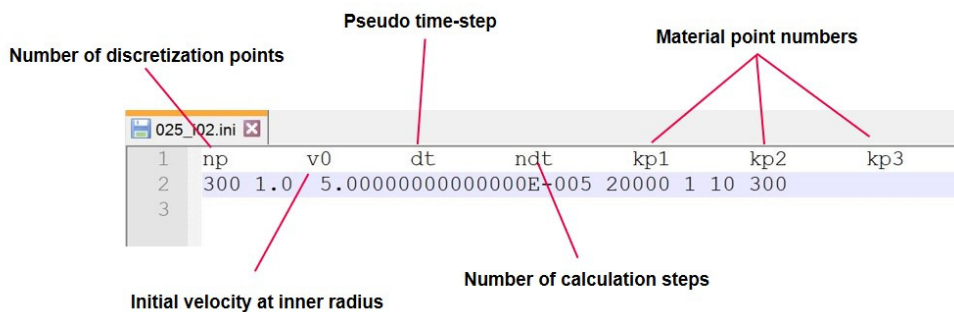


Fig. 42: Generated `*.ini`-file containing the calculation parameters

The third generated file is the `*.dat`-file which consists of 4 columns and a number of lines corresponding to the given number of discretization points (300 lines in case of 300 discretization points). The first column consists of the initial radii for each discretization point. The second and the third column represent the initial values for the radial and

tangential stresses p_r and p_θ in each material point and the last column depicts the initial void ratios. As for the spherical cavity expansion an initial homogenous and hydrostatic stress field is assumed, the values for p_r and p_θ in this file are the same for each material point. An example for the first 10 lines of this file from a spherical cavity expansion with $p_0 = 0.3$ MPa and an initial void ratio e of 0.735 is shown in Fig. 43.

	Material point radius	Radial stress p_r	Tangential stress p_θ	Initial void ratios e
1	1.000000000000000E-001	-3.000000000000000E-001	-3.000000000000000E-001	7.350000000000000E-001
2	1.00558159304706E-001	-3.000000000000000E-001	-3.000000000000000E-001	7.350000000000000E-001
3	1.02232637218823E-001	-3.000000000000000E-001	-3.000000000000000E-001	7.350000000000000E-001
4	1.05023433742352E-001	-3.000000000000000E-001	-3.000000000000000E-001	7.350000000000000E-001
5	1.08930548875292E-001	-3.000000000000000E-001	-3.000000000000000E-001	7.350000000000000E-001
6	1.13953982617644E-001	-3.000000000000000E-001	-3.000000000000000E-001	7.350000000000000E-001
7	1.20093734969408E-001	-3.000000000000000E-001	-3.000000000000000E-001	7.350000000000000E-001
8	1.27349805930582E-001	-3.000000000000000E-001	-3.000000000000000E-001	7.350000000000000E-001
9	1.35722195501169E-001	-3.000000000000000E-001	-3.000000000000000E-001	7.350000000000000E-001
10	1.45210903681167E-001	-3.000000000000000E-001	-3.000000000000000E-001	7.350000000000000E-001

Fig. 43: First 10 lines from the *.dat-file

5.1.3 The Output Files

By running the second execution file, named penetr.exe, the expansion process can be started, and all calculation steps are passed through. Based on information taken from the files for the initial conditions, penetr.exe numerically solves the boundary value problem of the spherical cavity expansion and generates the 4 output-files *.kp1, *.kp2, *.kp3 and error.dat. The latter file provides some information on the calculation errors for the different material points.

The other three files contain the calculation results for the 3 chosen material points *kp1* (at the cavity wall), *kp2* (close to the cavity) and *kp3* (at the boundary). The most important file from which the limit pressure p_{LS} can be received is the file *.kp1. The results for material point *kp3* can be used to judge if the boundary radius was chosen large enough in order to receive almost no influence of the expansion on the stresses at the boundary. Fig. 44 exemplarily depicts the first few lines of the *.kp1 file to get an idea about its structure and contents.

Calculation steps	Current radius in [m] of point 1 = $r_0 + \text{Timestep} \times \text{Calculation step}$	Radial stress p_r [MPa]	Tangential stress p_θ [Mpa]	Void ratio e [-]	Velocity gradient $\frac{dv}{dr}$	v/r
1	1.000000E-001	-2.500000E-002	-2.500000E-002	1.210000E+000	-4.123422E+001	1.00000E+001
2	1.000500E-001	-2.940159E-002	-1.944070E-002	1.207680E+000	-4.026369E+001	9.995002E+000
3	1.001000E-001	-3.268917E-002	-1.705787E-002	1.205612E+000	-3.741441E+001	9.990010E+000
4	1.001500E-001	-3.544014E-002	-1.599692E-002	1.203841E+000	-3.475243E+001	9.985022E+000
5	1.002000E-001	-3.784565E-002	-1.549923E-002	1.202328E+000	-3.268472E+001	9.980040E+000
6	1.002500E-001	-4.000853E-002	-1.527693E-002	1.201016E+000	-3.109744E+001	9.975062E+000
7	1.003000E-001	-4.199021E-002	-1.520562E-002	1.199858E+000	-2.985460E+001	9.970090E+000
8	1.003500E-001	-4.383013E-002	-1.522469E-002	1.198822E+000	-2.885839E+001	9.965122E+000
9	1.004000E-001	-4.555547E-002	-1.530095E-002	1.197886E+000	-2.804205E+001	9.960159E+000
10	1.004500E-001	-4.718526E-002	-1.541545E-002	1.197030E+000	-2.736100E+001	9.955202E+000

Fig. 44: Structure and contents of the *.kp1 output-file

The value for the limit pressure p_{LS} can be taken from the very last line of the *.kp1-file. In case 20000 was chosen for the number of calculation steps, the last line is line 20000. As p_{LS} is defined as the limiting value for the radial stress component encountered during the expansion of a cavity within a soil body, p_{LS} can be taken from the second column of the file as illustrated in Fig. 45.

	1	2	3	4	5	6	7
19994	1.099650E+000	-3.559722E-001	-9.118933E-002	1.131454E+000	-1.818487E+000	9.093803E-001	
19995	1.099700E+000	-3.559731E-001	-9.118950E-002	1.131454E+000	-1.818487E+000	9.093389E-001	
19996	1.099750E+000	-3.559742E-001	-9.118970E-002	1.131454E+000	-1.818487E+000	9.092976E-001	
19997	1.099800E+000	-3.559752E-001	-9.118992E-002	1.131454E+000	-1.818487E+000	9.092562E-001	
19998	1.099850E+000	-3.559764E-001	-9.119017E-002	1.131454E+000	-1.818487E+000	9.092149E-001	
19999	1.099900E+000	-3.559776E-001	-9.119044E-002	1.131454E+000	-1.818487E+000	9.091736E-001	
20000	1.099950E+000	-3.559789E-001	-9.119075E-002	1.131454E+000	-1.818487E+000	9.091322E-001	

Fig. 45: The limit pressure p_{LS} from the *.kp1-file

5.2 Curve-fitting Procedures

In order to come up with the cone resistance curves for a certain material (Fig. 40) it is required to know the p_{LS} -value for every desired value of the relative density I_D and the mean effective stress p_0 . It would be quite cumbersome to do the calculation of the limit pressure for each different material state (I_D, p_0). Instead it is common to perform a series of 50 different spherical cavity expansion simulations at 5 different values for p_0 and 10 different values for I_D [41] and approximate the explicit values for p_{LS} by Eqn. (4.15) stated in chapter 4.3.1. For the purpose of the approximation, it is required to know the values of the KIM-parameters (a_i and b_i) which can be received from curve fitting using the least square method. An example of such approximated p_{LS} -lines for material PLM AZ28 from the KELLER-database can be seen in Fig. 46, where p_{LS} is plotted against the effective mean stress p_0 (named as p' in Fig. 46).

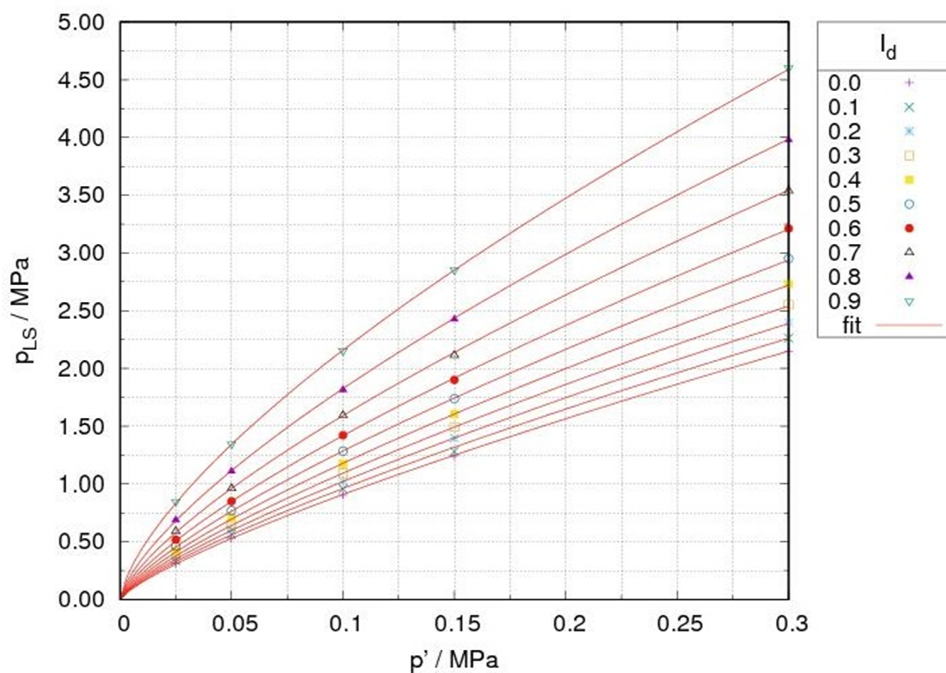


Fig. 46: p_{LS} -curves for material PLM AZ28 from the KELLER-database

5.2.1 The Least Square Method

The continuous curves in Fig. 46 follow the equation [8]

$$p_{LS} = a \cdot p_0^b \quad (5.4)$$

where a and b are coefficients which depend on the initial relative density I_D . Each curve corresponds to a certain value of I_D from the series of 10 different relative densities for which the spherical cavity expansion was performed. These values range from $I_D = 0.0$ to $I_D = 0.9$ in steps of $\Delta I_D = 0.1$.

First Step:

The first step of the curve fitting procedure involves the determination of a and b for each different relative density I_D used for the simulations. In order to come up with a best fitting line for a certain I_D it is required to reduce the sum of the squared errors S_{ID} between the explicit p_{LS} -values and the approximated values of p_{LS} at the considered values of p_0 within the series of simulations (i.e. $p_0 = 0.025, 0.05, 0.1, 0.15$ and 0.3 MPa as given in the lab report for project Port de la Mer [41]).

$$S_{ID}(p_0) = \sum_{i=1}^n [p_{LS,explicit,i} - a \cdot p_{0,i}^b]^2 \rightarrow \text{Minimum} \quad (5.5)$$

The reduction of S_{ID} can be done by using the solver-Add-on implemented in Excel. By this way it is possible to obtain the minimum of S_{ID} in terms of an automatic variation of the a - and b -values. Fig. 47 shows an extract from the Excel-file used for this task.

Labels in the image:

- Only used for the importation of $p_{LS,explicit}$ from the database (points to the p_0 column)
- Values to be varied by the solver (points to the a and b cells)
- $(p_{LS,explicit} - p_{LS \text{ approximated}})^2$ (points to the Error² column)
- $a \cdot p_0^b$ (points to the Sum of the error² cell)
- Cell value to be minimized (points to the Sum of the error² cell)

Calculated values for a and b	
a	10.50317929
b	0.686035179
I_D	0.9

p_0 [MPa]	$p_{LS \text{ explicit}}$ [MPa]	$p_{LS \text{ approximated}}$ [MPa]	Error ²
0.025	0.8489749000000000	0.8360866071214920	0.000166108
0.05	1.3467460000000000	1.3451429307437900	2.56983E-06
0.1	2.1549140000000000	2.1641412369461200	8.51419E-05
0.15	2.8538040000000000	2.8581854154357300	1.91968E-05
0.3	4.6026800000000000	4.5984086739111000	1.82442E-05

Sum of the error ²	0.0002912608538004
-------------------------------	--------------------

Fig. 47: First step of the curve-fitting procedure - extract from the Excel-file

A graphical representation of the first step of the curve-fitting procedure involving the solver-Add-on in Excel can be found in the figures below. Fig. 48 illustrates the approximated p_{LS} -line next to the $errors^2$, received at the considered values of p_0 , for $I_D = 0.9$ before the solver, correcting the values for a and b , was applied.

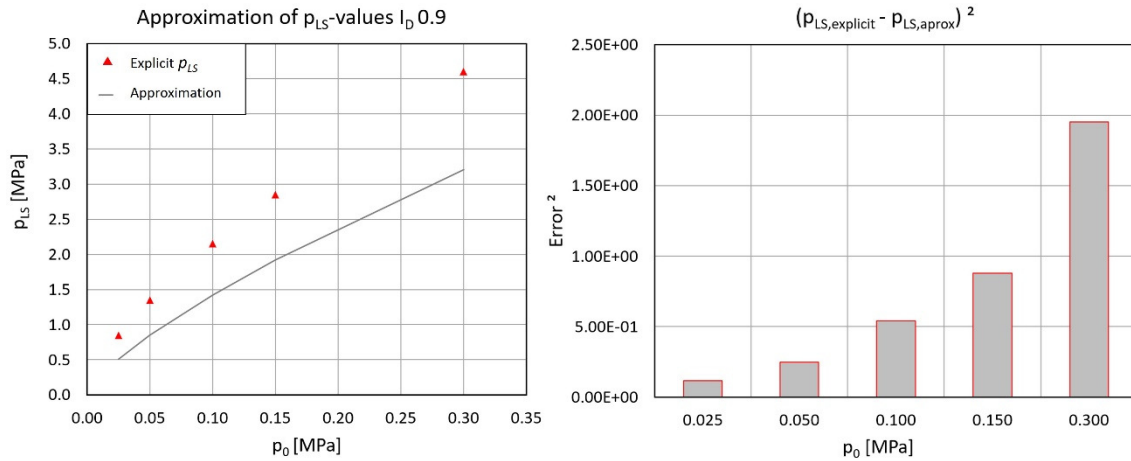


Fig. 48: Approximated p_{LS} -curve (left) and errors² at considered values of p_0 (right) before the solver was applied

In comparison the approximated p_{LS} -curve and the $errors^2$ obtained from the corrected values of a and b for the same relative density I_D are shown in Fig. 49. One can see, that the curve much better fits the explicit p_{LS} -values and the single $errors^2$ at different mean effective stresses are reduced.

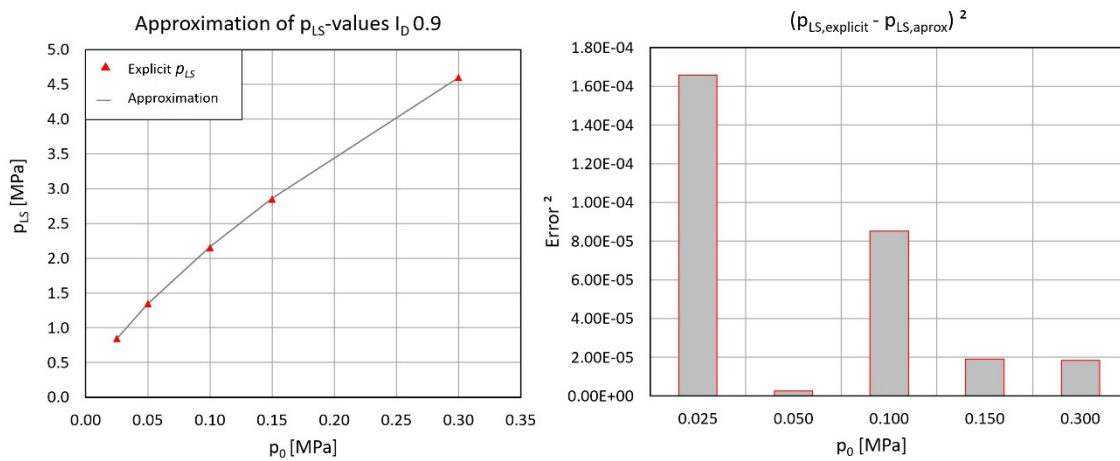


Fig. 49: Approximated p_{LS} -curve (left) and errors² at considered values of p_0 (right) after the solver was applied

After applying the explained curve-fitting procedure on each considered relative density from the series of simulations, one ends up with all values for a and b required for the determination of the KIM-parameters (a_i and b_i) within the subsequent step. Within the following tables the values for a and b received from the first step of the least-square curve-fitting approach for the materials PLM AZ28 and PLM BC36 are listed.

Tab. 6: Values for a and b from the first step of the curve-fitting (PLM AZ28)

First Step - Values for a and b (PLM AZ28)		
I_D	a	b
0	5.502131833	0.782764537
0.1	5.784311103	0.783236914
0.2	6.073021876	0.772752616
0.3	6.418804463	0.767250681
0.4	6.819941168	0.760972292
0.5	7.298014137	0.753404455
0.6	7.834037195	0.742188274
0.7	8.486030241	0.728191489
0.8	9.366829095	0.711776122
0.9	10.503077998	0.686030093

Tab. 7: Values for a and b from the first step of the curve-fitting (PLM BC36)

First Step - Values for a and b (PLM BC36)		
I_D	a	b
0	5.424740783	0.800726481
0.1	5.642132922	0.797544152
0.2	5.893985767	0.794411680
0.3	6.164326929	0.789403946
0.4	6.475942329	0.783879292
0.5	6.844334871	0.777980159
0.6	7.300451231	0.771973885
0.7	7.842205058	0.763467597
0.8	8.527104715	0.751391252
0.9	9.314093340	0.724789431

Second Step:

The second step of the curve-fitting procedure aims at determining the a_i - and b_i -parameters from the calculated values for a and b from step 1. The same least square procedure as used before is applied but with the only difference that now the $errors^2$ between the calculated a - and b - values, hereafter referred to as the explicit a - and b -values, and the approximated values of a and b must be minimized. The approximations are based on Eqn. (5.6) [8].

$$a = a_1 + \frac{a_2}{a_3 + I_D} \qquad b = b_1 + \frac{b_2}{b_3 + I_D} \qquad (5.6)$$

The expression for the $error^2$ -sums $S_{KIM,i}$ to be minimized in step 2 are given as follows:

$$S_{KIM,a}(I_D) = \sum_{k=1}^n \left[a_{explicit,k} - \left(a_1 + \frac{a_2}{a_3 + I_{D,k}} \right) \right]^2 \rightarrow Minimum \qquad (5.7)$$

$$S_{KIM,b}(I_D) = \sum_{k=1}^n \left[b_{explicit,k} - \left(b_1 + \frac{b_2}{b_3 + I_{D,k}} \right) \right]^2 \rightarrow Minimum \qquad (5.8)$$

An example of the Excel-file layout, used for the calculation of the a_i -parameters, can be found in Fig. 50. The same structure can be adopted to the calculation of b_i .

From step 1 of the curve-fitting procedure		Values to be varied by the solver	
Calculated values for a_i			
a_1	1.704880132		
a_2	-6.082828643		
a_3	-1.592582586		
			$(a_{explicit} - a_{approximated})^2$
ID	a explicit	a approximated	Error ²
0	5.50213183289882	5.52435467217396	4.939E-04
0.1	5.78431110319320	5.78025170429503	1.648E-05
0.2	6.07302187635340	6.07290016999260	1.481E-08
0.3	6.41880446290544	6.41082983764578	6.359E-05
0.4	6.81994116827764	6.80543141574009	2.105E-04
0.5	7.29801413716262	7.27226580863536	6.630E-04
0.6	7.83403719489827	7.83316479611192	7.611E-07
0.7	8.48603024067457	8.51974380379433	1.137E-03
0.8	9.36682909528007	9.37957390718725	1.624E-04
0.9	10.50307799757790	10.48770078276750	2.365E-04
Sum			0.0029837064897293
	$a_1 + \frac{a_2}{a_3 + I_D}$		Cell value to be minimized

Fig. 50: Determination of the a_i -parameters - extract from the Excel-file

The approximations of a and b given in Eqn. (5.6) are now comprising three unknown values (a_i and b_i) which must be determined by the solver by minimizing the $error^2$ -sum $S_{KIM,i}$. In case of three unknowns it was found that the solver solution is dependent on the initial values of a_i , b_i respectively, which are encountered just before the solver is applied. Hence, it was required to develop a procedure to come up with good guesses for the initial values.

It requires three equations in order to determine the three unknown values of a function. As from the first step of the curve-fitting procedure at least 10 values for a and b are known, the three equations can be easily obtained from taking into account the a - and b -values from three specific values of I_D . It was found that the equations received from $I_{D,I} = 0.1$, $I_{D,II} = 0.5$ and $I_{D,III} = 0.9$ can be used to end up with good guesses for the initial values of a_i and b_i . The 3 equations for the determination of the a_i -values are given as follows:

$$a_I = a_1 + \frac{a_2}{a_3 - I_{D,I}} \quad (5.9)$$

$$a_{II} = a_1 + \frac{a_2}{a_3 - I_{D,II}} \quad (5.10)$$

$$a_{III} = a_1 + \frac{a_2}{a_3 - I_{D,III}} \quad (5.11)$$

where a_I , a_{II} and a_{III} represent the calculated values for a from step 1 at the considered values of $I_{D,i}$. From Eqn. (5.9) a_1 can be received as

$$a_1 = a_I - \frac{a_2}{a_3 - I_{D,I}} \quad (5.12)$$

By inserting Eqn. (5.12) into Eqn. (5.10) a_2 can be expressed as

$$a_2 = \frac{(a_{II} - a_I) \cdot (a_3 + I_{D,I}) \cdot (a_3 + I_{D,II})}{I_{D,I} - I_{D,II}} \quad (5.13)$$

Putting together the equations for a_I and a_2 and inserting them into Eqn. (5.11) yields

$$a_{III} = a_I + \frac{1}{I_{D,I} - I_{D,II}} \cdot \left[\left(\frac{1}{a_3 + I_{D,III}} - \frac{1}{a_3 + I_{D,I}} \right) \cdot (a_{II} - a_I) \cdot (a_3 + I_{D,I}) \cdot (a_3 + I_{D,II}) \right] \quad (5.14)$$

This equation can be solved for the initial value of a_3 and a_2 and a_1 can be subsequently calculated from Eqn. (5.13) and Eqn. (5.12). Note, that the same equations are also valid for the determination of the initial b_i -values, when a_I , a_{II} and a_{III} are replaced by b_I , b_{II} and b_{III} .

The received values from this approach depict the starting points of the KIM-parameters for the solving-procedure within the Excel-file in which the sum of the $errors^2 S_{KIM,i}$ is minimized.

Fig. 51 shows the fitted curve (step 2) of the explicit a -values right next to the $errors^2$ calculated at the 10 different values of the relative density I_D . The same diagrams from the determination of the b_i -values can be seen in Fig. 52.

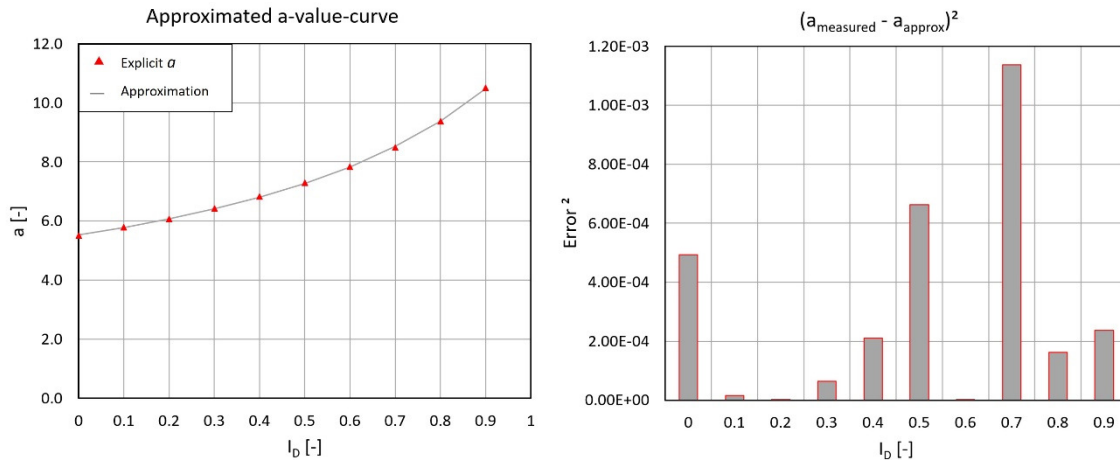


Fig. 51: Approximated a -curve (left) and $errors^2$ at considered values of I_D (right)

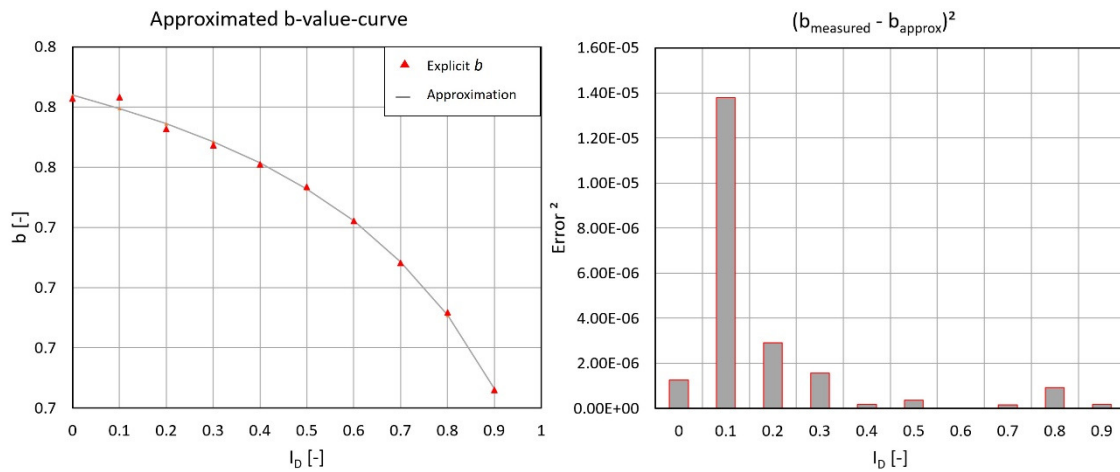


Fig. 52: Approximated b -curve (left) and $errors^2$ at considered values of I_D (right)

As a result of the whole curve-fitting approach the KIM-parameters a_i and b_i from the material under investigation are received which can further be used to approximate the cone penetration resistance q_c for every desired relative density I_D and mean effective pressure p_0 . Tab. 8 lists the KIM-parameters for material PLM AZ28 from the KELLER-database (A. Tab. 5), for which the limit pressures p_{LS} (see Tab. 22 in chapter 6.6.4) were determined with the aid of the OSINOV code.

Tab. 8: KIM-parameters from OSINOV code calculations for material PLM AZ28

KIM-parameters	
a_1	1.705
a_2	-6.083
a_3	-1.593
b_1	0.842
b_2	0.084
b_3	-1.440

5.2.2 Gnuplot Curve-Fitting

Dr. Thomas Meier from Baugrund Dresden kindly made available a script-file which can be used within the computer program Gnuplot to conduct the curve-fitting of the KIM. By this means it was possible to verify if the presented curve-fitting procedure in chapter 5.2.1 can yield accurate results for the KIM-parameters.

The script-file extracts data from a text-file, named final.dat, and automatically creates several output-files containing information about the received KIM-parameters, graphical representations of the approximated a- and b-values and final diagrams for the q_c -curves. The final.dat file contains the limit pressures received from a series of 50 spherical cavity expansions conducted for the suggest 10 different values of I_D and 5 different values of p_0 . The data within final.dat has to be structured as can be seen in Fig. 53.

Row	p_0 [kPa]	p_{LS} [kPa]	I_D
1	25	311.305	0.0
2	50	528.591	
3	100	904.914	
4	150	1243.52	
5	300	2145.7	
6			
7	25	331.981	0.1
8	50	564.57	
9	100	958.151	
10	150	1281.86	
11	300	2262.12	
12			
13	25	355.979	0.2
14	50	604.884	
15	100	1020.57	
16	150	1396.89	
17	300	2398.04	
18			

Fig. 53: Structure of the final.dat-file for the Gnuplot curve-fitting approach

It is possible to make use of an auxiliary-program, which was also provided by Dr. Meier, to automatically generate the final.dat file from the received *.kpl files from the series of simulations done with the OSINOV code. It has to be noted that by means of this, the extracted limit pressure p_{LS} will only be taken into account up to a maximum accuracy of

three digits after the comma. This may result in slight differences of the received KIM-parameters from the curve-fitting approach stated in chapter 5.2.1 and the KIM-parameters obtained from the Gnuplot curve-fit. Fig. 56 to Fig. 55 present some of the diagrams which were automatically generated by the script-file run with Gnuplot.

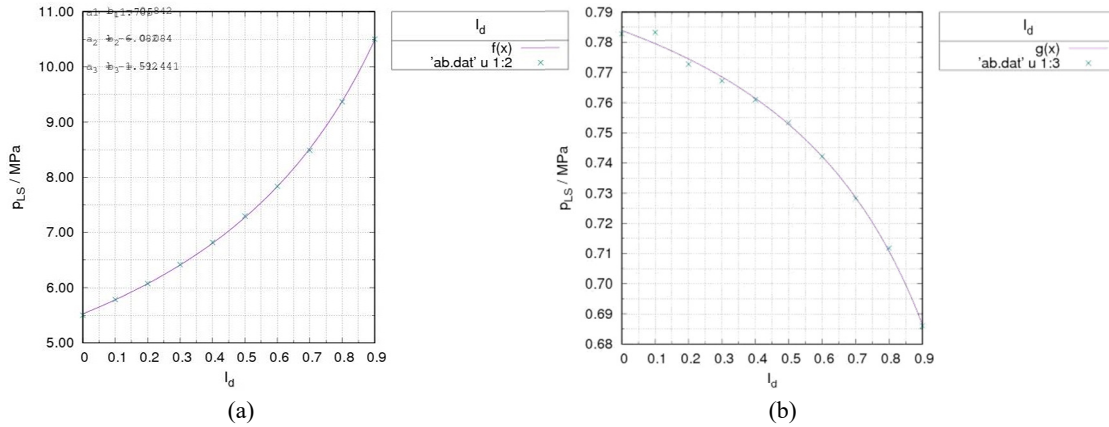


Fig. 56: Approximated a-curves (a) and b-curves (b) from Gnuplot

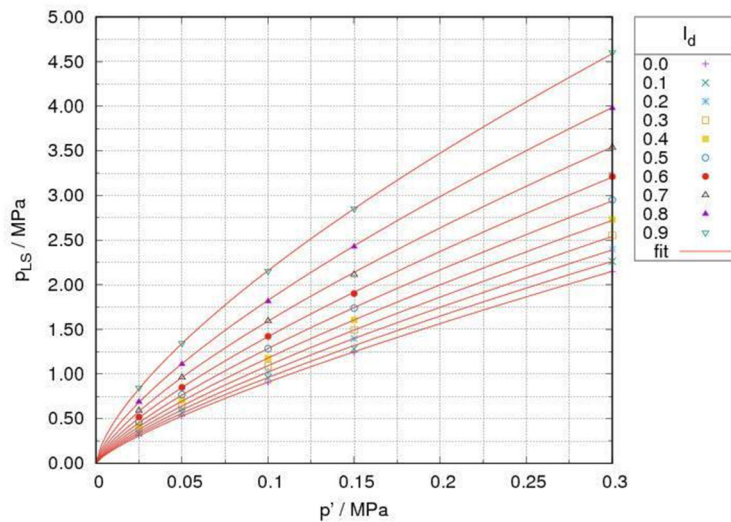


Fig. 54: Approximated p_{LS} -curves from Gnuplot

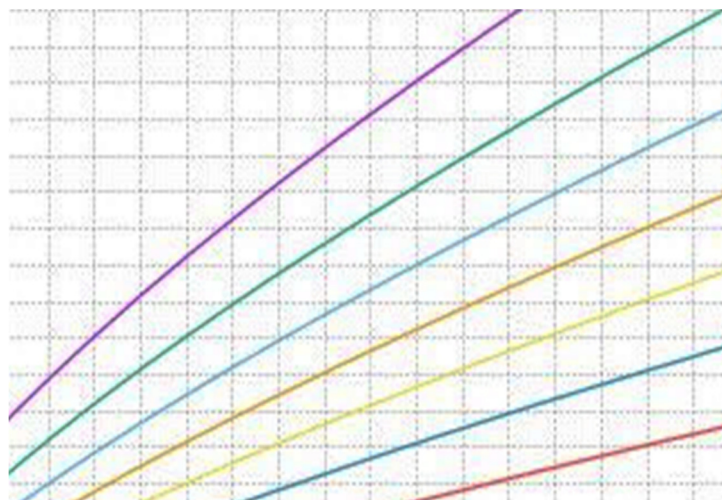


Fig. 55: Final q_c -curves from Gnuplot

It is worth to mention that the K_0 -coefficient depicted in Fig. 56, which can be used for the calculation of the effective mean pressure p_0 , can be estimated with the standard equation acc. to Jaky for normally consolidated soils.

$$K_0 = 1 - \sin \varphi_c \quad (5.15)$$

5.2.3 Comparison of Curve-Fitting Approaches

A comparison of the received KIM-parameters from both curve-fitting approaches stated in chapter 5.2, for which the limit pressures p_{LS} were obtained from calculations with the OSINOV Code, yielded the conclusion that the curve-fitting approach using the Excel-file works sufficiently. The received limit pressures for material PLM AZ28 can be found in Tab. 22 in chapter 6.6.4 and for material PLM BC36 in A. Tab. 7 within Appendix E. Comparisons were made for material PLM AZ28 and PLM BC36 by the author of this thesis. Further comparison for material Palm Jumeirah and Palm Deira were done by Slawik [9] and can be found in Appendix D. All of the mentioned materials are part of the KELLER-database. The hypoplastic parameters for these materials are given in A. Tab. 5.

Tab. 9: Comparison of KIM-parameters – Material PLM AZ28

	Report [41]	Excel Curve-Fit	Gnuplot Curve-Fit
a_1	1.666	1.705	1.705
a_2	-6.152	-6.083	-6.082
a_3	-1.597	-1.593	-1.592
b_1	0.835	0.842	0.842
b_2	0.073	0.084	0.084
b_3	-1.395	-1.440	-1.441

Tab. 10: Comparison of KIM-parameters – Material PLM BC36

	Report [41]	Excel Curve-Fit	Gnuplot Curve-Fit
a_1	2.550	2.038	2.042
a_2	-4.477	-5.697	-5.689
a_3	-1.544	-1.682	-1.681
b_1	0.841	0.829	0.829
b_2	0.060	0.037	0.037
b_3	-1.460	-1.261	-1.261

Both curve-fitting approaches, practically speaking, ended up with the same values for a_i and b_i proving that the curve-fitting procedure implemented in Excel works quite well. When the results, however, are compared to the given values within the lab-report from project Port de la Mer [41] significant differences, especially for material PLM BC36, can be made out. This is connected to the very strong sensitivity of the results from the

curve-fitting procedure w.r.t to the considered limit pressures p_{LS} from the simulations. Slight differences in the limit pressures may result in different values for a_i and b_i . It is believed that the accuracy of the used hypoplastic parameters and different considered calculation parameters, for the calculations within the report, produced limit pressure p_{LS} , which are slightly different from the limit pressures obtained within the present studies. This may have led to the encountered discrepancies between the obtained KIM-parameters and the parameter given in the report.

However, the KIM-parameters must not be considered individually but have to be seen as a whole. They are all used together in one single equation for the calculation of the q_c -curves and therefore only the whole set of KIM-parameters is affecting the final results. Studies on the influence of the different sets of KIM-parameters on the q_c -curves were conducted which proved that also in case of material PLM BC36, where the biggest differences between the KIM-parameters from the report and the calculations of this thesis were encountered, the final q_c -curves are identical. Fig. 57 shows the q_c -curves over the depth for material PLM BC36 at a relative density of $I_D = 0.9$. In the context of this chapter only the red line and the two blue lines should be considered, which were calculated with the listed KIM-parameters in Tab. 10. The lines are congruent, proving that there is no influence of the different KIM-parameter-sets on the final results.

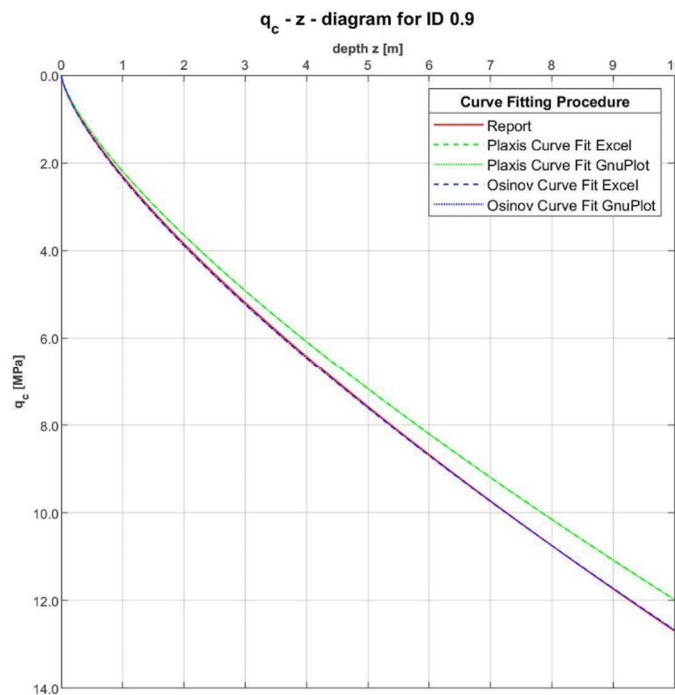


Fig. 57: q_c over depth: Influence of KIM-parameters on the final results (PLM BC36)

5.2.4 Improving the Simulation Series

As already stated within chapter 5.2 it is common to perform the curve fitting on 50 different explicit values for p_{LS} obtained from calculations with different relative densities I_D and mean effective stresses p_0 .

It is quite time consuming to perform 50 calculations and evaluate the results. Hence it was tried to reduce the number of simulations and to find out how the values of the KIM-parameters and the subsequently calculated approximations for a and b are affected.

One first try was based on the received limit pressures from the OSINOV simulation series conducted on material PLM AZ28 (KELLER-database). However, within the curve-fitting procedure not all p_{LS} -values for all I_D from the series of 50 simulations were considered, but only the values at $I_D = 0.1, 0.2, 0.7$ and 0.9 . The considered initial mean pressures p_0 (25, 50, 100, 150 and 300 kPa) remained the same as within the whole series. This makes a total of 25 different limit pressures p_{LS} for which the curve-fitting, using the Excel-method, was done. Within Tab. 11 the resulting values for the KIM-parameters from the 25 p_{LS} -values are compared to the KIM-parameters received from the series of 50 simulations.

Tab. 11: KIM-parameters - 25 vs. 50 simulations

	25 Simulations	50 Simulations
<i>a1</i>	1.442205961	1.705
<i>a2</i>	-5.643900476	-6.083
<i>a3</i>	-1.557151936	-1.593
<i>b1</i>	0.815662467	0.842
<i>b2</i>	0.057108618	0.084
<i>b3</i>	-1.351357059	-1.440

As for the approximation of the limit pressure p_{LS} from the initial mean effective stress p_0 the factor a and the exponent b play an important role, the a- and b- values were subsequently calculated from the received KIM-parameters using Eqn. (4.16) and again compared to the results of the whole series. The comparisons can be found within Tab. 12.

Looking at the differences Δa and Δb one can see that the received a – and b-values are only slightly different from the results of the whole series. The b-values stay in fact the same, whereas the biggest difference can be made out for the a-values at $I_D = 0.0$. For higher values of the relative density, as encountered in vibro compaction works, the differences in the a-values are getting smaller. This is the reason why it is definitely a good idea to think about a reduction of the number of simulations within the series in order to save up on calculation time and effort with respect to the evaluation of the results.

Tab. 12: Values for a and b - 25 vs. 50 simulations

I_D	50 Simulations		25 Simulations			
	a	b	a	b	Δa	Δb
	[-]	[-]	[-]	[-]	[%]	[%]
0	5.163457846	0.772842942	5.066708069	0.773402269	1.9	-0.1
0.1	5.394322232	0.769635958	5.315446860	0.770025119	1.5	-0.1
0.2	5.660921191	0.765858062	5.600841649	0.766061332	1.1	0
0.3	5.972247519	0.761341905	5.931639826	0.761343511	0.7	0
0.4	6.340587756	0.755847653	6.319612548	0.755633883	0.3	0
0.5	6.783182158	0.749018970	6.780984885	0.748582953	0	0.1
0.6	7.325001115	0.740302500	7.338762467	0.739655172	-0.2	0.1
0.7	8.003624629	0.728789867	8.026686773	0.727986104	-0.3	0.1
0.8	8.878351898	0.712878562	8.896324754	0.712084184	-0.2	0.1
0.9	10.04854194	0.689452342	10.030631510	0.689135992	0.2	0

Although the considered set of relative densities and initial mean effective pressures already yielded good results, further research is necessary to find the best combination of relative densities and initial mean effective pressures to be considered within the simulation series of the KIM.

5.3 Sensitivity Study by Slawik

A sensitivity study with the OSINOV code was performed by Slawik [9] to find out to what extent the calculated limit pressures p_{LS} depend on single input parameters. Therefore, the reference limit pressures, calculated with the suggested numerical parameters and the given hypoplastic parameters for different materials, were compared to the limit pressures received from calculations, for which a single parameter was changed by a certain factor. Slawik [9] investigated three different materials from the KELLER-database, including material PLM AZ28.

Tab. 13 and Tab. 14 demonstrate the changes of the limit pressures p_{LS} for PLM AZ28 resulting from a change of different numerical parameters by the given factors. Tab. 13 refers to an initial effective mean pressure of $p_0 = 0.05$ MPa, whereas Tab. 14 shows the differences of the limit pressures for $p_0 = 0.3$ MPa. The results suggest that the OSINOV limit pressures are very sensitive to varying numerical input parameters.

Tab. 13: PLM AZ28 – Sensitivity of p_{LS} on the numerical parameters (OSINOV) for $p_0 = 0.05$ MPa

PORT DE LA MER				ϕ_c	h_s	n	e_{d0}	e_{c0}	e_{i0}	α	β
				36,30	39,00	0,53	0,74	1,26	1,45	0,05	1,97
$p_0=0,05$ MPa											
	$l_d=0,2$			$l_d=0,5$			$l_d=0,8$				
	Factor	p_{LS}	Change	Factor	p_{LS}	Change	Factor	p_{LS}	Change		
Control result	-	-0,6048838	-	-	-0,760495	-	-	-1,109462	-		
Calculation parameters											
Calculation steps	/10	-0,5216281	-13,8%	/10	-0,6649212	-12,6%	/10	-0,9597621	-13,5%		
Calculation steps	x1,5	-0,6285552	3,9%	x1,5	-0,8014652	5,4%	x1,5	-1,141382	2,9%		
Discretization	/2	-0,6395419	5,7%	/2	-0,845144	11,1%	/2	-1,337755	20,6%		
Discretization	x1,666	-0,6053387	0,1%	x1,666	-0,7722239	1,5%	x1,666	-1,115676	0,6%		
Initial radius	/2	-0,5986801	-1,0%	/2	-0,7642037	0,5%	/2	-1,104351	-0,5%		
Initial radius	x10	-0,5725258	-5,3%	x10	-0,7272511	-4,4%	x10	-1,040294	-6,2%		
Radius boundary	/10	-0,481466	-20,4%	/10	-0,5318789	-30,1%	/10	-0,5940341	-46,5%		
Radius boundary	x4	-0,8534688	41,1%	x5	-1,30183	71,2%	x5	-1,585525	42,9%		
Time step	/10	-0,5792326	-4,2%	/10	-0,7442952	-2,1%	/10	-1,098693	-1,0%		
Time step	x5	-0,6044695	-0,1%	x5	-0,7652222	0,6%	x4	-1,102246	-0,7%		

Tab. 14: PLM AZ28 – Sensitivity of p_{LS} on the numerical parameters (OSINOV) for $p_0 = 0.30$ MPa

PORT DE LA MER				ϕ_c	h_s	n	e_{d0}	e_{c0}	e_{i0}	α	β
				36,30	39,00	0,53	0,74	1,26	1,45	0,05	1,97
$p_0=0,3$ MPa											
	$l_b=0,2$			$l_b=0,5$			$l_b=0,8$				
	Factor	p_{LS}	Change	Factor	p_{LS}	Change	Factor	p_{LS}	Change		
Control result	-	-2,398035	-	-	-2,950882	-	-	-3,978223	-		
Calculation parameters											
Calculation steps	/10	-2,073838	-13,5%	/10	-2,554281	-13,4%	/10	-3,462995	-13,0%		
Calculation steps	x1,5	-2,501417	4,3%	x1,5	-3,07111	4,1%	x1,5	-4,117093	3,5%		
Discretization	/2	-2,476652	3,3%	/2	-3,090752	4,7%	/2	-4,308621	8,3%		
Discretization	x1,666	-2,406685	0,4%	x1,666	-2,963104	0,4%	x1,666	-4,003093	0,6%		
Initial radius	/2	-2,382207	-0,7%	/2	-2,934327	-0,6%	/2	-3,960722	-0,4%		
Initial radius	x10	-2,271059	-5,3%	x10	-2,784244	-5,6%	x10	-3,743111	-5,9%		
Radius boundary	/10	-2,240042	-6,6%	/10	-2,627252	-11,0%	/10	-3,168289	-20,4%		
Radius boundary	x5	-2,819525	17,6%	x5	-3,757654	27,3%	x5	-5,950857	49,6%		
Time step	/10	-2,271743	-5,3%	/10	-2,796863	-5,2%	/10	-3,79458	-4,6%		
Time step	x10	-2,297202	-4,2%	x10	-2,730633	-7,5%	x10	-3,377166	-15,1%		

5.4 Automatic Diagram Generation using MATLAB

During the expansion of a cavity within a continuum the stresses around the cavity are changing. Not only the stresses are affected, but also the density of the surrounding soil body, which may be observed by changing values for the void ratio e . The simplest way to study the relationship between the stresses and strains encountered during the cavity expansion is the plotting of stress-path-diagrams and pressure-expansion-curves.

For this purpose, two scripts in MATLAB-R2108a were created which can be used to automatically extract data from the *.kpl-files (= OSINOV code output-file corresponding to a point at the cavity wall) and generate a couple of different diagrams describing the expansion-process. Note that the .kpl extension from these files must be replaced by a simple .txt-extension as problems with the extraction will arise in MATLAB if the file-extension remains unaltered.

5.4.1 CODE “StressPaths_1ID_Allp.m”

One of the two created scripts (StressPaths_1ID_Allp.m) can be utilised to produce diagrams containing curves from up to 5 different mean pressures p_0 and one desired value of the relative density I_D . The addressing of the desired input-files (.txt-files = former *.kpl-files) works as shown in Fig. 58. The same name convention as used for the calculations with the OSINOV code is adopted, i.e. 025_09.txt, representative for the file that holds the information from the SCE-simulation performed at $p_0 = 0.025$ MPa and $I_D = 0.9$. The script should only be run in case that the five addressed files refer to the same relative density but different effective mean pressures. The vector N in Fig. 58 can be used to deselect certain input-files and suppress the output of the corresponding curves. The numbers within vector N simply refer to the FileName-number of the addressed files. Once a number is excluded from N the output of the corresponding curve is suppressed.

```
N=[1 2 3 4 5];

%Id
FileName{1} = '025_i09.txt';   %MaterialID_1(p0 = 25[kPa])
FileName{2} = '050_i09.txt';   %MaterialID_2(p0 = 50[kPa])
FileName{3} = '100_i09.txt';   %MaterialID_3(p0 = 100 [kPa])
FileName{4} = '150_i09.txt';   %MaterialID_4(p0 = 150 [kPa])
FileName{5} = '300_i09.txt';   %MaterialID_5(p0 = 300 [kPa])
```

Fig. 58: Addressing of the input-files within the MATLAB-script

By running the script in MATLAB, six different diagrams are generated, namely:

- s - t -diagram $s = (p_r + p_\theta)/2$ $t = (p_r - p_\theta)/2$
- p - q -diagram $p = (p_r + 2p_\theta)/3$ $q = p_r - p_\theta$
- $\log(p)$ - e -diagram
- r_a/r_a^0 - p_r -diagram $r_a/r_a^0 = \text{expansion ratio}$

- r_a/r_a^0 - p_θ -diagram r_a/r_a^0 = expansion ratio
- r_a/r_a^0 - e -diagram r_a/r_a^0 = expansion ratio

Examples of the created diagrams for material PLM AZ28 from the KELLER-database for two different relative densities ($I_D = 0.0$ and $I_D = 0.9$) can be found in the following. The dashed line CSL represents the critical state line.

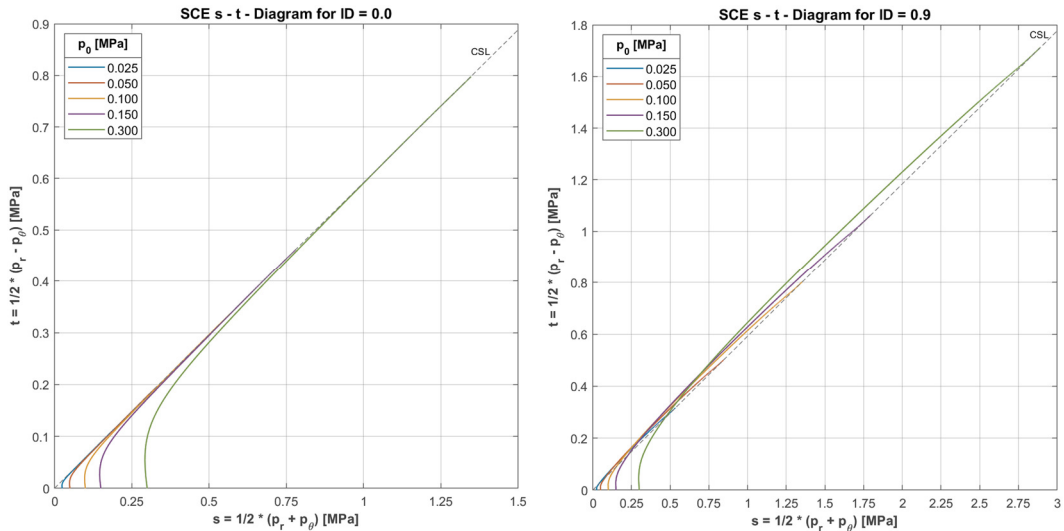


Fig. 59: $s - t$ - diagrams for PLM AZ28 for 5 different p_0 and $I_D = 0.0$ (left) and $I_D = 0.9$ (right)

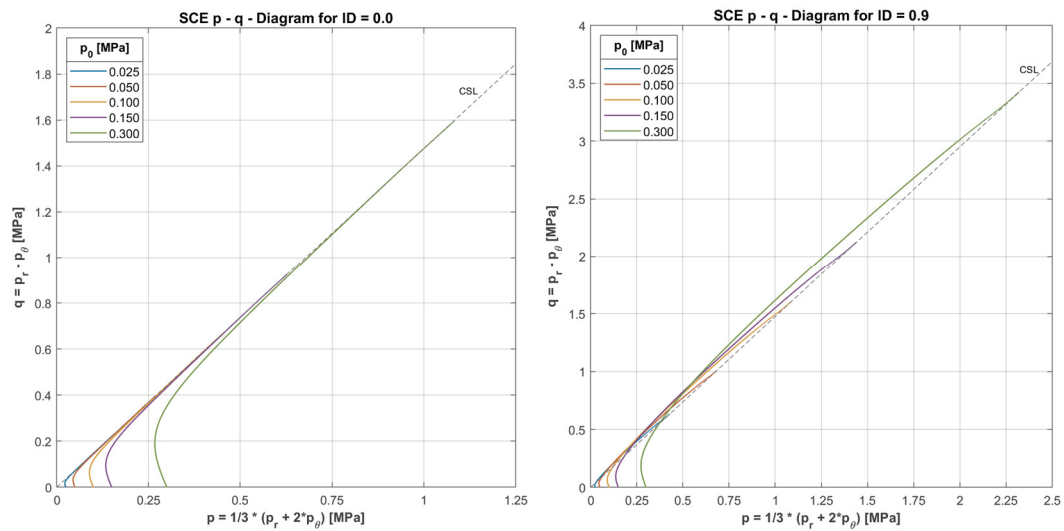


Fig. 60: $p - q$ - diagrams for PLM AZ28 for 5 different p_0 and $I_D = 0.0$ (left) and $I_D = 0.9$ (right)

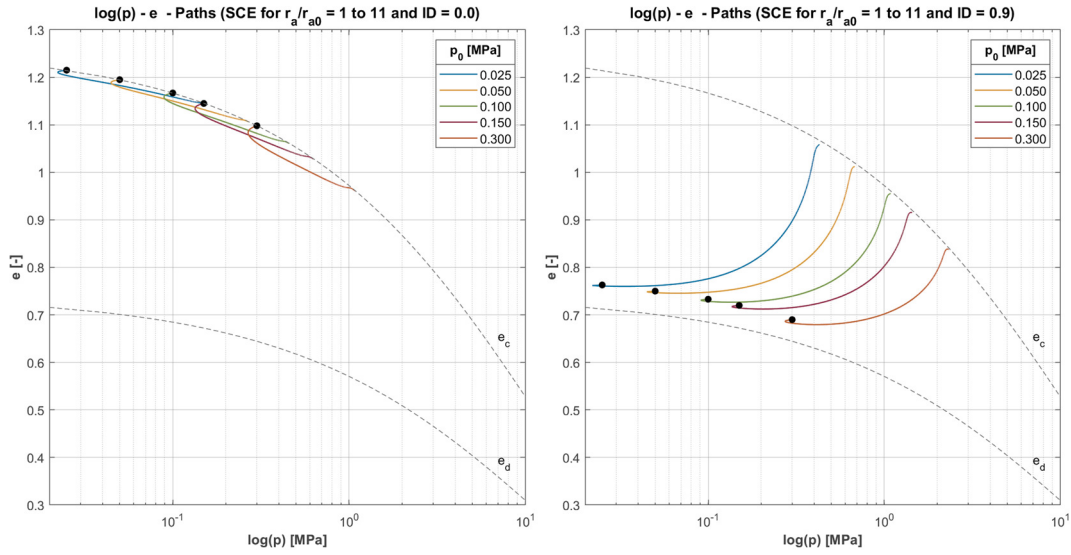


Fig. 61: $\log(p)$ - e diagrams for PLM AZ28 for 5 different p_0 and $I_D = 0.0$ (left) and $I_D = 0.9$ (right)

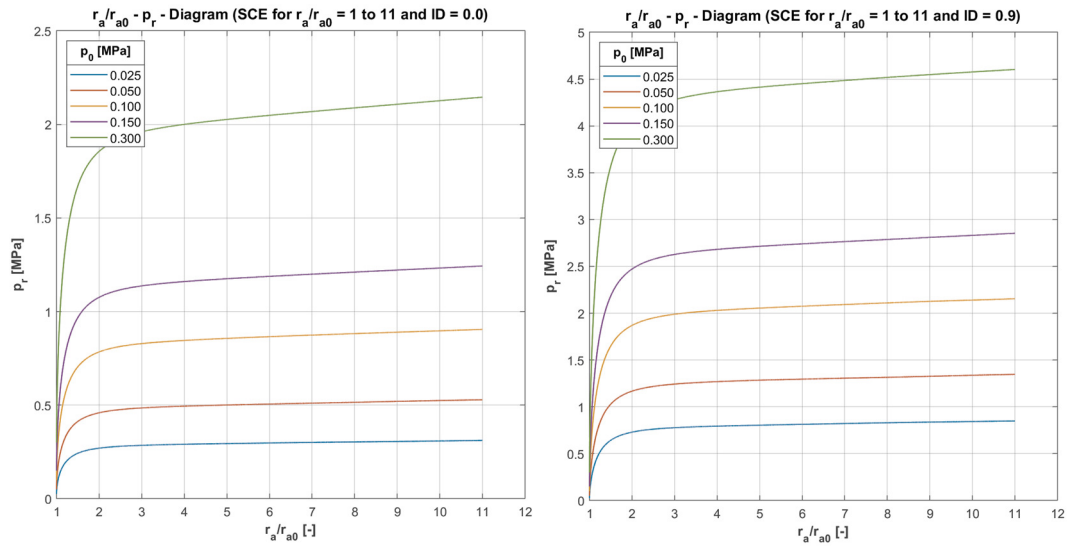


Fig. 62: r_a/r_{a0}^0 - p_r diagrams for PLM AZ28 for 5 different p_0 and $I_D = 0.0$ (left) and $I_D = 0.9$ (right)

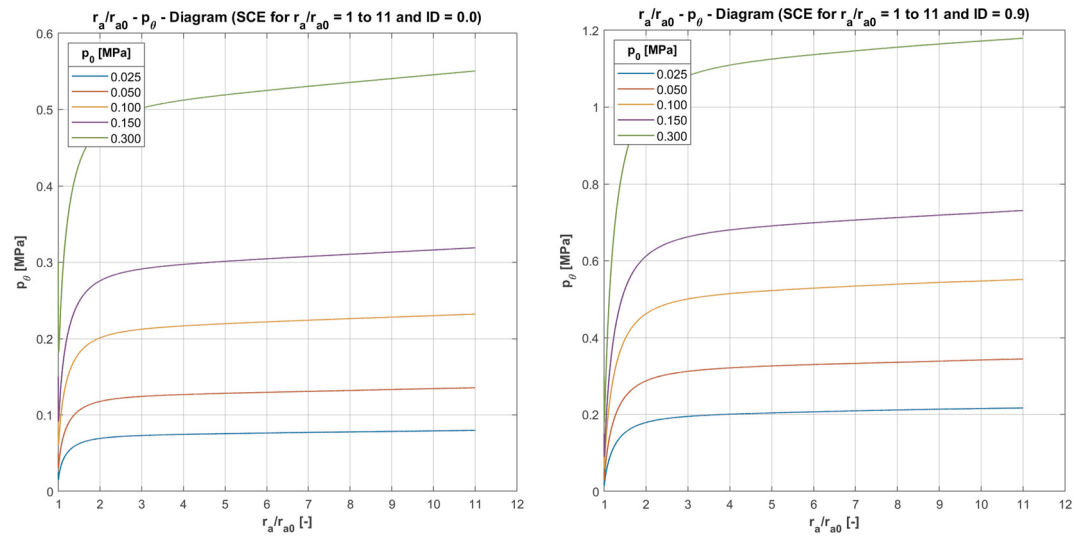


Fig. 63: r_a/r_{a0}^0 - p_θ diagrams for PLM AZ28 for 5 different p_0 and $I_D = 0.0$ (left) and $I_D = 0.9$ (right)

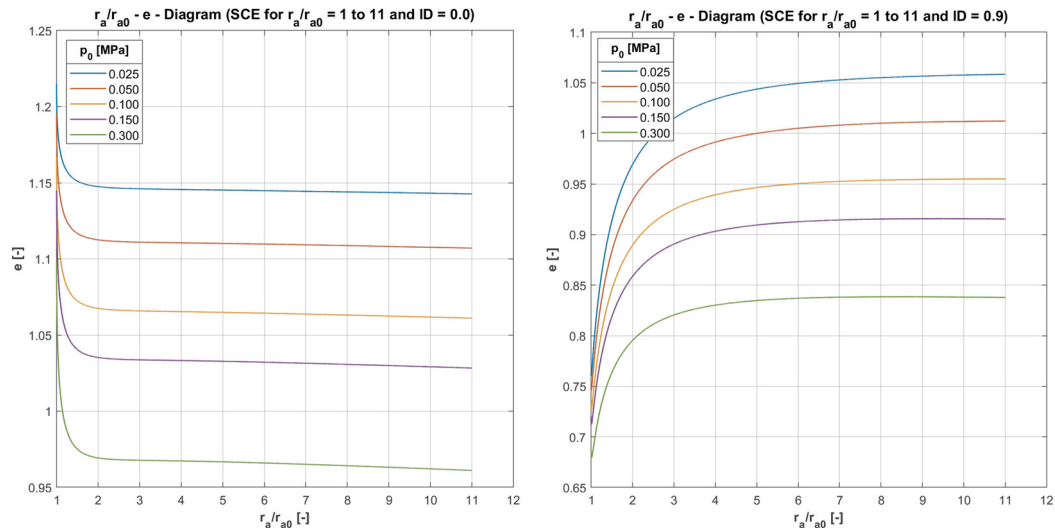


Fig. 64: $r_a/r_a^0 - e$ - diagrams for PLM AZ28 for 5 different p_0 and $I_D = 0.0$ (left) and $I_D = 0.9$ (right)

The reduction of the mean effective stress p in Fig. 60 right at the beginning of the expansion may be explained due to the fact that the material first experiences compression which leads to a decrease of the tangential stresses p_θ [8]. Due to the scale of the presented diagram in Fig. 63 this behaviour may not be detected at first hand. In Fig. 61 it can be seen that a loose state of the soil will result in an overall decrease of the void ratios, whereas the dense sample experiences an overall increase of the volume, except at the beginning of the expansion.

Fig. 62 shows the progression of the radial stresses p_r with ongoing expansion. In disagreement with the definition of the limit pressure p_{LS} , a horizontal course of p_r for increasing expansion ratios is never reached when using the OSINOV code. It is therefore not possible to determine the limit pressure p_{LS} from the presented diagram without knowing that p_{LS} corresponds to the last point of the curve, associated with the highest value of p_r (line 20000 within the *kp1.file). It is believed that the calculation parameters, suggested for the usage of the OSINOV code, account for the missing capability of the code to end up with a horizontal line for p_r and that these parameters are therefore used as a substitute limit criterion for p_r in order to come up with proper values for the limit pressures p_{LS} .

The code used within StressPaths_1ID_Allp.m, as well as the generated diagrams for material PLM BC36 can be found in A. Fig 2 to A. Fig 7 within Appendix D.

5.4.2 CODE “StressPaths_1p_AllID.m”

The second script (StressPaths_1p_AllID.m) may be used to generate the same kind of diagrams as presented in 5.4.1, but with the difference that only one value for the effective mean pressure p_0 and up to 10 different relative densities can be considered. The addressing of the input files works just like for the other script.

In the following, the diagrams for material PLM AZ28 are shown, whereas the code of the script, as well as the diagrams for PLM BC36 can be found in A. Fig 8 to A. Fig 14 in Appendix D.

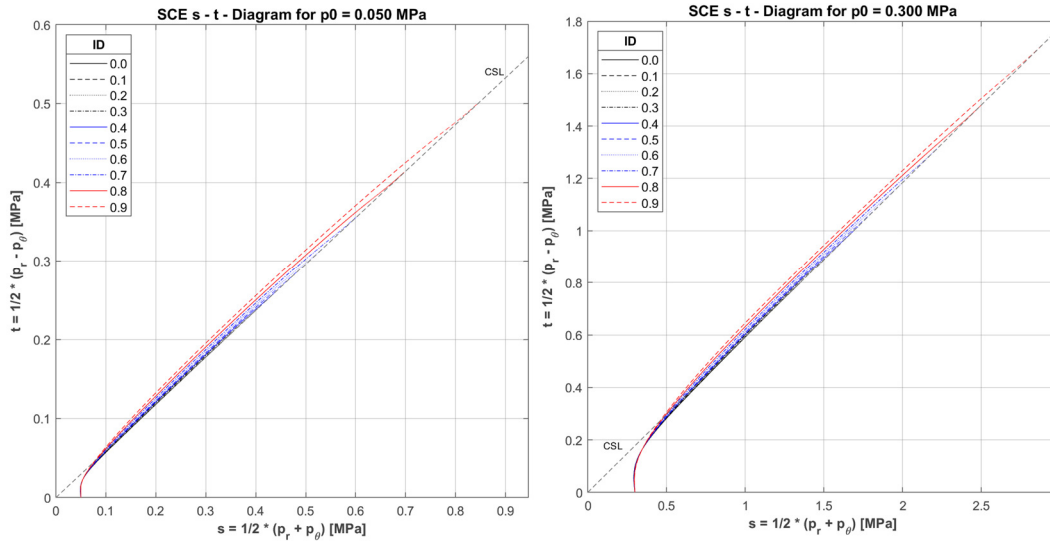


Fig. 65: $s - t$ - diagrams for PLM AZ28 for 10 different I_D and $p_0 = 0.050$ MPa (left) or $p_0 = 0.300$ MPa (right)

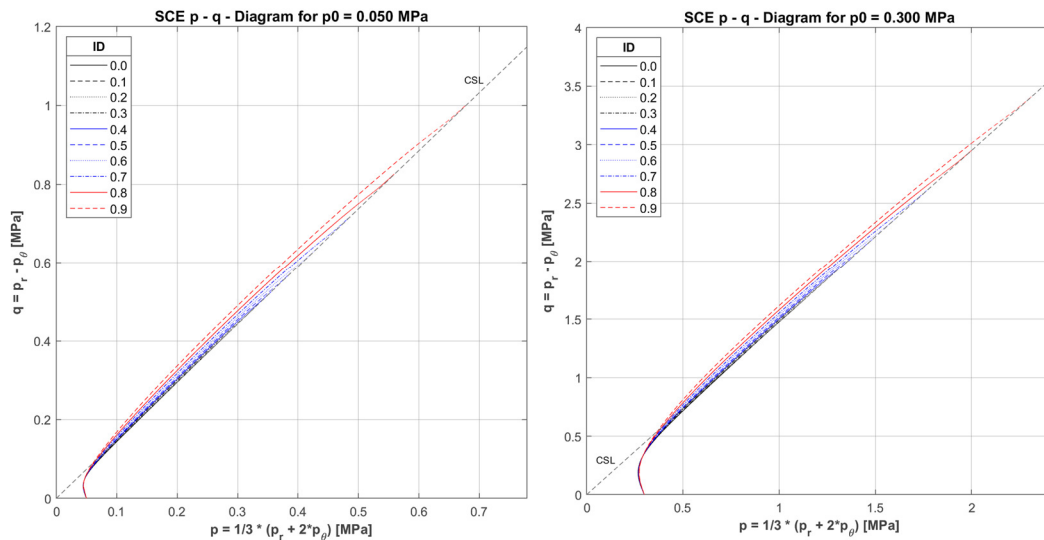


Fig. 66: $p - q$ - diagrams for PLM AZ28 for 10 different I_D and $p_0 = 0.050$ MPa (left) or $p_0 = 0.300$ MPa (right)

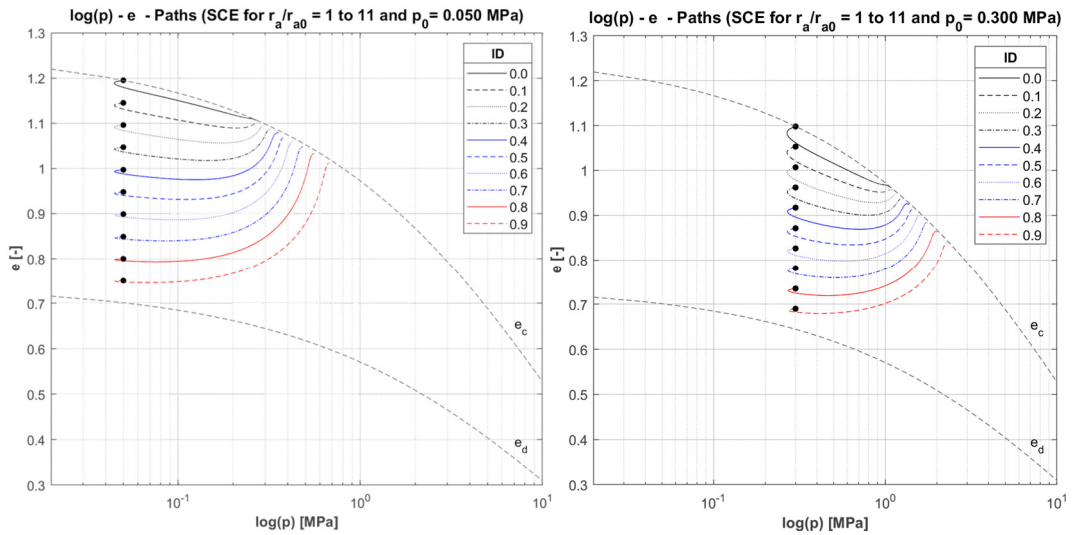


Fig. 67: $\log(p) - e$ - diagrams for PLM AZ28 for 10 different I_D and $p_0 = 0.050$ MPa (left) or $p_0 = 0.300$ MPa (right)

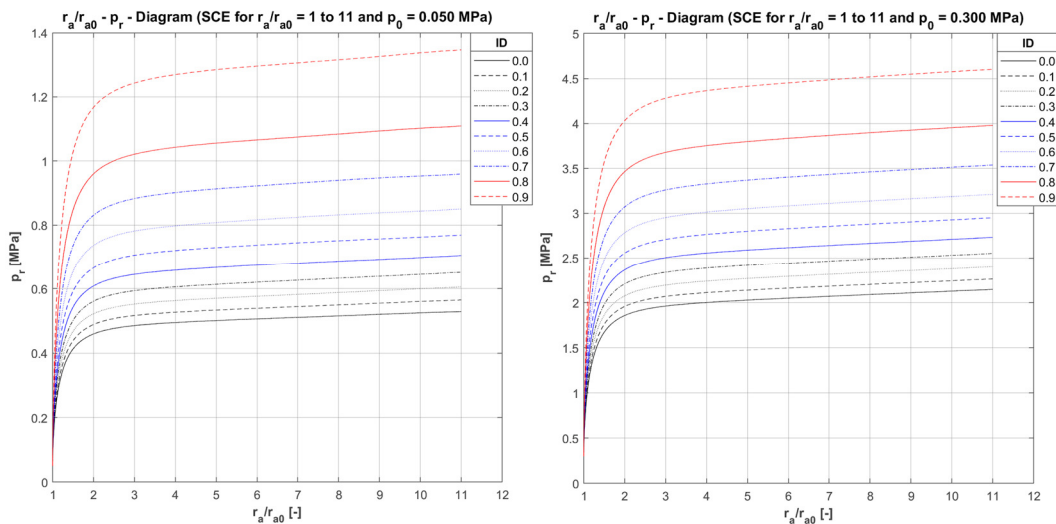


Fig. 68: $r_a/r_a^0 - p_r$ - diagrams for PLM AZ28 for 10 different I_D and $p_0 = 0.050$ MPa (left) or $p_0 = 0.300$ MPa (right)

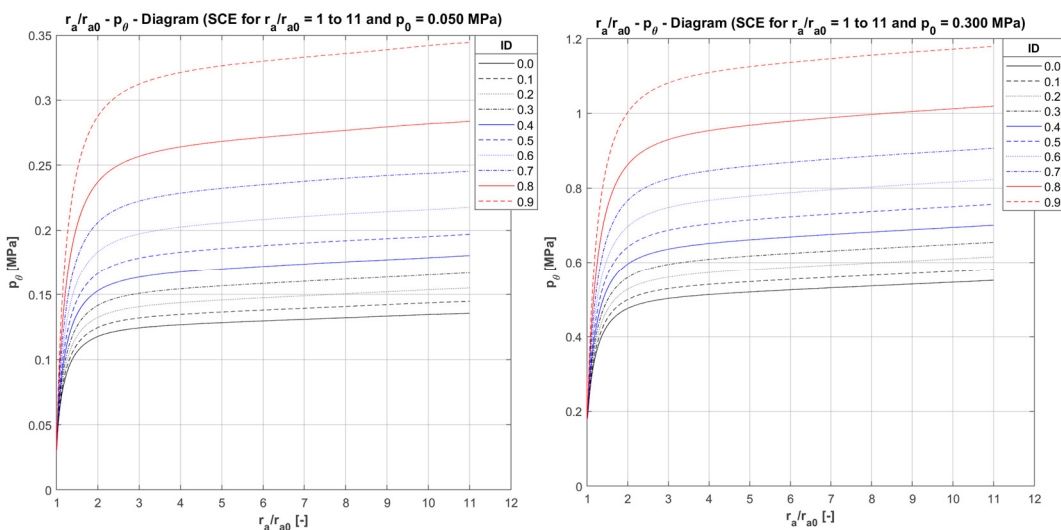


Fig. 69: $r_a/r_a^0 - p_\theta$ - diagrams for PLM AZ28 for 10 different I_D and $p_0 = 0.050$ MPa (left) or $p_0 = 0.300$ MPa (right)

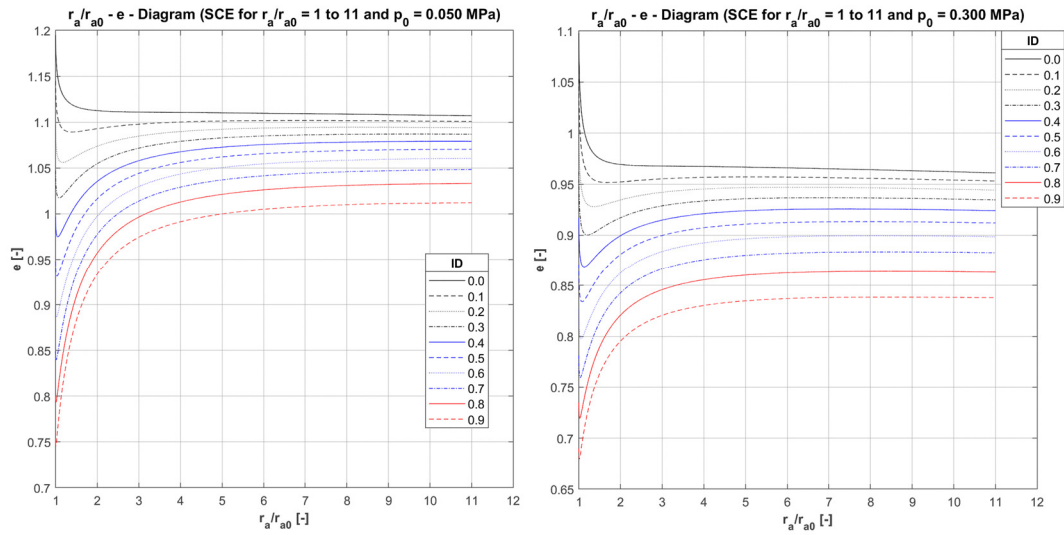


Fig. 70: $r_a/r_{a0} - e$ - diagrams for PLM AZ28 for 10 different ID and $p_0 = 0.050$ MPa (left) or $p_0 = 0.300$ MPa (right)

6 PLAXIS FEM-Model

As already stated in chapter 5, the usage of the OSINOV code for the determination of the limit pressure p_{LS} is subject to some major constraints.

First, the code is based on the hypoplastic constitutive model by “von Wolffersdorff” [23] which is only suitable for describing the mechanical behaviour of granular materials, such as gravel and sand. The users of the code are not given the possibility to utilise any other constitutive model in order to account for the intrinsic characteristics of different materials.

Another constraint may be connected to the numerical input parameters which govern the calculation process. As mentioned, the composition of these parameters largely depends on the experience of a particular user. Different values of the numerical parameters may result in very different values of the calculated limit pressures p_{LS} . This strong sensitivity of the results on the input parameters was proven by the studies of Slawik [9]. Unexperienced users are expected to make use of a suggested set of numerical parameters which may not be the best choice for all materials.

A third constraint is associated with the continuously rising radial pressures p_r throughout the whole simulated expansion of the cavity. A pronounced horizontal course of the pressure-expansion-curve is never reached. In other words, no stationary value for the radial pressure p_r will be encountered for which the limit pressure p_{LS} is defined. Hence, in turn, it only depends on the user’s experience to set an appropriate limit for the expansion to the extent at which the limit pressures can be read off.

To overcome the explained shortcomings of the OSINOV code the spherical cavity expansion problem was modelled with the aid of the FEM-software PLAXIS. Chapter 6 provides information on the persuaded approaches to come up with a working model in PLAXIS. The single steps taken during the model improvement will be explained. Calculation results for the spherical cavity expansion inside a continuum, modelled with the MC constitutive law, will be presented and a closed-form solution of the SCE problem, used for the model verification, will be introduced. Further the CPT interpretation method acc. to Randolphs et al., based on the mentioned closed-form solution, will be touched on. Calculations performed with the hardening soil model and two full KIM-analysis for two hypoplastic materials (PLM AZ28 and PLM BC36) from the KELLER-database will also be part of this chapter. Finally, the approach for the calculation of the q_c -curves over the depth will be covered, accompanied by the MATLAB-implementation of this task.

6.1 Model Implementation in PLAXIS

The implementation of the spherical cavity expansion model in PLAXIS is largely based on the studies by Xu [43]. For reasons of simplicity and to allow for a validation with the aid of an analytical closed-form solution, the Mohr-Coulomb constitutive law was used for the basic model. The updated mesh option available in PLAXIS was selected for all calculations to allow for a more realistic modelling of the cavity expansion involving large strain deformations. Fig. 71 shows the basic parts of the FEM-model.

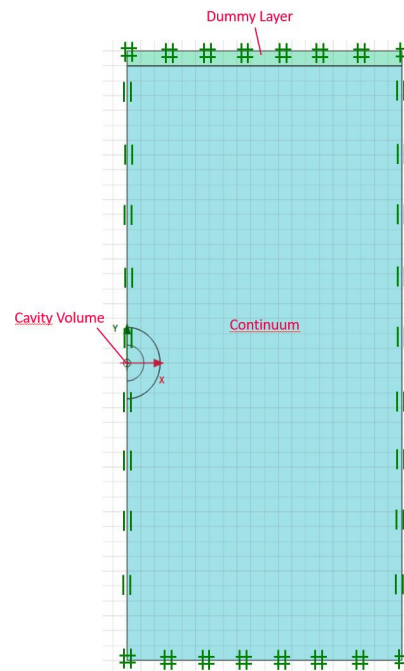


Fig. 71: Basic parts of the PLAXIS FEM-model

6.1.1 Used Soil Models

The material within the cavity (cavity cluster) was modelled linear elastic. The only purpose of it is the causing of the expansion which doesn't require a more sophisticated constitutive model.

The dummy layer was modelled linear elastic as well. It is exclusively used to generate the initial stresses. Except from the unit weight γ' , no other soil parameters assigned to the dummy layer influence the calculation results.

The continuum was modelled with the purpose of representing the mechanical behaviour of a specific material. Within the basic model it was chosen as an elastic-perfectly plastic Mohr-Coulomb (MC) material. This simplified the validation of the FEM-model results with the aid of an analytical solution to the problem incorporating the MC constitutive law.

Other constitutive laws used for the continuum were the hardening soil model (HS) and the hypoplastic constitutive law with the name "Sand hypoplasticity" which represents a

further development of the basic model by “von Wolffersdorff” [23]. This soil model was mainly applied to the calculations from the conducted KIM-analysis. The “Sand hypoplasticity” model can be downloaded from the website “soilmodels.com”.

6.1.2 Mesh Set-up

The basic model was build up from an axi-symmetric mesh comprising 15-noded triangular elements with 12 gauss stress points. Fig. 72 illustrates the locations of the element-nodes and gauss points for the triangular elements.

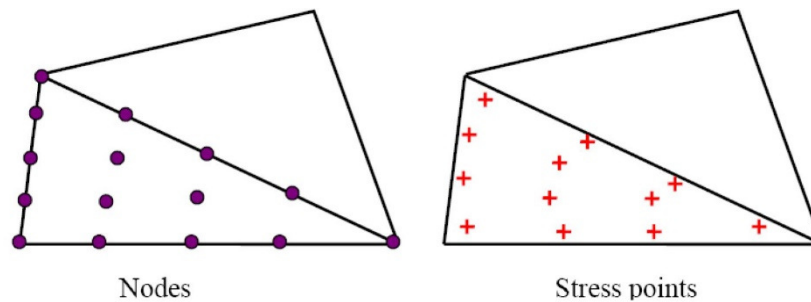


Fig. 72: Locations of nodes and stress (gauss) points for a triangular element [43]

The initial cavity radius was chosen with 0.1 m . The expansion of the cavity was achieved by the application of positive volumetric strains to the cavity cluster. As suggested by Xu [43] and to be consistent in the data output the cavity cluster in all models was divided into four triangular elements, unless otherwise stated. In agreement with the model by Xu [43] nine nodes and ten stress points were selected for the output of radial displacements and radial stresses. Fig. 73 shows a typical mesh of the FEM-model next to an example of the 4-element-discretization of the cavity cluster.

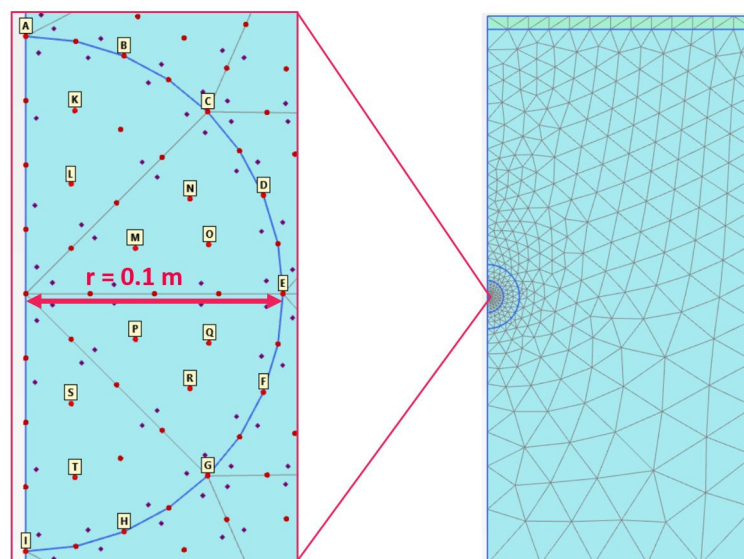


Fig. 73: Typical mesh (right) and 4-element-discretization of the cavity cluster (left)

To allow for a better mesh graduation around the cavity, two concentric half circles were added to the model. The selected nodes A to I within Fig. 73 were used for the output of the radial displacements $|u|$, whereas the results for the stresses σ_I' could be received from nodes K to T. The pressure-expansion-curves were received from an averaging of the results from the different nodes.

The deformation boundaries of the model were chosen as can be seen in Fig. 71 with the bottom and the top boundary as totally fixed and the x_{min} - and x_{max} - boundary as normally fixed.

6.1.3 Generation of Initial Stresses

The 1 m-thick dummy layer that sits on top of the FEM-model was used for the generation of an initial hydrostatic and homogenous stress field, in terms of the K_0 -procedure. This specific kind of stress field is assumed within the interpretation method (KIM) by Cudmani [8]. Both, the cavity and the continuum were assigned with a unit weight of $\gamma' = 0 \text{ kN/m}^3$ to account for the homogeneity and a K_0 of 1.0 to account for the isotropy of the initial stresses. The value for the initial mean effective pressure p_0 was controlled by the unit weight of the dummy layer. As the thickness was chosen with 1 m the unit weight equaled the desired value for p_0 . Fig. 74 shows the initial stress field w.r.t. p for a model with $p_0 = 50 \text{ kPa}$.

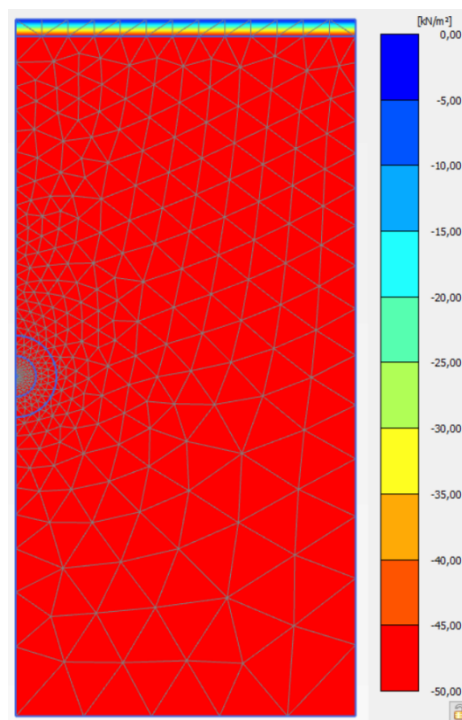


Fig. 74: Initial stress field p for a model with $p_0 = 50 \text{ kPa}$

As can be seen, the value of p is only changing within the dummy layer, due to the assigned effective unit weight. The rest of the model (with $\gamma' = 0 \text{ kN/m}^3$ and $K_0 = 1.0$) is subjected to a homogenous and isotropic stress field.

6.1.4 Calculation Phases

The initial phase generated the initial stresses with the aid of the K_0 -procedure implemented into PLAXIS. Thereby the effective vertical pressures are generally calculated with $\sigma_v' = \gamma' \cdot depth$ and the horizontal stresses are received from $\sigma_h' = \sigma_v' \cdot K_0$.

In subsequent calculation phases, referred to as the expansion phases, positive volumetric strains were applied to the cavity. Depending on possible errors received during the calculations, numerical issues or the desired rapidness of the expansion the volumetric strains for each phase were usually chosen in-between 100 and 200 %. From the maximum displacements of the selected output nodes A to I it was concluded if a further expansion phase had to be added in order to receive the pressure-expansion-curves up to the desired expansion-ratios.

To receive proper results for the curves, especially when the hypoplastic constitutive law was utilized, the maximum step size (load fraction per step) was usually reduced from the default value to a value of 0.01 or 0.005 for early phases. The MC model yielded good results even for a chosen step size of 0.1.

The tolerated error for the calculation phases was chosen with the default value, except in cases when an error arose, and the calculation was aborted. Changing the tolerated error within certain expansion phases to a higher value helped to overcome the problems. In some situations, the expansion stopped before the desired expansion ratio was achieved due to a “soil body seems to collapse”- error (mostly encountered in connection with the MC constitutive model). It was found that reducing the tolerated error of the last expansion phase can keep the expansion ongoing.

Further, the updated mesh option (large strain analysis) was chosen for all calculation phases and the arch-length control option in PLAXIS was deselected, as this option generally leads to unstable results for the encountered SCE problem.

It is also worth noting that the reset displacements to zero option was chosen for the first expansion phase. Furthermore, it is suggested using 10,000 for the maximum number of calculation steps to make sure that the volumetric strains assigned to the cavity can be applied to the full extent in one expansion phase and the calculation of the subsequent phase can start.

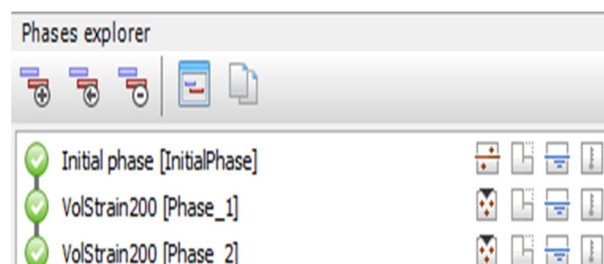


Fig. 75: Typical phases of the FEM-model ($\text{VolStrain200} \triangleq \epsilon_v = 200\%$)

6.1.5 Output

The pressure-expansion-curves can be received from the Curves manager implemented in PLAXIS. In a first place it is required to plot the calculated total displacements $|u|$ received for each element node (A to I) against the maximum principal stresses σ_I (\triangleq expansion pressure) from the stress points K to T. Fig. 76 shows the results received from the PLAXIS Curves manager for a MC-FEM-model.

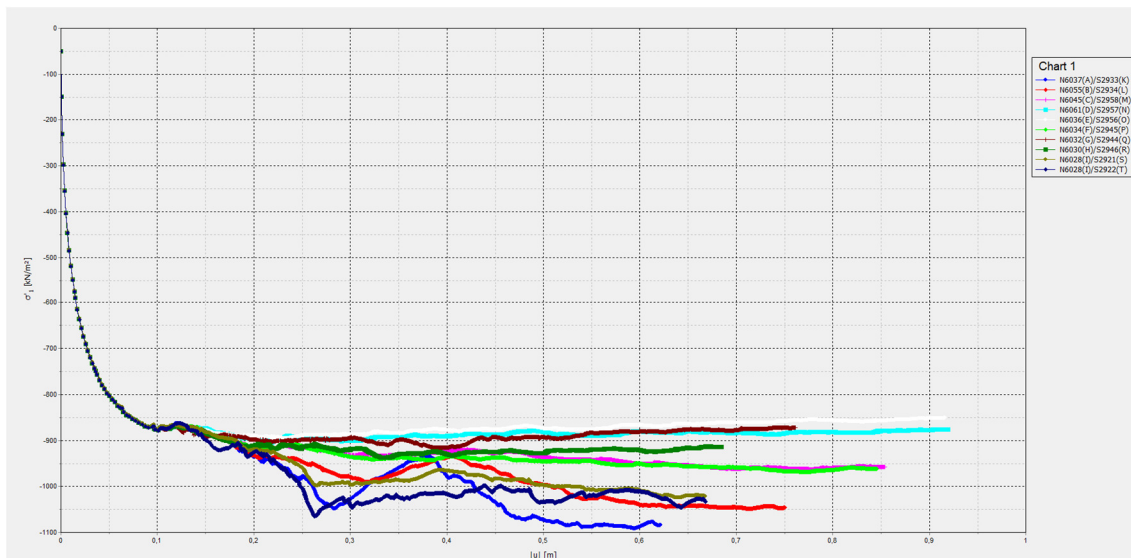


Fig. 76: Pressure-expansion-curves from the PLAXIS Curves Manager as typically received for a MC-model with a non-associated flow rule

As can be seen in the figure above, the curves plotted from different points are subjected to a large scattering which is connected to the assigned flow-rule of the MC-material. In extreme cases the lines can vary by up to 300 kPa which would lead to a misinterpretation of the value for the limit pressure p_{LS} , in case only one line for the pressure-expansion-curve is considered. To compensate for the large scatter and to receive proper values for the limit pressures the mean values of the stresses and displacements of all points have to be considered for the final pressure-expansion-curve.

Therefore, the results from the Curves manager were exported into Excel, where the averaging over all selected nodes was done. For the displacements, the mean values of the results from node A to I were calculated and for the stresses, the mean values of the results from node K to T were determined. The pressure-expansion-curve was finally received from the averaged values. In Fig. 77 an example of such an averaged curve can be seen depicted by the orange line. The black line represents the closed-form solution. The good agreement of both curves is proving that the FEM-model is able to reproduce the analytical results when the same material is considered.

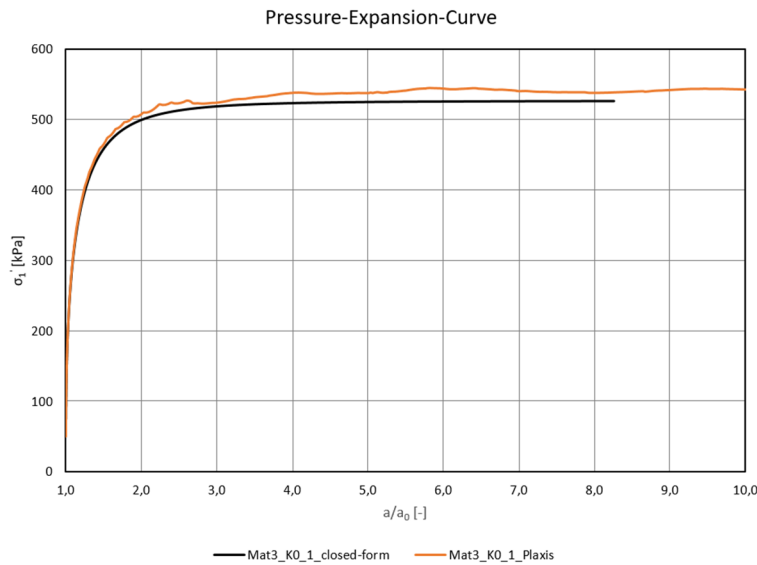


Fig. 77: Example of an “averaged” pressure-expansion-curve

6.2 Closed-form Solution of the SCE

For validation purpose of the FEM-model, the closed-form solution of the spherical cavity expansion by Yu & Houlsby [44] was used and implemented into a MATLAB-script. This analytical expression is based on an elastic-perfectly plastic material model with a Mohr-Coulomb failure criterion and a constant dilation rate. The created MATLAB-script (A. Fig 15) can be used to generate pressure-expansion-curves which can subsequently be compared to the curves received from the PLAXIS model.

6.2.1 Construction of the Pressure-Expansion-Curve

To come up with the pressure-expansion-curve based on the solution by Yu and Houlsby [44] for the expansion of a cylindrical or a spherical cavity within an infinite continuum the following steps have to be taken:

- 1) Choosing of the desired input parameters, i.e. E (Young’s modulus), ν (Poisson’s ratio), c (cohesion), φ (friction angle), ψ (dilatancy angle), p_0 (initial mean pressure), m ($m=1$ for cylindrical expansion and $m=2$ for spherical expansion).
- 2) Calculation of the following terms used within the solution:

$$G = \frac{E}{2(1-\nu)} \quad (6.1)$$

$$M = \frac{E}{1-\nu^{2(2-m)}} \quad (6.2)$$

$$M = \frac{2c \cos \varphi}{1 - \sin \varphi} \quad (6.3)$$

$$\alpha = \frac{1 + \sin \varphi}{1 - \sin \varphi} \quad (6.4)$$

$$\beta = \frac{1 + \sin \psi}{1 - \sin \psi} \quad (6.5)$$

$$\gamma = \frac{\alpha(\beta + m)}{m(\alpha - 1)\beta} \quad (6.6)$$

$$\delta = \frac{Y + (\alpha - 1)p_0}{2(m + \alpha)G} \quad (6.7)$$

$$\eta = \exp \left\{ \frac{(\beta + m)(1 - 2\nu)[Y + (\alpha - 1)p_0][1 + (2 - m)\nu]}{E(\alpha - 1)\beta} \right\} \quad (6.8)$$

$$\xi = \frac{[1 - \nu^2(2 - m)](1 + m)\delta}{(1 + \nu)(\alpha - 1)\beta} \times \left[\alpha\beta + m(1 - 2\nu) + 2\nu - \frac{m\nu(\alpha + \beta)}{1 - \nu(2 - m)} \right] \quad (6.9)$$

- 3) Calculation of the expansion ratio a/a_0 (a = current cavity radius and a_0 = initial cavity radius) from the small strain elastic expression (Eqn. 6.11) for pressure p less than p_l required to initiate plastic deformations.

$$p_1 = 2mG\delta + p_0 \quad (\text{yielding pressure}) \quad (6.10)$$

$$\frac{(a - a_0)}{a_0} = \frac{p - p_0}{2mG} \quad (6.11)$$

- 4) Calculation of the pressure ratio R for pressure p in-between p_l from Eqn. (6.10) and the limit pressure p_{lim} .

$$R = \frac{(m + \alpha)[Y + (\alpha - 1)p]}{\alpha(1 + m)[Y + (\alpha - 1)p]} \quad (6.12)$$

5) Evaluation of a/a_0 from Eqn. (6.13)

$$\frac{a}{a_0} = \left\{ \frac{R^{-\gamma}}{(1-\delta)^{\frac{(\beta+m)}{\beta}} - \left(\frac{\gamma}{\eta}\right) \Lambda_1(R, \xi)} \right\}^{\frac{\beta}{(\beta+m)}} \quad (6.13)$$

where Λ_1 represents an infinite series (evaluation of this series for a few terms is sufficient, i.e. 10 terms)

$$\Lambda_1(x, y) = \sum_{n=0}^{\infty} A_n^1 \quad (6.14)$$

$$A_n^1 = \begin{cases} \frac{y^n}{n!} \ln x & \text{if } n = \gamma \\ \frac{y^n}{n!(n-\gamma)} [x^{n-\gamma} - 1] & \text{otherwise} \end{cases} \quad (6.15)$$

Repeating of steps 4 and 5 can be done to construct the complete cavity pressure-expansion relationship. By sending a/a_0 in Eqn. (6.13) against $+\infty$ the limit pressure p_{lim} can be received. Fig. 78 shows the generated pressure-expansion-curve from the MATLAB-script found in A. Fig 15.

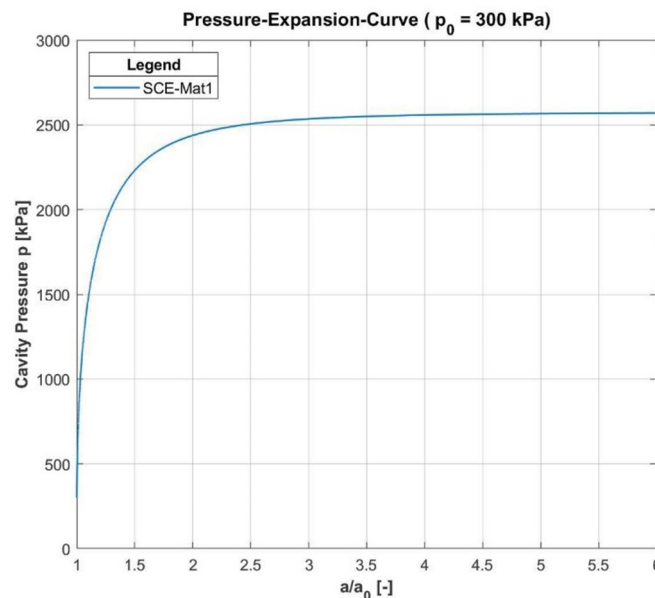


Fig. 78: Generated pressure-expansion curve from the script (closed-form)

6.2.2 CPT Interpretation Method acc. to Randolphs et al.

For the sake of completeness and as it might be of large interest to the KELLER Grundbau GmbH, it was decided to shortly touch on the CPT interpretation method by Randolphs

et. al [45] within this chapter. This method was originally proposed with the purpose to calculate the base resistance of driven piles, but as stated within [45] it may also be applied to the calculation of the cone penetration resistance q_c from CPT testing. The expression for q_c which comprises the limit pressure p_{lim} received from the presented closed form solution is given as follows:

$$q_c = p_{lim} (1 + \tan \delta \tan \alpha) \quad (6.16)$$

where δ is the interface friction angle between the cone and the soil and α can be taken as 60° (cone angle). To get detailed information on how to derive the soil parameters for which the spherical cavity expansion must be performed to come up with the limit pressure p_{lim} of a certain material, reference is made to [45].

Further, there was not enough time in the course of this Master's thesis to verify the performance of this method and more studies on this method need to be conducted, especially in connection with carbonate sands.

6.3 Improvements of the PLAXIS Model

From having set-up the basic model, it was now required to check the influence of certain model properties on the calculation results and improve the model settings. A MC-material was chosen for the modelling of the continuum in combination with soil parameters which were assumed to result in a numerically stable calculation process. The soil parameters of this material and the soil parameters of the cavity and the dummy layer used for the improvement procedure are summarized in Tab. 15.

Tab. 15: Initial material parameters used for the improvement of the FEM-model

Material	Soil parameters			Constitutive model
Cavity	E'	2,000	[kPa]	Linear elastic
	ν	0.2	[-]	
	γ'	0.0	[kN/m ³]	
	K_0	1.0	[-]	
Dummy Layer	E'	20,000	[kPa]	Linear elastic
	ν	0.2	[-]	
	γ'	50.0	[kN/m ³]	
Continuum	E'	25,000	[kPa]	MC
	ν	0.2	[-]	
	ϕ'	30	[°]	
	ψ	0	[°]	
	c'	0.0	[kPa]	
	γ'	0.0	[kN/m ³]	
	K_0	1.0	[-]	

6.3.1 Influence of the Domain Size and Boundary Conditions

To check the influence of the domain size on the SCE results, 4 different models with different dimensions were created and compared to the closed-form solution calculated with the MATLAB code. Further, the influence of the boundary conditions was studied, and calculations were performed with the y_{max} -boundary either set to free or fully fixed.

Checked domain sizes:	Small domain	$b = 8 \text{ m}$	$h = 16 \text{ m}$
	Medium domain	$b = 15 \text{ m}$	$h = 30 \text{ m}$
	Large domain	$b = 20 \text{ m}$	$h = 40 \text{ m}$
	Very large domain	$b = 50 \text{ m}$	$h = 100 \text{ m}$

The values for b and h refer to the width and the height of the modelled continuum. The models were meshed with the aim to come up with a good graduation of the mesh around the cavity. The mesh for the small domain comprised 567 elements, the medium domain mesh 786 elements, the large domain mesh 740 elements and the very large domain mesh 1184 elements. The almost equal number of elements for the medium domain mesh and the large domain mesh may be explained by the fact that the dimensions of the models differed only slightly, and an overall courser mesh was chosen for the large model. Fig. 79 shows parts of the mesh around the cavity as used for the large domain model.

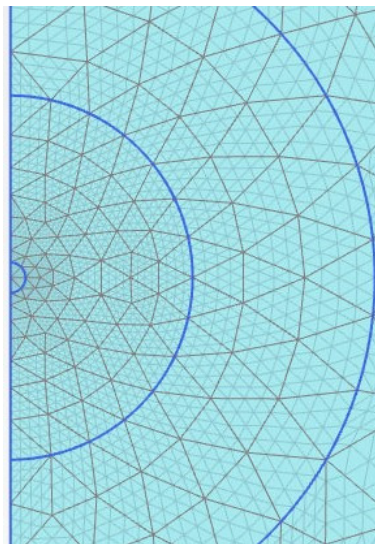


Fig. 79: Mesh around the cavity for the large domain model

In a first step the models were calculated with the deformation boundary y_{max} set to free. It was found that the deformations and the stresses within the cavity become more symmetric with increasing domain-size. The theoretical cavity expansion problem is a purely symmetric problem and therefore a symmetric behavior wants to be achieved. It is believed that both, the dimensions of the model and the quality of the mesh around the cavity are responsible for the symmetry of stresses and displacements. The mesh quality was generally better for the larger models, as it was easier to achieve a good mesh for

larger model dimensions. Fig. 80 depicts the mesh qualities for the models with different domain sizes.

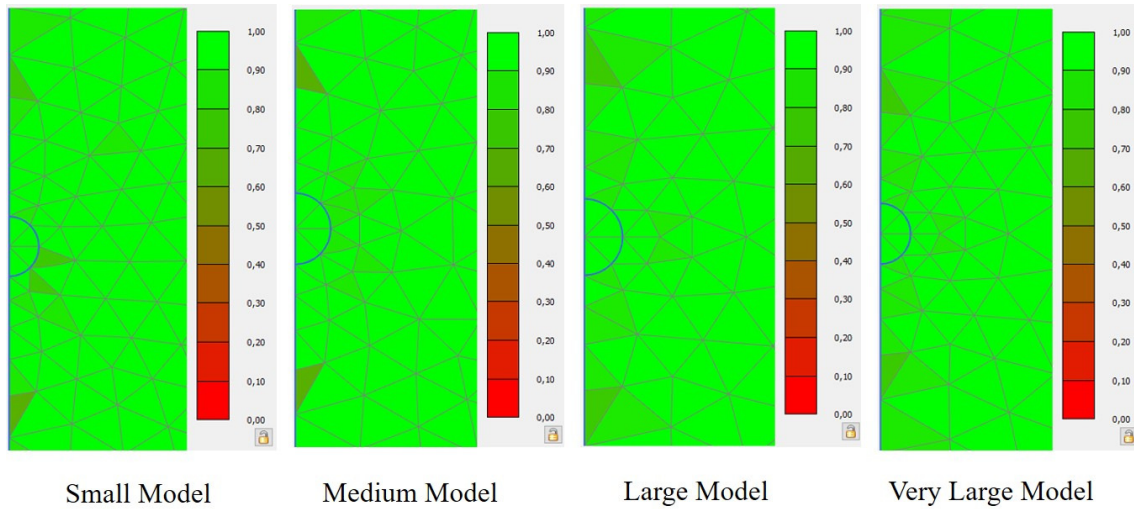


Fig. 80: Mesh quality for models with different domain sizes

The following figures (Fig. 81 to Fig. 84) represent the distributions of the effective stresses σ_1' and p' and the total displacements $|u|$ across the cavity after the expansion was finished for different model dimensions to depict the influence of the geometry on the symmetry of the results.

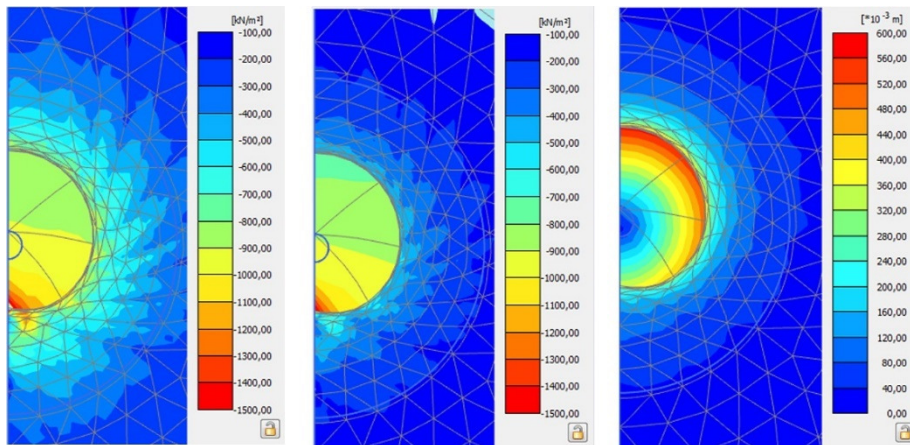


Fig. 81: σ_1' p' and $|u|$ across the cavity – Small model

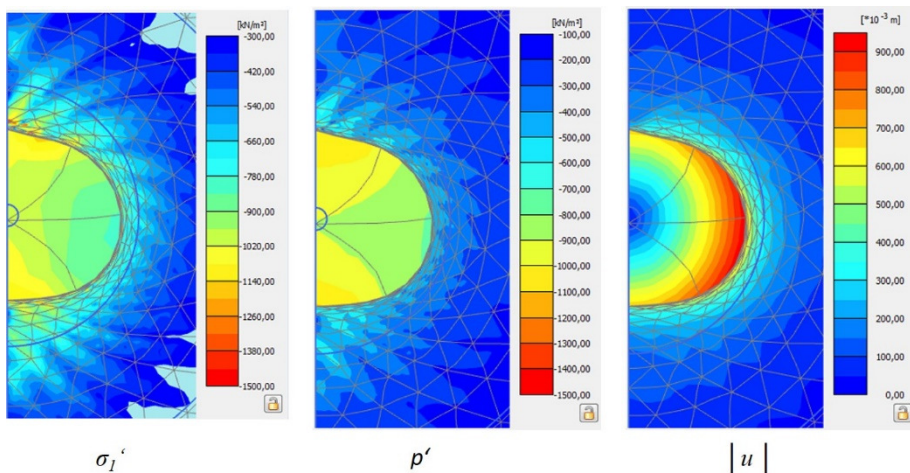


Fig. 82: σ_1' p' and $|u|$ across the cavity – Medium model

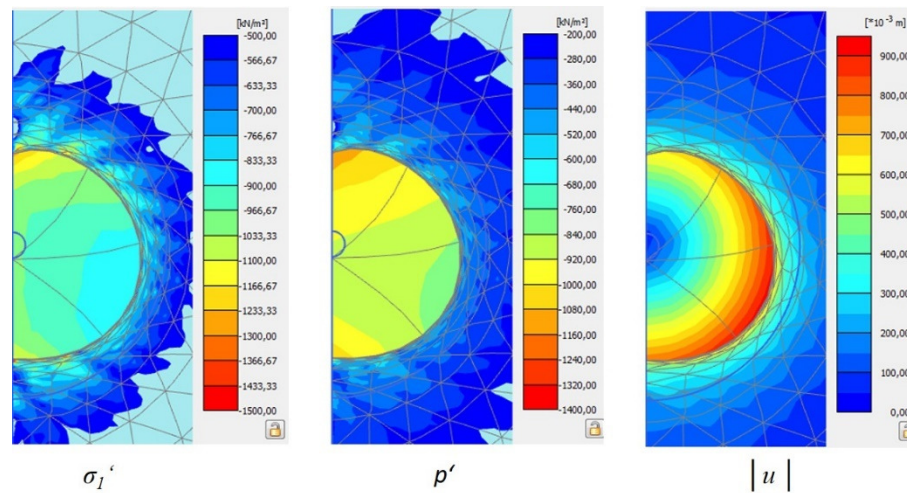


Fig. 83: Distribution of σ_1' , p' and $|u|$ across the cavity – Large model

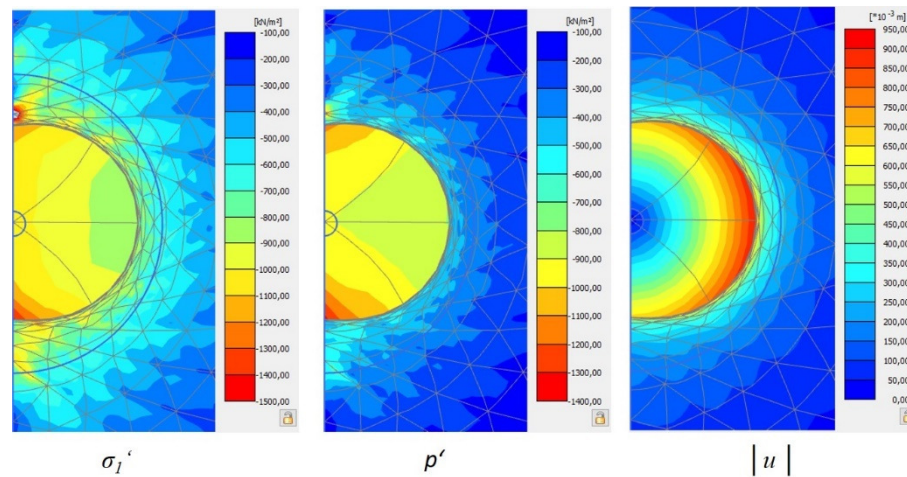


Fig. 84: Distribution of σ_1' , p' and $|u|$ across the cavity – Very large model

From the results of the averaged pressure-expansion curves from the different selected nodes it was found that the curves tend to converge to the closed-form solution at smaller expansion-ratios for increasing dimensions of the model. It was observed that for the investigated MC-material it is necessary to continue with the expansion until an expansion-ratio of around 8 to 9 is reached. Otherwise no “stationary state”-progression of the stresses will be reached by the resulting curves of the different models. The pressure-expansion-curves determined from the models with different dimensions are compared to the closed-form solution in Fig. 86.

Fixing the y_{\max} -boundary of the models caused somehow smoother progressions of the curves. The peaks of the curves were indeed reached after bigger expansion ratios in general for fixed y_{\max} -boundaries but the results from the closed form solution could more accurately be approached. For the small model the expansion could only be realized up to an expansion ratio of around 6 as the soil body collapsed within one calculation phase which is associated with the unsymmetrical deformations (Fig. 81) caused by the expanding cavity. The comparison between the closed-form solution and the pressure-expansion curves determined from different models with y_{\max} fixed is shown in Fig. 87.

From the curves generated within the PLAXIS Curves manager it was concluded that it would be a good approach to neglect the results of the southern- and northern-most selected nodes (A and I) and stress points (K and T) within the averaging procedure (chapter 6.1.5) as the curves of these points were subjected to a much greater scatter than the rest of the curves. It is noted that within the present improvement step (domain size and boundary conditions) this elimination was not yet considered, and a separate improvement step was taken to precisely figure out its effects. Fig. 85 depicts an example for the outlier curves (blue lines) from nodes A, I, K and T.

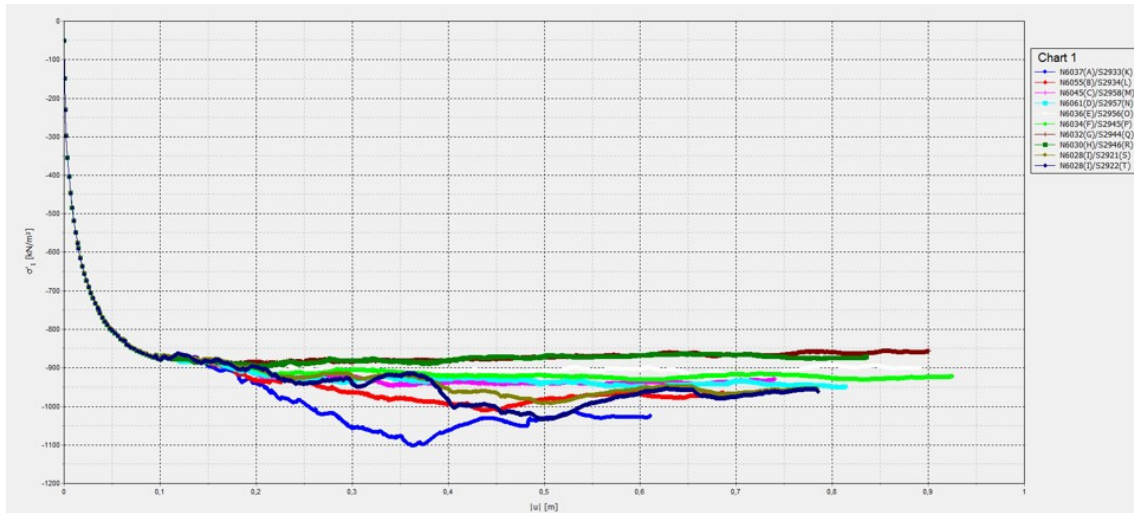


Fig. 85: Outlier curves (blue lines) from nodes A, I, K and T in PLAXIS

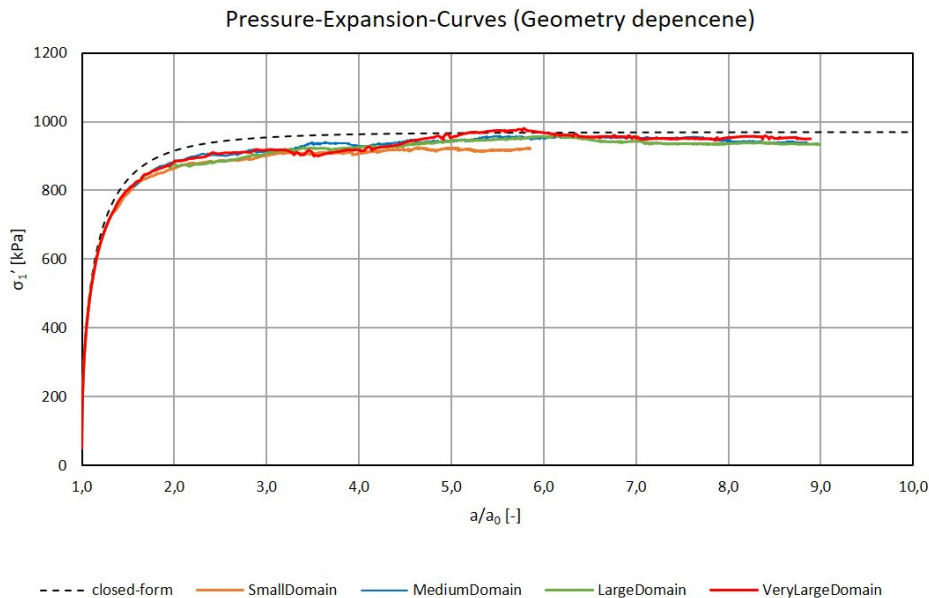


Fig. 86: Final pressure-expansion-curves for different domain sizes ($y_{max} = \text{free}$)

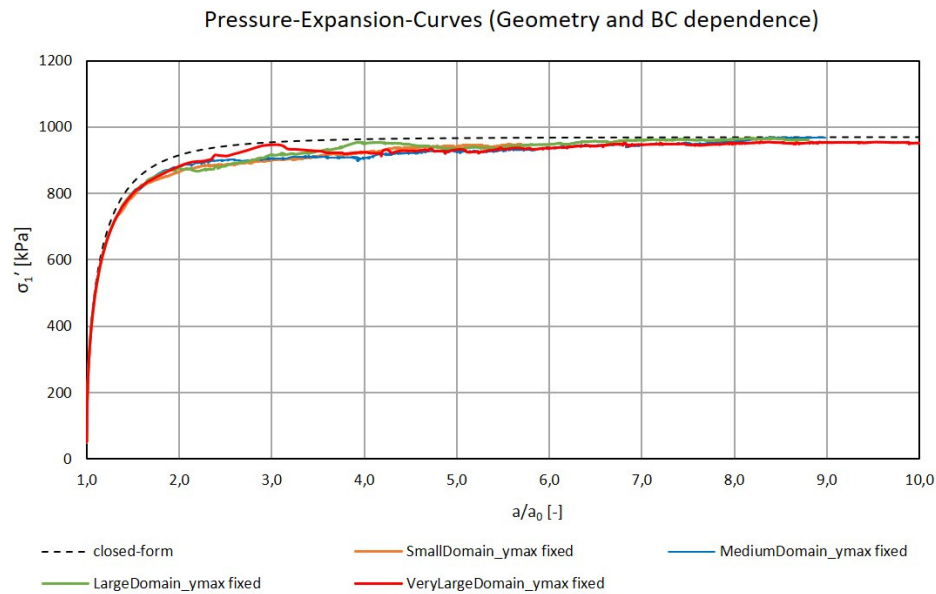


Fig. 87: Final pressure-expansion-curves for different domain sizes ($y_{max} = \text{fixed}$)

From the study on the influence of the different model sizes and boundary conditions it was found that the large domain model (20x40 m) with the y_{max} -boundary chosen fixed (green line in Fig. 87) provided the smoothest curves and the best agreement with the closed-form solution. The mentioned domain with the fixed y_{max} -boundary was therefore adopted for all further improvement steps, unless otherwise stated, and except for the studies within chapter 6.3.2 as the results from the present chapter were not yet evaluated and the best model size was not yet known.

6.3.2 Influence of E and ν of the Cavity Material

Within this improvement step six different models, based on the very large domain from chapter 6.3.1, with varying values for the Young's modulus E and the Poisson's ratio ν of the cavity were evaluated and the determined pressure-expansion-curves were compared to the closed-form solution. The nodes for the output were chosen acc. to Xu [43] and the elimination of the northern- and southern-most nodes and stress points were not yet considered within the averaging. The y_{max} -boundary was chosen as fixed.

Created models:	CavityE250	$E = 250 \text{ kPa}$	$\nu = 0.2$
	CavityE250_ny0	$E = 250 \text{ kPa}$	$\nu = 0.0$
	CavityE1000	$E = 1000 \text{ kPa}$	$\nu = 0.2$
	CavityE1000_ny0	$E = 1000 \text{ kPa}$	$\nu = 0.0$
	CavityE2000	$E = 2000 \text{ kPa}$	$\nu = 0.2$
	CavityE2000_ny0	$E = 2000 \text{ kPa}$	$\nu = 0.0$

It should be noted that it was also tried to calculate a model with a cavity Young's modulus chosen with 100 kPa. During the expansion, however, the error message "NaN found in an element stiffness matrix" appeared and the calculation was aborted. This model could therefore not be evaluated. The resulting pressure-expansion-curves from the other models in comparison with the closed-form solution can be found in Fig. 88.

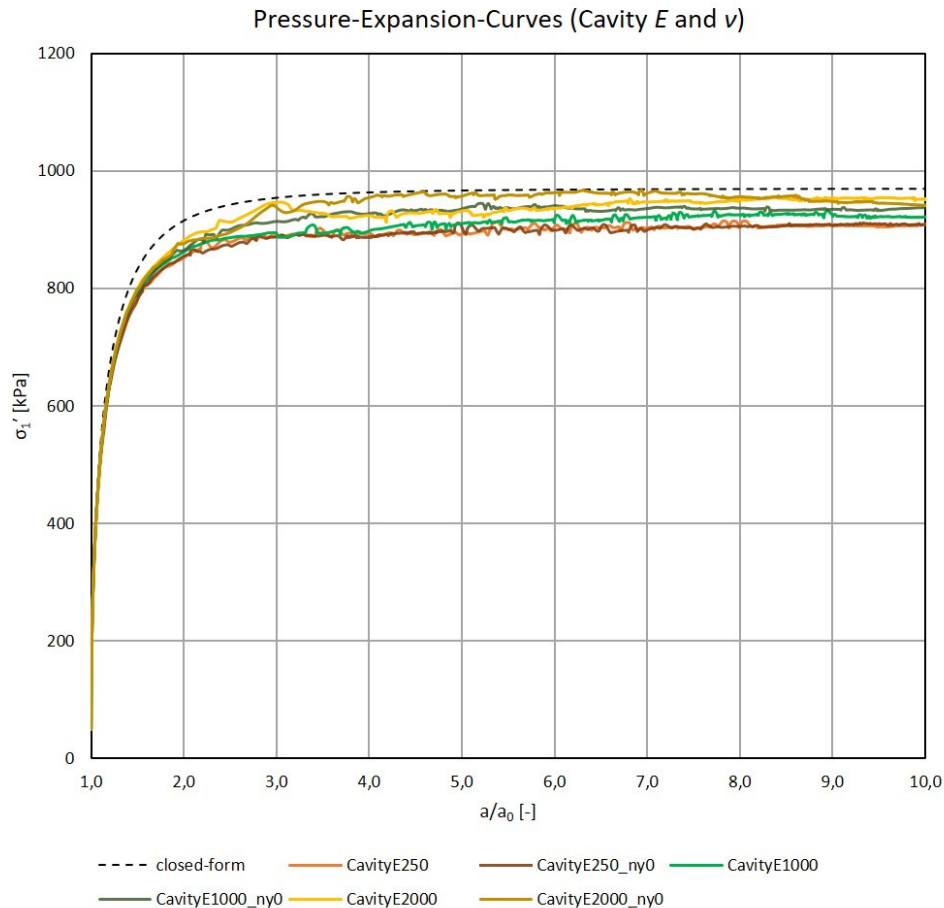


Fig. 88: Final pressure-expansion-curves for different cavity E and ν

The studies regarding changing E and ν of the cavity cluster showed that the pressure-expansion-curves are sensitive to changing Young's moduli of the cavity cluster. The models with E chosen with 250 kPa resulted in curves about 60 kPa below the closed-form limit pressure. The models with E of the cavity of 2000 kPa showed results which are more or less in good agreement with the closed-form solution while a Young's modulus of 1000 kPa resulted in curves ending up in between the results for $E = 250$ kPa and $E = 2000$ kPa.

While changing the Poisson's ratio of the cavity cluster from 0.2 to 0.0 had in fact no influence on the results for the models with a cavity $E = 250$ kPa, it could be shown that the pressure-expansion-curves for the models with a higher Young's modulus reached its maximum values at lower expansion ratios and rather developed a horizontal progression than the models with $\nu = 0.2$.

Even though the curves for the models with a value of $E = 2000$ kPa for the cavity cluster approached the limit pressure of the closed-form solution they were still not able to reproduce the analytical pressure-expansion-curve for expansion ratios within 1.25 and 3.5.

Taking a look on the curves from the Plaxis Curves Manager it could not be concluded that lower values for the cavity Poisson's ratio produce more homogeneous stress fields across the cavity. Also, with changing values of the cavity Young's modulus the scattering of the different curves from the PLAXIS output was not getting less. Fig. 89 shows a typical output from the PLAXIS curves manager for the calculations conducted within the present chapter on the example of model CavityE2000_ny0.

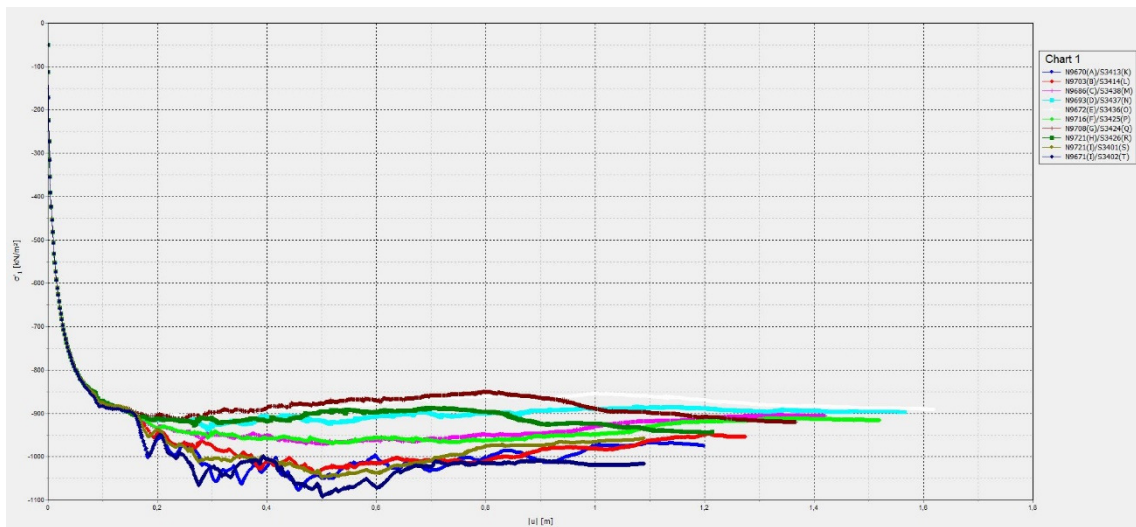


Fig. 89: Typical output from PLAXIS for the studies on changing cavity E and ν (CavityE2000_ny0)

From the studies on different assigned values to the Young's modulus and Poisson's ratio of the cavity cluster it was concluded that the most reliable pressure-expansion-curve in agreement with the closed-form solution may be obtained from a model with E of the cavity of 2000 kPa and $\nu = 0.0$.

The distributions of the stresses and deformations across the cavity after the expansion was finished for the different models of this chapter can be found in Appendix E within the figures A. Fig 16 to A. Fig 21.

6.3.3 Influence of the Cavity Discretization

The influence of the cavity discretization on the calculation results was studied based on the medium and large domain models with a Young's modulus of the cavity of 1000 kPa and a Poisson's ratio ν of 0.0. The reason why $E=2000$ kPa (suggested from chapter 6.3.2) was not assigned to the cavity cluster is that no proper evaluation of the models from

chapter 6.3.2 had been done at the moment when the studies from the present chapter were conducted. The y_{max} -boundary was chosen as fixed for all created models.

Created models:

33CavityElem_Medium	b = 15 m	h = 30 m
33CavityElem_Large	b = 20 m	h = 40 m

The meshing of the models was not an easy task as it took a few tries to come up with a good graduation of the mesh. A rectangle around the cavity and the concentric half circles had to be added to the model, which can be seen in Fig. 90, to generate a mesh of acceptable quality. The cavity in case of both generated models was comprising 33 elements. As the output nodes suggested by Xu [43] are only defined for a 4-element discretization, these points could not be chosen for the created FEM-models. Hence, the 10 points from A to J were chosen for the output of the displacements and the 10 points from K to T were chosen for the stress output. The locations of these points can also be found within Fig. 90.

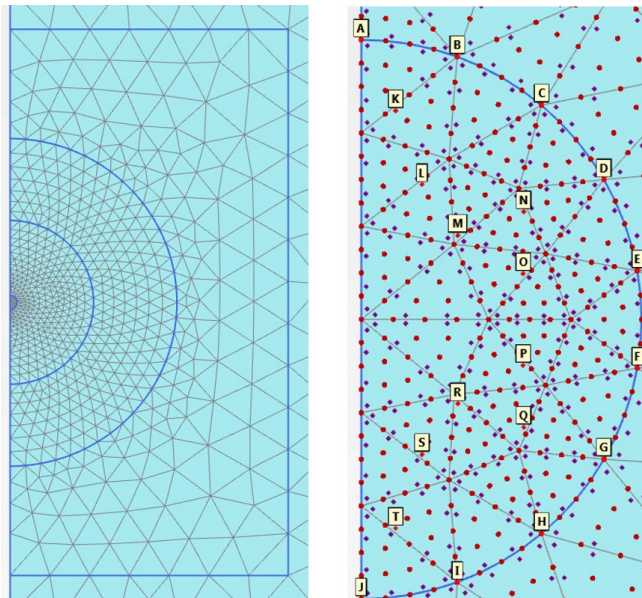


Fig. 90: Mesh graduation for the models with 33 elements within the cavity (left) and the selected nodes within these models (right)

For the medium domain a mesh with 1297 element was generated and the large domain mesh comprised 1854 elements.

From the resulting distributions of the stresses and deformations at the end of the expansion it was observed that the 33-element-discretization of the cavity yields a very unsymmetrical response of both models to the expanding cavity. The distributions of σ_I' , p' and $|u|$ across the cavity after the finished expansion for both models are shown in the following figures.

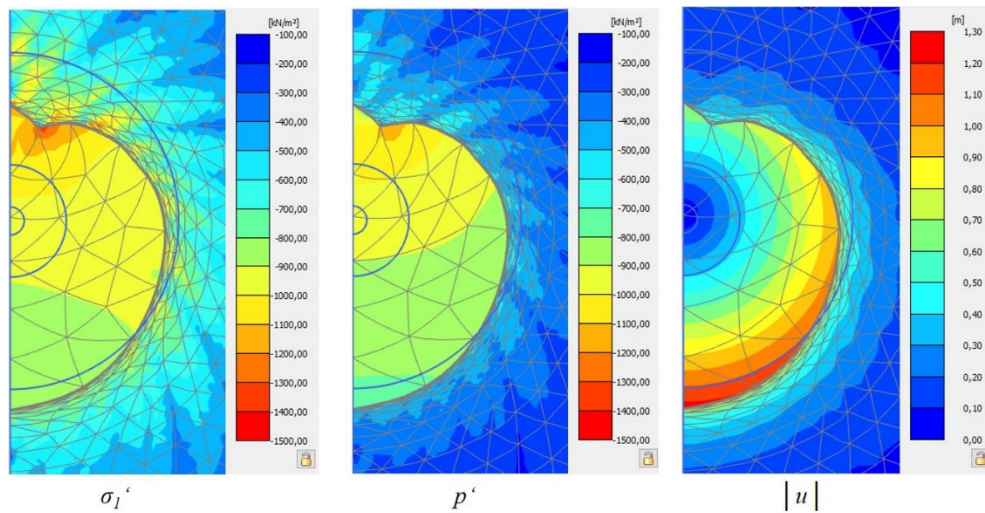


Fig. 91: Distribution of σ_1' , p' and $|u|$ across the cavity – 33CavityElem_Medium model

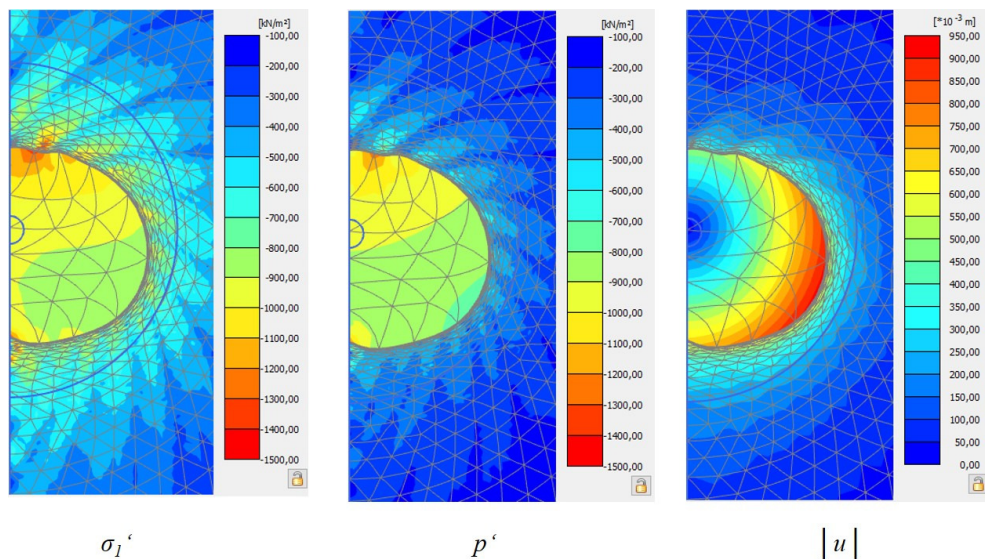


Fig. 92: Distribution of σ_1' , p' and $|u|$ across the cavity – 33CavityElem_Large model

The resulting pressure-expansion-curves for both models were received from an averaging done over all selected nodes and are plotted next to the closed-form solution in Fig. 93.

The calculations performed on the model 33CavityElem_Large (20x40 m) with the 33-element-cavity-cluster-discretization yielded good results in agreement with the closed-form solution especially up to an expansion ratio of 3.5. After reaching its peak at an expansion ratio of around 4 the curve from the large model tended to decrease, and the limit pressure of the analytical solution was never reached. The medium model (15x30 m) with the fine mesh discretization performed bad, especially at the beginning of the expansion. After a sufficient amount of expansion (expansion ratio ≈ 6.5) the curves from both models were crossing.

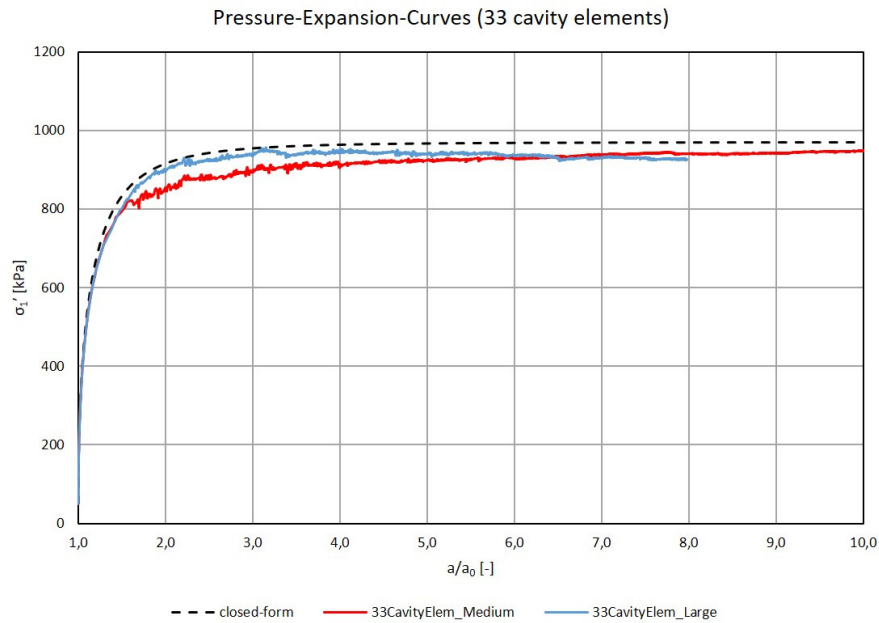


Fig. 93: Pressure-expansion-curves for the models with 33 elements within the cavity

A valid connection between the cavity discretization and a clear improvement of the results could not be observed. The fact that for the suggested large geometry (chapter 6.3.1) the pressure-expansion-curve starts to decrease at relatively low expansion ratios and the curve never ends up in a horizontal course makes very fine meshes rather inappropriate for models aiming at solving the spherical cavity expansion problem. It is believed that the decrease of the blue curve in Fig. 93 is associated with the large unsymmetrical deformations of the cavity. The calculation times for the models with the finer mesh were much longer than for the models with the 4-element-discretization of the cavity. For the mentioned reasons it is not suggested to use models with very fine meshes in context with the spherical cavity expansion problem and the 4-element-discretization can be considered the right choice.

6.3.4 Influence of the Flow Rule

Concluding from the first calculations with the spherical cavity expansion model it was believed that the unsymmetrical deformations and the big scatter of the stresses across the cavity might be a result of the incorporated flow rule of the MC-model. It was further assumed that using an associated flow rule for the material assigned to the continuum might bring some improvements with respect to the smoothness of the results. For this reason, 5 different models with an associated flow rule assigned to the continuum were created comprising rather synthetic values for the friction and dilatancy angle ranging from 10° to 30° . Additionally, it was tried to find out if the Young's modulus of the cavity has some influence on the final results when an associated flow rule is applied and $E=2000$ and 5000 kPa were used.

All created models are based on the very large domain since the large geometry was not yet found to be the best choice when the calculations were done. The y_{max} -boundary was chosen fixed and the Poisson's ratio ν of the cavity was set to 0.0. Initial stresses of $p_0 = 50$ kPa were generated with the aid of the dummy layer and the nodes for the output were chosen acc. to Xu [43].

Created models:	Associated10	$\varphi' = 10^\circ$	$\psi = 10^\circ$	Cavity: $E = 2000$ kPa
	Associated15	$\varphi' = 15^\circ$	$\psi = 15^\circ$	Cavity: $E = 2000$ kPa
	Associated20	$\varphi' = 20^\circ$	$\psi = 20^\circ$	Cavity: $E = 5000$ kPa
	Associated25	$\varphi' = 25^\circ$	$\psi = 25^\circ$	Cavity: $E = 5000$ kPa
	Associated30	$\varphi' = 30^\circ$	$\psi = 30^\circ$	Cavity: $E = 5000$ kPa

Changing the flow rule from non-associated to associated led to uniform distributions of the stresses and deformations across the cavity at the end of each expansion for all models. Fig. 94 shows the uniformly distributed stresses σ_I' and p' and displacements $|u|$ on the example of model Associated20.

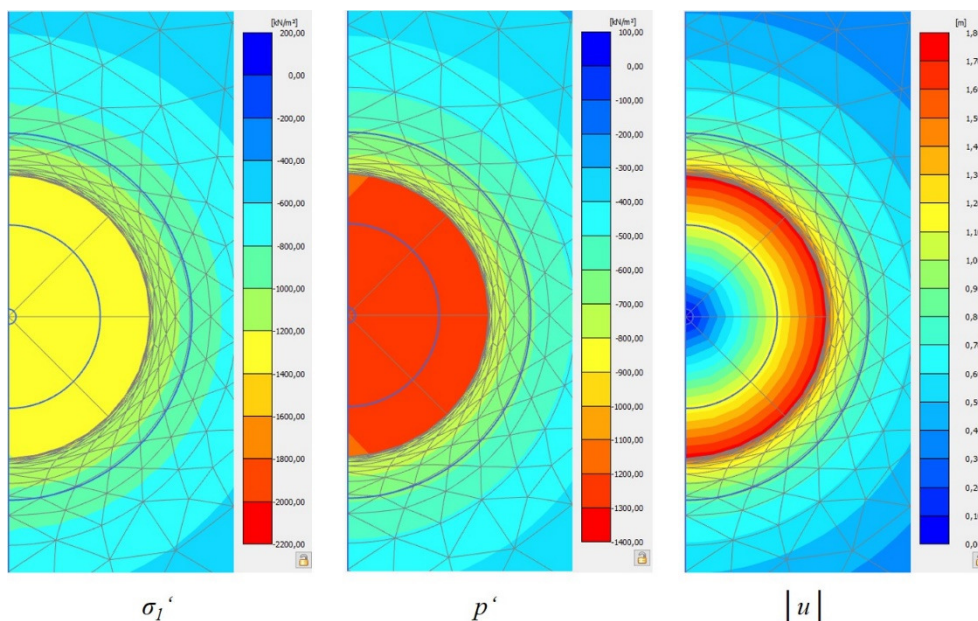


Fig. 94: Distribution of σ_I' , p' and $|u|$ across the cavity – Associated20 model

From comparing the obtained pressure-expansion-curves to the closed-form solution of each considered material it was found that an associated flow rule applied to the continuum of the spherical cavity expansion models can yield good agreements between the FEM-solution and the analytical solution, at least for friction angles up to 20° . This is an indicator that the FEM-model is working well, and hence, only minor adjusting of the basic model properties has to be done when different constitutive models want to be used for the continuum.

In the following diagrams (Fig. 95) the pressure-expansion-curves obtained from the 5 different FEM-models are plotted next to the closed-form solution of the corresponding materials.

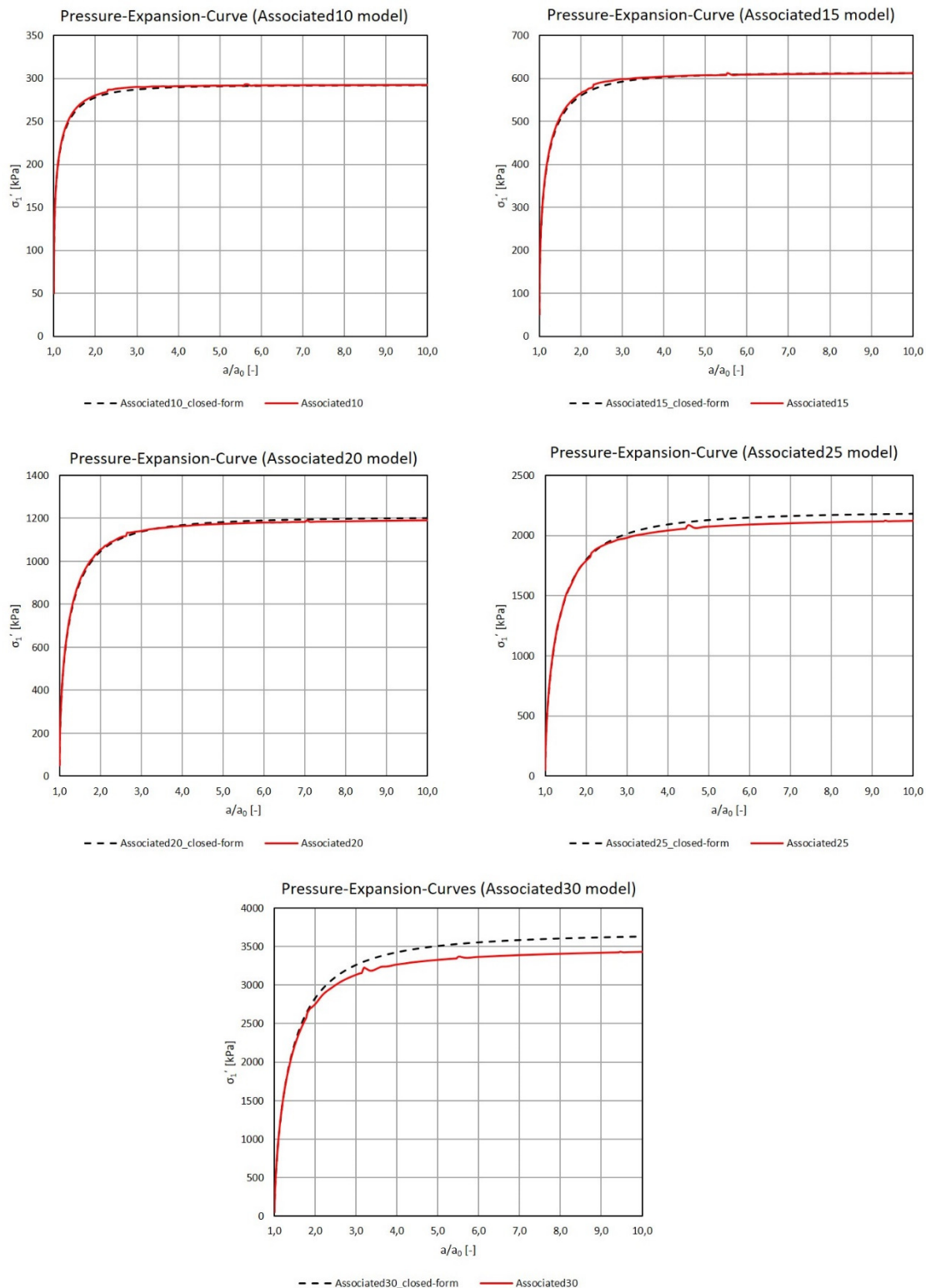


Fig. 95: Associated flow rule models: Pressure-expansion-curves

The models with friction angles of the continuum-material of up to 20° performed quite well in the comparisons and were able to reproduce the exact same pressure-expansion curves as calculated from the analytical solution. Even when changing the Young's modulus of the cavity from 2000 kPa to 5000 kPa, in case of the Associated20 model, the performance was not subjected to a deterioration. This is the reason, why it is believed

that the Young's modulus of the cavity has only minor influence on the results of different associated models.

For the models with friction angles of the continuum of 25° and 30° the pressure-expansion curves ended-up around 2 to 4 % below the closed-form solution.

However, smooth curves were obtained in all associated cases which clearly shows that the flow rule was causing the scattering in the PLAXIS curves from previous studies. An example of the output of the PLAXIS Curves manager for the model Associated20 can be found in Fig. 96. The curves received from the different output nodes are congruent for all models in case of an associated flow rule.

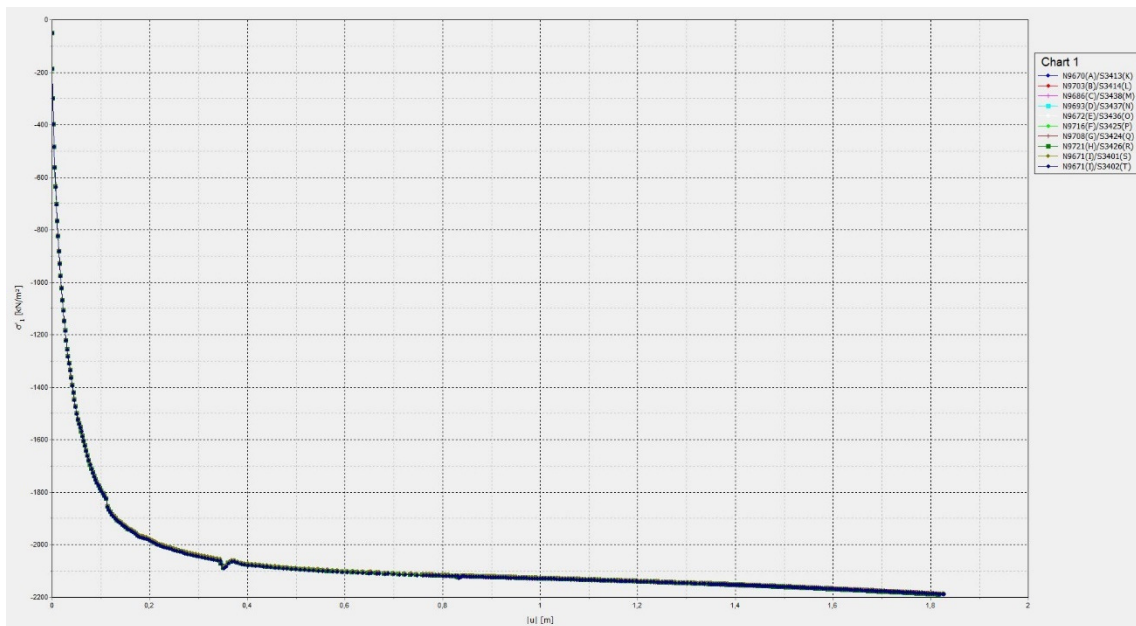


Fig. 96: Output PLAXIS Curves manager – Associated flow rule

6.3.5 Influence of Different Selected Output Nodes

To see whether different selected nodes for the output can result in pressure-expansion-curves which are in better agreement with the closed-form solution than the suggested output nodes by Xu [43], different models based on the large domain size (20x40 m) with selected stress points, located either outside (“node-configuration 1”) or inside the cavity (“node-configuration 2”), were created. As the information of the displacements wants to be directly received at the cavity wall, the nodes by Xu selected for the output of the total displacements $|u|$ were adopted for all created models. Fig. 97 depicts the two-different node-configurations as used within the created models for the output within the PLAXIS Curves manager.

Only one calculation was performed with “node-configuration 1” (stress points outside) as it was concluded from the output that this set of nodes was not able to yield accurate results with respect to the pressure-expansion-curve. In Fig. 98 the received curves from the PLAXIS Curves manager are depicted. It can be seen that the curves obtained from the different selected stress-points are subjected to a heavy scattering with differences in

σ'_l of the different curves of up to 2400 kPa, which is why node-configuration 1 was rejected.

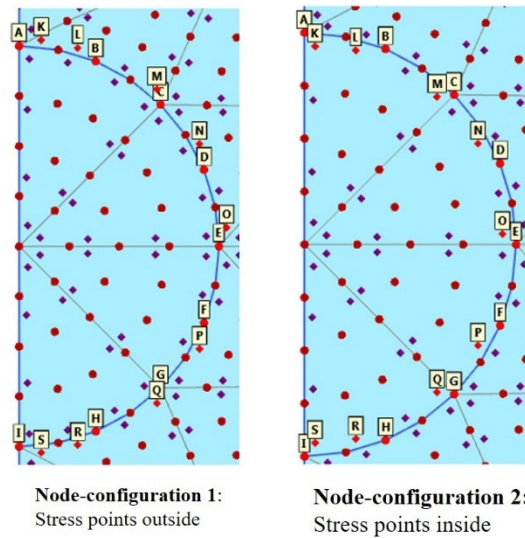


Fig. 97: Different node-configuration with stress points outside and inside the cavity

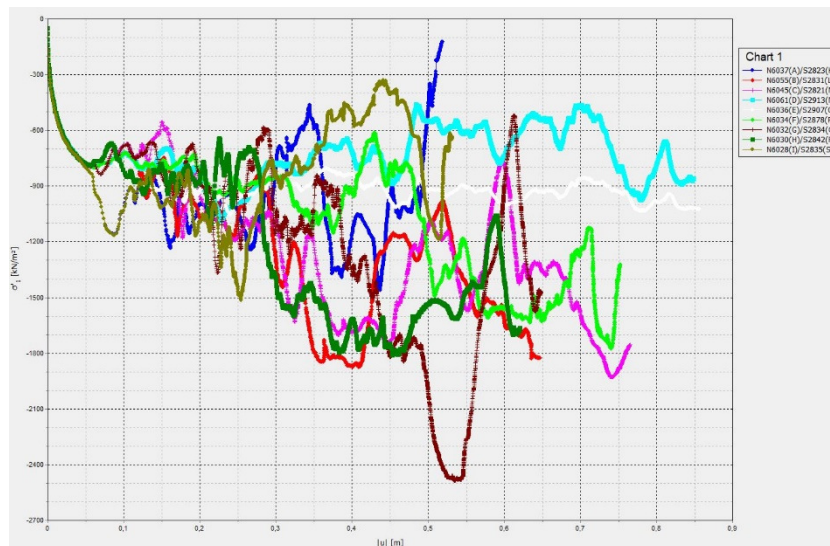


Fig. 98: PLAXIS Curves manager results for stress points chosen outside the cavity

To depict the performance of the remaining “node-configuration 2” in dependency of the cavity Young’s modulus, 4 models with different values of E (1000, 2000, 5000, 10000 kPa) for the cavity, with stress points chosen inside, were set up and compared to the same models with stress points chosen according to Xu. The large domain (20x40 m) with y_{max} set to fixed was used for all models.

Created models:	NodeCon2_E1000	Nodeconfig. 2	Cavity: $E = 1000$ kPa
	Xu_E1000	Nodes acc. to Xu	Cavity: $E = 1000$ kPa
	NodeCon2_E2000	Nodeconfig. 2	Cavity: $E = 2000$ kPa
	Xu_E2000	Nodes acc. to Xu	Cavity: $E = 2000$ kPa

NodeCon2_E5000	Nodeconfig. 2	Cavity: $E = 5000$ kPa
Xu_E5000	Nodes acc. to Xu	Cavity: $E = 5000$ kPa
NodeCon2_E10000	Nodeconfig. 2	Cavity: $E = 10000$ kPa
Xu_E10000	Nodes acc. to Xu	Cavity: $E = 10000$ kPa

For each of the models the averaging of the curves received from the PLAXIS Curves manager was done both for all selected nodes and for the remaining nodes, when the northern- and southern-most displacement nodes and stress points were eliminated (recommendation see chapter 6.3.1). Resulting from this, for each of the models two different pressure-expansion-curves were calculated.

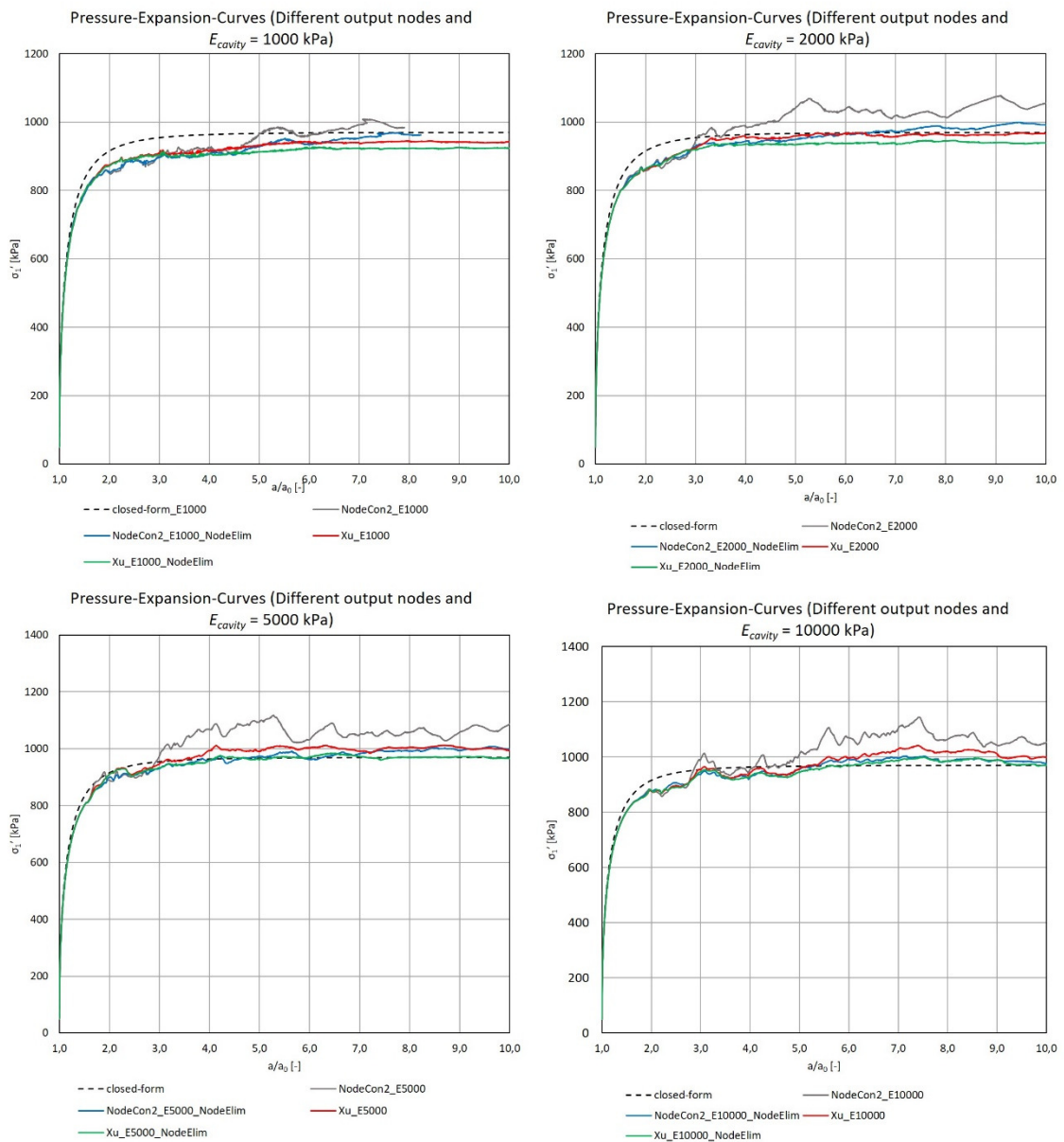


Fig. 99: Pressure-expansion-curves – Influence of different nodes

Fig. 99 shows four diagrams in which the curves received from the different models and both averaging approaches are compared. Each diagram depicts the curves for models comprising the same E of the cavity. The addition “NodeElim” to the curve names within

the diagrams indicates for which curves the mentioned node elimination for the averaging was done.

The worst results for the pressure-expansion-curves were obtained from models incorporating the proposed “node-configuration 2” without the elimination of the northern- and southern-most points for the output. This can be associated with the distinct unsymmetrical stress and strain distributions across the cavity during the expansion.

An improvement was recognised when the outlier curves remained unconsidered within the averaging process to come up with the pressure-expansion-curves. Much smoother curves were obtained when critical output nodes were eliminated. One side effect of the elimination is connected to a decrease of the maximum values of the received-pressure-expansion curves. This effect was encountered for both models with nodes chosen acc. to Xu and models with “node-configuration 2”. Especially, for the models with $E = 1000$, and $E = 2000$ respectively, this decrease resulted in a poorer agreement with the analytical solution.

However, the models with nodes chosen acc. to Xu [43] without the elimination of critical points in the averaging procedure overall performed better than models incorporating “node configuration 2” and especially the results from model Xu_E2000 almost depicted a perfect fit with the closed-form solution. Nevertheless, the elimination of certain nodes in the averaging procedure is recommended, as smoother curves might be obtained.

When the elimination is applied to model Xu_E2000, which is depicted by the green line in the top right diagram in Fig. 99, however, the agreement with the analytical solution is getting worse due to the decrease of the attained maximum pressure σ_I' . This problem can simply be solved by increasing the Young’s modulus of the cavity from 2000 to 5000 kPa. In doing this, the best agreement of all curves in Fig. 99 with the closed-form solution is accomplished by the model Xu_E5000_NodeElim, which incorporates the nodes selected by Xu including the elimination of critical nodes for the output.

6.3.6 The Final Plaxis Model

The findings from all conducted studies within chapter 6.3 were combined to come up with an improved version of the basic FEM-model.

The final PLAXIS model is based on the large domain ($b = 20$ m, $h = 40$ m, +1 m dummy layer) with the deformation boundaries y_{max} and y_{min} chosen fixed and x_{max} and x_{min} chosen normally fixed. The initial cavity radius a_0 is chosen with 0.1 m

The mesh of the improved model incorporates a 4-element-discretization of the cavity and comprises 740 elements in total. Two concentric half circles around the cavity were used to allow for a better mesh graduation. The nodes for the output were chosen in agreement with the nodes acc. to Xu [43] considering the elimination of the nodes A, I,

K and T within the averaging procedure needed for the determination of the pressure-expansion-curves (chapter 6.1.5).

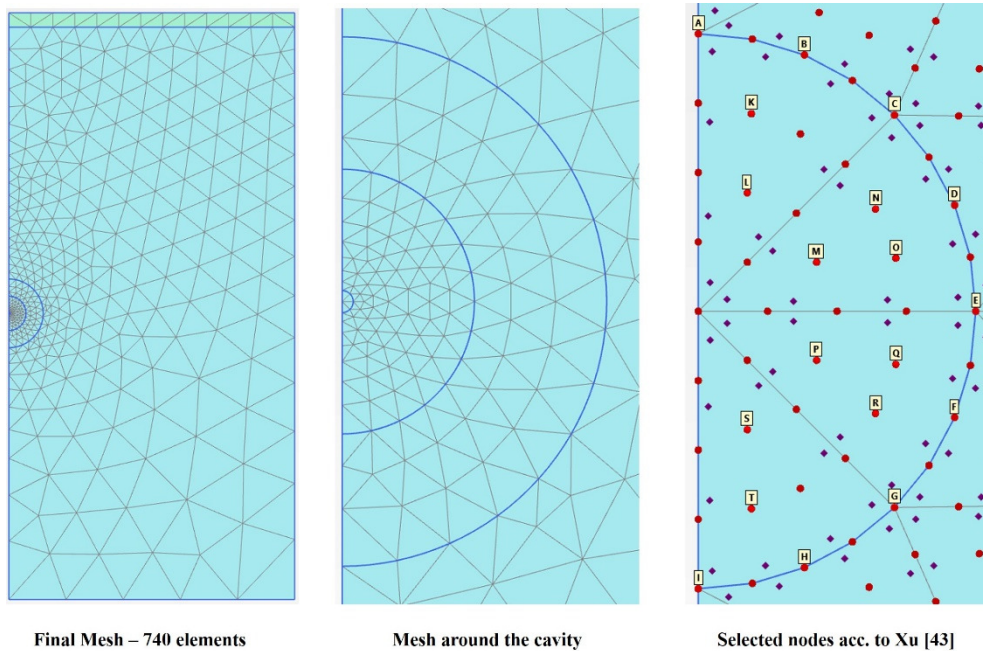


Fig. 100: Mesh of the final model

The following soil parameters are used for the materials with a linear elastic constitutive model assigned to the cavity and the dummy layer. In general, it was found that taking the E of the cavity with $1/5$ of the surrounding continuum stiffness yields good results.

Tab. 16: Initial material parameters used for the improvement of the FEM-model

Material	Soil parameters			Constitutive model
	E'	ν	K_0	
Cavity	E'	$1/5$ continuum E	[kPa]	Linear elastic
	ν	0.0	[-]	
	γ'	0.0	[kN/m ³]	
	K_0	1.0	[-]	
Dummy Layer	E'	20,000	[kPa]	Linear elastic
	ν	0.2	[-]	

The K_0 procedure is used for the generation of the initial stresses and the reset displacements to zero option is selected within the first calculation phase.

For all calculation phases the updated mesh option is chosen and the arch-length control is switched off.

It is suggested to use a maximum load fraction per step of 0.05 or smaller, especially when the cavity gets subjected to larger volumetric strains. Typical values for the positive volumetric strains assigned to the cavity in one calculation phase are +250% or +500%.

6.3.7 Comparison with Curves found in Literature

With the final settings and soil parameters for the dummy layer and the cavity of the improved model it was tried to obtain pressure-expansion-curves for two different materials found in literature. The materials for the continuum used for this study were taken from the dissertation of Xu [43]. All calculations were performed with an effective mean pressure of $p_0 = 120$ kPa. The soil parameters of the considered materials can be found in the table below.

Tab. 17: Continuum materials found from literature [43]

Continuum Material	Soil parameters			Constitutive model
MC1	E'	5,000	[kPa]	MC
	ν	0.2	[-]	
	c'	0.0	[kPa]	
	φ'	20	[°]	
	ψ	0	[°]	
	γ'	0.0	[kN/m ³]	
	K_0	1.0	[-]	
MC2	E'	100,000	[kPa]	MC
	ν	0.2	[-]	
	c'	0.0	[kPa]	
	φ'	42	[°]	
	ψ	12	[°]	
	γ'	0.0	[kN/m ³]	
	K_0	1.0	[-]	

Despite the fact that two very synthetic materials with numerically difficult to handle soil parameters were considered in the calculations a good agreement in comparison with the closed-form solution was achieved in case of both materials. From the comparisons with the curves received by Xu [43] it was further concluded that the produced PLAXIS model from the studies of the present thesis was even more accurate than the model by Xu as bigger differences between the FEM-solution and the analytical solution were observed from his results. It is worth mentioning that Xu used the same analytical expression derived by Yu and Houlyby [44] to come up with the closed-form solution, as was explained in chapter 6.2.

The comparisons between the pressure-expansion-curve obtained from the improved PLAXIS model of this thesis and the closed-form solution can be found next to the graphical results by Xu in Fig. 101 for material MC1 and in Fig. 102 for material MC2.

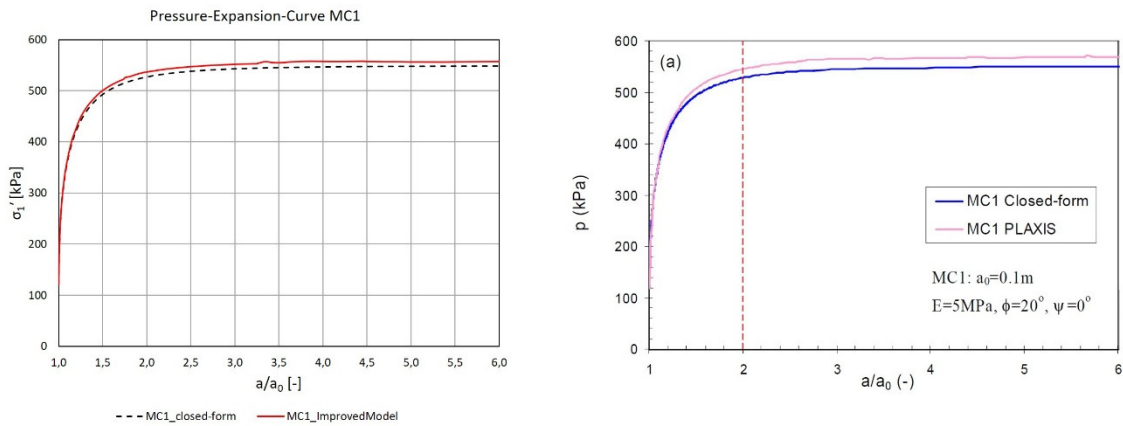


Fig. 101: Pressure-expansion-curves for material MC1 from improved PLAXIS model (left) and from Xu [43] (right)

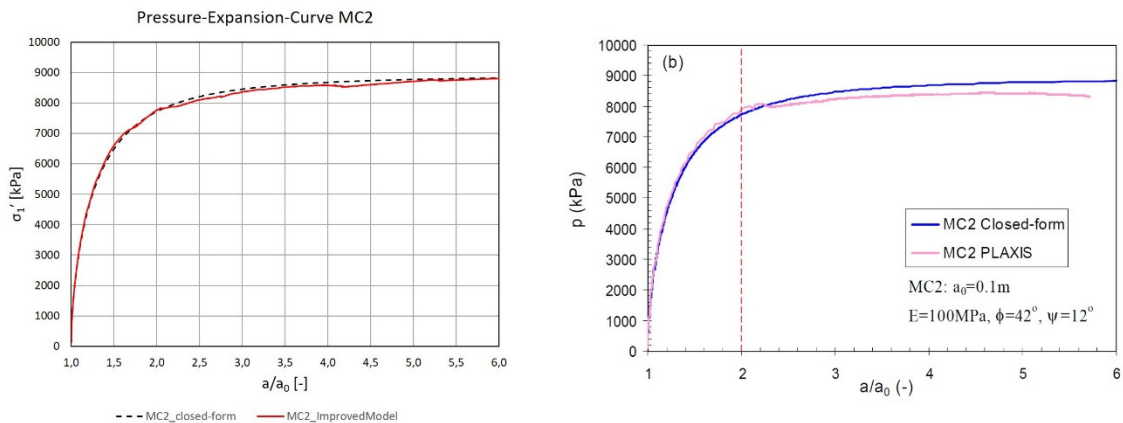


Fig. 102: Pressure-expansion-curves for material MC2 from improved PLAXIS model (left) and from Xu [43] (right)

Within the diagrams produced from the results of the improved PLAXIS model the expansion ratio a/a_0 is plotted against the effective vertical stress σ_1' , whereas Xu plotted the expansion ratio against the mean effective stress p within his diagrams. It can be easily shown that both considerations depict the same pressure-expansion relationship, as p can be calculated from $p = (\sigma_1 + 2\sigma_3)/3$. For the assumption in cavity expansion theory of a hydrostatic pressure within the cavity, where $\sigma_1 = \sigma_3$, the equation for p reduces to $p = (3\sigma_1)/3$, and further $p = \sigma_1$.

6.4 Mohr-Coulomb Material Study – Final Model

The studies from the previous chapter were all aiming at the improvement of the basic PLAXIS FEM-model. The following sections within chapter 6.4 are focusing on the performance of the improved FEM-Model for different MC-materials assigned to the continuum. Thereby, materials with rather different soil parameters were considered. Tab. 18 gives an overview of the investigated materials.

Tab. 18: Investigated MC-materials assigned to the continuum

Material	E' [kPa]	ν [-]	c' [kPa]	ϕ' [°]	ψ [°]
1	25000	0.2	0	30	0 or 30
2	50000	0.2	0	40	0 or 40
3	8000	0.2	3	27	0 or 27

Each of the three materials was calculated with both, an associated and a non-associated flow rule. The calculated pressure-expansion-curves with $K_0 = 1.0$ and $p_0 = 50$ kPa for all materials can be found in the following figures.

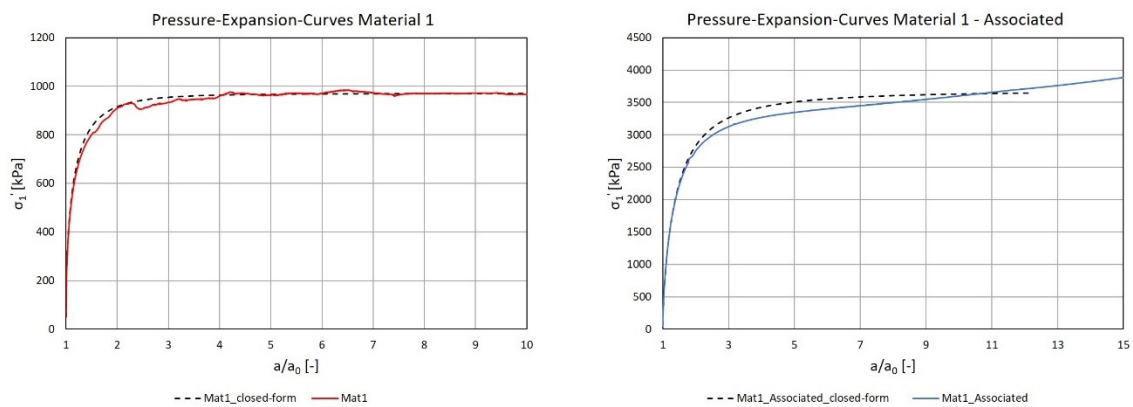


Fig. 103: Pressure-expansion-curves for Material 1 – non-associated (left) vs. associated flow rule (right)

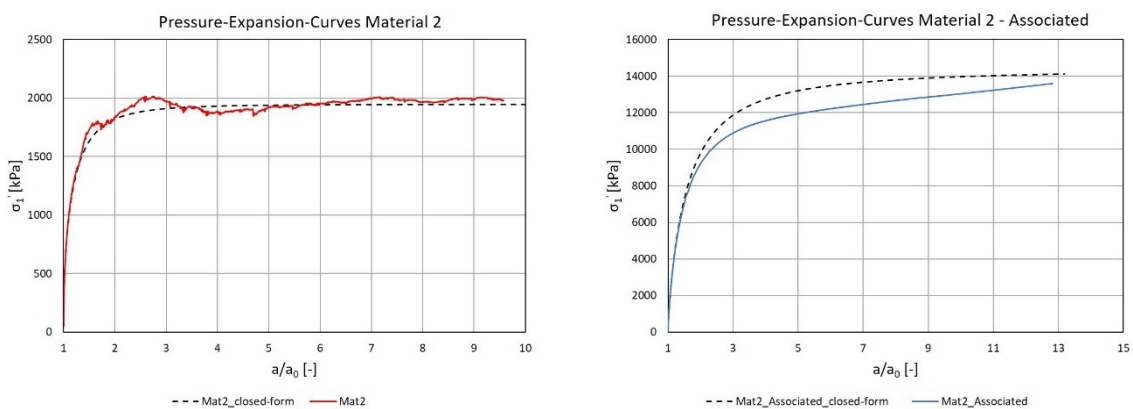


Fig. 104: Pressure-expansion-curves for Material 2 – non-associated (left) vs. associated flow rule (right)

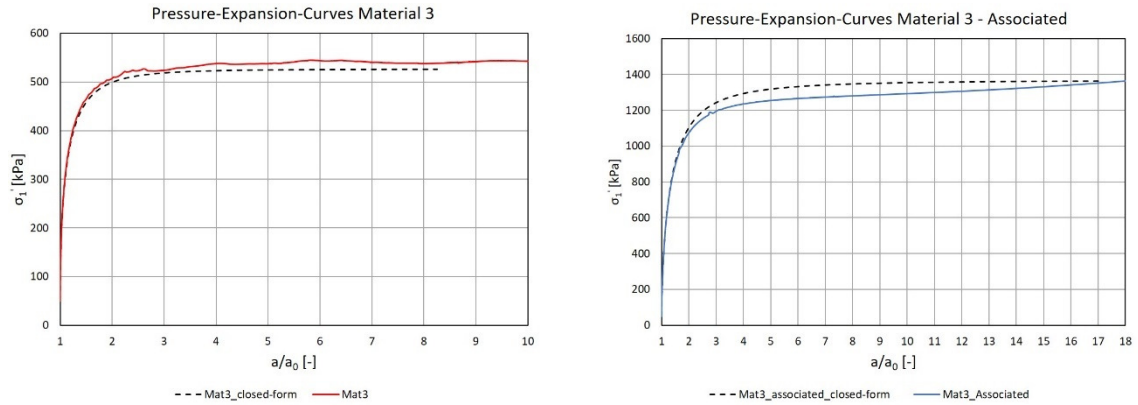


Fig. 105: Pressure-expansion-curves for Material 3 – non-associated (left) vs. associated flow rule (right)

For all models incorporating the non-associated flow rule with $\psi = 0.0^\circ$ very good agreements with the closed-form solution were obtained. The best results were obtained for Material 1. The soil parameters of this material were also probably those which can most likely be encountered for sands.

The differences between the FEM- and the analytical solution for the materials comprising the associated flow rule were found to be larger than in the non-associated cases. From the studies within the previous chapter it was found that an exact agreement with the closed-form curve can only be received for $\varphi = \psi$ of up to 20° . As all considered friction angles of the materials were above this limiting value the differences can most probably be justified by this statement. The biggest deviations from the closed-form solution are encountered for Material 2 with the highest value of the friction angle. However, the curves are found to be much smoother than in the non-associated cases. Nevertheless, the results of the associated models might be unappropriated for the determination of the limit pressure p_{LS} as a horizontal course of the curves is never reached and the effective stresses keep steadily increasing with increasing expansion ratios a/a_0 .

6.4.1 Variation of E for Material 1 and Material 3

To depict the influence of a changing stiffness of the continuum-material on the resulting pressure-expansion-curves, and hence the values of the limit pressures p_{LS} , several calculations were performed based on Material 1 and Material 3 (Tab. 18) with the aid of the improved PLAXIS model. Thereby, values for E four-times smaller and four-times larger than the value from the basic materials were considered within the calculations. The different investigated material sets are listed in Tab. 19.

Tab. 19: Used material sets – Variation of E for Material 1 and Material 3

Material	E' [kPa]	ν [-]	c' [kPa]	ϕ' [°]	ψ [°]
Mat1	25,000	0.2	0	30	0
Mat1_SmallE	6,250	0.2	0	30	0
Mat1_LargeE	100,000	0.2	0	30	0
Mat3	8,000	0.2	3	27	0
Mat3_SmallE	2,000	0.2	3	27	0
Mat3_LargeE	32,000	0.2	3	27	0

Calculations were performed for an initial mean effective stress of $p_0 = 50$ kPa and a value of $K_0 = 1.0$ (continuum). The resulting pressure-expansion-curves are depicted in Fig. 106 for the models based on Material 1 and Material 3.

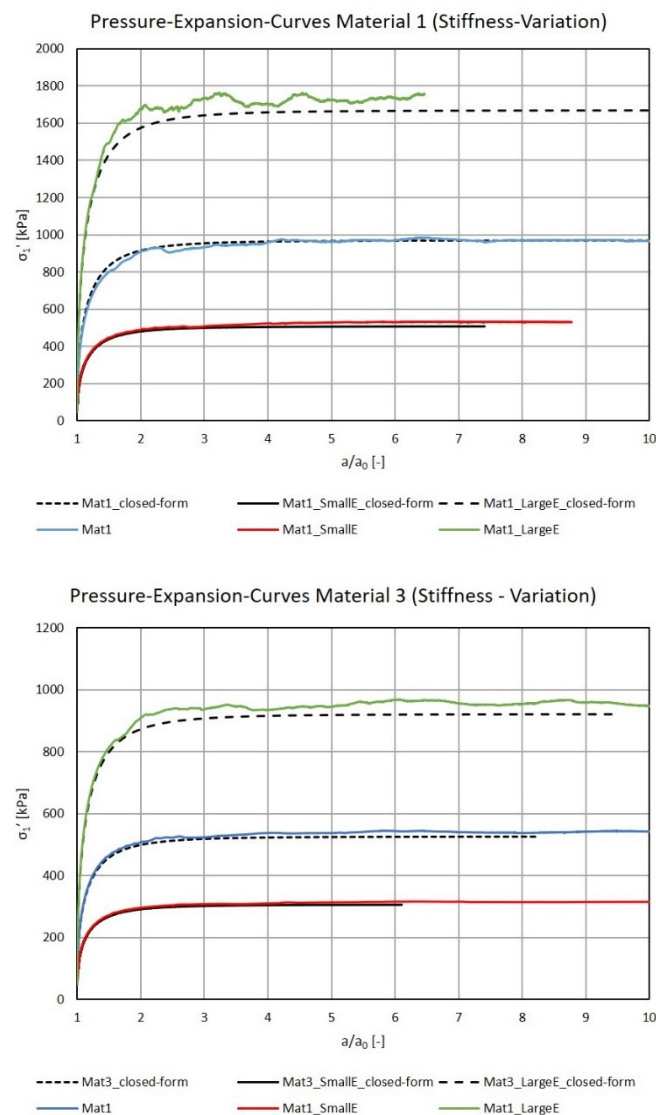


Fig. 106: Pressure-expansion-curves for changing E of Material 1 (above) and Material 3 (below)

The studies clearly show that the limit pressure p_{LS} (maximum stress at “horizontal” parts of the curve) in fact not only depends on the strength but also on the stiffness of the surrounding soil body. This is due to a failure mechanism that stays confined without a rupture extending to the surface [45].

In case of both materials it could be shown, that an increase or decrease of the continuum-stiffness by a factor of 4 results in maximum stress-values of the pressure-expansions-curves about 2 times higher or lower compared to the values from the curves of the basic materials.

It could also be shown that the smoothness of the curves depends to a great extent on the chosen values for the stiffness of the continuum. Lowering the stiffness resulted in smoother curve progressions, whereas for an increase of E the curves ended up proceeding rather jagged.

6.4.2 Variation of K_0 for Material 1 and Material 3

Calculations were performed for Material 1 and Material 3 (Tab. 18) with changing values of K_0 . The values of K_0 (continuum) were chosen with 0.5, 1.0 and 2.0. The initial stresses were produced with the aid of the K_0 procedure in PLAXIS and a unit weight of $\gamma' = 50$ kPa was taken into account for the dummy layer. The input parameters for the different created models, shown in Tab. 20, were considered within the calculations.

Tab. 20: Used material sets – Variation of K_0 for Material 1 and Material 3

Material	E' [kPa]	ν [-]	c' [kPa]	ϕ' [°]	ψ [°]	K_0 [-]
Mat1	25,000	0.2	0	30	0	1.0
Mat1_K0_05	25,000	0.2	0	30	0	0.5
Mat1_K0_2	25,000	0.2	0	30	0	2.0
Mat3	8,000	0.2	3	27	0	1.0
Mat3_K0_05	8,000	0.2	3	27	0	0.5
Mat3_K0_2	8,000	0.2	3	27	0	2.0

The results for the pressure-expansion-curves for Material 1 and Material 3 can be found within Fig. 107.

Generally, it can be stated that increasing values for K_0 lead to an increase of the maximum stresses attained within the spherical cavity expansion, and therefore the received limit pressure p_{LS} .

The conclusion of this short study is that the coefficient of lateral earth pressure K_0 of the continuum has a significant influence on the value of the limit pressure and that it can therefore not be neglected within the calculations.

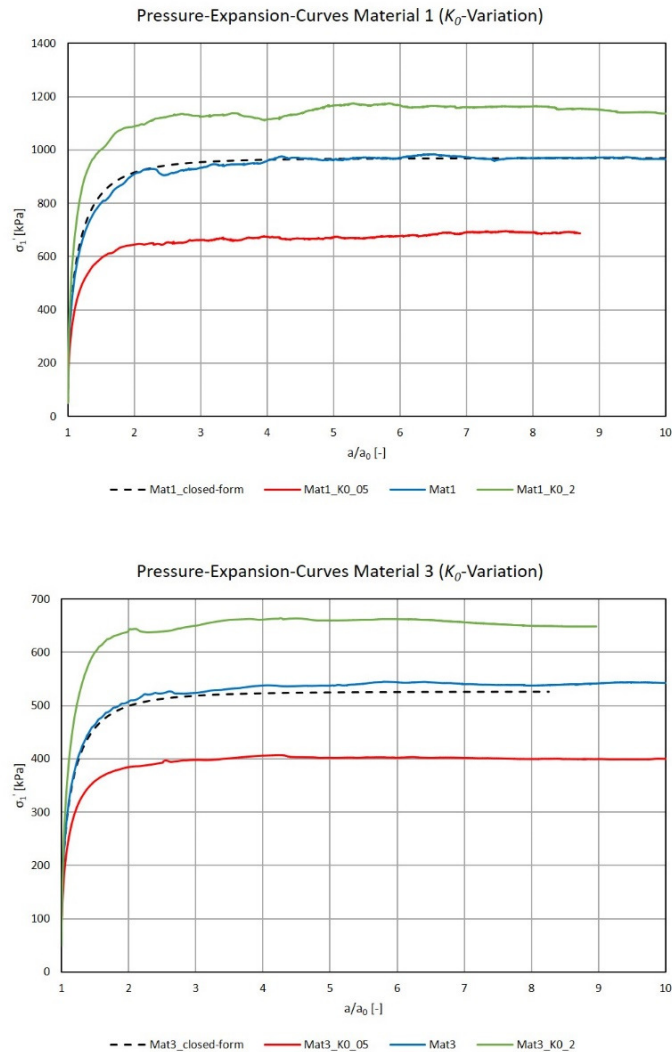


Fig. 107: Pressure-expansion-curves for changing K_0 of Material 1 (above) and Material 3 (below)

It should further be mentioned that only the closed-form curves for $K_0 = 1.0$ are plotted within the shown diagrams as the analytical solution is solely defined for an isotropic initial stress field.

6.4.3 Variation of p_0 for Material 1 and Material 3

The last studies conducted with the models comprising the Mohr-Coulomb material model were performed with the intention to depict the influence of the initial mean effective pressure p_0 on the attained limit pressures from the spherical cavity expansion.

Again, Material 1 and Material 3 (Tab. 18) served as the basis continuum-materials for the created models based on the improved PLAXIS model. Three different pressure levels were considered within the calculations, namely $p_0 = 50, 150$ and 300 kPa, and the unit weight of the dummy layer was changed correspondingly ($\gamma' = 50, 150$ and 300 kN/m³).

The obtained pressure-expansion-curves from the study on the influence of different initial mean effective stresses p_0 are shown in Fig. 108. The curves for Material 1 can be found within the top diagram and for Material 3 within the diagram at the bottom.

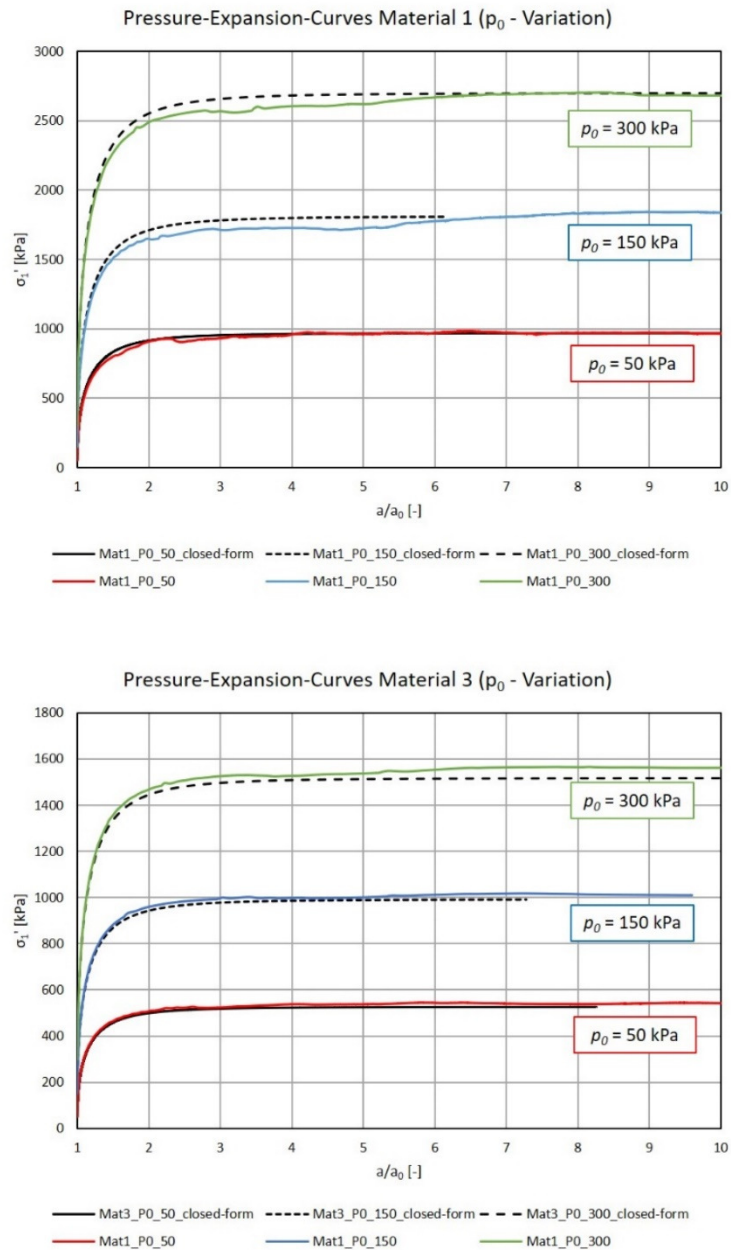


Fig. 108: Pressure-expansion-curves for changing p_0 of Material 1 (above) and Material 3 (below)

The results of all models show good agreement with the closed-form solution. With rising mean effective stress p_0 , the maximum attained stresses, and hence the values of the limit pressures, increase. It was found that the value of p_0 , in contrast to the considered value of the stiffness E , has in fact no influence on the smoothness of the obtained curves.

6.5 PLAXIS Calculations – Hardening Soil Model

The hardening-soil model was used for further studies with the final FE-models of the spherical cavity expansion problem in PLAXIS. The results for 7 different materials found in literature (Dissertation Xu [43]) were compared to the actual results of the PLAXIS models. The stiffnesses of the materials were given at a reference pressure of $p_{ref} = 120$ kPa. This is also the value for the effective mean pressure p_0 for which the SCE-simulations were performed (γ' dummy layer = 120 kN/m³). For all materials a cohesion of $c'_{ref} = 0.2$ kPa and a Poisson's ratio of $\nu = 0.2$ was taken into account. Additionally, K_0 was chosen with 1.0 and the unit weight of the continuum was set to zero. The values for E_{ur}^{ref} were given with $3 \cdot E_{50}^{ref}$ and E_{oed}^{ref} was considered with the same value as E_{50}^{ref} . The remaining soil parameters from the different materials can be found in Tab. 21.

Tab. 21: Material parameters – HS-materials

	HS-Materials						
	HS1	HS2	HS3	HS4	HS5	HS6	HS7
Xu's designation	Mat. 2 UL	Mat. 2 LL	Mat. 4 UL	Mat. 13 UL	Mat. 13 LL	Mat. 18 UL	Mat. 18 LL
E_{50}^{ref} [kPa]	10,000	50,000	50,000	50,000	30,000	100,000	5,000
φ [°]	40	40	20	40	33	42	20
ψ [°]	0	0	0	10	3	12	0
m [-]	1	0.5	1	0.5	1	0.5	1
e_{min} [-]	0.49	0.49	0.49	0.49	0.49	0.49	0.49
e_{max} [-]	0.78	0.78	0.78	0.78	0.78	0.78	0.78
e_{init} [-]	0.68	0.5	0.68	0.5	0.68	0.5	0.68

UL = Upper Layer LL = Lower layer

The Young's modulus of the cavity was chosen with 1/5 of the E_{50}^{ref} -values. For the determination of the pressure-expansion-curves the nodes A, I, K and T were rejected and not considered within the averaging. The results for the pressure-expansion-curves from Xu and the received curves from the PLAXIS models can be found in Fig. 109 and Fig. 110.

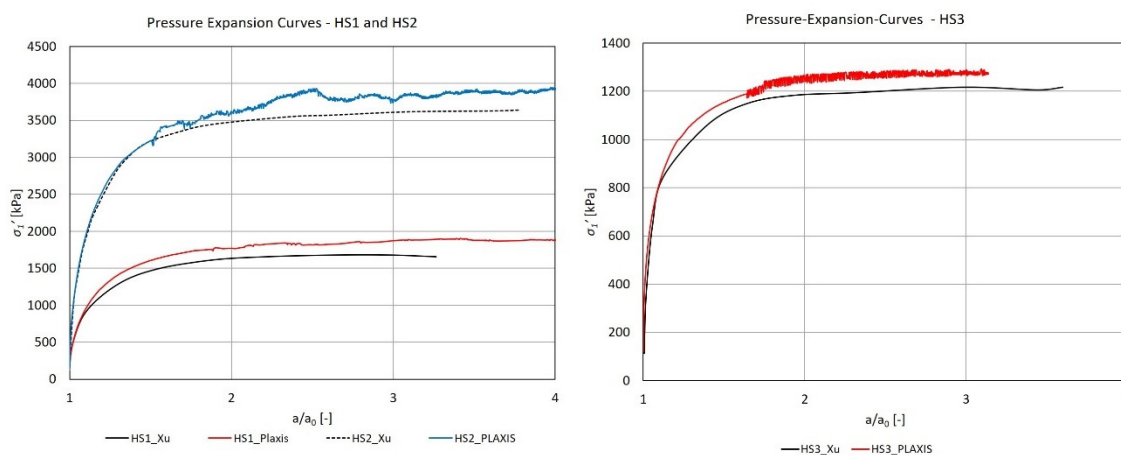


Fig. 109: Pressure-expansion-curves for materials HS1, HS2 and HS3

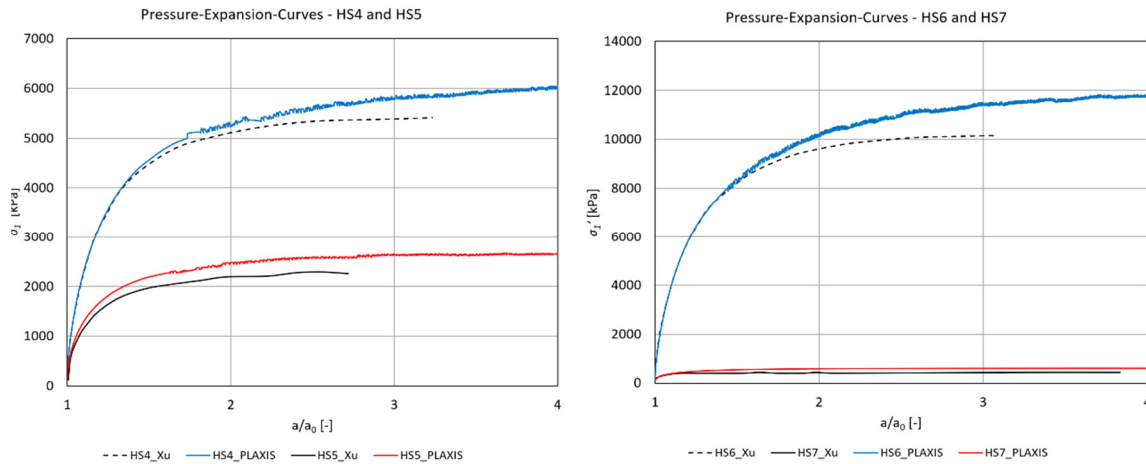


Fig. 110: Pressure-expansion-curves for materials HS4, HS5, HS6 and HS7

It can be seen that the curves from the PLAXIS calculations follow the once by Xu until the stresses start to rise beyond the reference curves at certain expansion ratios a/a_0 . It is believed that this is a result of the non-uniform initial stress fields that Xu's models were subjected to, as he modelled the continuum with a non-zero unit weight, with $p_0 = 120$ kPa only at the level of the cavity.

However, the problems in connection with the non-associated flow-rule were also encountered when the HS-model was used. That's the reason why some of the curves in Fig. 109 and Fig. 110 proceed rather jagged at higher expansion ratios than perfectly smooth. When it was tried to perform the calculation based on material HS2 with an associated flow-rule and a friction angle of 20° , the problems disappeared and the curves from the PLAXIS Curves manager were congruent, indicating a uniform distribution of the stresses and strains across the cavity.

It has to be noted that the time was too short to make detailed investigations on the performance of the cavity expansion models in connection with the hypoplastic constitutive law. Nevertheless, the first calculations suggested that this soil model might yield proper results in case further improvements with respect to different model settings and material properties are made.

6.6 PLAXIS Calculations – Hypoplastic Model

After having the PLAXIS model improved and the investigations on the MC- and HS-materials finished the focus of the studies was shifted towards the hypoplastic constitutive law.

PLAXIS allows for the utilization of different constitutive laws by adding the desired .ddl-files, containing the code with the mathematical formulations of the constitutive models, into the PLAXIS folder for user-defined soil models. For the studies within chapter 6.6 the “Hypoplastic Sand” model, containing the hypoplastic constitutive law by “von Wolffersdorff” [23], was downloaded from the website “soilmodels.com” and implemented into PLAXIS.

6.6.1 General Aspects – Hypoplastic Model in PLAXIS

The utilized soil model requires 8 hypoplastic parameters to be inputted all of which were discussed in chapter 4.2. Additionally, the initial void ratio e_0 has to be provided for the calculations to define the initial density state of the soil. Attention must be paid to the definition of e_0 , because it is defined at a pressure level of zero. Another parameter, namely p_t , is required to account for the shift of the mean stresses due to cohesion. For basic hypoplasticity, however, p_t , can be assumed with a very small value, i.e. $1E-5$.

It was found that for the void ratio e_{init} within the general tab from the PLAXIS material editor also the initial void ratio has to be entered, but at the level of the initial mean effective stress p_0 . This value might not have any influence on the received pressure-expansion-curves of the model but on the correctly depicted distributions of the void ratios within the PLAXIS output.

Once the material tab sheet of the hypoplastic model wants to be closed and the default values for the interface stiffness and the interface cohesion, within the interfaces tab, are kept, error messages will keep occurring until certain values are entered. In case the PLAXIS model doesn't comprise the definition of an interface these values don't have an effect on the results.

6.6.2 Advantage of Hypoplasticity over Elasto-Plasticity

The application of the hypoplastic constitutive law to the FEM-simulations of the spherical cavity expansion is accompanied by one major advantage over the commonly used elasto-plastic soil models.

As the nature of the hypoplastic constitutive model forgoes the definition of a flow-rule and describes the stress-strain relationship of a material solely based on one tensorial equation, the hypoplastic model was found to perform much more stable on the

considered large-deformation problem of the spherical cavity expansion than the previously utilized elasto-plastic models. Independent of the investigated materials and initial material states, with respect to density and stresses, the simulations with the hypoplastic model resulted in uniform distributions of the stresses and strains across the cavity. This behaviour was observed for any considered expansion ratios which implied that the curves received from different output nodes within the PLAXIS Curves manager were always congruent. An example of this curves from the PLAXIS output for one of the conducted calculations with the hypoplastic constitutive model can be found in Fig. 111.

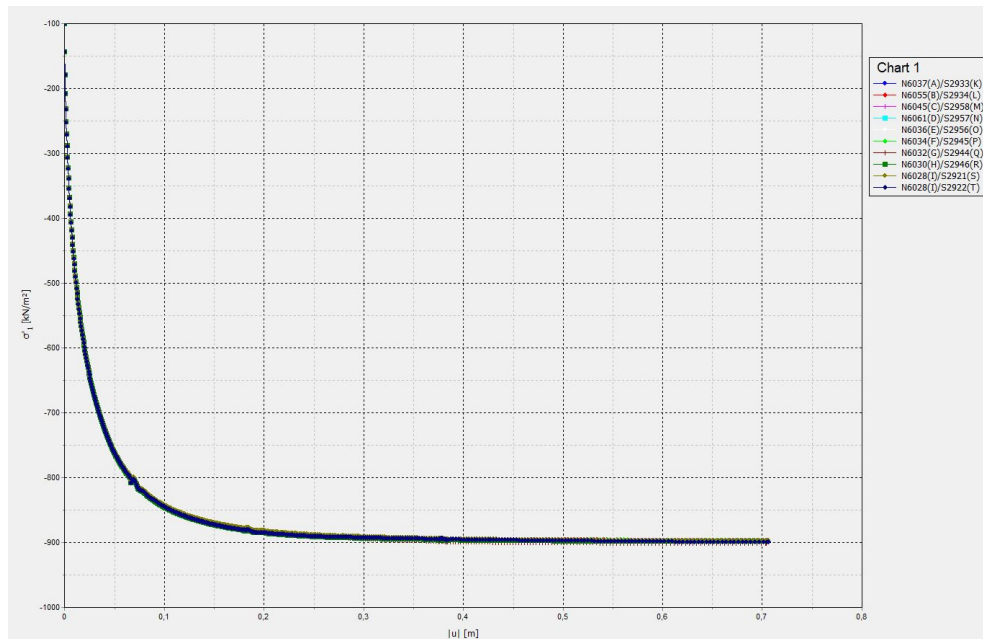


Fig. 111: Example of the curves from the PLAXIS Curves manager for the hypoplastic models

Due to the symmetry of the stresses and deformations across the cavity and the congruent lines within the PLAXIS Curves manager the pressure-expansion-curves could actually be obtained from just one single curve from the PLAXIS output without applying the averaging procedure (see chapter 6.1.5). But to be consistent with the previous suggestions the averaging procedure for the determination of the pressure-expansion-curve was still applied to the hypoplastic FEM-models, investigated in the course of this thesis.

Fig. 112 presents a typical example of a pressure-expansion-curve received from the final PLAXIS model for which the continuum comprises the hypoplastic constitutive model. The determination of the limit pressures p_{LS} was an easy task as the pressure-expansion-curves of all created models proceeded very smooth and practically ended-up with a horizontal course.

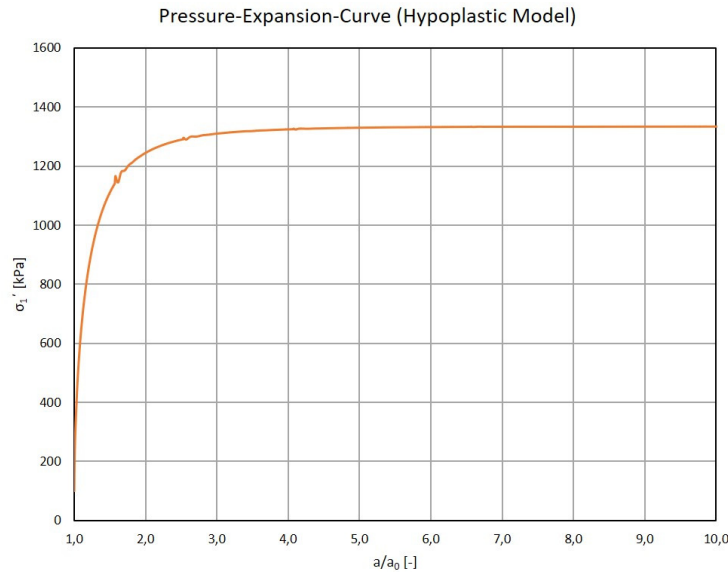


Fig. 112: Typical pressure-expansion-curve as received from the hypoplastic model

6.6.3 Automatic Model Generation for KIM-Analysis

In order to use Cudmani's [8] equation for the approximation of the limit pressure p_{LS} (see chapter 4.3.1), the KIM-parameters (a_i and b_i) for a certain material must be known. The determination of the KIM-parameters requires the conduct of curve-fitting (chapter 5.2) of a number of explicit p_{LS} -values obtained from the simulation of the spherical cavity expansion. It is common to perform 50 different simulations, with 5 different values for the initial mean effective stress p_0 and 10 different values for the initial relative density I_D .

For every changing value of I_D only two parameters within the PLAXIS model have to be adjusted, namely e_{init} (initial pressure-dependent void ratio at p_0) and e_0 (initial void ratio at zero pressure), whereas the unit weight γ' of the dummy layer stays the same.

Every time a different value for p_0 wants to be considered, the pressure-dependent void ratio e_{init} and the unit weight γ' of the dummy layer must be changed, and the initial void ratio e_0 remains the same. The void ratios e_{init} and e_0 can both be calculated with Eqn. (5.3) from chapter 5.1.1 taking into account the corresponding values for p' .

It would be very exhausting to manually adjust e_{init} , e_0 and γ' (Dummy layer) within each of the models from the series. Fortunately, PLAXIS allows to run Python-scripts within the program with the aid of which the adjustments can be done automatically.

Hence, for the given task of creating 50 different models with slightly different soil parameters a Python-script was created. For the usage of this code it has to be remarked that a sufficient number of expansion phases has to be added to the basic model to prevent

calculations from finishing at rather low expansion ratios. The code used within the Python-script can be found in Appendix E within A. Fig 22.

6.6.4 KIM-Analysis using the PLAXIS Model

Two full KIM-analysis were conducted with the aid of the final PLAXIS model based on the hypoplastic parameters (A. Tab. 5) from material PLM AZ28 and PLM BC36 from the KELLER-database. The results for the limit pressures, the a- and b-values from the approximation of the limit pressures and the KIM-parameters were then compared to the OSINOV code results to get information on the performance of the PLAXIS model.

The presented Python-script was utilized to come up with the 50-different models for one material and the pressure-expansion-curves were determined using the averaging procedure on the curves from the different output nodes. Thereby, the suggested elimination of the crucial output nodes (A,I,K,T) was considered. The simulations were performed for 10 different values of I_D (0.0, 0.1, 0.2, 0.3, 0.4, 0.5, 0.6, 0.7, 0.8, 0.9) and 5 different values of p_0 (25, 50, 100, 150 and 300 kPa). The resulting pressure-expansion-curves for different values of p_0 and I_D from material PLM AZ28 can be found within the following figures. The results for material PLM BC36 are shown in Appendix E.

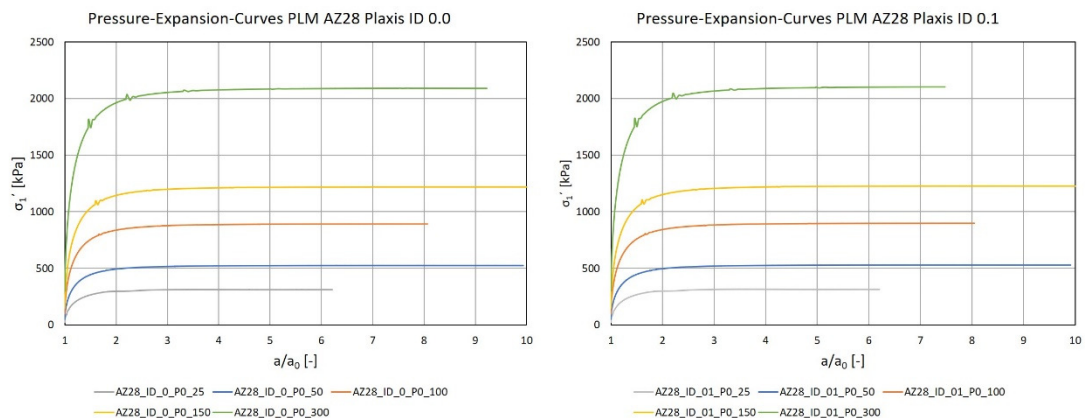


Fig. 113: Pressure-expansion-curves PLM AZ28 for I_D 0.0 and 0.1 (Plaxis)

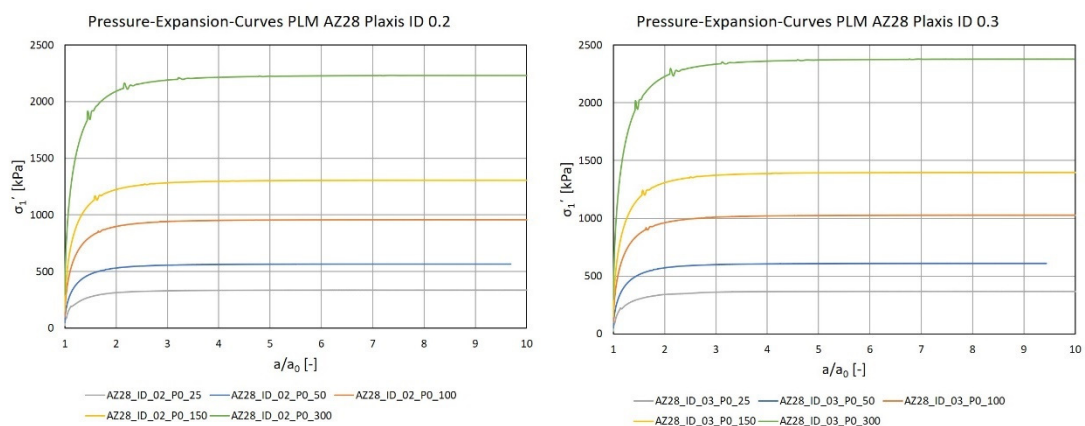


Fig. 114: Pressure-expansion-curves PLM AZ28 for I_D 0.2 and 0.3 (Plaxis)

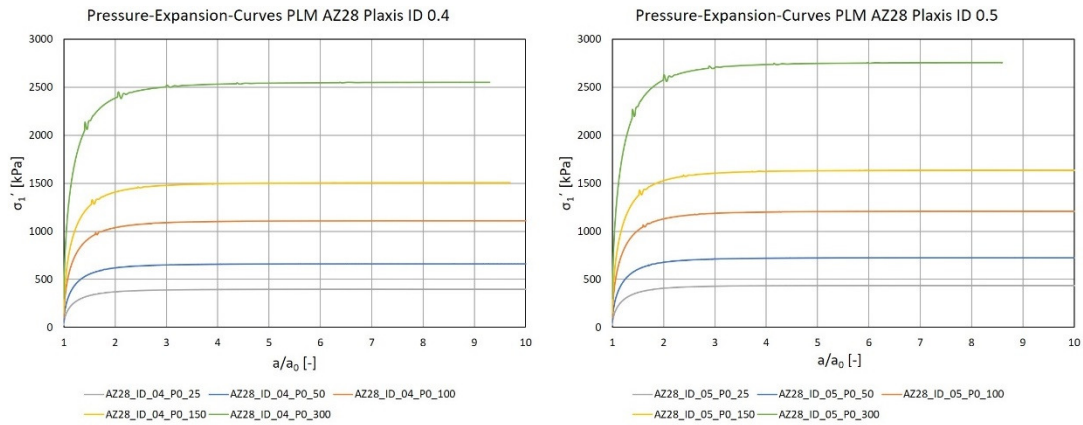


Fig. 115: Pressure-expansion-curves PLM AZ28 for I_D 0.4 and 0.5 (Plaxis)

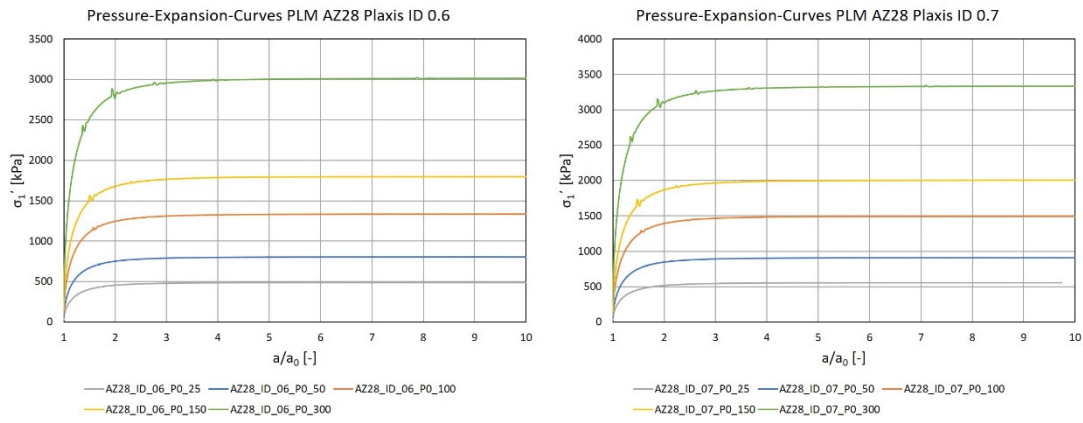


Fig. 116: Pressure-expansion-curves PLM AZ28 for I_D 0.6 and 0.7 (Plaxis)

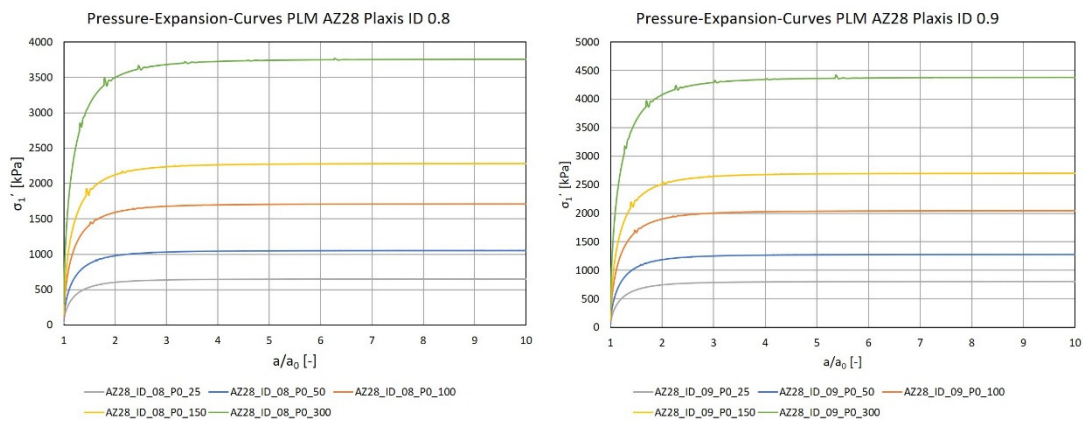


Fig. 117: Pressure-expansion-curves PLM AZ28 for I_D 0.8 and 0.9 (Plaxis)

The resulting limit pressures p_{LS} from the PLAXIS calculations (maximum values from the pressure-expansion-curves) were then compared to the limit pressures received from the calculations with the OSINOV code. It was concluded that the PLAXIS model calculates limit pressures which are always below the values from the OSINOV calculations (maximum difference $\approx 7\%$). Tab. 22 list the limit pressures received from the PLAXIS Model and the OSINOV code for material PLM AZ28. The limit pressures for material PLM BC36 can be found in A. Tab. 7.

Tab. 22: Limit Pressures – PLAXIS vs. OSINOV (PLM AZ28)

Limit Pressures - Material PLM AZ28							
I_D [-]	p_0 [kPa]	p_{LS} (PLAXIS) [kPa]	p_{LS} (OSINOV) [kPa]	I_D [-]	p_0 [kPa]	p_{LS} (PLAXIS) [kPa]	p_{LS} (OSINOV) [kPa]
0.0	25	311	311	0.5	25	435	462
	50	525	529		50	725	769
	100	892	905		100	1208	1284
	150	1220	1244		150	1635	1738
	300	2092	2146		300	2756	2951
0.1	25	315	332	0.6	25	487	517
	50	529	565		50	805	850
	100	898	958		100	1334	1422
	150	1228	1282		150	1798	1900
	300	2103	2262		300	3022	3212
0.2	25	336	356	0.7	25	554	588
	50	566	605		50	909	960
	100	958	1021		100	1495	1593
	150	1306	1397		150	2004	2113
	300	2232	2398		300	3344	3538
0.3	25	367	385	0.8	25	651	688
	50	609	651		50	1052	1109
	100	1027	1091		100	1712	1814
	150	1397	1491		150	2281	2425
	300	2378	2552		300	3769	3978
0.4	25	396	419	0.9	25	805	849
	50	661	705		50	1278	1347
	100	1109	1174		100	2045	2155
	150	1505	1605		150	2702	2854
	300	2550	2732		300	4383	4603

As was explained in chapter 5.2 the obtained KIM-parameters from the curve-fitting procedure are very sensitive with respect to the considered values for the limit pressures p_{LS} . Due to the fact that the calculated PLAXIS limit pressures were always below the received limit pressures from the OSINOV-calculations the KIM-parameters received

from both calculation-approaches also ended up being very different, especially with respect to the a_i -parameters. The KIM-parameters (Excel curve-fit) from both calculation approaches are given in Tab. 23 for material PLM AZ28 and for material BC36 in Tab. 24.

Tab. 23: Comparison of KIM-parameters – PLAXIS vs. OSINOV (PLM AZ28)

	PLAXIS	OSINOV
a_1	1.950	1.705
a_2	-4.795	-6.083
a_3	-1.492	-1.593
b_1	0.812	0.842
b_2	0.052	0.084
b_3	-1.323	-1.440

Tab. 24: Comparison of KIM-parameters – PLAXIS vs. OSINOV (PLM BC36)

	PLAXIS	OSINOV
a_1	2.347	2.038
a_2	-4.053	-5.697
a_3	-1.518	-1.682
b_1	0.834	0.829
b_2	0.058	0.037
b_3	-1.458	-1.261

The differences between the results of both calculation approaches can also be seen within the diagrams representing the approximated p_{LS} -curves.

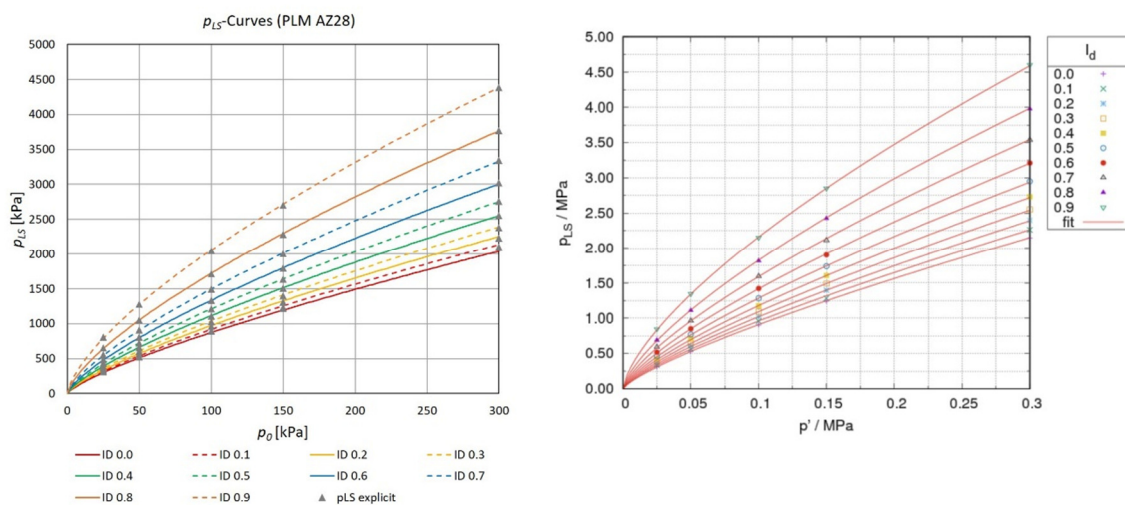


Fig. 118: Approximated p_{LS} -curves for material PLM AZ28 – PLAXIS calculation (left) and OSINOV calculation (right)

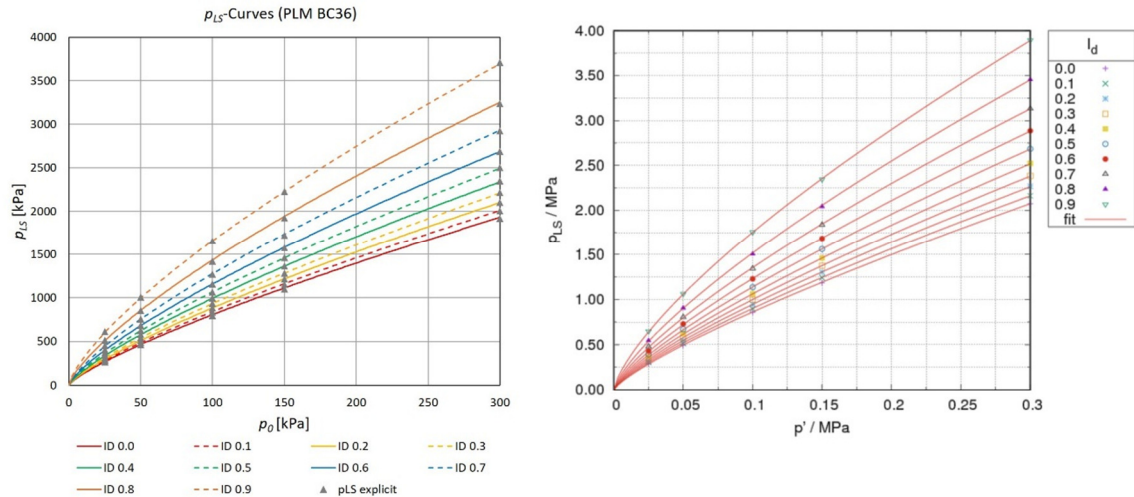


Fig. 119: Approximated p_{LS} -curves for material PLM BC36 – PLAXIS calculation (left) and OSINOV calculation (right)

The studies showed, that PLAXIS can be a very useful tool for the simulations of the spherical cavity expansions as required for the KIM-analysis of different materials. The received limit pressures from the FEM-models were indeed smaller than from the OSINOV simulations, but only up to a maximum difference of around 7 %. The same qualitative behaviour of the pressure-expansion-curves was observed for both calculation approaches in dependence of the considered initial relative densities and initial mean pressures.

From the studies of Slawik [9] regarding the utilization of varying calculation parameters it was concluded that the OSINOV code behaves very sensitive to changing input parameters which in many considered cases resulted in differences between the received limit pressure p_{LS} and the reference values of more than the 7 %. This fact led to the conclusion that the results received from the PLAXIS calculations are quite good and the FEM calculations can serve as a valuable tool for the interpretation of cone penetration tests using the KIM.

6.6.5 Sensitivity Study – PLAXIS Model (Hypoplasticity)

The next step involved the execution of studies on the sensitivity of the PLAXIS calculations incorporating the hypoplastic constitutive law to see how they perform in comparison to the OSINOV calculations.

Based on the studies from Slawik [9] the material PLM AZ28 was used for the investigation of the sensitivity. The results for the limit pressures of the two calculations performed with the final FEM-model for initial relative densities of $I_D = 0.2$ and 0.8 and an initial mean effective stress of $p_0 = 50$ kPa served as reference values to be compared to.

Three factors influencing the results of the models, namely the domain size, the mesh coarseness and the chosen value for the tolerated error were investigated within the sensitivity studies which can more or less be compared to the boundary radius, the discretization and the time step of the OSINOV code.

Three continuum sizes different to the reference models (20 x 40 m) were considered with 10 x 20 m, 15 x 30 m and 50 x 100 m. The tolerated errors for the study were chosen with 0.001 and 0.025 (reference model - 0.01). The meshes included 431 and 1627 elements (reference model – 740 elements) for the generated models for which the domain size was not changed from the reference size. For every performed calculation only one model property was changed, the rest remained the same. The results from the sensitivity study can be found within Tab. 25.

Tab. 25: Received limit pressures p_{LS} from the sensitivity study in PLAXIS

	Model	Mesh - elements	p_{LS} [kPa]	Δp_{LS} (from Reference) [%]
$I_D=0.2$ $p_0=50$ kPa	Reference	740	565.935	-
	Coarse Mesh	431	570.924	0.88
	Fine Mesh	1627	566.766	0.15
	Error 0.001	740	564.969	-0.17
	Error 0.025	740	566.172	0.04
	10 x 20 m	455	593.105	4.80
	15 x 30 m	786	569.634	0.65
	50 x 100 m	1184	567.114	0.21
$I_D=0.8$ $p_0=50$ kPa	Reference	740	1052.390	-
	Coarse Mesh	431	1055.806	0.32
	Fine Mesh	1627	1052.672	0.03
	Error 0.001	740	1051.676	-0.07
	Error 0.025	740	1054.543	0.20
	10 x 20 m	455	1106.058	5.10
	15 x 30 m	786	1059.586	0.68
	50 x 100 m	1184	1052.734	0.03

From the differences Δp_{LS} from Tab. 25 it is concluded that the PLAXIS models are practically not sensitive to any changes of the considered model properties. Only the domain size was found to have an influence when the dimensions of the models are getting too small. The largest difference Δp_{LS} was received for the model comprising $I_D = 0.8$, $p_0 = 50$ kPa and a continuum size of 10 x 20 m with +5.1 %.

To illustrate the sensitivity of both, the PLAXIS and the OSINOV models for $p_0 = 50$ kPa, diagrams were created which show the maximum deviations of the received limit pressures from the reference limit pressures for all investigated model properties. The graphs regarding the OSINOV code were produced using the results from Slawik's

sensitivity study presented in Tab. 13 and Tab. 14 within chapter 5.2.4. Some of the created diagrams depicting the sensitivities of the PLAXIS and the OSINOV models for $I_D = 0.2$ can be found in the following, whereas two further diagrams for $I_D = 0.2$ and the diagrams for $I_D = 0.8$ can be found within Appendix E.

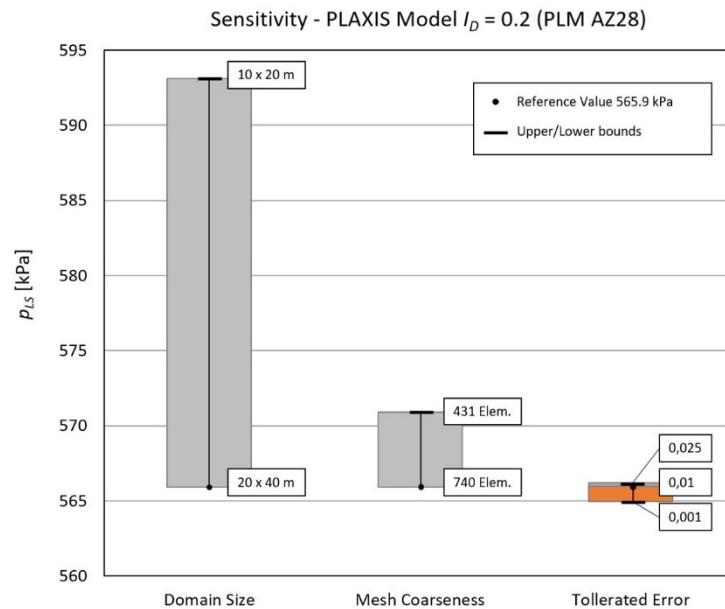


Fig. 120: Sensitivity diagram p_{LS} -range – PLAXIS $I_D = 0.2$ (PLM AZ28)

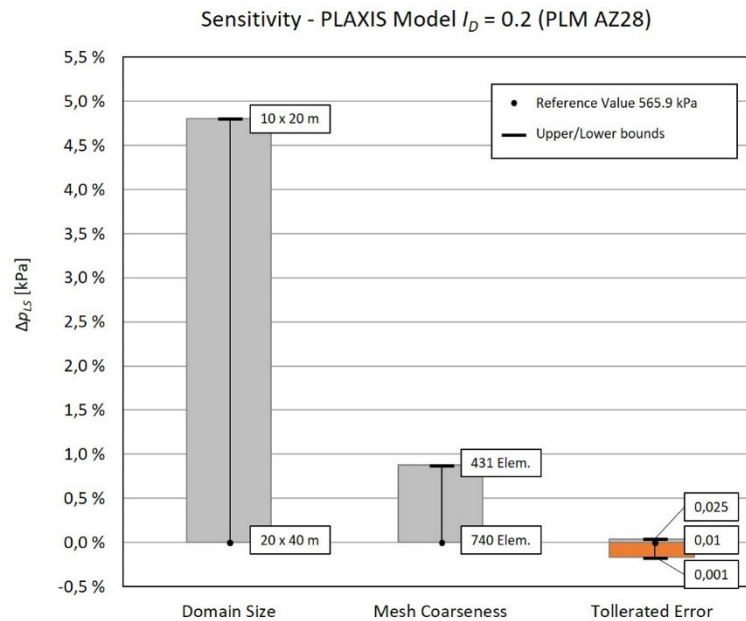


Fig. 121: Sensitivity diagram Δp_{LS} -range – PLAXIS $I_D = 0.2$ (PLM AZ28)

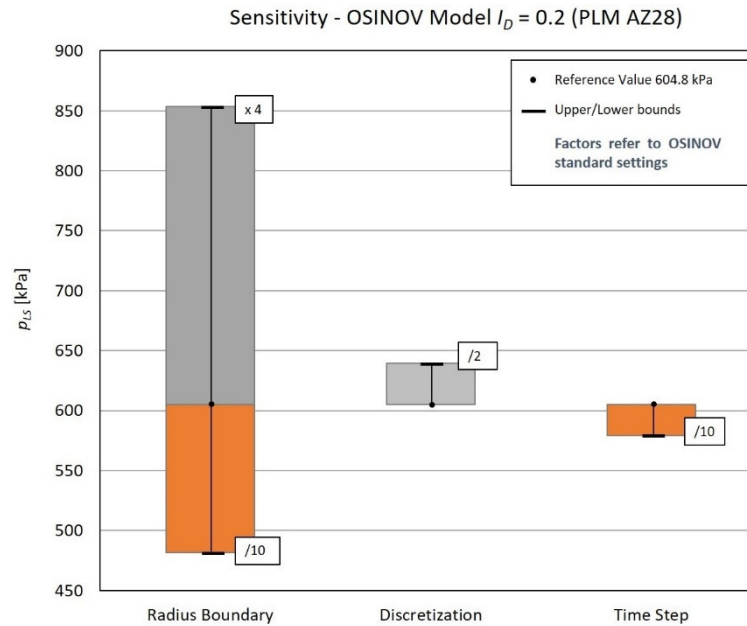


Fig. 122: Sensitivity diagram p_{LS} -range – OSINOV $I_D = 0.2$ (PLM AZ28)

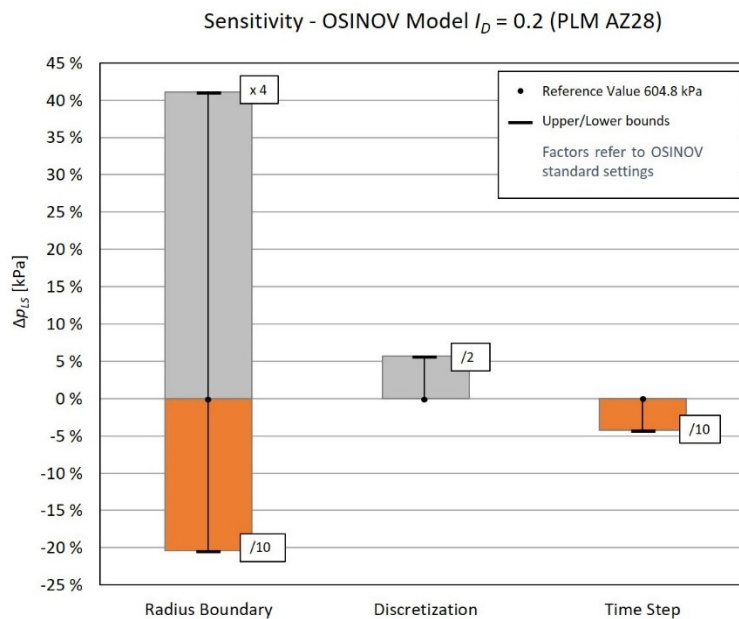


Fig. 123: Sensitivity diagram Δp_{LS} -range – OSINOV $I_D = 0.2$ (PLM AZ28)

Within the conducted sensitivity study, it could be shown that the PLAXIS model, in contrast to the OSINOV model, is in fact not sensitive to any changes of the considered model properties. However, it must be noted that the made changes to the calculation parameters within the OSINOV sensitivity study were probably out of any conventional ranges, for which the OSINOV code originally may not have been designed.

It is true that the PLAXIS model might be more user friendly than the OSINOV Code as the latter one is much more sensitive on mistakenly wrong inputs. But in case the suggested material properties and calculation parameters are used, both models seem to perform quite well with only minor differences in the received limit pressures.

6.7 Calculation of the q_c -Curves over Depth

The final equation for the calculation of the cone penetration resistances q_c as a function of the depth z is given as follows.

$$q_c = \left(1.5 + \frac{5.8 \cdot I_D^2}{I_D^2 + 0.11} \right) \cdot \left(a_1 + \frac{a_2}{a_3 + I_D} \right) \cdot p'(z)^{\left(b_1 + \frac{b_2}{b_3 + I_D} \right)} \quad (6.17)$$

where the first term in brackets is representative for the shape factor k_q .

Once the KIM-parameters for a certain material are known and a target value for I_D is chosen, the calculation of q_c over depths z requires the determination of the respective effective mean pressures $p'(z)$ which can be received from the effective vertical stresses $\sigma_v'(z)$ and the coefficient of lateral earth pressure K_0 .

$$p'(z) = \frac{1}{3} \cdot \sigma_v'(z) \cdot (1 + 2 \cdot K_0) \quad (6.18)$$

In case the in-situ value for K_0 is unknown the standard equation acc. to Jaky can be applied for granular materials, i.e. sands.

$$K_0 = 1 - \sin \varphi_c \quad (6.19)$$

Due to the fact that the mean effective stresses over depth are increasing the calculated void ratio at the target relative density e_{target} is continuously decreasing. The void ratio e_{target} can be calculated from the pressure-dependent limit void ratios e_c and e_d .

$$I_D = \frac{e_c - e_{target}}{e_c - e_d} \rightarrow e_{target}(z) = e_c - I_D \cdot (e_c - e_{min}) \quad (6.20)$$

where the pressure-dependent limit void ratios can be calculated from $p'(z)$ and the compression law acc. to Bauer [32].

Decreasing void ratios lead to an increase of the dry density ρ_d . The grain density ρ_s and the determined value for e_{target} go into the equation below

$$\rho_d(z) = \frac{\rho_s}{1 + e_{target}} \quad (6.21)$$

Together with an assumed moisture content w and the gravitational acceleration g , the bulk unit weight γ_{target} at the target relative density can be determined from

$$\gamma_{target}(z) = (1 + w) \cdot \rho_d(z) \cdot g \quad (6.22)$$

Finally, the bulk unit weight γ_{target} can be used for the calculation of the vertical effective stress $\sigma_v'(z)$ which goes into the equation for $p'(z)$.

$$\sigma_v'(z) = \int_0^z \gamma_{target}(z) \cdot dz \quad (6.23)$$

In case the desired depth is below the ground water table it is necessary to determine the buoyant unit weight γ' . For this task it is required to come up with the saturated density ρ_{sat} of the soil below the groundwater table in a first step.

$$\rho_{sat}(z) = \frac{\rho_s + (e_{target} \cdot \rho_w)}{1 + e_{target}} \quad (6.24)$$

The buoyant unit weight γ' can further be obtained from

$$\gamma'(z) = \rho_{sat}(z) \cdot g - \gamma_w \quad (6.25)$$

For a depth of the groundwater table of $z = z_{GW}$ the final equation for $\sigma_v'(z)$ with $z > z_{GW}$ is given by

$$\sigma_v'(z) = \int_0^{z_{GW}} \gamma_{target}(z) \cdot dz + \int_{z_{GW}}^z \gamma'(z) \cdot dz \quad (6.26)$$

For the given task of calculating q_c over the depth z a MATLAB code was written which allows for the calculation of the q_c -curves for a hypoplastic material at 3 different relative densities I_D . It requires the hypoplastic material parameters, the KIM-parameters, the 3 desired values for the relative density, the depth of the ground water table z_{GW} and the desired water content w as an input. The code can be found within Appendix E in A. Fig 36.

The following figure shows the received q_c -curves over depth z for material PLM AZ28 from the KELLER-database (A. Tab. 5) for different curve fitting approaches (Excel, GnuPlot) and calculation approaches (PLAXIS, OSINOV, report) with a ground water table lying 2 m below the ground surface. The results are plotted for a target relative density of $I_D = 0.9$ and an assumed water content of $w = 20\%$. As was already discussed within the previous chapter, the PLAXIS KIM-parameters are producing results which are slightly below the results received from the OSINOS KIM-parameters and the parameters from the report [41]. The used KIM-parameters can be found in chapter 5.2.3 and 6.6.4.

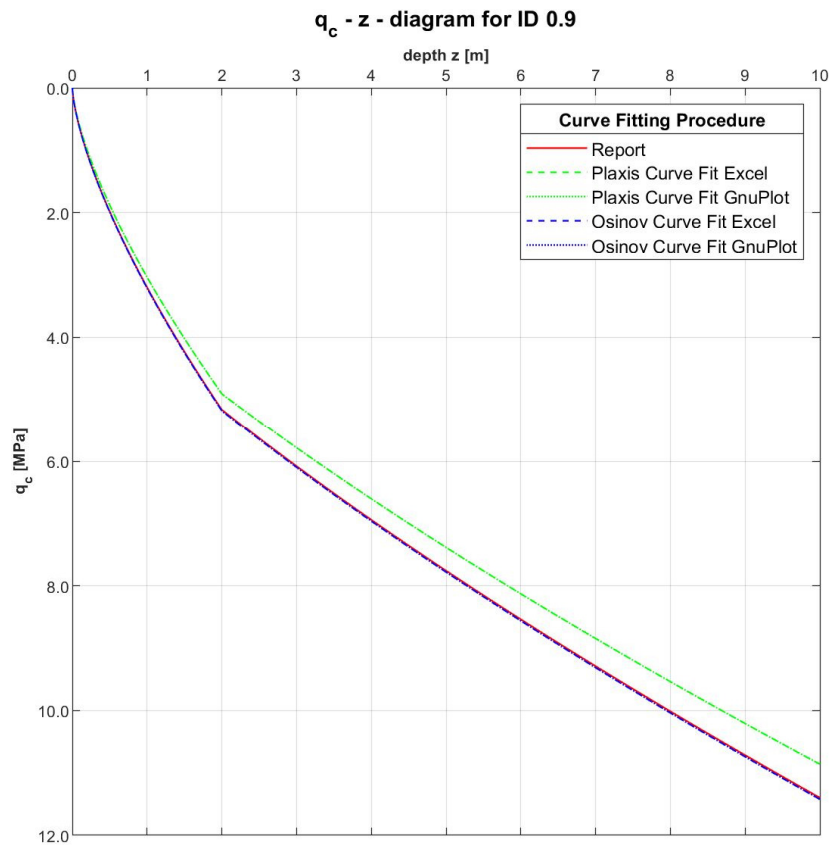


Fig. 124: q_c vs z for $I_D = 0.9$ and GW 2 m below ground surface (PLM AZ28)

More diagrams for the materials PLM AZ28 and PLM BZ36 and different relative densities for an assumed moisture content of $w = 20\%$ can be found within Appendix E.

7 Studies on the Hypoplastic Parameter Calibration

One of the most crucial influencing factors in connection with the determination of the limit pressures from spherical cavity expansion simulations within the KIM is the calibration of the hypoplastic parameters of the materials found on site. Without a proper calibration it is not possible to account for the materials' true mechanical behaviour and sufficient values for the limit pressures p_{LS} will never be reached even when sophisticated material models are applied.

In connection with the KIM-analysis the hypoplastic parameter calibration is generally carried out based on matching the measurement curves from oedometric compression tests and triaxial compression tests with the results from lab test simulations performed with the hypoplastic constitutive law. In case of sands containing a high amount of breakable grains the oedometer tests are usually carried out under very high pressures of up to 25 MPa to ensure that extensive crushing of these grains will occur during the tests. This grain crushing, which is also frequently encountered in cone penetration testing in such materials, can then be indirectly incorporated within the material calibration and further on within the simulations of the cavity expansion.

Chapter 7 introduces the recently launched online tool ExCalibre ("soilmodel.com) to the readers which can be used for the automatic calibration of hypoplastic constitutive models. Issues with the usage of ExCalibre will be pointed out and two calibration trials on material PLM AZ28 and PLM BC36 from the KELLER-database will be presented. Further it will be shown, on the example of two materials from the "soilmodel.com"-database, how changing single hypoplastic parameters effects the results of the lab test simulation performed with the PLAXIS SoilTest tool. Finally, the suggested calibration procedure by Meier [6] for the hypoplastic sand model acc.to "von Wolffersdorff" [23] will be explained and the results from the try to recalculated each single calibration step that Meier went through on calcareous Dubai sand (A. Tab. 2) will be presented.

7.1 ExCalibre – Automatic Calibration Tool

ExCalibre is an online tool which can be found on the website "soilmodel.com" and enables users to automatically calibrate advanced soil constitutive models such as the hypoplastic sand model by "von Wolffersdorff" [23]. It adopts a model-specific calibration algorithm to come up with a reliable set of parameters to be used in geotechnical simulations. After the calibration, the user can manually change different parameters for fine tuning or to investigate the effect of individual parameters on the lab test simulations. The whole input for the calibration can simply be collected within an Excel spreadsheet (template is also provided on "soilmodels.com") which can subsequently be uploaded to the website for the evaluation of the hypoplastic parameters.

In addition to the automatic calibration, ExCalibre also acts as an element test driver simulating standard laboratory tests.

7.1.1 Input – Excel Template

The Excel input-file contains several tab-sheets for the collection of data connected to the considered material for which the calibration wants to be done.

The first tab-sheet called “NOTES” requires the input of some general information regarding the soil type of the material, the locality and the sampling method. The information provided within this tab-sheet is not used for the evaluation of the hypoplastic parameters and the input fields can be therefore be left blank.

Within the second tab-sheet “IDX AND GRAD” the specific gravity, the angle of repose and the sieve-passings in % can be provided. On the basis of this input the grading-curves are generated.

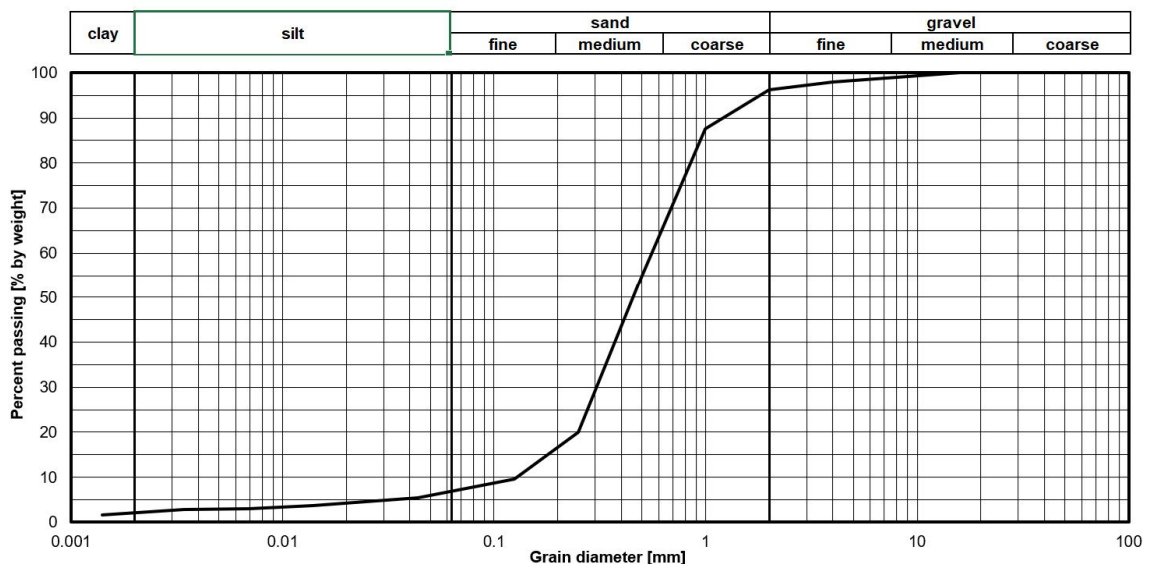


Fig. 125: ExCalibre input – grading curve

The third tab-sheet “OED-REC-1” is connected to the input of the lab data received from oedometric compression tests. As suggested by Meier [6] the data from a test performed on a loose sample should be entered in this sheet. Besides the initial void ratio, the vertical pressures σ_{ax} and the corresponding strains ε_{ax} from the lab test should be provided. A diagram containing the compression curve will be generated which can be seen in Fig. 126.

As was concluded from subsequent calibration trials the results for the hypoplastic parameters, especially the granulate hardness h_s and the exponent n , will be affected by the sampling rate. It is therefore suggested to provide the lab data at a sufficient resolution.

The users have the opportunity not only to account for the testing data of one oedometer test but can add the data from more compression tests by adding further tab-sheets using the same name convention, i.e. “OED-REC-2”. Adding the data of an oedometer test performed on a dense sample can yield more representative values for the exponent β [6].

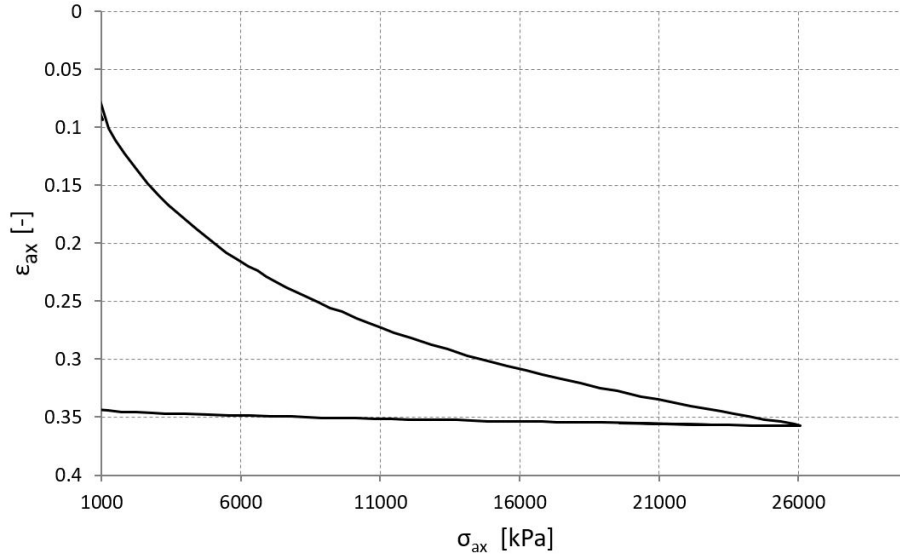


Fig. 126: ExCalibre input – oedometric compression curve

Finally, tab-sheet 4 “CID-REC-1” is used for the provision of the triaxial testing data, in terms of the initial void ratio, the vertical strains ε_{ax} and the corresponding values for the cell pressures, the deviatoric stresses $q = \sigma_1 - \sigma_3$ and the volumetric strains ε_v . It must be noted that dilatancy is defined negative in ExCalibre. Just like with the data from the oedometric test, users can account for several triaxial tests by adding further tabs following the name convention. Fig. 127 shows the generated curves from the triaxial test tab-sheet.

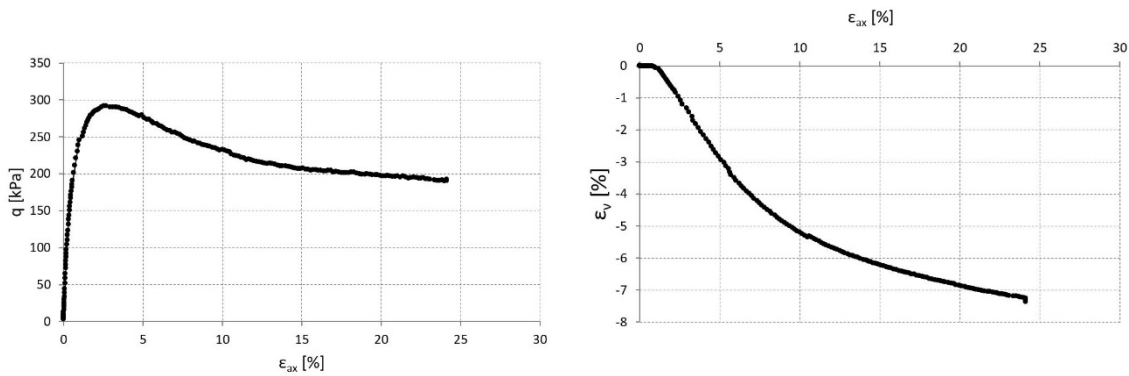


Fig. 127: ExCalibre input – triaxial testing curves

As can be seen within the ε_{ax} - ε_v -diagram in Fig. 127 the depicted volumetric strains are negative. Acc. to the definition of dilatancy being negative within ExCalibre this implies that the sample experiences an increase in volume.

7.1.2 Calibration - Material PLM AZ28

The hypoplastic parameters for material PLM AZ28 from the KELLER-database (A. Tab. 5) had already been determined by a lab in Dresden (lab report [41]) before the calibration with ExCalibre was performed. Tab. 26 list this parameters for material PLM AZ28 from the lab.

Tab. 26: Hypoplastic parameters from report – PLM AZ28

Material	φ_c [°]	hs [kPa]	n [-]	e_{d0} [-]	e_{c0} [-]	e_{i0} [-]	α	β
PLM AZ28	36.3	39000	0.525	0.74	1.261	1.450	0.050	1.97

The KELLER Grundbau GmbH thankfully provided the measurement data from the performed lab tests on PLM AZ28 which were further used for the parameter calibration with ExCalibre. The main aim of this study was to find out if ExCalibre is able to come up with a set of parameters somehow close to the already determined values from Tab. 26. It has to be noted, that only the lab data from the oedometric compression test performed on a loose sample and the triaxial test data from two tests performed on dense samples were provided and therefore available for the calibration. However, it was believed that the usable amount of data is sufficient. Nevertheless, adding the information of an oedometer test performed on a dense sample might have been advantageous for yielding a better representation of the stiffness of the material in a very dense state in terms of a more accurate value for the calibrated exponent β . The following figures illustrate the provided diagrams from the performed tests.

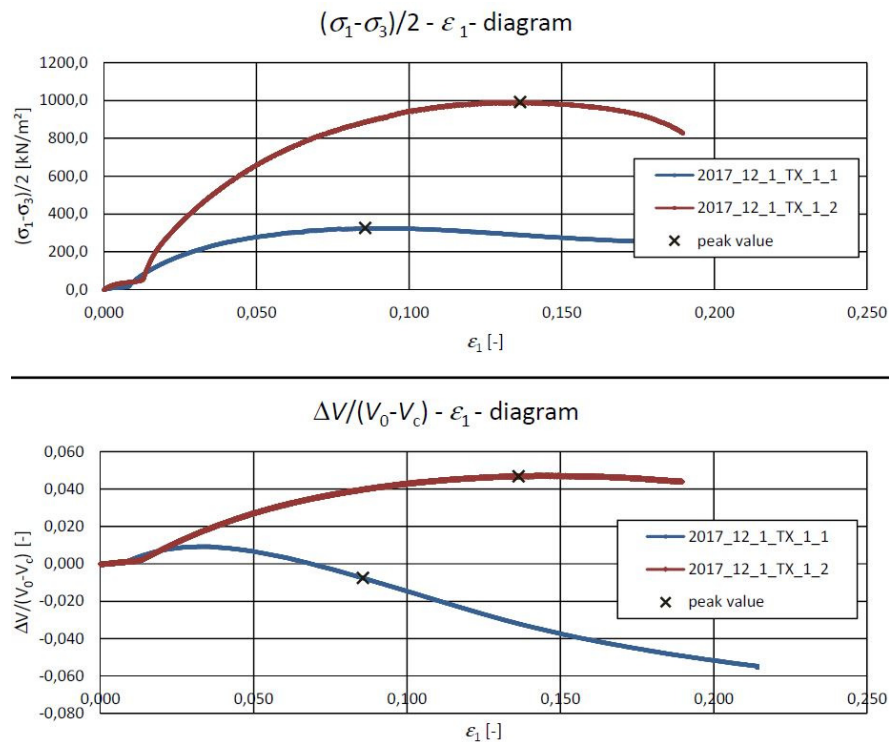


Fig. 128: Curves from 2 triaxial tests on dense samples – PLM AZ28 (provided by KELLER-Grundbau GmbH)

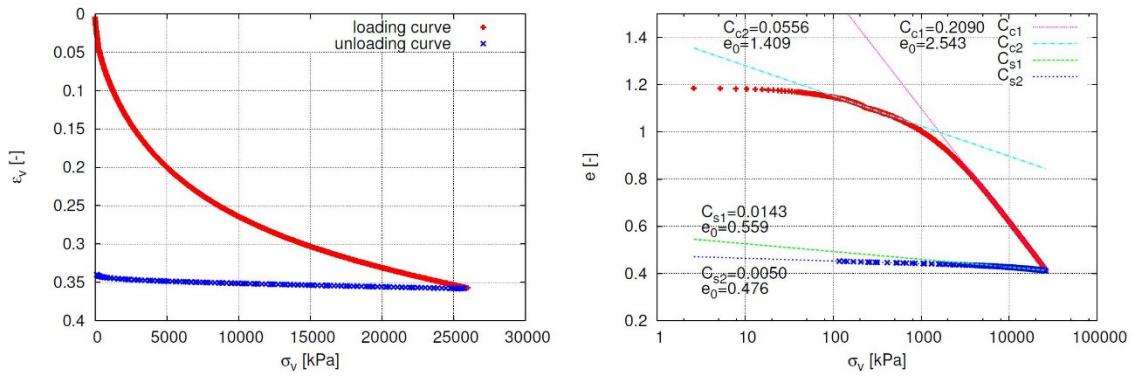


Fig. 129: Curves from oedometer test on loose sample – PLM AZ28 (provided by KELLER-Grundbau GmbH)

The triaxial tests were performed at cell pressures of 100 and 600 kPa. As stated within the final report for project Port de la Mer a dilatant behaviour within the triaxial tests was only observed for tests conducted at cell pressures of 100 kPa as for higher pressure levels the grains started to crush and dilatancy was not able to evolve. Outside ExCalibre negative volumetric strains would indicate contraction and not dilation. Both statements combined do not agree with the lines given in the $\varepsilon_v - \varepsilon_l$ - diagram in Fig. 128, i.e. the blue line would be representative for a decrease in volume and therefore contraction. It is believed that these diagrams originate from a kind of pre-report and hence, the signs were changed within the final report, as all diagrams within the final report [41] are correctly depicted. It has to be mentioned that the deviatoric stresses within Fig. 128 are given with $q = (\sigma_1 - \sigma_3)/2$ and ExCalibre assumes $q = \sigma_1 - \sigma_3$.

No matter of this, the data from the triaxial test at 100 kPa cell pressure was considered with a dilatant behaviour (negative) in ExCalibre and the data from 600 kPa cell pressure with a contractive behaviour (positive). The oedometric test data was adopted as shown in Fig. 129. The resulting hypoplastic parameters from the calibration in ExCalibre can be found within Tab. 27.

Tab. 27: Hypoplastic parameters from ExCalibre – PLM AZ28

Material	φ_c [°]	hs [kPa]	n [-]	e_{d0} [-]	e_{c0} [-]	e_{i0} [-]	α	β
PLM AZ28	35.4	34335	0.466	0.606	1.211	1.453	0.36	2.1

After the calibration was finished a few things could be observed. The critical friction angle was not taken as provided within the input-file as the angle of repose but it was somehow calculated from the triaxial testing curves.

It is not possible to use the limit void ratios determined from the standard lab tests as an input for the Excel template. Hence, ExCalibre has to come up with these three hypoplastic parameters on its own, which may be different from the values determined from the index tests.

The values for the granulate hardness h_s and the exponent n were not too far away from the parameters of the report and the values are considered to be within the acceptable range which will also always be present when manual calibration is done by different researchers.

The exponent β from the report was very well reproduced by ExCalibre but the determined value for the exponent α was found to yield the biggest disagreement of all parameters. With 0.36 it was more than 7 times higher than the values received from the lab. However, the simulated curves from the triaxial test performed at the cell pressure of 100 kPa showed that the higher value for α is able to result in a much better reproduction of the q - ϵ_{ax} -curve, whereas the smaller value from the report yielded a better reproduction of the volumetric behaviour.

It was made use of the recalibration option which allows to have the recalibrated curves plotted next to the curves received from the hypoplastic parameters obtained from the calibration with ExCalibre. The hypoplastic parameters from the report were taken for the recalibration. The following figures depict the resulting curves from the simulations with the ExCalibre-parameters (green) and the parameters of the recalibration (red) together with the black curves showing the measurement. The oedometric compression test simulation was not able to be performed with the recalibrated parameters as ExCalibre seems to have issues with certain kinds of parameter combinations. The exact reason, however, is not known up to this point.

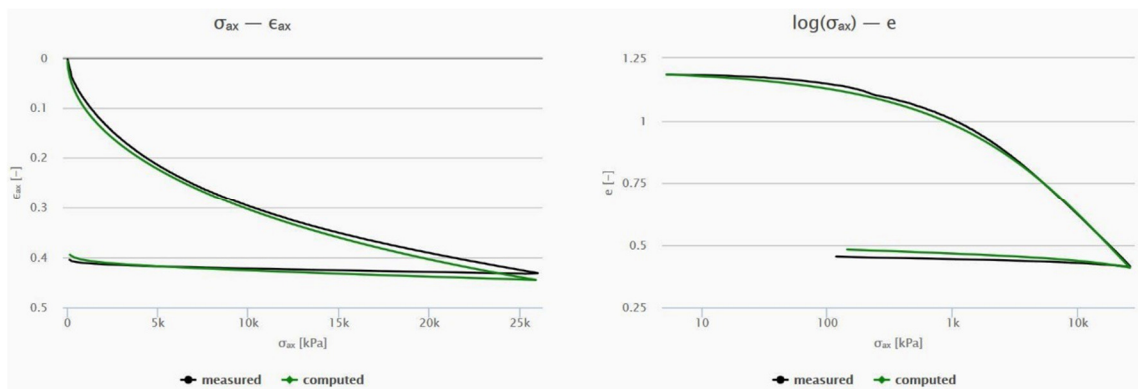


Fig. 130: Simulated and measured compression curves from ExCalibre output (PLM AZ28)

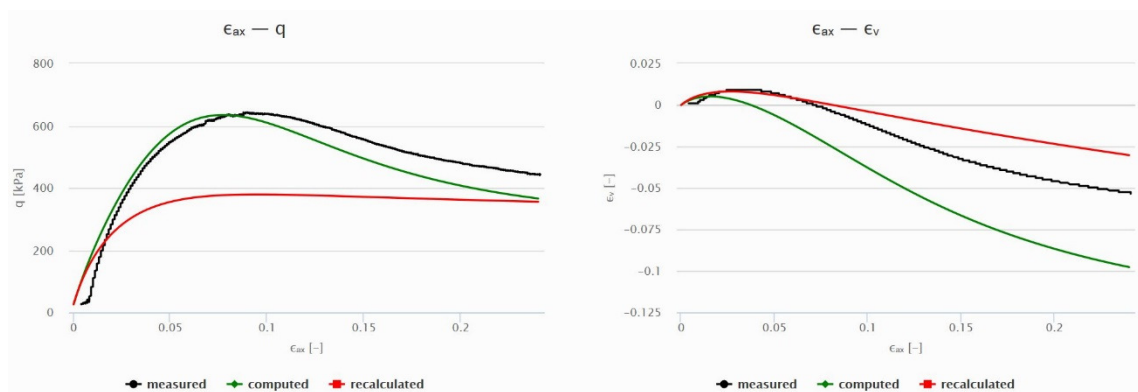


Fig. 131: Simulated and measured triaxial curves (100 kPa cell pressure) from ExCalibre output (PLM AZ28)

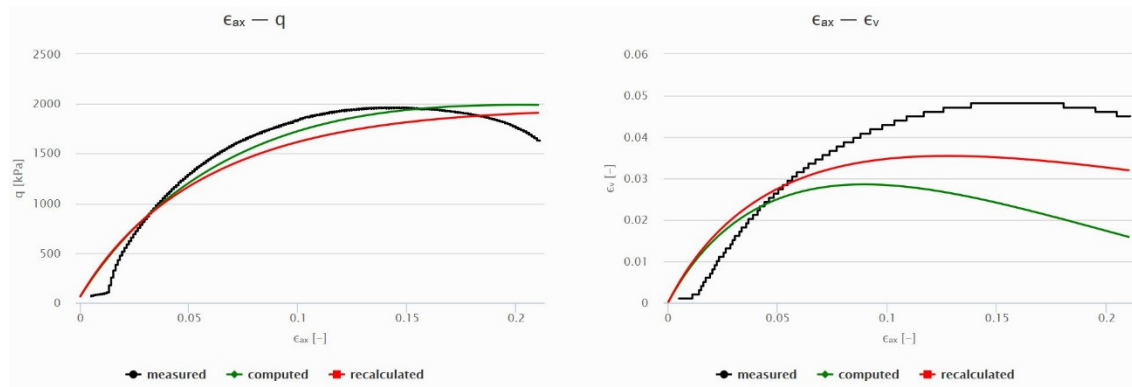


Fig. 132: Simulated and measured triaxial curves (600 kPa cell pressure) from ExCalibre output (PLM AZ28)

While the measurement data of the oedometer test could be well approached by the simulations using the ExCalibre-parameters, difficulties with the parameter calibration were encountered within the simulation of the triaxial testing curves. In case of both triaxial tests, the q - ε_{ax} -relationship was better reproduced by ExCalibre, whereas the recalibrated parameters yielded a better reproduction of the volumetric strains. It is now a matter of the desired application of the calibrated hypoplastic model if rather the stresses or the volumetric strains should be correctly described.

To make a statement on how the two different parameter sets perform on the specific application of the simulation of the spherical cavity expansion the limit pressures for $p_0 = 100$ kPa and $I_D = 0.5$ for both parameter sets were determined with the aid of the final PLAXIS model presented in chapter 6.3.6. Fig. 133 depicts the expansion curves from the PLAXIS Curves manager received for both sets of parameters.

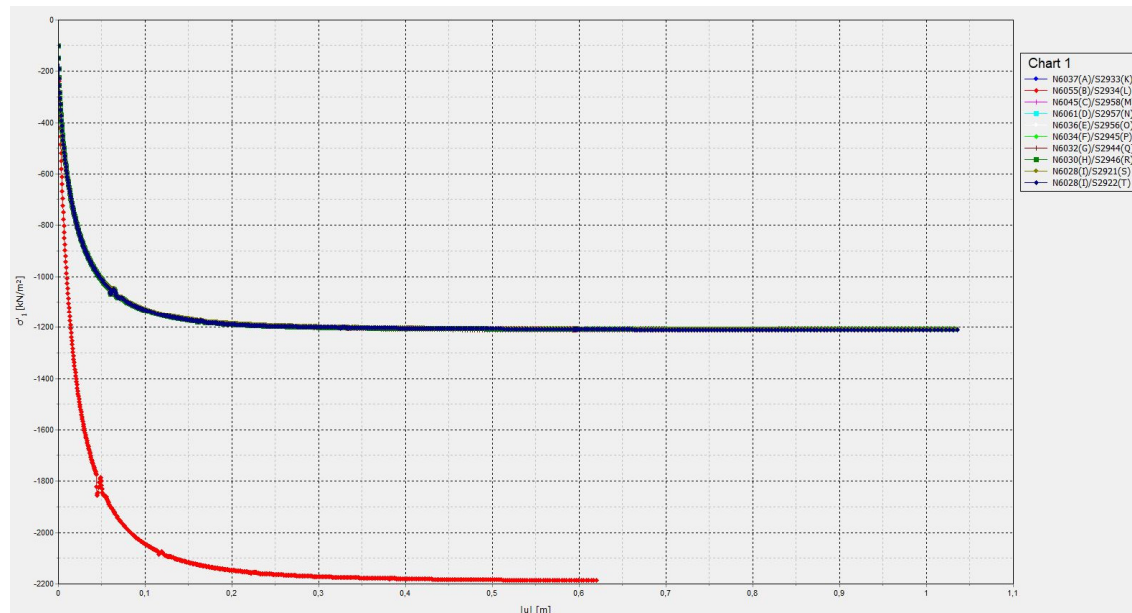


Fig. 133: Pressure-expansion-curves PLM AZ28 for $p_0 = 100$ kPa and $I_D = 0.5$ – ExCalibre parameters (red curve) and report parameters (blue curve)

The differences in the received maximum stresses from the curves calculated with the different parameter sets were huge and the resulting limit pressure from the ExCalibre-

parameters ended up being almost 2-times higher than from the hypoplastic parameters of the report. It was assumed that this was a result of the very different value for the exponent α . This parameter governs the dilatancy behaviour which is crucial for the results of the cavity expansion. To prove this assumption another calculation of the pressure-expansion-curve was conducted but now taking into account the α -value from the report in combination with the other parameters from ExCalibre.

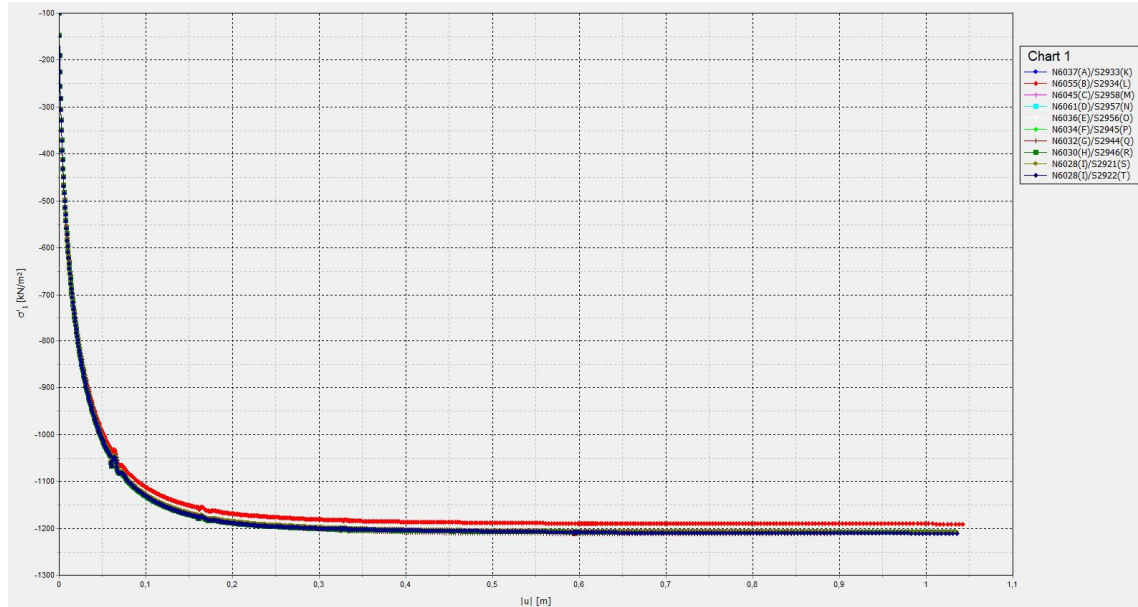


Fig. 134: Pressure-expansion-curves PLM AZ28 for $p_0 = 100$ kPa and $I_D = 0.5$ – ExCalibre parameters+ α -report (red curve) and report parameters (blue curve)

The received curves were now almost identical showing that the exponent α has a main influence on the resulting limit pressures p_{LS} .

7.1.3 Calibration - Material PLM BC36

In the same manner as with material PLM AZ28 the calibration was performed on material PLM BC36 with the aid of ExCalibre. The hypoplastic parameters from the report [41] are listed in Tab. 28.

Tab. 28: Hypoplastic parameters from report – PLM BC36

Material	φ_c [°]	hs [kPa]	n [-]	e_{d0} [-]	e_{c0} [-]	e_{i0} [-]	α	β
PLM BC36	36.5	49000	0.48	0.79	1.384	1.592	0.045	1.40

Only the measurement results from an oedometer test performed on a loose sample were used for the calibration of PLM BC36. Additionally, the results of four triaxial tests performed on loose and dense samples with cell pressures of 100 and 600 kPa were taken into account for the input. The measurement results for the triaxial tests were taken directly from the depicted diagrams within the report [41]. The following figures show the diagrams received from the lab tests which correspond to the used input data.

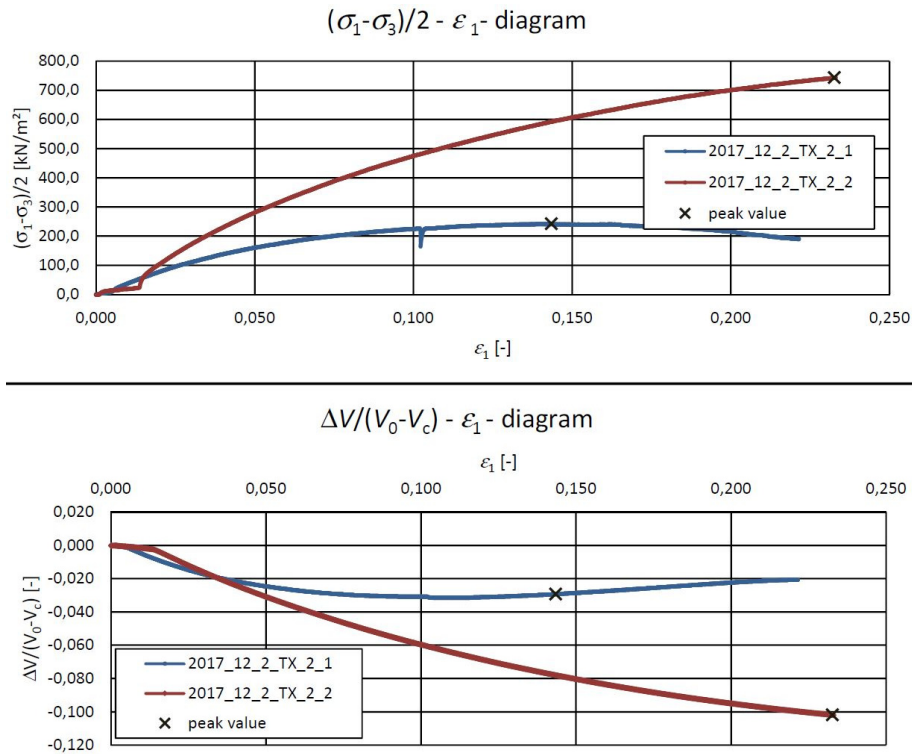


Fig. 135: Curves from 2 triaxial tests on loose samples – PLM BC36 [41]

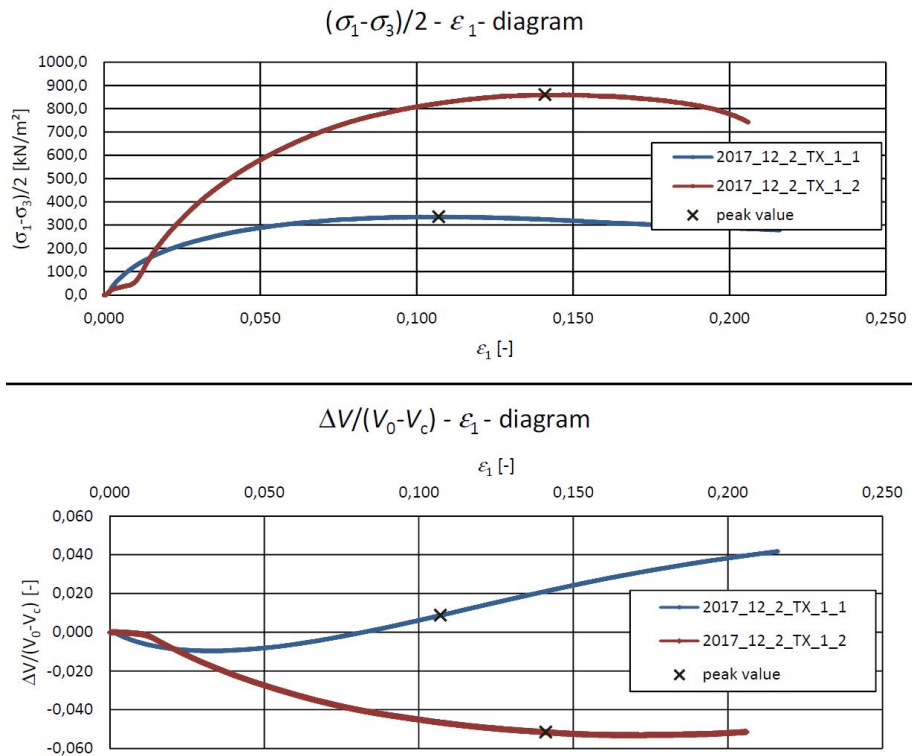


Fig. 136: Curves from 2 triaxial tests on dense samples – PLM BC36 [41]

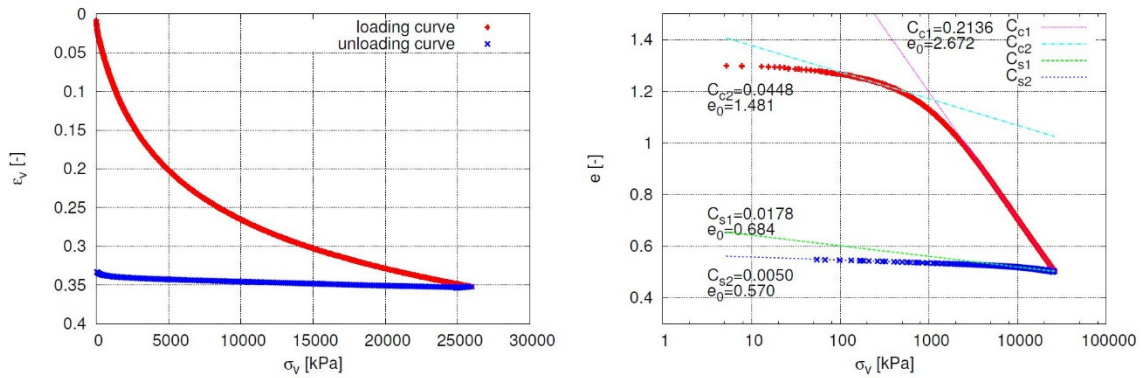


Fig. 137: Curves from oedometer test on loose sample – PLM BC36 (provided by KELLER-Grundbau GmbH)

As can be seen from the diagrams of the triaxial tests dilatant behaviour is only encountered for the test performed on the dense sample with a cell pressure of 100 kPa. All other triaxial test are showing a well distinct contraction. As the diagrams were taken directly from the report the volumetric strains were depicted with the correct sign unlike in the diagrams from the triaxial tests of material PLM AZ28. The results for the hypoplastic parameters from the calibration in ExCalibre are presented in Tab. 29.

Tab. 29: Hypoplastic parameters from ExCalibre – PLM BC36

Material	φ_c [°]	h_s [kPa]	n [-]	e_{d0} [-]	e_{c0} [-]	e_{i0} [-]	α	β
PLM BC36	34.2	35689	0.423	0.667	1.333	1.600	0.16	2.6

The results from ExCalibre were not as good as for Material PLM AZ28 in comparison to the parameters given in the report.

The critical friction angle φ_c was about 2° below the report value which is based on the results from the angle of repose test. Due to the fact that ExCalibre determines the friction angle directly from the measurement results it is believed that this value is more representative for the considered material.

The granulate hardness h_s was received with 35689 kPa which is about 12000 kPa below the value from the report. However, the exponent n was calibrated in good agreement.

Also, the obtained limit void ratios approached the values received from the standard lab tests quite well although the lower bound limit void ratio e_{d0} showed a slight difference.

The exponent α again caused the greatest disagreement being more than 4-times off the value from the report. This time also the exponent β was received with a value about 2-times higher than given in Tab. 28.

The following figures illustrate the received curves from ExCalibre where the black curve depicts the measurement, the green curve the simulations with the ExCalibre-parameters and the red curve the recalibration using the parameters from the report. Again, ExCalibre was not able to come up with the recalibrated curve for the oedometer test and additionally the triaxial test performed on the dense sample with a cell pressure of 100 kPa.

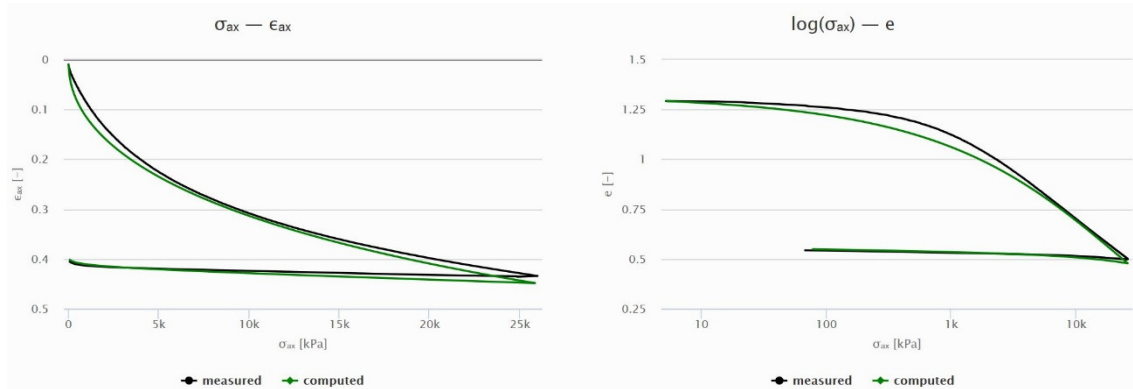


Fig. 138: Simulated and measured compression curves from ExCalibre output (PLM BC36)

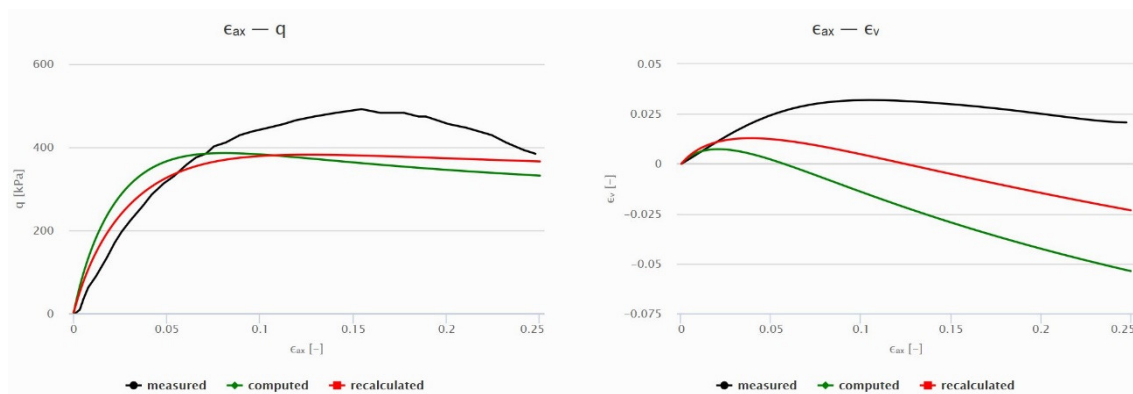


Fig. 139: Simulated and measured triaxial curves (100 kPa cell pressure-loose) from ExCalibre output (PLM BC36)

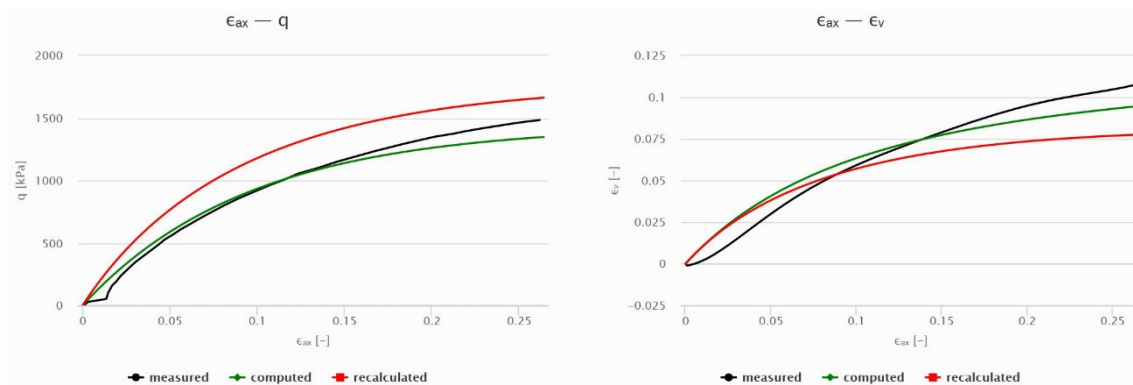


Fig. 140: Simulated and measured triaxial curves (600 kPa cell pressure-loose) from ExCalibre output (PLM BC36)

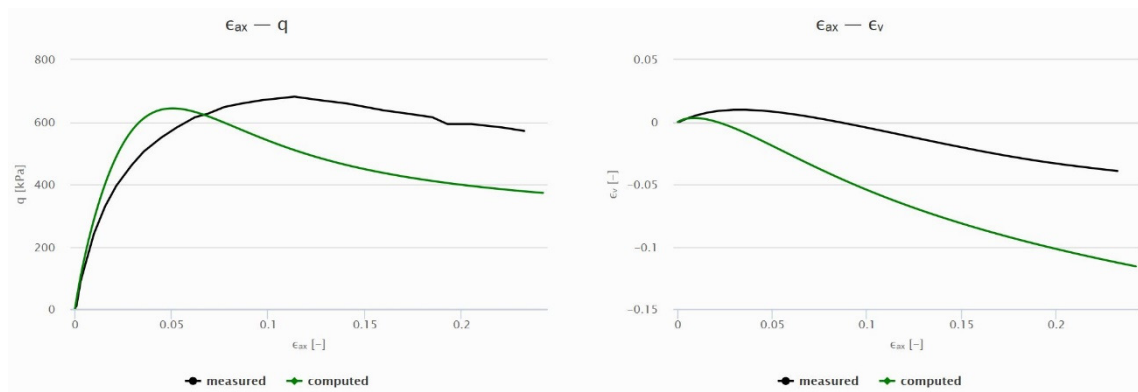


Fig. 141: Simulated and measured triaxial curves (100 kPa cell pressure-dense) from ExCalibre output (PLM BC36)

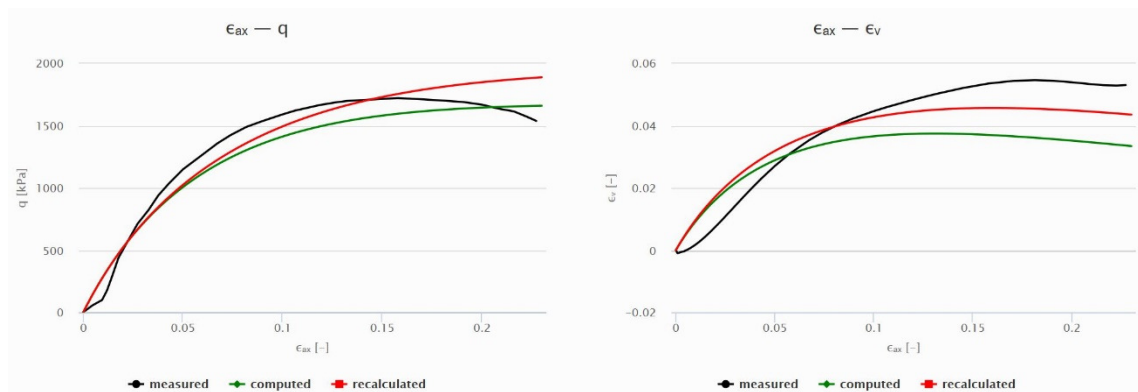


Fig. 142: Simulated and measured triaxial curves (600 kPa cell pressure-dense) from ExCalibre output (PLM BC36)

No clear tendency could be recognized regarding the suitability of one parameter set to better describe the measurements than the other as both sets were not able to reproduce the measurements in all cases.

The calculations of the limit pressures p_{LS} in PLAXIS with both different parameter sets for $p_0 = 100$ kPa and $I_D = 0.5$ were also performed for material PLM BC36. Fig. 143 shows the resulting pressure-expansion-curves received from both parameter sets. (red curve – ExCalibre, blue curve – report parameters).

As has already been encountered for material PLM AZ28, the pressure-expansion-curve received from the ExCalibre parameter set shows maximum stresses which are almost 500 kPa higher than for the parameters of the report. In the next calculation step it was tried to lower the value for the exponent α within the ExCalibre parameter set to the value given in Tab. 28. Afterwards the comparison of the pressure-expansion-curves was done again in Fig. 144.

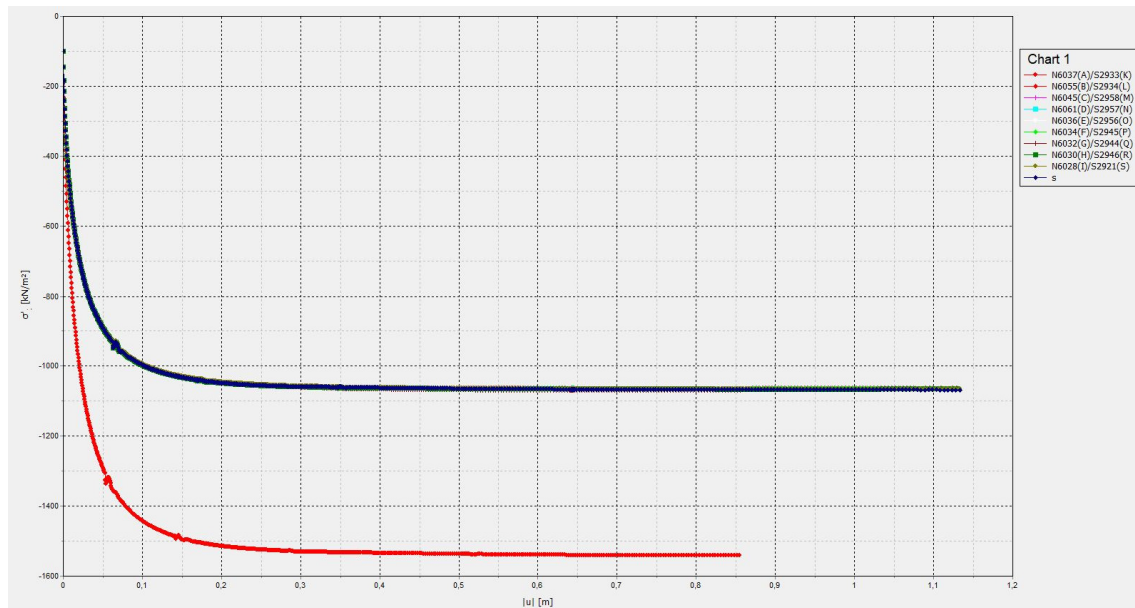


Fig. 143: Pressure-expansion-curves PLM BC36 for $p_0 = 100$ kPa and $I_D = 0.5$ – ExCalibre parameters (red curve) and report parameters (blue curve)

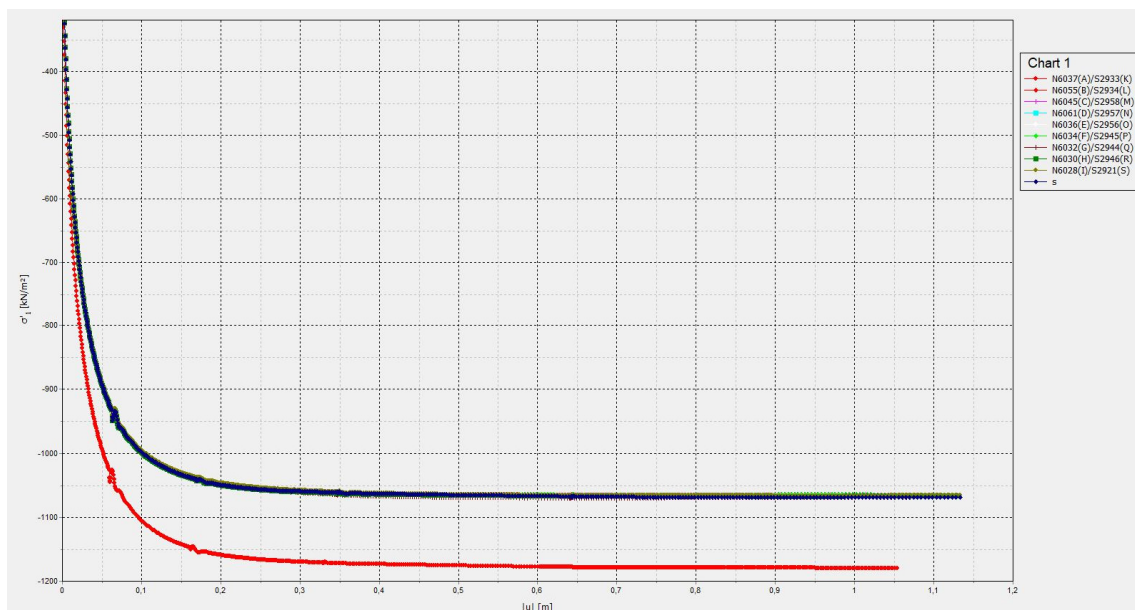


Fig. 144: Pressure-expansion-curves PLM BC36 for $p_0 = 100$ kPa and $I_D = 0.5$ – ExCalibre parameters+ α report (red curve) and report parameters (blue curve)

Changing α within the ExCalibre parameter set resulted in a better agreement of both curves, but still the ExCalibre parameters yielded higher limit pressures than the values of the report, proving that it is not sufficient to only change one parameter to come up with the same results as received from the report parameters.

Concluding from the findings obtained so far it necessary to conduct further studies to get a better understanding of the principles of the implemented algorithm and to find out if ExCalibre is really able to provide parameters which can be successfully applied in geotechnical practice.

7.2 The Influence of single Parameters on Lab-Test Simulations

The next step towards a better understanding of the parameter calibration procedure was to depict the influence of single hypoplastic parameters on the lab-test simulation results. Two materials from the database found on the website “soilmodels.com” were used for the studies. Besides the hypoplastic parameters, the curves from one oedometer test and two triaxial tests performed on the materials with cell pressures of 50 and 200 kPa were taken as a reference. The hypoplastic parameters of both materials, which could also be exactly recalculated with ExCalibre, are shown in Tab. 30.

Tab. 30: Hypoplastic parameters from materials of the „soilmodel.com“-database

Material	φ_c [°]	h_s [kPa]	n [-]	e_{d0} [-]	e_{c0} [-]	e_{i0} [-]	α	β
Dobrany sand	36.5	49846	0.243	0.572	1.144	1.372	0.09	4.5
Rohatec sand	34.3	61377	0.462	0.379	0.757	0.909	0.11	3.3

The simulations within this study were performed using the PLAXIS SoilTest tool. For each simulation one parameter of one material was modified and the resulting curves were collected in diagrams and compared to each other.

7.2.1 PLAXIS SoilTest Tool – General Information

At first hand it was not possible to come up with reasonable results for the oedometer test as indeed strains were induced but the stresses were not updated during the test and therefore remained at 0 kPa. From correspondence with Dr. David Mašín, an associate professor at Charles University in Prague and the administrator of the website “soilmodels.com”, it was concluded that the issues are related to the used step size which was too large.

It took a few tries to solve the problem and it was found that the very first stress increment of the oedometric compression test must be chosen with -1 kPa and 10,000 steps. All other load increments can be chosen as desired.

The value for the initial void ratio e_0 for both, the triaxial and the oedometer test simulations has to be provided at zero mean effective pressure within the PLAXIS.

7.2.2 Dobrany Sand

The most extensive study regarding the influence of single hypoplastic parameters was performed on Dobrany sand. The influence of five different constitutive model parameters was investigated, namely the influence of φ_c , h_s , n , α and β . The limit void ratios within all simulations remained the same as they are usually a result of standard lab

tests, and hence don't need to be calibrated. For each simulation one out of the chosen five parameters was adjusted while keeping the other values the same as for the basic material (Tab. 30). Each parameter was adjusted 3-times which makes a total of 15 simulations performed for each of the two triaxial tests and the oedometer test. Tab. 31 lists the basic values and the three modification values of the five considered parameters.

Tab. 31: Investigated values of 5 different hypoplastic parameters – Dobrany sand

	Basic Value	Value 1	Value 2	Value3
φ_c	36.5°	24°	28°	32°
h_s	49846 kPa	20000 kPa	35000 kPa	75000 kPa
n	0.243	0.1	0.2	0.35
α	0.09	0.05	0.2	0.3
β	4.5	1.5	3.0	6.0

The initial void ratios for the tests were taken as calculated with ExCalibre (Excel template of Dobrany sand was uploaded) and converted to zero pressure as required in PLAXIS, using Bauer's compression law [32]. Due to a lack of information on the isotropic pressure level for which the initial void ratio of the oedometer test was provided in ExCalibre it was just assumed to be the void ratio at zero pressure which was further used as e_0 for the simulations in PLAXIS. The uncertainty within the initial void ratio e_0 is the reason why the compression curve calculated with the hypoplastic parameters for Dobrany sand in Tab. 30 is not as close to the measured curve as should be. However, the goal of this study was to depict the influence of certain hypoplastic parameters and not to exactly reproduce the calibration results from ExCalibre.

Tab. 32: Initial void ratios used in PLAXIS – Dobrany sand

	Oedometer Test	Triax 50 kPa	Triax 200 kPa
e_0	0.996	0.651	0.882

The following diagrams (Fig. 145-Fig. 159) depict the simulated testing-curves from this study and the influence of changing single parameters. Each diagram contains 5 curves from which one curve refers to the measurement, one curve was calculated with the hypoplastic parameters of Dobrany sand from Tab. 30 and the three remaining curves were simulated with value 1, value 2 and value 3 of a certain parameter taken from Tab. 31.

It has to be noted that the same sign convention for the volumetric strains was used as defined in ExCalibre with dilatancy being negative.

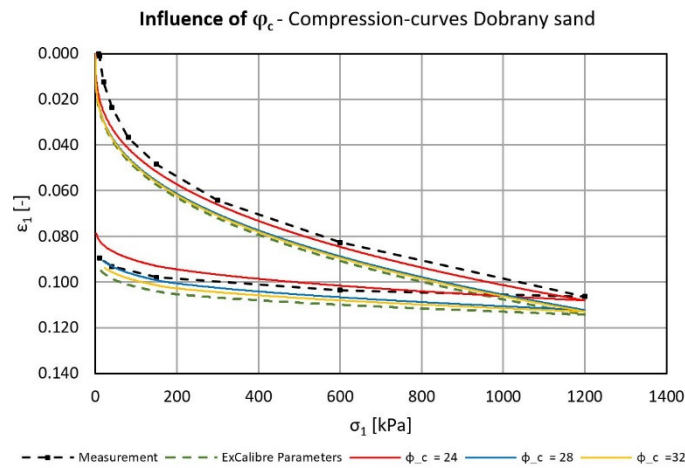


Fig. 145: Influence of φ_c on compression curve – Dobrany sand

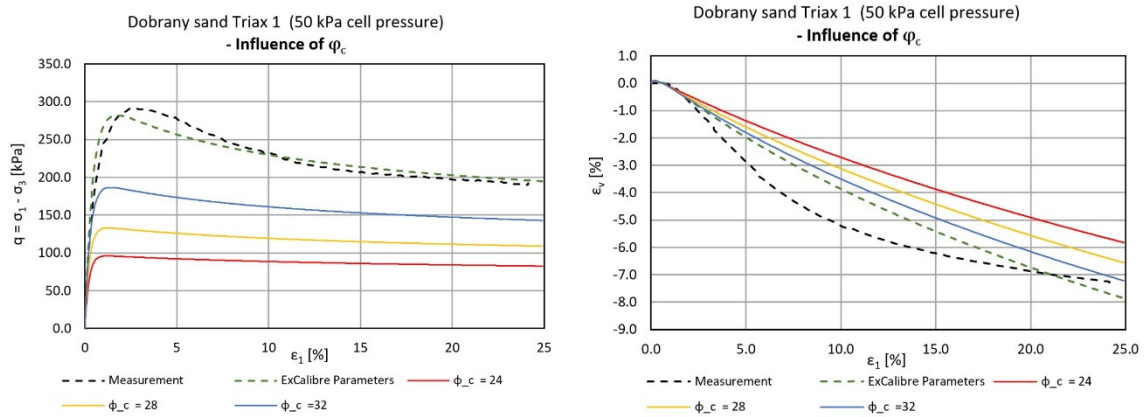


Fig. 146: Influence of φ_c on triaxial curves (50 kPa cell pressure) – Dobrany sand

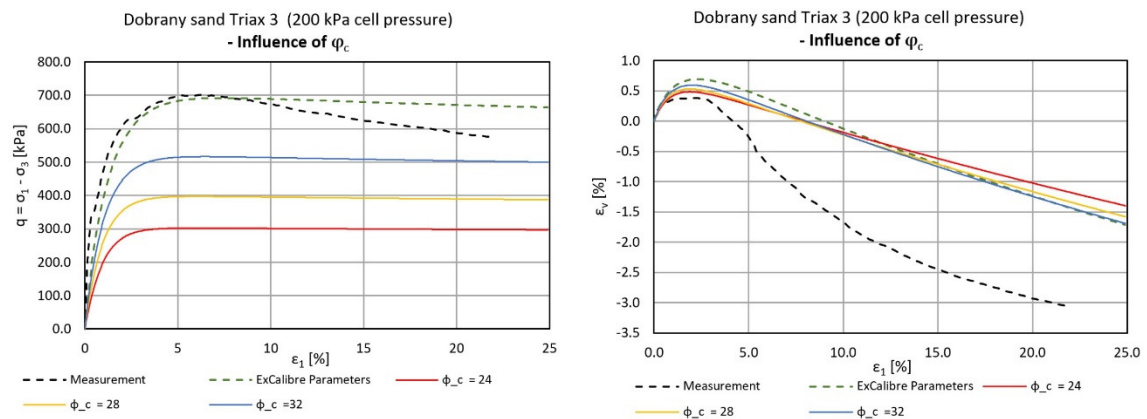


Fig. 147: Influence of φ_c on triaxial curves (200 kPa cell pressure) – Dobrany sand

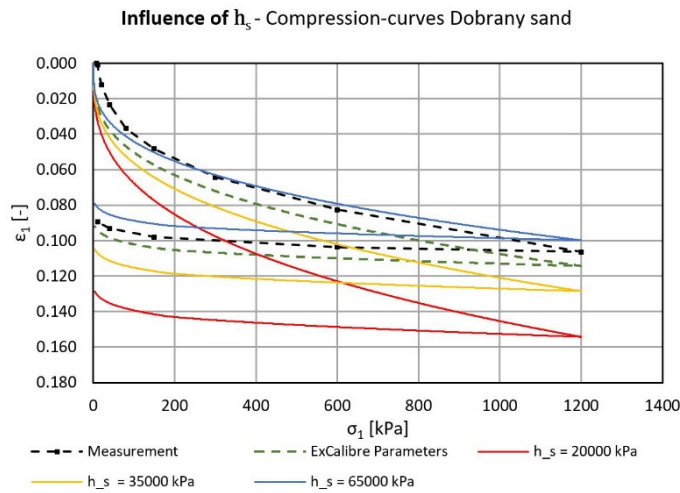


Fig. 148: Influence of h_s on compression curve – Dobransy sand

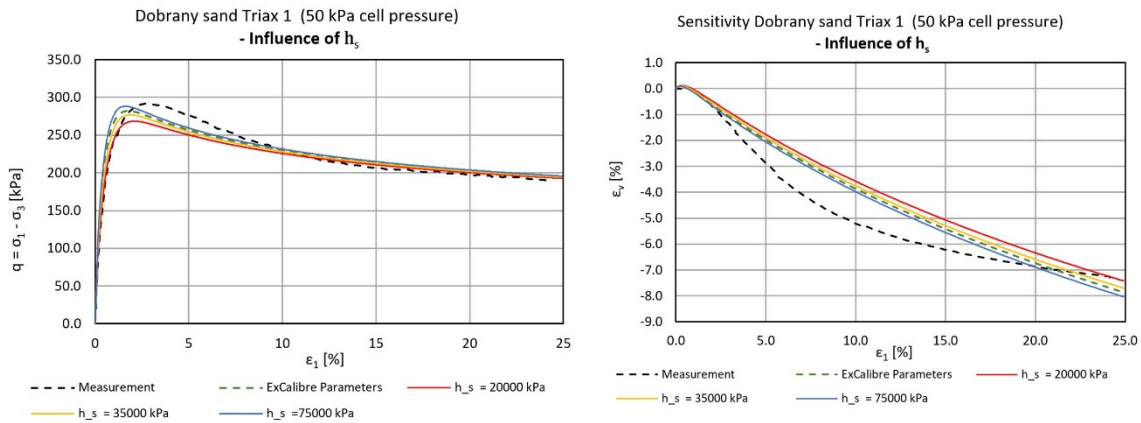


Fig. 149: Influence of h_s on triaxial curves (50 kPa cell pressure) – Dobransy sand

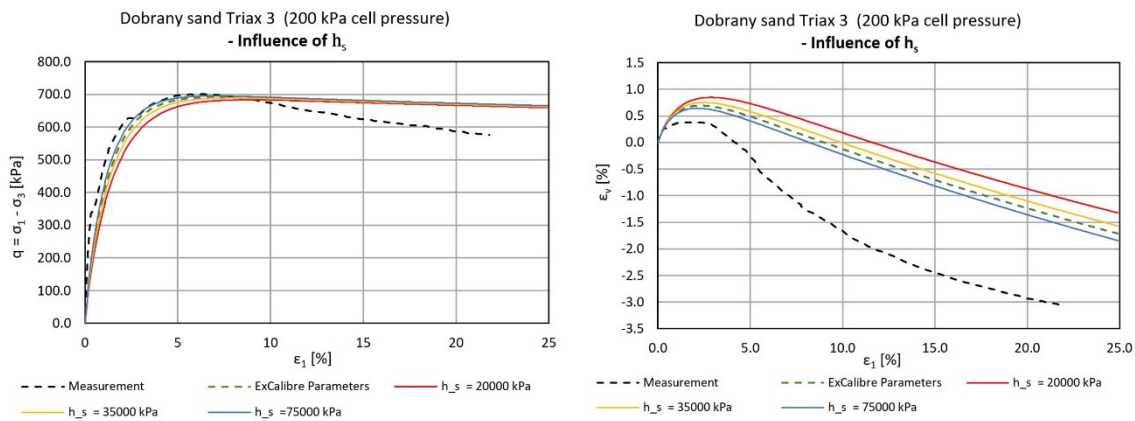


Fig. 150: Influence of h_s on triaxial curves (200 kPa cell pressure) – Dobransy sand

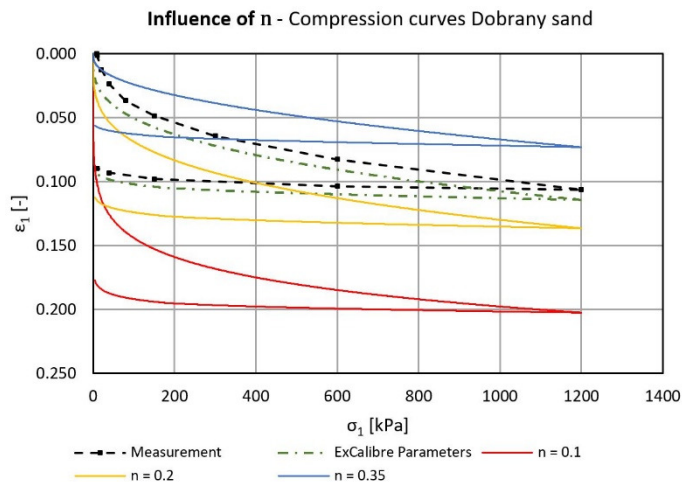


Fig. 151: Influence of n on compression curve – Dobransy sand

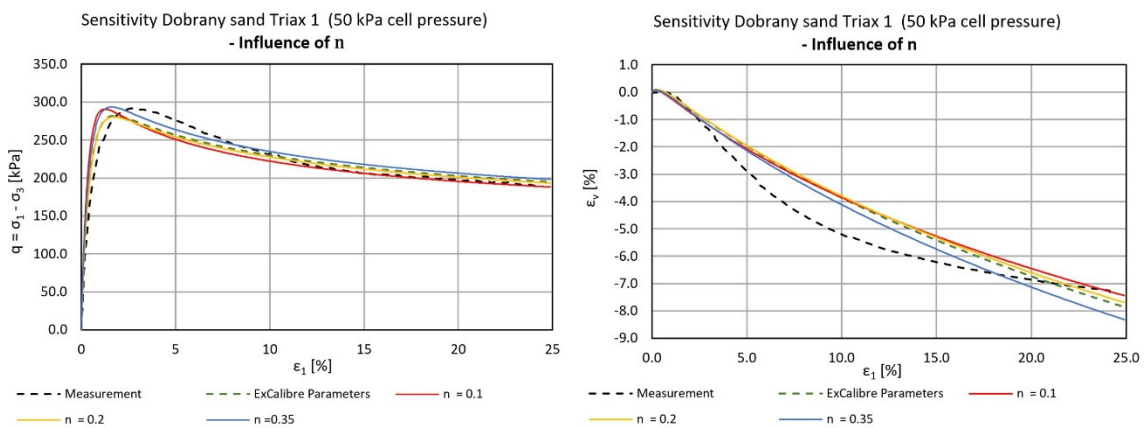


Fig. 152: Influence of n on triaxial curves (50 kPa cell pressure) – Dobransy sand

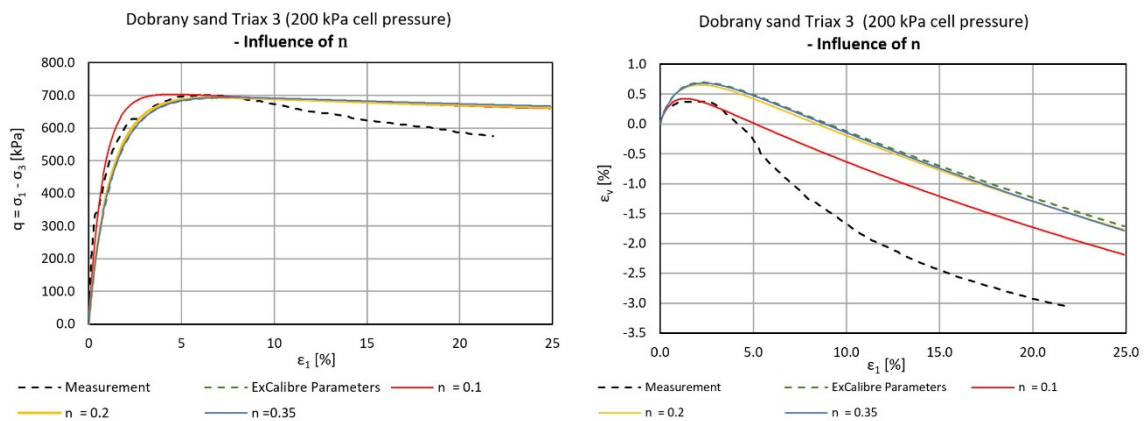


Fig. 153: Influence of n on triaxial curves (200 kPa cell pressure) – Dobransy sand

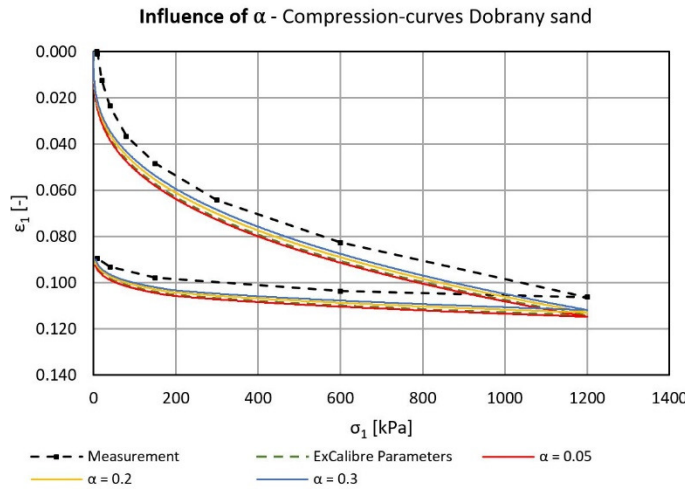


Fig. 154: Influence of α on compression curve – Dobransy sand

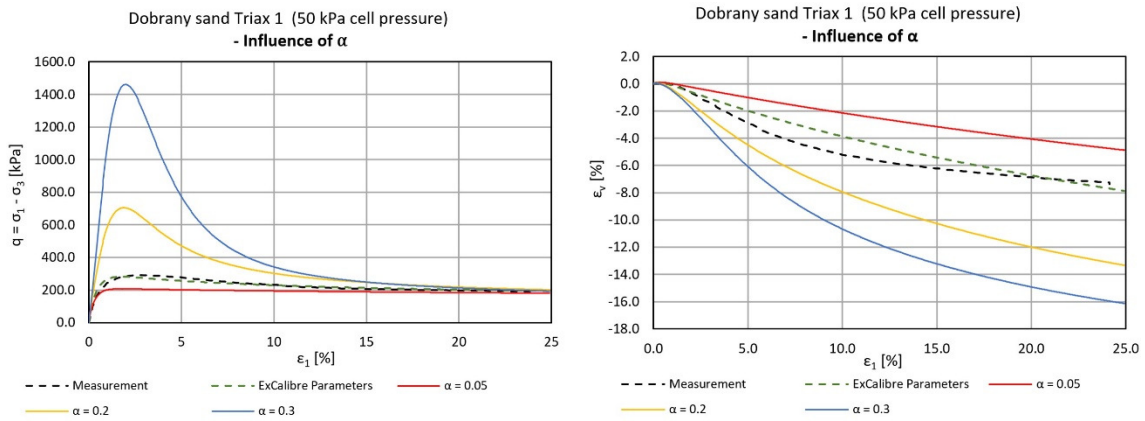


Fig. 155: Influence of α on triaxial curves (50 kPa cell pressure) – Dobransy sand

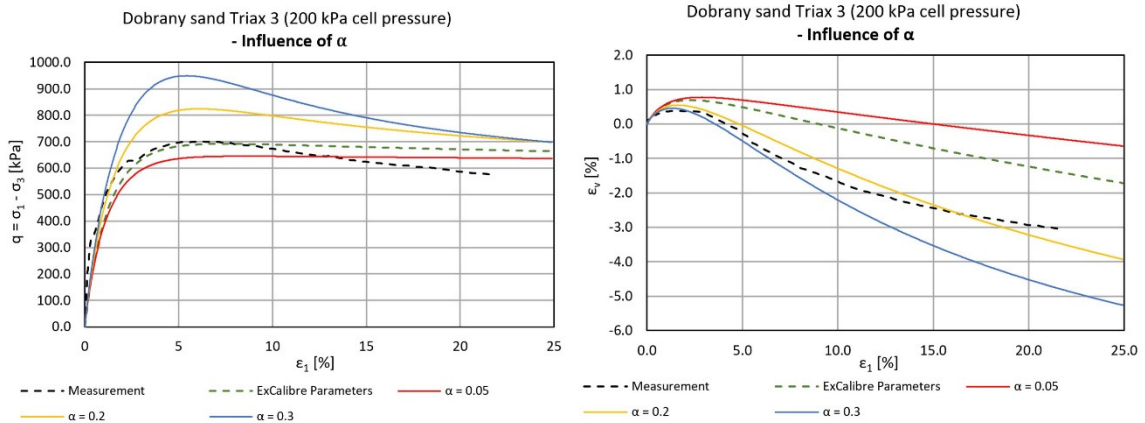


Fig. 156: Influence of α on triaxial curves (200 kPa cell pressure) – Dobransy sand

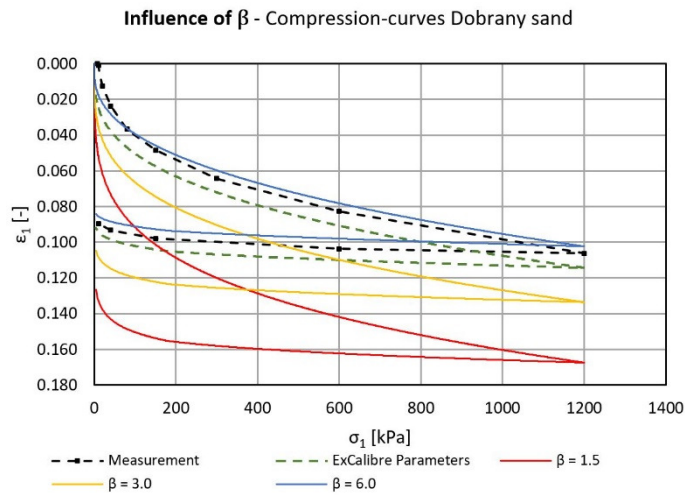


Fig. 157: Influence of β on compression curve – Dobransy sand

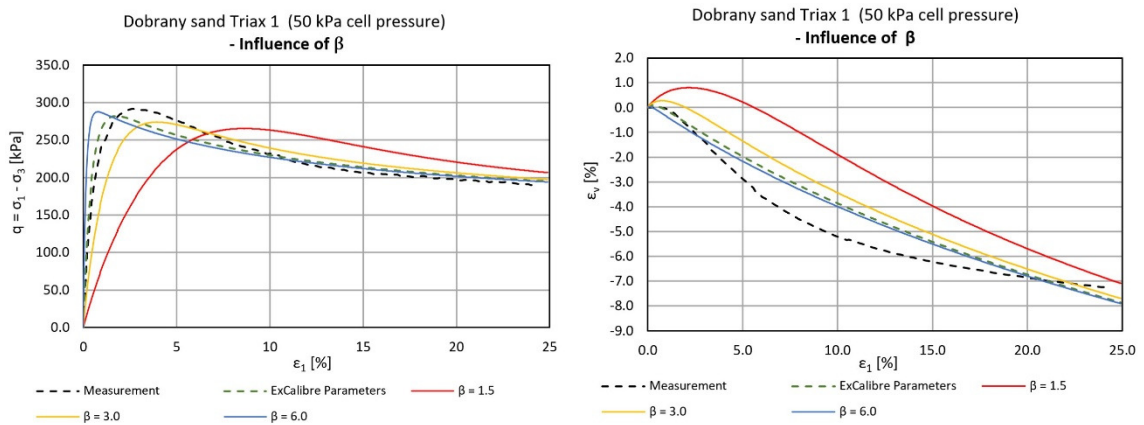


Fig. 158: Influence of β on triaxial curves (50 kPa cell pressure) – Dobransy sand

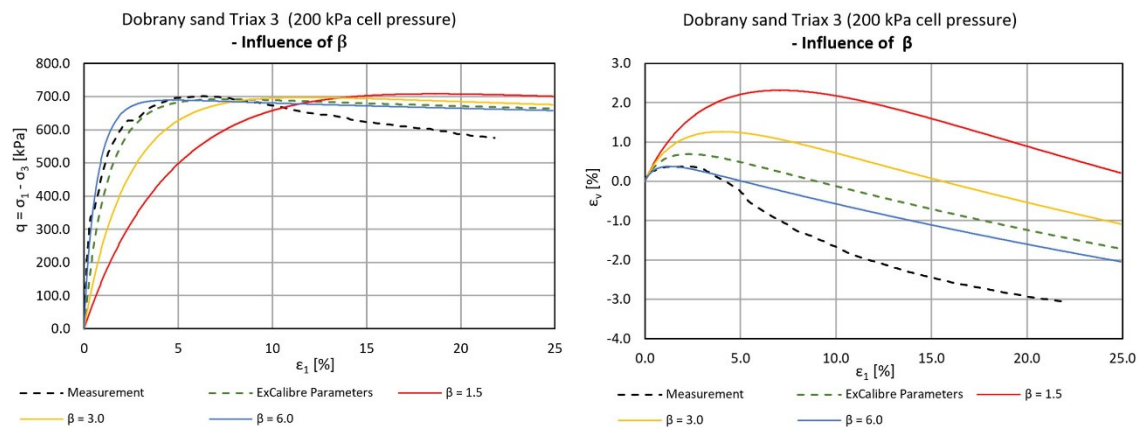


Fig. 159: Influence of β on triaxial curves (200 kPa cell pressure) – Dobransy sand

7.2.3 Rohatec Sand

The second material investigated within this chapter was Rohatec sand. The same calculations as already done for Dobrany sand were also carried out on this material with the only difference that each of the 5 considered hypoplastic parameters was only adjusted 2-times instead of 3-times. Tab. 33 shows the basic values of the 5 parameters next to the adjustment values.

Tab. 33: Investigated values of 5 different hypoplastic parameters – Rohatec sand

	Basic Value	Value 1	Value 2
φ_c	34.3°	28°	32°
h_s	61377 kPa	30000 kPa	90000 kPa
n	0.462	0.3	0.6
α	0.11	0.05	0.3
β	3.3	1	6

The initial void ratios were again obtained from a conducted calibration with ExCalibre and a subsequent transformation of the received values to a zero-pressure level. Also, in case of the material Rohatec sand it was not clear for which mean effective pressure the initial void ratio for the oedometer test was given in ExCalibre. Again, the received value of ExCalibre was assumed to correspond to zero pressure and was directly used for the initial void ratio in PLAXIS. The oedometer curves computed with the basic soil parameters in Plaxis and ExCalibre were slightly different (shifted on the vertical axis) which was justified by the uncertainties within the void ratios. The used void ratios can be found in Tab. 34.

Tab. 34: Initial void ratios used in PLAXIS – Rohatec sand

	Oedometer Test	Triax 50 kPa	Triax 200 kPa
e_0	0.721	0.468	0.515

The studies on material Rohatec sand showed the same dependencies of the simulated lab-curves on the changing hypoplastic parameters as already encountered for material Dobrany sand from the previous chapter. The diagrams depicting the influence of single parameters on the lab curves can be found within Appendix F in figures A. Fig 43-A. Fig 57.

To be consistent with the definition in ExCalibre dilatancy was assumed to be negative within the diagrams.

7.2.4 Conclusions

Different hypoplastic constitutive parameters have a different impact on the results of the simulated lab tests. While some parameters only affect the compression- or the triaxial testing curves, others influence both.

The main parameters governing the progression of the compression curve are the granulate hardness h_s , the exponent n and the exponent β . While varying values for the granulate hardness result in something like tilting of the curve, n can be used to adjust the curvature of the graph. Acc. to Meier [6] the exponent β can be utilized to modify the stiffness of a grain skeleton with $e < e_c$. This might explain the big influence that β showed to have on the compression curves of Dobrany and Rohatec sand as both oedometer tests were simulated with $e_0 < e_c$. Another model parameter that slightly influences the shape of the compression curves is the exponent α .

However, the exponent α is much more affecting the peak stresses and the volumetric behaviour in triaxial test simulations. The influence of the critical friction angle φ_c is almost solely restricted to the deviatoric stresses in triaxial test simulations. Increasing the friction angle results in a vertical shift of the curve upwards whereas varying values for n and β encourage a horizontal shift of the q - ε_I -curve. The influence of n and β on the volumetric behaviour in triaxial test simulations may also not be neglected.

It should be noted at this point that the conclusions in this chapter were only drawn from Dobrany and Rohatec sand based on the studies carried out. Further studies are required, especially in connection with calcareous sands, to find out if the same conclusions apply to this kind materials.

7.3 Calibration Procedure acc. to Meier

The last studies carried out in the course of this thesis refer to the manual calibration procedure suggested by Meier [6]. He explained this manual approach on the example of Dubai sand for which he received the following final hypoplastic parameters:

Tab. 35: Final hypoplastic parameters for Dubai sand [6]

Material	φ_c [°]	h_s [kPa]	n [-]	e_{d0} [-]	e_{c0} [-]	e_{i0} [-]	α	β
Dubai sand	37.7	95,000	0.500	0.762	1.223	1.406	0.13	1.1

In his calibration procedure Meier suggests choosing the values for the critical friction angle φ_c and the limit void ratios e_{d0} , e_{c0} and e_{i0} based on the results from the angle of repose test and the conducted standard index tests. All other values are a result of the calibration procedure and need to be altered subsequently in order to receive the best fit of the simulations with the measurements. In his example he used the results of an

oedometer test (OCT) performed on a loose sample and a triaxial test (TXC) performed on a dense sample as a reference for the calibration of the hypoplastic material. In addition, he made use of the results of an oedometer test performed on a dense sample for the final adjustment of the exponent β . The following diagram illustrates the principles of the suggested manual calibration procedure.

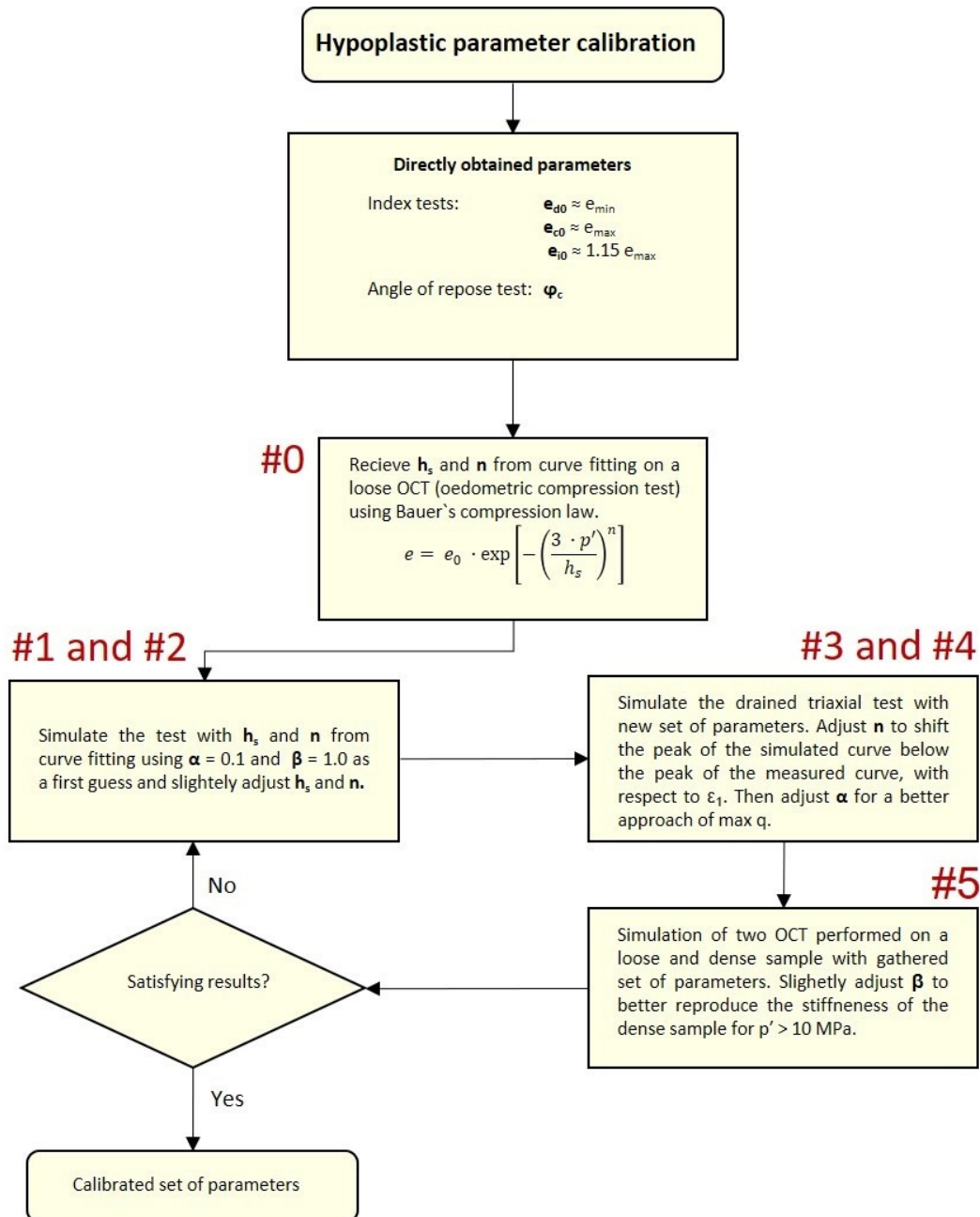


Fig. 160: Manual calibration procedure acc. to Meier [6]

The designations #x refer to the changes that he made to the set of h_s , n , α and β within each calibration step to iteratively better approach the measurement results. The different values for the mentioned hypoplastic parameters used within each calibration step can be found in Tab. 36.

Tab. 36: Iterative adjustments of parameters within each calibration step [6]

#	hs [kPa]	n [-]	α	β	Test results used
0	113,600	0.544	-	-	OCT (loose)
1	113,600	0.544	0.10	1.0	OCT (loose)
2	95,000	0.544	0.10	1.0	OCT (loose)
3	95,000	0.500	0.10	1.0	TXC (dense)
4	95,000	0.500	0.13	1.0	TXC (dense)
5	95,000	0.500	0.13	1.1	OCT (dense)

A flow chart representing the influence of changing parameter sets within every step of the calibration procedure on the simulated curves can be found in Appendix F. Note that dilatancy within these diagrams is positive.

It was tried to reproduce the exact same calibration procedure for the example of Dubai sand in order to understand the principles of this manual calibration approach and to make this method usable for further studies.

The first task was to determine the initial void ratios e_0 to be used for the different test simulations within the PLAXIS SoilTest tool. From the given relative densities of the oedometer tests (loose $I_D = 0.27$, dense $I_D = 0.79$) and the limit void ratios e_{c0} and e_{d0} , the initial void ratios e_0 were calculated with the use of Eqn. (5.1) for a pressure level of 0 kPa. The same was done for the triaxial test for which the initial relative density I_D was given with 0.88. As the corresponding cell pressure of the triaxial test was not provided it was simply assumed with 100 kPa. That this assumption was right could be proved by the comparison of the simulation results with the curves received by Meier [6]. Both curves showed a very good agreement. The calculated initial void ratios e_0 which were utilized for the simulations within PLAXIS are listed in Tab. 37.

Tab. 37: Initial void ratios used for the manual calibration procedure in PLAXIS – Dubai sand

	Oedometer Test (loose)	Oedometer Test (dense)	Triaxial Test (100 kPa cell pressure)
e_0	1.099	0.859	0.817

It has to be mentioned that Meier actually provided the value for the initial void ratio for the oedometer test on the loose sample with $e_0 = 1.085$ which could not be exactly reproduced by the approach using Eqn. (5.1) and the given relative density of $I_D = 0.27$. It was assumed that his value for the initial void ratio refers to a certain small pressure level which was present when the sample was fixed within the oedometer apparatus. However, to be consistent with the determination approach for the initial void ratio of the oedometer test performed on the dense sample, for which the value for e_0 was not

provided by Meier, the value for e_0 of both oedometer tests was used as received from Eqn. (5.1). Due to the explained uncertainties within the determination of the initial void ratios the curves from the oedometer test simulations with the different parameter sets are not a 100 % in agreement with the results from Meier [6], but they are very close.

To compare the curves from the oedometer test simulations to the curves from Meier which were given within e - p' -diagrams it was needed to do a conversion from volumetric strains (for oedometer tests $\varepsilon_l = \varepsilon_v$) to void ratios, as PLAXIS won't output the void ratios at first hand within the SoilTest tool. With reference to the PLAXIS user manual [46] the void ratio for each next calculation step $i+1$ was calculated with

$$e_{i+1} = e_i - (\varepsilon_{v,i+1} + \varepsilon_{v,i}) \cdot (1 + e_i) \tag{6.27}$$

Fig. 161 gives an example of the implementation of this equation within the used Excel-file.

Plaxis Calibration #1		
Sig1 [kPa]	epsv[-]	e [-]
0.000000	0.000000	1.09853
0.000100	0.000006	1.0985181
0.000200	0.000009	1.098511
0.000300	0.000012	1.0985053
0.000400	0.000014	1.0985004

$e_0 = 1.099$

$$e_{i+1} = e_i - (\varepsilon_{v,i+1} - \varepsilon_{v,i}) \cdot (1 + e_i)$$

Fig. 161: Calculation of e from the volumetric strains

The following diagrams show the resulting curves for the simulations performed with the different sets of parameters from each calibration step given in Tab. 36.

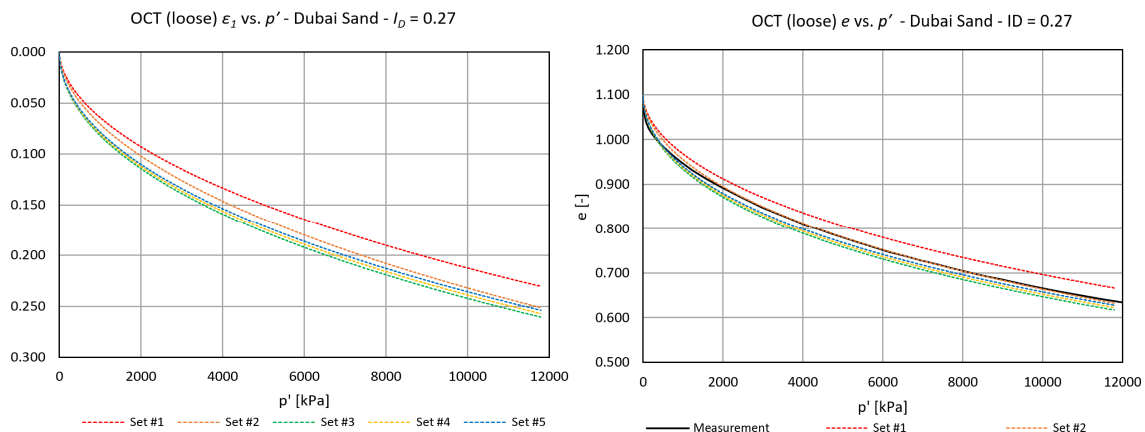


Fig. 162: Oedometer test (loose) simulation results for different parameter sets from PLAXIS – Manual calibration approach acc. to Meier [6]

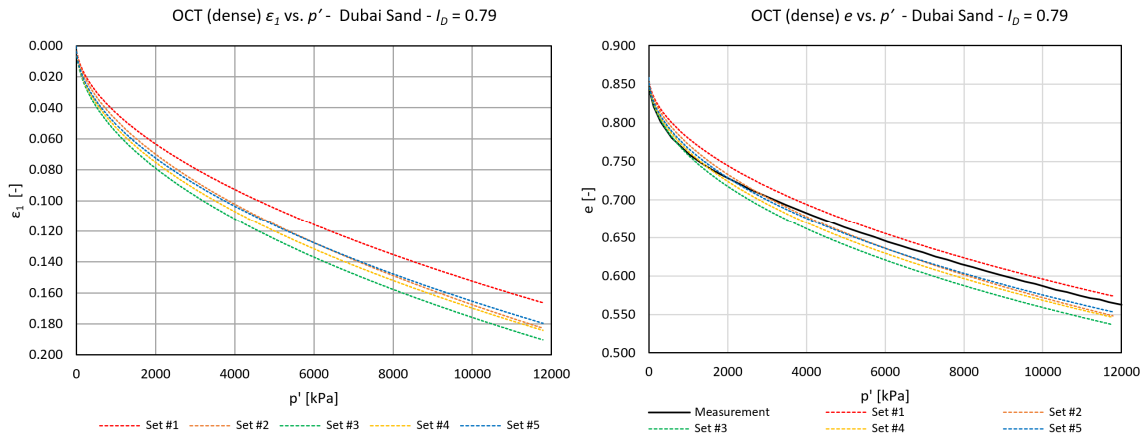


Fig. 163: Oedometer test (dense) simulation results for different parameter sets from PLAXIS – Manual calibration approach acc. to Meier [6]

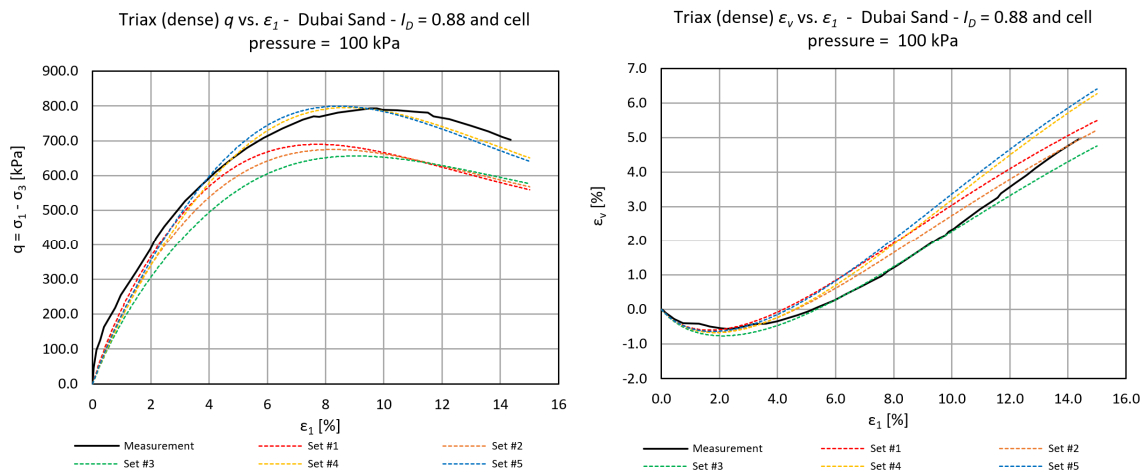


Fig. 164: Triaxial test simulation results for different parameter sets from PLAXIS – Manual calibration approach acc. to Meier [6]

Due to the fact that only the e - p' -diagrams for the oedometer tests were given by Meier [6] the measured curves from the lab-tests are not depicted within the ε_1 - p' -diagrams from Fig. 162 and Fig. 163.

In fact, it could be shown with this study that PLAXIS provides all the necessary capabilities to perform a manual calibration of a hypoplastic material. But further studies are required and experience with this calibration procedure needs to be gained to be able to approach a final set of parameters which can be used to describe the mechanical behaviour of the investigated material with the utilized constitutive law in the best way possible.

8 Summary and Outlook

The final chapter of this thesis sums up the main results of the accomplished studies and gives an outlook for further research regarding the KIM and the application of the spherical cavity expansion to other boundary value problems encountered in geotechnical engineering.

8.1 Summary

In the course of this thesis the specific characteristics of sands containing a high amount of breakable grains were discussed. Concluding from their special properties it was found that for the quality control of compaction measures, by means of cone penetrations testing, carried out in such materials it is essential to make use of interpretation methods which are able to reflect effects such as grain crushing. The commonly used interpretation methods in geotechnical practice were considered unsuitable for the application on carbonate sands, unless previously a cost-intensive and time-consuming calibration of the material constants was performed.

A relatively new interpretation method promising to be way more efficient and appropriate for the use in sands with a high tendency towards grain crushing was introduced. This method is known to be the Karlsruhe Interpretation Method or in short, the KIM.

A finite difference code, the OSINV code, for the solution of the spherical cavity expansion problem (SCE-problem), as part of the KIM, was discussed in detail and a general explanation of the correct usage of this code was made. On the basis of the studies carried out by Slawik it was shown that the resulting limit pressures of the OSINOV code are very sensitive to changes in the calculation parameters.

In order to come up with the KIM-parameters based on the obtained limit pressures received from a series of SCE-simulations, a well-working least square curve-fitting method was introduced and comparisons with the results of a curve-fitting program, as used in consultant practise, were made.

It was demonstrated that the simulation series of the KIM can be optimized, with respect to the numbers of conducted SCE-simulations at different mean effective pressures and relative densities, without having a significant influence on the accuracy of the subsequently determined KIM-parameters.

A working 2D finite-element model of the spherical cavity expansion has been developed and the averaging approach to come up with the resulting pressure-expansion-curves was explained. For the purpose of validation of the FEM-model a closed-form solution of the large-strain SCE-problem, comprising the MC yield criterion was implemented into a MATLAB-code. The influence of certain model properties on the resulting pressure

expansion curves was studied and an improved PLAXIS model for the final application was provided. From comparisons with pressure-expansion-curves found in literature, calculated with the Mohr-Coulomb constitutive law, it was proven that the final PLAXIS model can yield the desired accuracy. From studies with the MC-model it was found that not only the initial mean effective stress p_0 and the coefficient of lateral earth pressure K_0 have a significant influence on the received values for the limit pressure, but also the stiffness of the material as within cavity expansion a confined problem is considered.

Calculations with the PLAXIS models were also performed for the hardening soil constitutive law. It was concluded that a non-associated flow-rule causes the same problems as for the MC-models.

Further studies were made using the hypoplastic constitutive model acc. to “von Wolffersdorff” [23]. The advantages of the hypoplastic models over commonly used elasto-plastic models for the application on large-strain problems were clarified by the fact that much smoother pressure-expansion-curves without heavy scattering could be received.

Two full KIM-analysis were conducted on two materials from the KELLER-database, and it was observed that the limit pressures received from the PLAXIS-models generally tend to lie below the values received from the OSINVO code (max. around -7 %), at least when the suggested calculation parameters are used within the finite-difference code. The different values of the limit pressures automatically led to different values in the KIM-parameters received from the two different calculation approaches.

In order to cut down on the effort for the creation of the many models required within the KIM-analysis, a Python script, to be run in PLAXIS, was provided which can be used for the automatic generation of spherical cavity expansion models comprising different initial mean effective stresses and initial relative densities.

Further, the sensitivity of the PLAXIS-models incorporating the hypoplastic constitutive law was investigated and it was concluded that the FEM-models aren't sensitive to the mesh-coarseness or the considered value for the tolerated error. A slight sensitivity of the models was only observed for domain sizes smaller than 15 x 30 m.

The final studies of this thesis were dealing with hypoplastic parameter calibration. The online tool ExCalibre was introduced which can be used for the calibration of the hypoplastic model based on the results of lab tests (sieving curve, oedometer test, triaxial test). The calibration for two materials from the KELLER-database was conducted with the aid of this online tool and it was found that the received hypoplastic parameters were in both cases close, but still different from the values given in the report. Especially the value for the exponent α caused the biggest discrepancies.

Furthermore, the influence of single hypoplastic parameters on the results of lab-test simulations performed with the aid of the PLAXIS SoilTest tool was studied, based on two sandy materials from the “soilmodels.com”-database.

Finally, the manual calibration procedure by Meier [6] was explained and it was tried to reproduce the results from each single calibration step within PLAXIS, which Meier received for a calibration performed on Dubai sand.

8.2 Outlook

The studies of this thesis helped to narrow the difficulties in connection with the determination of the pressure-expansion-curves and the limit pressures from the spherical cavity expansion problem. It has come to the situation in which both calculation approaches (FEM calculations and OSINOV code) can be handled quite well and only minor improvements with respect to the simulation procedures are still required. The greatest need for research is related to the calibration of the hypoplastic parameters as these values are the basis for the accurate representation of the real material behaviour. The shape factor defined within the KIM also comprises big uncertainties. It is therefore required to improve the definition of the shape factor and include a dependence not only on the relative density but also on other state variables.

The following points depict the topics that still need to be covered in further research in order to improve the accuracy of the KIM and to yield a usable interpretation approach to be applied in geotechnical practice:

- **Improving the simulation series**

It is required to improve the simulation series of the KIM and reduce the number of needed simulations to save up on time for the calculation and evaluation of the models. The considered values for the initial relative densities and effective mean pressures have to be optimized to keep the accuracy of the subsequently determined KIM-parameters high.

- **Automatic output generation in PLAXIS**

An addition to the used Python script in this thesis could be made which allows for the automatic generation of the pressure-expansion-curves based on the explained averaging procedure over different output nodes.

- **Investigation of the influence of the dilatancy angle on the resulting limit pressures p_{LS}**

As concluded, the flow-rule has a major impact on the resulting limit pressures and the pressure-expansion-curves from the simulations of the spherical cavity expansion. To get detailed information on how the chosen values for the dilatancy angle affect the calculation results and under which conditions the expansion yields a non-uniform distribution of stresses and strains across the cavity, studies with varying values for the dilatancy angle should be conducted with the aid of the PLAXIS models and the closed-form solution.

- **KIM-analysis with different materials**

To confirm the findings of this thesis it is required to perform further KIM-analysis with different hypoplastic materials.

- **Establishment of a new shape factor k_q**

A new shape factor, especially suited for calcareous sands, could be established by performing calibration chamber tests on this type of materials and solving the corresponding spherical cavity expansion problem to receive the limit pressure p_{LS} .

- **Further investigations on the calibration procedure**

Further studies with respect to the calibration procedure have to be conducted. Independent of which calibration approach is used (ExCalibre or manual calibration) it needs to be figured out which lab-tests have to be taken as a reference to yield the most representative set of hypoplastic parameters. It further, has to be worked out whether approaching the stresses or the volumetric behaviour within the calibration is causing more realistic values for the subsequently calculated limit pressures. To get a better understanding of the functionality of ExCalibre more tests with different materials must be carried out. The manual calibration of the same materials should be done simultaneously to hopefully reduce the differences in the results of both approaches.

- **Application of more sophisticated soil models**

The hypoplastic material model by “von Wolffersdorff” [23] is not able to directly consider grain crushing which is a very typical behaviour of calcareous sands when they are subjected to higher pressure levels. More sophisticated material models could be applied within the KIM to take into account the effect of potential particle breakage and to make one step further towards a more realistic modelling.

- **Application of the SCE-model to other boundary values**

The application of the spherical cavity expansion problem is not solely limited to the interpretation of cone penetration tests performed in sand. The models could also be adopted in connection with the determination of the base resistance from piles or the interpretation of cone penetration test performed in fine grained soils, such as silts and clays.

9 Bibliography

- [1] J. van't Hoff and A.N. van der Kolff, "Hydraulic Fill Manual," CRC Press, 2012.
- [2] J. Reinisch, "Estimating the relative density in calcareous sands with the Karlsruhe Interpretation Method," Master's thesis, Graz University of Technology, 2018.
- [3] J. H. Schmertmann, "An Updated Correlation between Relative Density, Dr, & Fugro-Type Electric Cone Bearing, qc," Contract Report DACW39-76-M-6646, WES, Vicksburg, Miss., 1976.
- [4] M. Jamiolkowski, D. C. Lo Presti and M. Manassero, "Evaluation of Relative Density and Shear Strength of Sands from CPT and DMT," *Geotechnical Special Publication*, 2003.
- [5] T. Meier, and W. Wehr, "Influence of the Calcite Content of Sands on the CPT-Resistance," *Keller Holding GmbH*, 2014.
- [6] T. Meier, "Application of Hypoplastic and Viscohypoplastic Constitutive Models for Geotechnical Problems," PhD thesis, Universität Fridericiana Karlsruhe, 2007.
- [7] M. Almeida, M. Jamiolkowski and R. Peterson, "Preliminary Result of CPT Tests in Calcareous Quiou Sand," in *Proceedings of the First International Symposium on Calibration Chamber Testing*, Potsdam, New York, 1991.
- [8] R. Cudmani, "Statische, alternierende und dynamische Penetration in nichtbindigen Böden," PhD thesis, Universität Fridericiana Karlsruhe, 2000.
- [9] S. Slawik, "Numerical studies on KIM employing the Cavity Expansion Method," Master's thesis, Gdansk University of Technology, 2018.
- [10] R. Kolman and J. van't Hoff, "Port Expansion trough Land Reclamation," *Port Technology International*, 2013.
- [11] "Dredging and Spoil Disposal Policy," Australian Government, Townsville, Queensland, 2004.
- [12] J. Stimpson, "New Civil Engineer," [Online]. Available: <https://www.newcivilengineer.com/london-gateway-in-the-pipeline/8608149.article>. [Accessed 8 September 2018].

- [13] M.R. Coop and D.W. Airey, "Carbonate sands," in *Characterization and Engineering Properties of Natural Soils*, Tan et al. (eds), 2003, pp. 1049-1086.
- [14] A.R. Clark and B.F. Walker, "A proposed scheme for the classification and nomenclature for use in the engineering description of Middle Eastern sedimentary rocks," 1977.
- [15] K. Kirsch and F. Kirsch, *Ground Improvement by Deep Vibratory Methods - Second Edition*, Boca Raton, FL: CRC Press, 2017.
- [16] "Deep Vibro Techniques - Brochure 10-02E," 25 September 2018. [Online]. Available: <http://www.kellerholding.com/deep-vibro-techniques.html>.
- [17] T. Lunne and P.K. Robertson, *Cone Penetration Testing in Geotechnical Practice*, E & FN Spon, 1987.
- [18] "Gouda Geo-Equipment B.V.," [Online]. Available: <https://www.gouda-geo.com/index.php>. [Accessed 27 October 2018].
- [19] P.K. Robertson and K.L. Cabal (Robertson), "Guide to Cone Penetration Testing for Geotechnical Engineering," Gregg Drilling & Testing, Inc., Signal Hill, California, 2012.
- [20] P.W. Mayne and F. H. Kulhawy, "Calibration Chamber Database and Boundary Effects Correction for CPT Data," in *Proceedings of the First International Symposium on Calibration Chamber Testing*, Potsdam, New York, 1991.
- [21] H.J. Lang, J. Huder, P. Amann and A.M. Puzrin, *Bodenmechanik und Grundbau - Das Verhalten von Böden und Fels und die wichtigsten grundbaulichen Konzepte*, vol. 9, Heidelberg: Springer-Verlag Berlin Heidelberg, 2011.
- [22] G. Baldi, R. Bellotti, N. Ghioanna, M. Jamiolkowski and E. Pasqualini, "Interpretation of CPTs and CPTUs, 2nd Part: drained penetration of sands," in *Proceedings of the 4th International Geotechnical Seminar, Field Instrumentation and In-Situ Measurements*, Singapore, 1986.
- [23] P.-A. v. Wolffersdorff, "A hypoplastic relation for granular materials with a predefined limit state surface," *Mechanics of Cohesive-Frictional Materials*, vol. 1, pp. 251-271, 1996.
- [24] W. Fellin, "Hypoplasticity for beginners," IGT, Universität Innsbruck, Innsbruck, 2002.

- [25] D. Kolymbas, "A rate-dependent Constitutive Equation for Soils," *Mechanics Research Communications*, vol. 4(6), pp. 367-372, 1977.
- [26] D. Kolymbas, *Introduction to Hypoplasticity - Advances in Geotechnical Engineering and Tunneling 1*, Rotterdam: A.A.Balkema, 2000.
- [27] A. Niemunis and I. Herle, "Hypoplastic model for cohesionless soils with elastic strain range," *Mechanics of Cohesive-Frictional Materials*, vol. 2, pp. 279-299, 1997.
- [28] D. Mašín, "A hypoplastic constitutive model for clays," *International Journal for Numerical and Analytical Methods in Geomechanics*, no. 4, pp. 311-336, 2005.
- [29] W. Fellin and D. Kolymbas, "Universität Innsbruck," [Online]. Available: <https://www.uibk.ac.at/geotechnik/res/paper/lfortgeschrittene.pdf>. [Accessed 29 September 2018].
- [30] I. Herle and G. Gudehus, "Determination of parameters of a hypoplastic constitutive model from grain assemblies," *Mechanics of Cohesive-Frictional Materials*, vol. 4(5), pp. 461-486, 1999.
- [31] A. Niemunis, "Extendet hypoplastic models for soils," PhD thesis, Bochum, 2002.
- [32] E. Bauer, "Calibration of a Comprehensive Hypoplastic Model for Granular Materials," *Soils and Foundations*, vol. 36, no. 1, pp. 13-26, 1996.
- [33] I. Herle, "Granulometric Limits of Hypoplastic Models," *TASK Quaterly: scientific bulletin of Academic Computer Centre in Gdansk*, vol. 4, no. 3, pp. 389-408, 2000.
- [34] I. Herle, *Hypoplastizität und Granulometrie einfacher Korngerüste*, Karlsruhe: Institut für Bodenmechanik und Felsmechanik der Universität Fridericiana in Karlsruhe, 1997.
- [35] D. Mašín, "Hypoplasticity for Practical Applications - Determination of material paramters," 2015.
- [36] H.-S. Yu, *Cavity Expansion Methods in Geomechanics*, Dordrecht: Springer Science+Business Media, 2000.
- [37] R. Cudmani and V.A. Osinov, "The cavity expansion problem for the interpretation of cone penetration and pressuremeter tests," *Canadian Geotechnical Journal*, vol. 38, pp. 622-638, 2001.

- [38] M. Uhlig and I. Herle, "Bestimmung der Porenzahl aus Drucksondierungen," in *Aktuelle Forschung in der Bodenmechanik 2015 - Tagungsband zur 2. Deutschen Bodenmechanik Tagung*, Bochum, 2015.
- [39] V.A. Osinov and R. Cudmani, "Theoretical investigations of the cavity expansion problem based on a hypoplasticity model," *International Journal for Numerical and Analytical Methods in Geomechanics*, no. 25, pp. 473-495, 2001.
- [40] K. Been, J.H.A. Crooks, D.E. Becker and M. G. Jefferies, "The cone penetration test in sands: Part 1, state parameter interpretation," *Geotechnique*, vol. 36, no. 2, pp. 239-249, 1986.
- [41] T. Meier, "KIM-Report: Project Port de la Mer, Dubai," Baugrund Dresden Ingenieurgesellschaft mbH, Dresden, 2012.
- [42] V. Osinov, Finite Difference Code (c) - Numerical solution of the spherical cavity expansion problem.
- [43] X. Xu, Investigation of the End Bearing Performance of Displacement Piles in Sand, PhD thesis, University of Western Australia, 2007.
- [44] H.S. Yu and G.T. Houlsby, "Finite cavity expansion in dilatant soils: loading analysis," *Geotechnique*, vol. 41, no. 2, pp. 173-183, 1991.
- [45] M. F. Randolph, J. Dolwin and R. Beck, "Design of driven piles in sand," *Geotechnique*, vol. 44, no. 3, pp. 427-448, 1994.
- [46] "PLAXIS 2D Reference Manual 2018," [Online]. Available: https://www.plaxis.com/?plaxis_download=2D-2-Reference.pdf. [Accessed 15 October 2018].
- [47] T. Meier, "KIM-Report: Project Palm Deira / Palm Jumeirah, Dubai," Baugrund Dresden Ingenieurgesellschaft mbH, Dresden, 2015.

Appendix A for Chapter 2

A. Tab. 1: Investigated materials by Reinisch [2]

<i>Material</i>	$CaCO_3$ [%]	φ_c [°]	e_{min}	e_{max}	ρ_s [g/cm ³]	<i>source</i>
M0 Karlsruhe	0	31	0.531	0.875	2.647	[16]
Al Zour LNG	9.73	31	0.365	0.747	2.663	KELLER
Jurong sand	11	33	0.690	1.030	-	[16]
M15	13.5	31.1	0.579	0.859	2.671	[16]
M30	27	31.6	0.618	0.948	2.694	[16]
Sheikh Jaber	28.6	31	0.385	1.015	2.650	KELLER
Al Zour Package 5	42.45	33	0.410	0.84	2.670	KELLER
M60	54	32.2	0.653	1.014	2.742	[16]
JAT4: island	60.9	34.5	0.680	0.977	2.749	KELLER
JAT4: south side	63.3	39.5	0.979	1.504	2.777	KELLER
Palm Jumeirah	73.6	35	0.583	0.922	2.741	KELLER
Quiou	77	36	0.831	1.281	2.662	[5]
M100 Dubai sand	90	37.7	0.762	1.223	2.805	[16]
Dogs Bay	90	40.3	0.981	1.827	2.750	[5]
Cabo Rojo	92.8	-	1.340	1.710	2.860	[52]
BAE	93	-	0.979	1.551	2.840	[52]
S1	95	-	0.741	1.278	2.840	[52]
Palm Deira	96.2	36	0.725	1.226	2.800	KELLER
Kenya sand	97	-	1.282	1.776	2.785	[52]
BAW	98	-	0.843	1.392	2.840	[52]
PLM - AZ28	100	36.3	0.740	1.261	2.791	KELLER
PLM - BC36	100	36.5	0.79	1.384	2.791	KELLER
Zakkum Island	100	34	0.831	1.338	2.833	KELLER

Appendix B for chapter 3

A. Tab. 2: Index properties of Dubai sand and Karlsruhe sand [6]

Material	CaCO ₃ content	ρ_s [g/cm ³]	d_{10} [mm]	d_{60} [mm]	C_U = d_{60}/d_{10}	e_{min}	e_{max}	φ_c
Dubai sand	90 %	2.805	0.13	0.53	4.1	0.762	1.223	36.0°
Karlsruhe sand	≈ 0 %	2.647	0.14	0.31	2.2	0.531	0.875	31.0°

A. Tab. 3: Results of calibration chamber tests performed by Meier [6]

Test	p_0 [kPa]	K	e	I _D [%]	$q_{c,m}$ [MPa]	$q_{c,c}$ [MPa]
M0-1	39	0.20	0.83	13	1.0	1.0
M0-2	77	0.41	0.81	18	1.8	1.9
M0-3	151	0.44	0.81	18	4.0	4.3
M0-4	226	0.46	0.82	17	5.5	5.8
M0-5	38	0.21	0.70	51	4.5	5.4
M0-6	149	0.47	0.69	52	12.7	15.2
M0-7	230	0.49	0.69	53	17.8	21.4
M0-8	41	0.26	0.66	61	5.5	6.8
M0-9	79	0.41	0.61	77	18.5	24.2
M0-10	157	0.50	0.65	64	18.7	23.4
M0-11	224	0.51	0.66	63	23.5	29.2
M15-1	43	0.57	0.90	-8*	1.5	1.5
M15-2	77	0.53	0.90	-7*	2.0	2.0
M15-3	147	0.50	0.90	-7*	4.0	4.0
M15-4	226	0.50	0.89	-5*	6.0	6.0
M15-5	44	0.53	0.75	40	4.8	5.4
M15-6	77	0.58	0.75	41	7.3	8.2
M15-7	146	0.53	0.73	48	13.8	15.8
M15-8	222	0.55	0.73	46	20.0	22.7
M15-9	27	0.49	0.69	59	13.0	15.3
M30-1	80	0.50	0.64	81	20.5	24.7
M30-2	80	0.50	0.77	43	10.9	12.0
M30-3	80	0.50	0.96	-14*	2.2	2.2
M30-4	143	0.50	0.64	81	26.5	31.9
M30-5	150	0.50	0.77	43	17.5	19.3
M60-1	80	0.50	0.72	76	17.8	20.4
M60-2	80	0.50	0.81	54	12.5	13.8
M60-3	150	0.50	0.72	76	22.5	25.9
M60-4	150	0.50	0.81	54	17.0	18.8

Continued on next page

*void ratio is greater than e_{max} from standard laboratory tests

Continuation						
Test	p_0 [kPa]	K	e	I_D [%]	$q_{c,m}$ [MPa]	$q_{c,c}$ [MPa]
M100-1	51	0.38	1.16	13	2.2	2.3
M100-2	73	0.35	1.15	14	3.3	3.3
M100-3	146	0.43	1.11	25	5.3	5.6
M100-4	218	0.46	1.14	17	8.5	8.8
M100-5	39	0.29	0.94	60	3.8	4.2
M100-6	72	0.48	0.98	53	5.6	6.2
M100-7	76	0.40	0.96	56	7.4	8.3
M100-8	143	0.42	0.97	54	13.5	15.1
M100-9	221	0.43	0.98	53	9.8	10.9
M100-10	43	0.26	0.74	104	24.3	30.1
M100-11	79	0.42	0.75	102	24.3	30.0
M100-12	155	0.47	0.82	87	27.0	32.3

A. Tab. 4: B from k_c provided by Meier vs. B from accurate k_c for all performed CCTs by Meier [6]

Test	$k_{c,table}$	$B_{calculated}$	$k_{c,calculated}$	B_{M100}
M0-1	1.05	3.589	1.04614	3.882
M0-2	1.06	4.161	1.06445	3.882
M0-3	1.07	3.584	1.06445	3.882
M0-4	1.06	3.930	1.06077	3.882
M0-5	1.19	3.949	1.19360	3.882
M0-6	1.20	3.842	1.19775	3.882
M0-7	1.20	3.916	1.20191	3.882
M0-8	1.24	3.820	1.23574	3.882
M0-9	1.31	3.841	1.30629	3.882
M0-10	1.25	3.864	1.24868	3.882
M0-11	1.24	3.945	1.24435	3.882
M15-1	1.00	-*	0.97794	4.830
M15-2	1.00	-*	0.98067	4.830
M15-3	1.00	-*	0.98067	4.830
M15-4	1.00	-*	0.98615	4.830
M15-5	1.12	4.755	1.11802	4.830
M15-6	1.12	4.873	1.12114	4.830
M15-7	1.14	4.935	1.14324	4.830
M15-8	1.14	4.729	1.13689	4.830
M15-9	1.18	4.802	1.17886	4.830
M30-1	1.20	5.985	1.20273	5.911
M30-2	1.10	6.077	1.10296	5.911
M30-3	1.00	-*	0.96860	5.911

Continued on next page

*the log from a negative number is not defined

Continuation				
Test	$k_{c,table}$	$B_{calculated}$	$k_{c,calculated}$	B_{M100}
M30-4	1.20	5.985	1.20273	5.911
M30-5	1.10	6.077	1.10296	5.911
M60-1	1.15	7.325	1.15142	7.261
M60-2	1.10	7.632	1.10537	7.261
M60-3	1.15	7.325	1.15142	7.261
M60-4	1.10	7.632	1.10537	7.261
M100-1	1.03	5.924	1.02726	6.511
M100-2	1.03	6.380	1.02939	6.511
M100-3	1.05	6.902	1.05308	6.511
M100-4	1.04	5.839	1.03580	6.511
M100-5	1.13	6.613	1.13217	6.511
M100-6	1.12	6.300	1.11589	6.511
M100-7	1.12	6.656	1.12284	6.511
M100-8	1.12	6.419	1.11820	6.511
M100-9	1.12	6.300	1.11589	6.511
M100-10	1.24	6.513	1.24007	6.511
M100-11	1.24	6.387	1.23495	6.511
M100-12	1.20	6.428	1.19721	6.511

Appendix C for Chapter 4

A. Tab. 5: Hypoplastic parameters of the materials within the KELLER-database [2]

<i>Material</i>	$CaCO_3$ [%]	φ_c [°]	e_{d0}	e_{c0} [-]	e_{i0}	h_s [MPa]	n	α [-]	β
Al Zour LNG	9.73	31	0.365	0.747	0.859	102	0.542	0.095	1.43
Sheikh Jaber	28.6	31	0.385	1.015	1.167	40	0.375	0.140	1.40
Al Zour Package 5	42.45	33	0.41	0.84	0.966	175	0.483	0.130	1.74
JAT4: island	60.9	34.5	0.68	0.977	1.124	80	0.550	0.150	1.20
JAT4: south side	63.3	39.5	0.979	1.504	1.729	28	0.500	0.500	0.10
Palm Jumeirah	73.6	35	0.583	0.922	1.060	270	0.430	0.140	0.17
M100 Dubai sand	90	37.7	0.762	1.223	1.406	95	0.500	0.130	1.10
Palm Deira	96.2	36	0.725	1.226	1.410	80	0.480	0.230	0.70
PLM - AZ28	100	36.3	0.740	1.261	1.450	39	0.525	0.050	1.97
PLM - BC36	100	36.5	0.79	1.384	1.592	49	0.480	0.045	1.40
Zakkum Island	100	34	0.831	1.338	1.540	80	0.440	0.100	1.75

Appendix D for Chapter 5

A. Tab. 6: Comparison of KIM-parameters – Palm Jumeirah (values from [9])

	Report [43]	Excel Curve-Fit	Gnuplot Curve-Fit
a_1	2.277	2.967637	2.968853
a_2	-7.917	-6.27069	-6.26844
a_3	-1.615	-1.48249	-1.48233
b_1	0.876	0.890223	0.890316
b_2	0.082	0.105079	0.105235
b_3	-1.303	-1.41504	-1.41563

Appendix Tab. 7: Comparison of KIM-parameters – Palm Deira (values from [9])

	Report [43]	Excel Curve-Fit	Gnuplot Curve-Fit
a_1	-0.827	0.745923	0.751336
a_2	-12.483	-7.85557	-7.84595
a_3	-1.771	-1.48906	-1.48854
b_1	0.936	0.966421	0.966492
b_2	0.199	0.24011	0.240216
b_3	-1.375	-1.47082	-1.47099

```

%+++++
%Stress-Path-Diagrams and Pressure-Expansion-Curves for the Cavity expansion
%*****For 1 Id and up to 5 different presssures p0*****
%+++++
%
%*****
%Specifitcation of the hypoplastic soil parameters, the initial conditions
%and the desired input data files
%*****
clc
clear
close all

%)Initialize Hypoplastic Soil Parameters
hs = 39; %[MPa]
n = 0.525; %[-]
ed0 = 0.74; %[-]
ec0 = 1.261; %[-]
phi_c = 36.3; %[°]

%)Initialize initial geometry
ra0=0.1;
rb0=50;

%)Specify the Linestyles of the plottet lines
%plotStyle={'-b','-r','-g','-b','-r','--r',':r','-r','-k','--k'}; Not in
%use

```

```

%)Specify the Filenames *.txt files and the pressures p0 for which the curves
%will be plotted

%)Choose which curves to be plotted
%Example: p0= 0.025 and p0 =0.1 MPa ---> N =[1 3]
%The numbers within N correspond to the MaterialID

N=[1 2 3 4 5];

%)Filename Specification of 5 different files at same relative density
FileName{1} ='025_i09.txt'; %MaterialID_1(p0 = 25[kPa])
FileName{2} ='050_i09.txt'; %MaterialID_2(p0 = 50[kPa])
FileName{3} ='100_i09.txt'; %MaterialID_3(p0 = 100 [kPa])
FileName{4} ='150_i09.txt'; %MaterialID_4(p0 = 150 [kPa])
FileName{5} ='300_i09.txt'; %MaterialID_5(p0 = 300 [kPa])

ID1string = string(strcat({' ',FileName{1}(6),'.',FileName{1}(7)}));

Pstring={[]};

for i = 1:length(N)
    Pstring{i} = strcat('0.',FileName{N(i)}(1:3));
    j=j+1;
end
clear j

%Extraction of data from the text files produced by OSINOV - CODE

M ={[]};

for i = 1:length(N)
    M{i}=ExtractInputDataALL_OSINOV(FileName{N(i)});
end

%*****
%1)s-t Stress Path
%*****

%Critical state Line
sC=linspace(0,5,500);
tC = sin(phi_c*pi()/180)*sC;

%Actual Stress Paths
ST={[]};
for i = 1:length(N)
    ST{i} = s_t_Calc(M{i}(:,2),M{i}(:,3));
end

PlotST_Allp(ID1string,ST,Pstring,N,sC,tC)

%*****
%2)p - q - Stress Path
% p = (Sigma1+2Sigma3)/3    q = Sigma1 - Sigma3
%*****

%Critical state Line
pC = linspace(0,5,500);
qC = 6*pC*sin(phi_c*pi()/180)/(3-sin(phi_c*pi()/180));

```

```

%Actual p/q values

PQ={[]};
for i = 1:length(N)
PQ{i} = p_q_Calc(M{i}(:,2),M{i}(:,3));
end

PlotPQ_Allp(ID1string,PQ,Pstring,N,pC,qC)

%*****
%3)log p - e - Diagram (including the lines for ec and ed dependent
%on pressure)
%ec = ec0*exp[-(3*p/hs)^n]   ed = ed0*exp[-(3*p/hs)^n]
%*****

p_range=linspace(0,10,500);
ec = transpose(ec0*exp(-(3*p_range/hs).^n)); %limit void ratio
ed = transpose(ed0*exp(-(3*p_range/hs).^n)); %limit void ratio

VOIDRAT={[]};
for i=1:length(N)
    VOIDRAT{i}=M{i}(:,4);    %Void ratios SCE
end

PlotLogP_E_Allp(ID1string,p_range,ec,ed,PQ,VOIDRAT,Pstring,N)

hold off
%*****
%4)ra/ra0 - Diagrams
%*****

ra_ra0={[]};
for i = 1:size(M,2)
    ra_ra0{i}=M{i}(:,1)/ra0;
end

%ra/ra0 - pr - Diagram

figtit = strcat('r_{a}/r_{a0} - p_{r} - Diagram(SCE for r_{a}/r_{a0} = 1 to 11 and ID =
',ID1string,')');
figure('Name',figtit,'NumberTitle','off','color','white')

axis square
grid on
hold on
box on

for i = 1:length(N)
plot(ra_ra0{i},M{i}(:,2)*-1,'-','Linewidth',1.0);
xlim([1 12]);
end
xticks(1:12);
title(figtit,'fontweight','bold','fontsize',12);
xlabel('r_{a}/r_{a0} [-]','fontsize',11,'fontweight','bold');
ylabel('p_{r} [MPa]','fontsize',11,'fontweight','bold');
leg=legend(Pstring,'Location','northwest');
title(leg,'p_{0} [MPa]');
set(leg,'fontsize',10);

```

```

%)ra/ra0 - p_Phi - Diagram (p_Phi = tangential stresses)

figtit = strcat('r_{a}/r_{a0} - p_{\theta} - Diagram (SCE for r_{a}/r_{a0} = 1 to 11 and
ID = ',ID1string,')');
figure('Name',figtit,'NumberTitle','off','Color','white')

axis square
grid on
hold on
box on

for i = 1:length(N)
plot(ra_ra0{i},M{i}(:,3)*-1,'-','Linewidth',1.0);
xlim([1 12]);
end
xticks(1:12);
title(figtit,'fontweight','bold','fontsize',12);
xlabel('r_{a}/r_{a0} [-]','fontsize',11,'fontweight','bold');
ylabel('p_{\theta} [MPa]','fontsize',11,'fontweight','bold');
leg=legend(Pstring,'Location','northwest');
title(leg,'p_{0} [MPa]');
set(leg,'fontsize',10);

%)ra/ra0 - e - Diagram

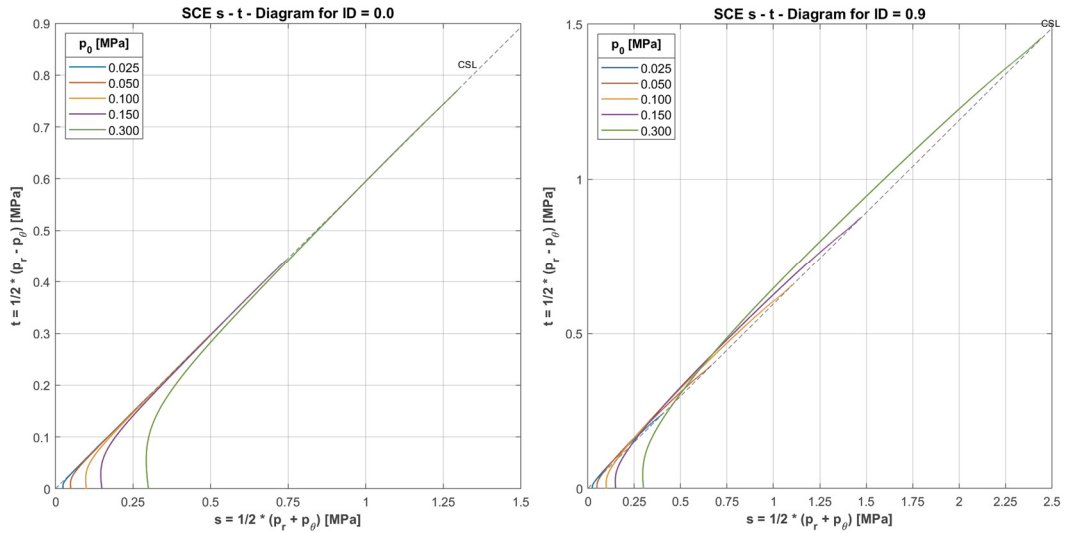
figtit = strcat('r_{a}/r_{a0} - e - Diagram (SCE for r_{a}/r_{a0} = 1 to 11 and ID =
',ID1string,')');
figure('Name',figtit,'NumberTitle','off','Color','white')

axis square
grid on
hold on
box on

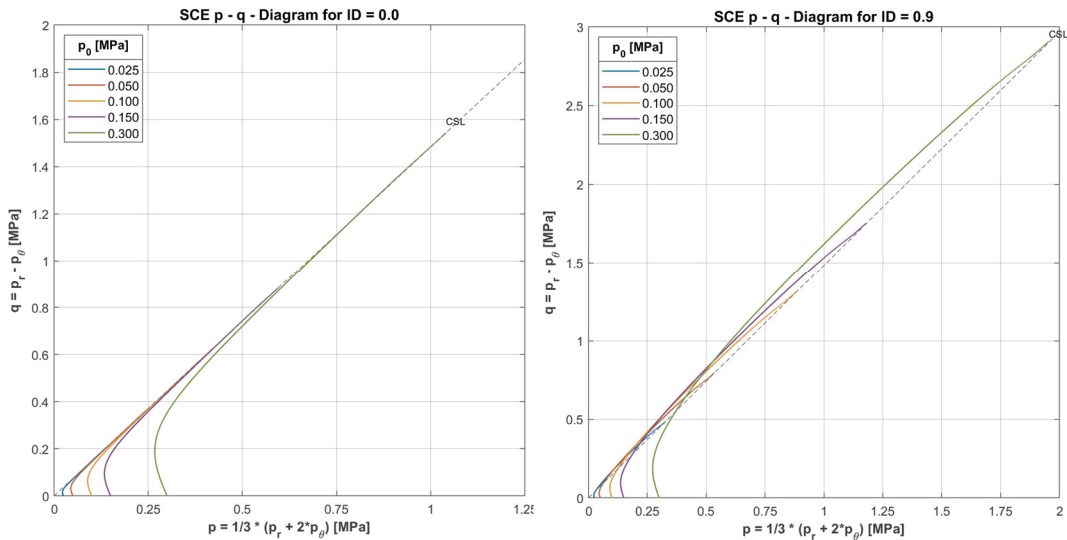
for i = 1:length(N)
plot(ra_ra0{i},M{i}(:,4),'-','Linewidth',1.0);
xlim([1 12]);
end
xticks(1:12);
title(figtit,'fontweight','bold','fontsize',12);
xlabel('r_{a}/r_{a0} [-]','fontsize',11,'fontweight','bold');
ylabel('e [-]','fontsize',11,'fontweight','bold');
leg=legend(Pstring,'Location','northwest');
title(leg,'p_{0} [MPa]');
set(leg,'fontsize',10);

```

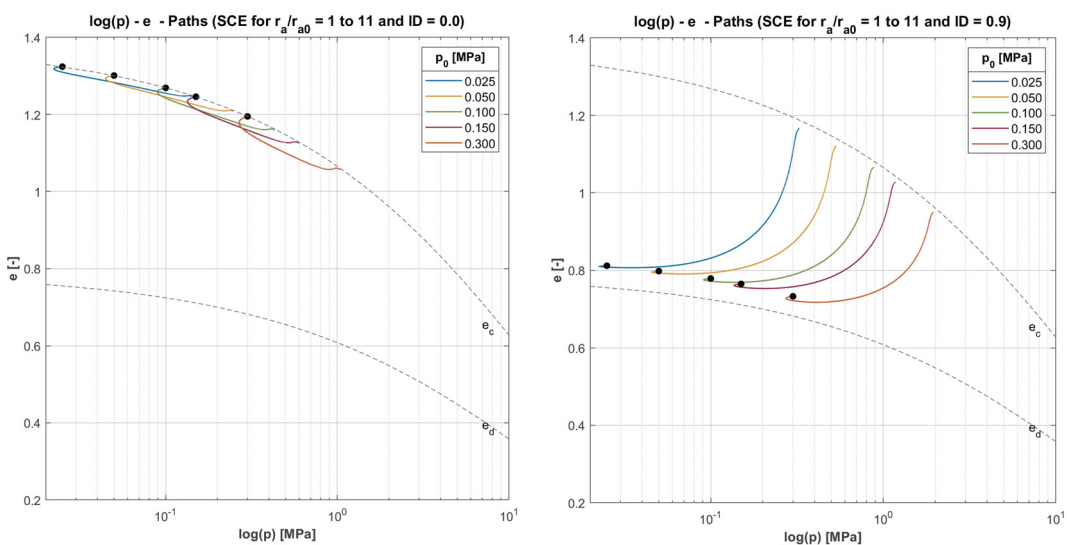
A. Fig 1: MATLAB-code from the StressPaths_IID_Allp.m script



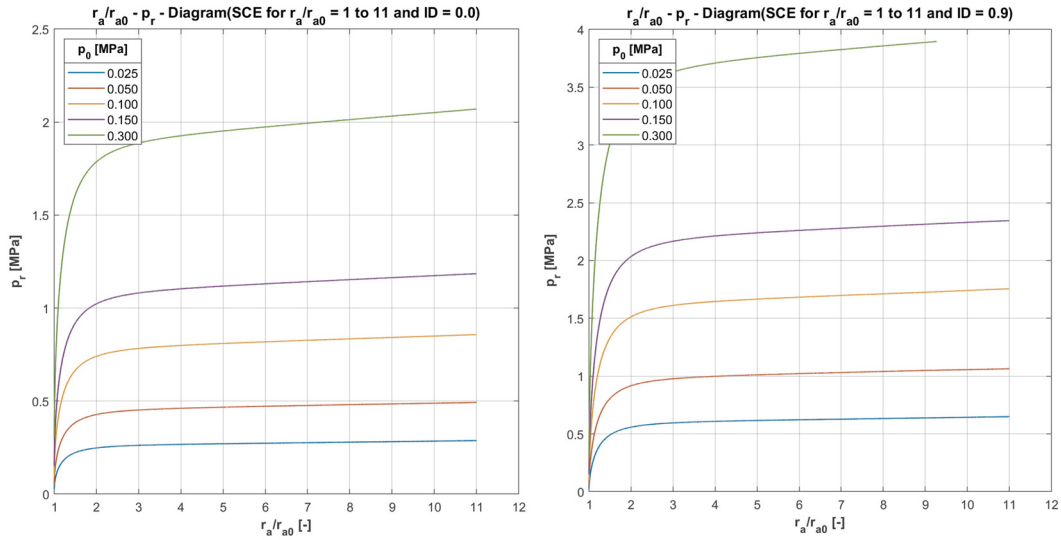
A. Fig 2: $s - t$ - diagrams for PLM BC36 for 5 different p_0 and $I_D = 0.0$ (left) and $I_D = 0.9$ (right)



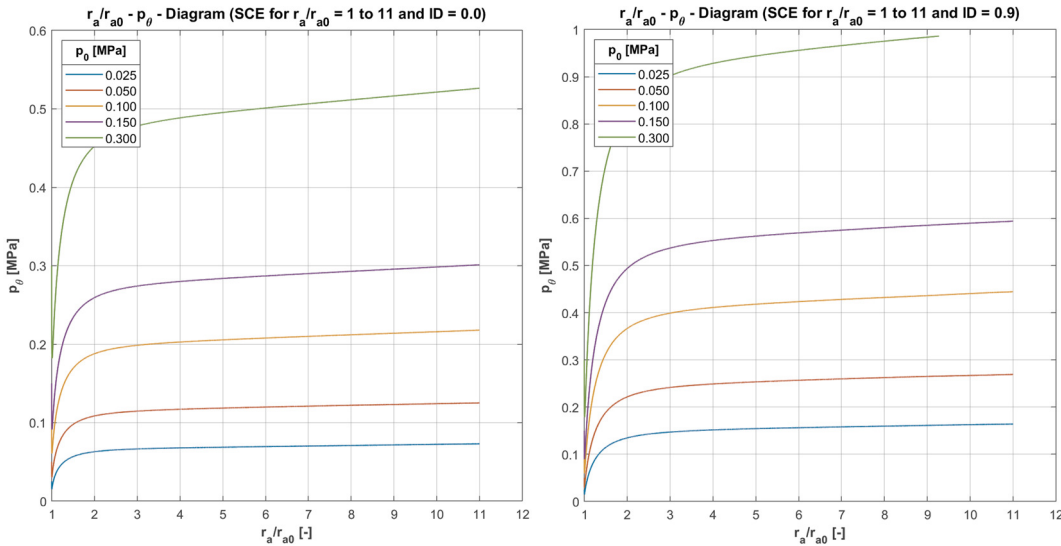
A. Fig 3: $p - q$ - diagrams for PLM BC36 for 5 different p_0 and $I_D = 0.0$ (left) and $I_D = 0.9$ (right)



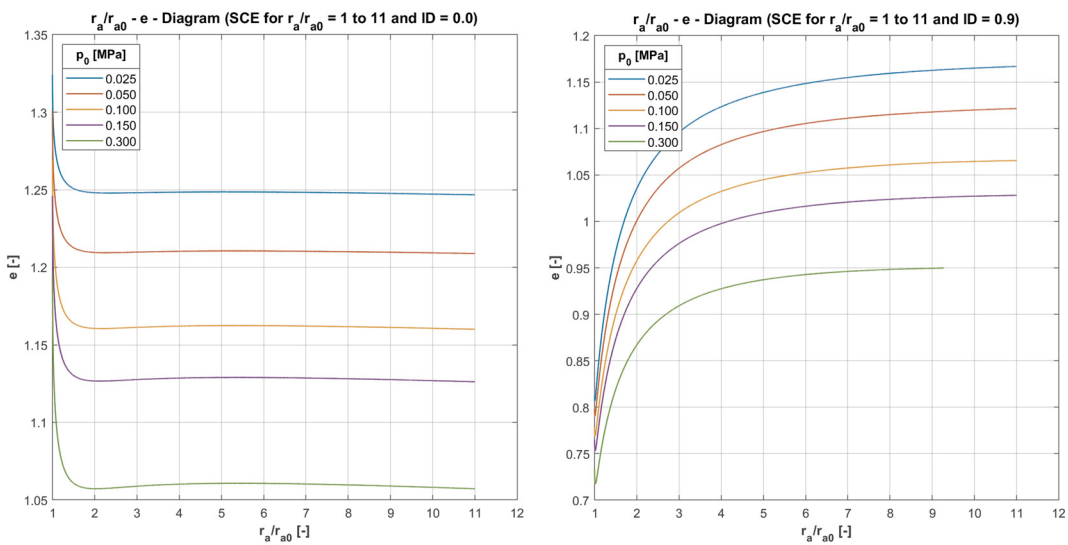
A. Fig 4: $\log(p) - e$ - diagrams for PLM BC36 for 5 different p_0 and $I_D = 0.0$ (left) and $I_D = 0.9$ (right)



A. Fig 5: $r_a/r_a^0 - p_r$ - diagrams for PLM BC36 for 5 different p_0 and $I_D = 0.0$ (left) and $I_D = 0.9$ (right)



A. Fig 6: $r_a/r_a^0 - p_\theta$ - diagrams for PLM BC36 for 5 different p_0 and $I_D = 0.0$ (left) and $I_D = 0.9$ (right)



A. Fig 7: $r_a/r_a^0 - e$ - diagrams for PLM BC36 for 5 different p_0 and $I_D = 0.0$ (left) and $I_D = 0.9$ (right)

```

%+++++
%Stress-Path-Diagrams and Pressure-Expansion-Curves for the Cavity expansion
%*****For 1 p0 and up to 10 different ID*****
%+++++

%*****
%Specification of the hypoplastic soil parameters, the initial conditions
%and the desired input data files
%*****

clc
clear
close all

%Initialize Hypoplastic Soil Parameters
hs = 49; %[MPa]
n = 0.48; %[-]
ed0 = 0.79; %[-]
ec0 = 1.384; %[-]
phi_c = 36.5; %[°]

%Initialize initial geometry
ra0=0.1;
rb0=50;

%Specify the Linestyles of the plottet lines
plotStyle={'-b','--b',':k','-.k','-b','--b',':b','-.b','-r','--r'};

%)Specify the Filenames *.txt files and the IDs for which the curves
%will be plotted

%Vector N can be used to select certain IDs to be plotted.
%Just enter the MaterialID of the files from sequence below into N.
%i.e. N=[1 3 6 8] The numbers correspond to the MaterialID

N=[1 2 3 4 5 6 7 8 9 10];

FileName{1} = '300_i00.txt'; %MaterialID_1 (Id00 at p0 = 100 [kPa])
FileName{2} = '300_i01.txt'; %MaterialID_2 (Id01 at p0 = 100 [kPa])
FileName{3} = '300_i02.txt'; %MaterialID_3 (Id02 at p0 = 100 [kPa])
FileName{4} = '300_i03.txt'; %MaterialID_4 (Id03 at p0 = 100 [kPa])
FileName{5} = '300_i04.txt'; %MaterialID_5 (Id04 at p0 = 100 [kPa])
FileName{6} = '300_i05.txt'; %MaterialID_6 (Id05 at p0 = 100 [kPa])
FileName{7} = '300_i06.txt'; %MaterialID_7 (Id06 at p0 = 100 [kPa])
FileName{8} = '300_i07.txt'; %MaterialID_8 (Id07 at p0 = 100 [kPa])
FileName{9} = '300_i08.txt'; %MaterialID_9 (Id08 at p0 = 100 [kPa])
FileName{10} = '300_i09.txt'; %MaterialID_10 (Id09 at p0 = 100 [kPa])

pstring=strcat(' 0.',FileName{N(1)}(1:3));

IDstring={[]};
j=1;
for i = N
    IDstring{j} = strcat('0.',FileName{i}(7));
    j=j+1;
end
clear j

```

```

%)Extract the data from the text files produced by OSINOV - CODE

M ={[]};

for i = 1:length(N)
    M{i}=ExtractInputDataALL_OSINOV(FileName{N(i)});
end

%*****
%1)s-t Stress Path
%*****

%Critical State Line
sC=linspace(0,5,500);
tC = sin(pi()/180*phi_c)*sC;

%Actual s-t-values
ST={[]};
for i = 1:length(N)
    ST{i} = s_t_Calc(M{i}(:,2),M{i}(:,3));
end
PlotST_AllID(pstring,ST,plotStyle,IDstring,N,sC,tC)

%*****
%2)p - q - Stress Path
% p = (Sigma1+2Sigma3)/3   q = Sigma1 - Sigma3
%*****

%Critical State Line
pC = linspace(0,5,500);
qC = 6*pC*sin(phi_c*pi()/180)/(3-sin(phi_c*pi()/180));

%Actual p-q-values
PQ={[]};
for i = 1:length(N)
    PQ{i} = p_q_Calc(M{i}(:,2),M{i}(:,3));
end

PlotPQ_AllID(pstring,PQ,plotStyle,IDstring,N,pC,qC)

%*****
%3)log p - e - Diagram (including the lines for ec and ed dependent on
%pressure)
%ec = ec0*exp[-(3*p/hs)^n]   ed = ed0*exp[-(3*p/hs)^n]
%*****

%Void ratio limits
p_range=linspace(0,10,500);
ec = transpose(ec0*exp(-(3*p_range/hs).^n)); %limit void ratio
ed = transpose(ed0*exp(-(3*p_range/hs).^n)); %limit void ratio

%Actual e-values
VOIDRAT={[]};
for i=1:length(N)
    VOIDRAT{i}=M{i}(:,4);   %Void ratios SCE
end

PlotLogP_E_AllID(pstring,p_range,ec,ed,PQ,VOIDRAT,plotStyle,IDstring,N)

```

```

%*****
%4)ra/ra0 - Diagrams
%*****

ra_ra0={[]};
for i = 1:size(M,2)
    ra_ra0{i}=M{i}(:,1)/M{i}(1,1);
end

%*****ra/ra0 - pr - Diagram*****

Plot_rRatio_pr_AllID(pstring,ra_ra0,M,plotStyle,IDstring,N)

%*****ra/ra0 - p_Phi - Diagram*****

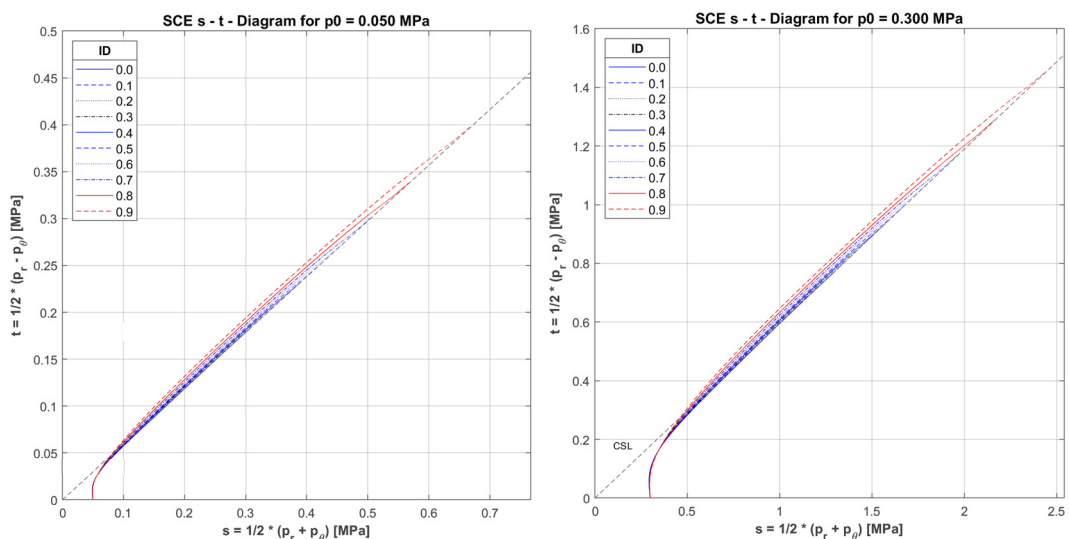
Plot_rRatio_pPhi_AllID(pstring,ra_ra0,M,plotStyle,IDstring,N)

%*****ra/ra0 - e - Diagram*****

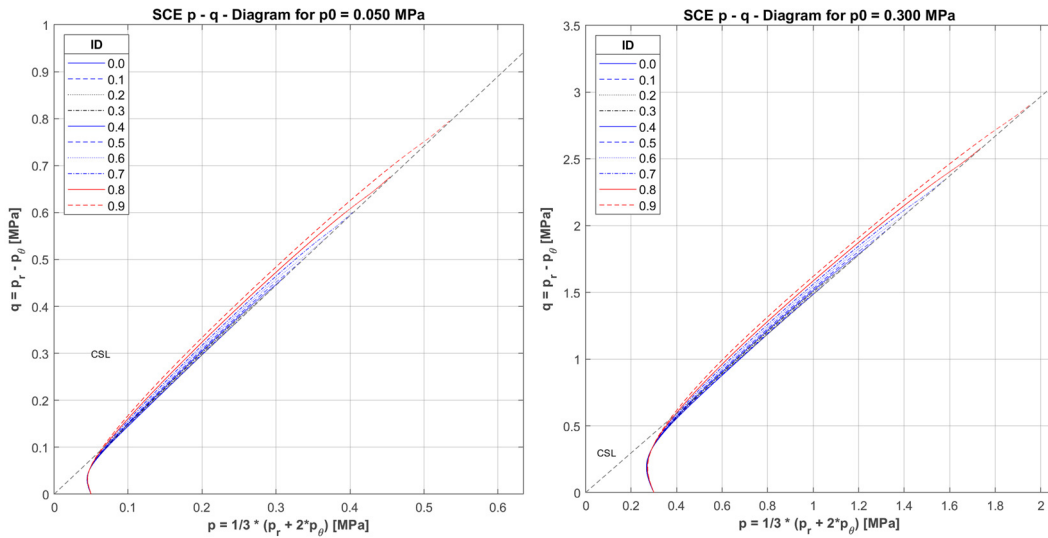
Plot_rRatio_e_AllID(pstring,ra_ra0,M,plotStyle,IDstring,N)

```

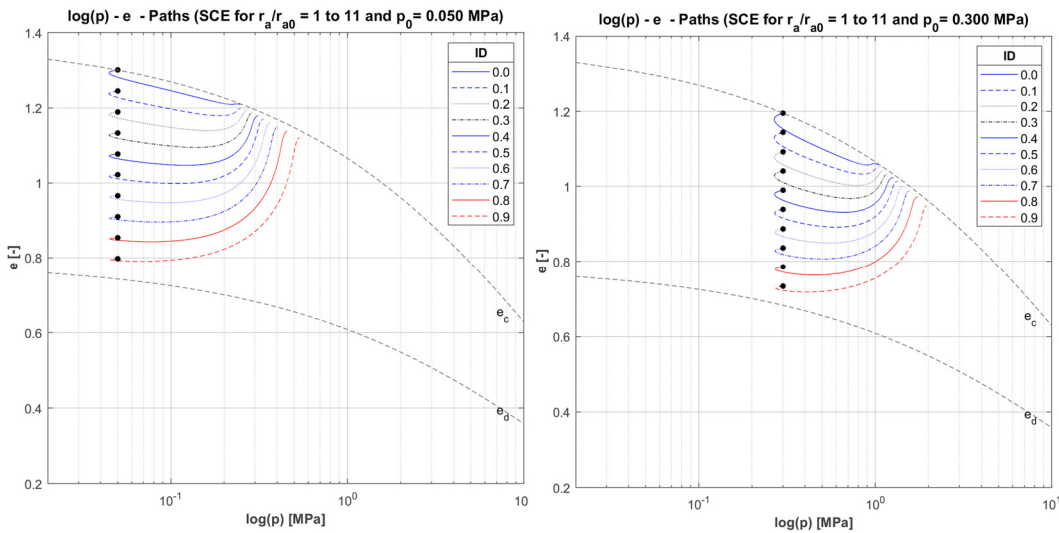
A. Fig 8: MATLAB-code from the StressPaths_1p_AllID.m script



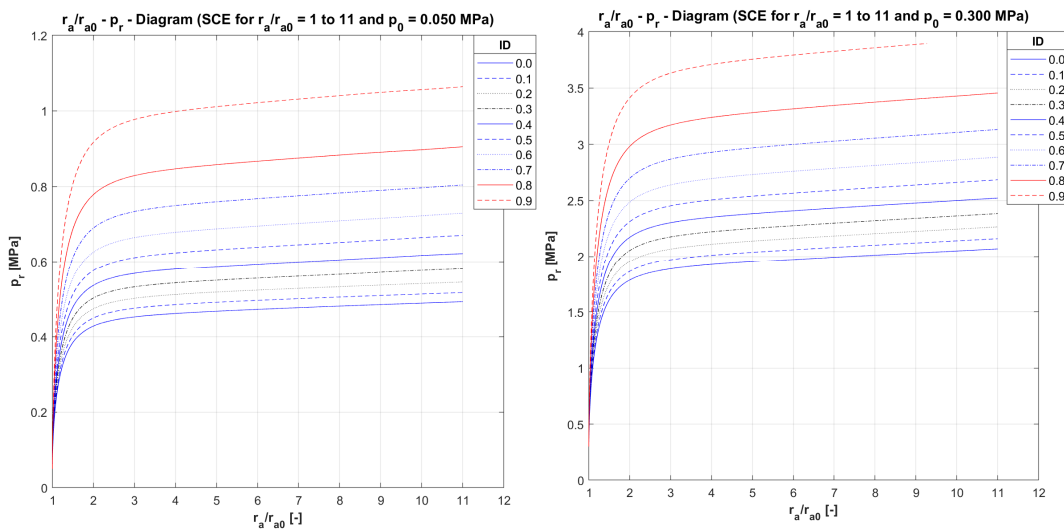
A. Fig 9: $s - t$ - diagrams for PLM BC36 for 10 different I_D and $p_0 = 0.050$ MPa (left) or $p_0 = 0.300$ MPa (right)



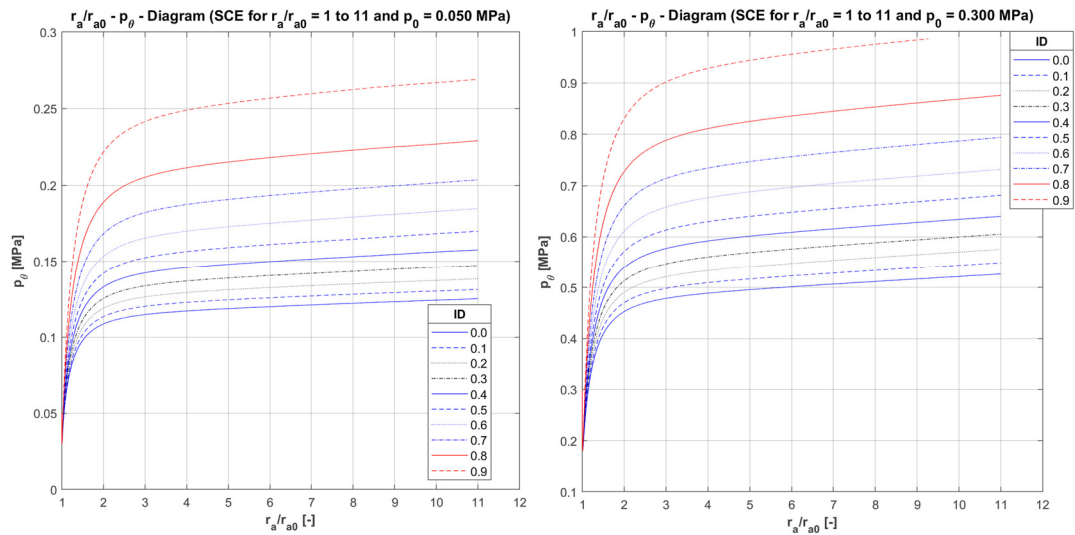
A. Fig 10: $p - q$ - diagrams for PLM BC36 for 10 different I_D and $p_0 = 0.050$ MPa (left) or $p_0 = 0.300$ MPa (right)



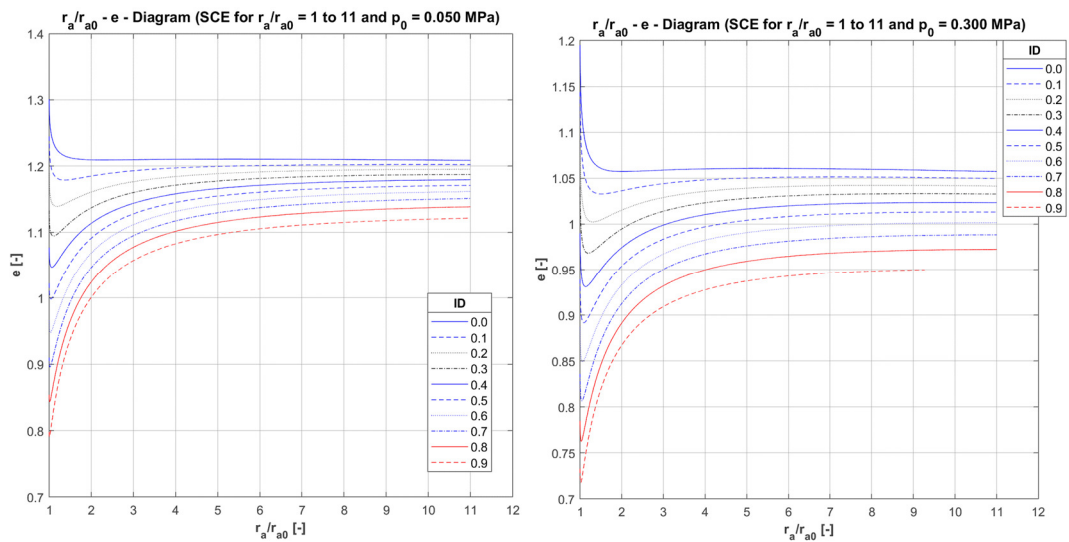
A. Fig 11: $\log(p) - e$ - diagrams for PLM BC36 for 10 different I_D and $p_0 = 0.050$ MPa (left) or $p_0 = 0.300$ MPa (right)



A. Fig 12: $r_a/r_a^0 - p_r$ - diagrams for PLM BC36 for 10 different I_D and $p_0 = 0.050$ MPa (left) or $p_0 = 0.300$ MPa (right)



A. Fig 13: r_a/r_{a0}^0 - p_{θ} - diagrams for PLM BC36 for 10 different I_D and $p_0 = 0.050$ MPa (left) or $p_0 = 0.300$ MPa (right)



A. Fig 14: r_a/r_{a0}^0 - e - diagrams for PLM BC36 for 10 different I_D and $p_0 = 0.050$ MPa (left) or $p_0 = 0.300$ MPa (right)

Appendix E for Chapter 6

```

%SPHERICAL CAVITY EXPANSION inside an INFINITE, LINEAR ELASTIC - PERFECTLY PLASTIC soil
body
%The closed form solution acc. to Yu and Houlsby (1991) is used within the code

clc
clear
close all

%*****
%1) *****Choose input soil parameters E,ny,coh, phi, psi, p0*****
%*****

Materialname=strcat('Mat1');
m=2; %1 for cylindrical expansion and 2 for spherical expansion

E = 25000; %Young's modulus in [kPa]
ny = 0.2; %Poisson's ratio [-]
coh = 0; %Cohesion in [kPa]
phi = 30; %Friction angle [°]
psi = 0; %Dilatancy angle [°]

p0 = 300; %initial isotropic pressure [kPa]
n_series=10; %Number of terms for infinite series

%*****
%2) Calculation of the derived parameters G, Y, alpha, beta, gamma,delta*
%*****

G = E/(2*(1+ny)); %Shear Modulus [kPa]

M=E/(1-ny^2*(2-m));
%The MC Yield Criterion is given by Alpha*Sigma1-Sigma3 = Y
Y = 2*coh*cos(phi*pi()/180)/(1-sin(phi*pi()/180));

alpha = (1+sin(phi*pi()/180))/(1-sin(phi*pi()/180));

beta = (1+sin(psi*pi()/180))/(1-sin(psi*pi()/180));

gamma = alpha*(m+beta)/(m*(alpha-1)*beta);

delta = (Y+(alpha-1)*p0)/(2*(m+alpha)*G);

eta=exp((beta+m)*(1-2*ny)*(Y+(alpha-1)*p0)*(1+(2-m)*ny)/(E*(alpha-1)*beta));

chi=(1-ny^2*(2-m))*(1+m)*delta/((1+ny)*(alpha-1)*beta)*(alpha*beta+m*(1-2*ny)...
+2*ny-m*ny*(alpha+beta)/(1-ny*(2-m)));

%*****
%3) ***** Elastic calculation part *****
%*****

p1_Elast=2*m*G*delta+p0; %yielding pressure
p_Elast=transpose(linspace(p0,p1_Elast,100)); %vector of varying p
p_Elast(1)=[]; %p>p0!

```

```

p_Elast(end)=[]; %p<yielding pressure
aa0_Elast=zeros([length(p_Elast) 1]);
for i=1:length(p_Elast)
    aa0_Elast(i)=(p_Elast(i)-p0)/(2*m*G)+1; %calculate elastic a/a0
end
% plot(aa0_Elast,p_Elast);

%*****
%4)*****Elastic-Plastic Calculation part*****
%*****

%Finding the limit pressure

An1_infinite=@(~)0;
for i=0:n_series
    if i==gamma
        An1_Current_inf=@(x)chi^i/factorial(i)*ln(x);
    else
        An1_Current_inf=@(x)chi^i/(factorial(i)*(i-gamma))*(x^(i-gamma)-1);
    end
    An1_infinite=@(x)An1_infinite(x)+An1_Current_inf(x);
end

LHS_infinite=eta/gamma*(1-delta)^((beta+m)/beta);
func_infinite=@(x)LHS_infinite-An1_infinite(x);
R_infinite=fsolve(func_infinite,15); %<-----Modify Initial Guess (3Digits)

p_infinite=1/(alpha-1)*((R_infinite*(alpha*(1+m)*(Y+(alpha-1)...
*p0))*1/(m+alpha))-Y);

%Calculating the pressure-expansion-curve

p_Plust=transpose(linspace(round(p1_Elast),floor(p_infinite),10000));
R_Plust=(m+alpha)*(Y+(alpha-1).*p_Plust)/(alpha*(1+m)*(Y+(alpha-1)*p0));

An1_finite=zeros([length(R_Plust) 1]);

for j=1:length(R_Plust)
    for i=0:n_series
        if i==gamma
            An1_Current=chi^i/factorial(i)*ln(R_Plust(j));
        else
            An1_Current=chi^i/(factorial(i)*(i-gamma))*(R_Plust(j)^(i-gamma)-1);
        end
        An1_finite(j)=An1_finite(j)+An1_Current;
    end
end

aa0_Plust=zeros([length(R_Plust) 1]);
for i=1:length(p_Plust)
    aa0_Plust(i)=(R_Plust(i)^(-gamma)/((1-delta)^((beta+m)/beta)-(gamma/eta)*...
    An1_finite(i)))^(beta/(beta+m));
end

%*****
%5)*****Plotting the Results*****
%*****

```

```

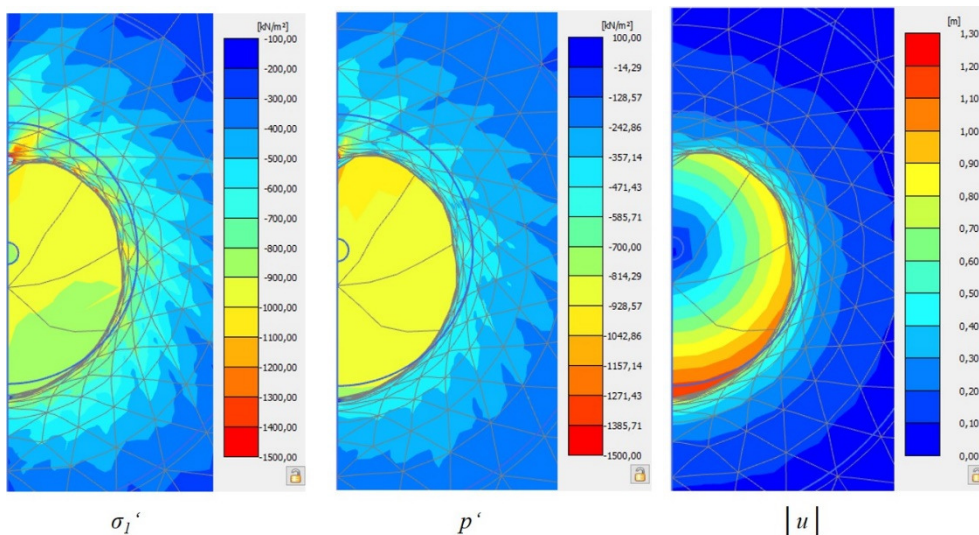
aa0_Collected=vertcat(aa0_Elast,aa0_Plast);
p_Collected=vertcat(p_Elast,p_Plast);

figtit = 'Pressure-Expansion-Curve ( p_{0} = 300 kPa)';
figure('Name',figtit,'NumberTitle','off','Color','white')
grid on
box on
hold on
b={[]};
plot(aa0_Collected,p_Collected,'Linewidth',1);
xlim([1 6]);
title(figtit,'fontweight','bold','fontsize',12);
xlabel('a/a_{0} [-]','fontsize',11,'fontweight','bold');
ylabel('Cavity Pressure p [kPa]','fontsize',11,'fontweight','bold');
leg=legend(strcat('SCE-',Materialname),'Location','northwest');
title(leg,'Legend');
set(leg,'fontsize',10);

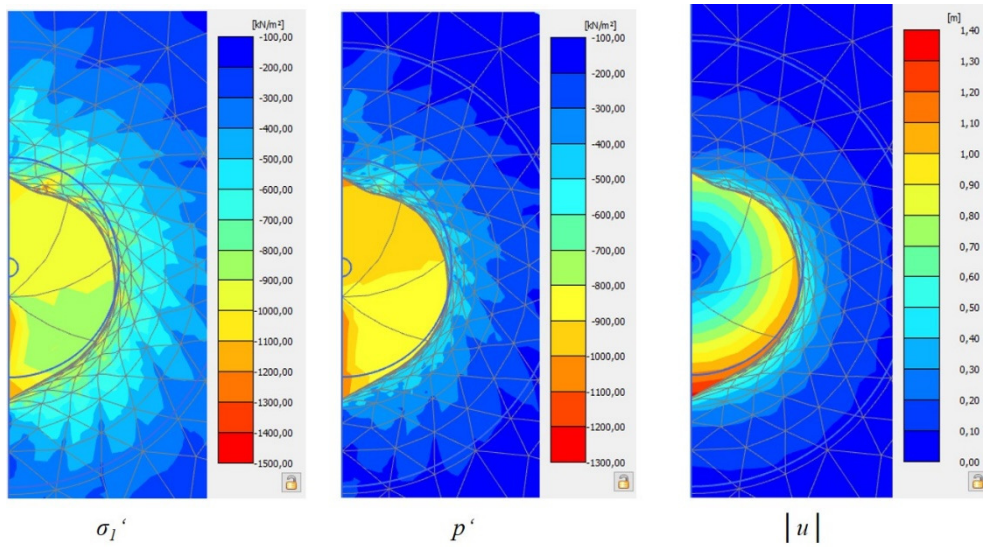
%*****
%6)*****Writing into Textfile*****
%*****
filename=strcat('PAA0_Data_', Materialname, '.txt');
table1=table(aa0_Collected,p_Collected);
writetable(table1,filename);

```

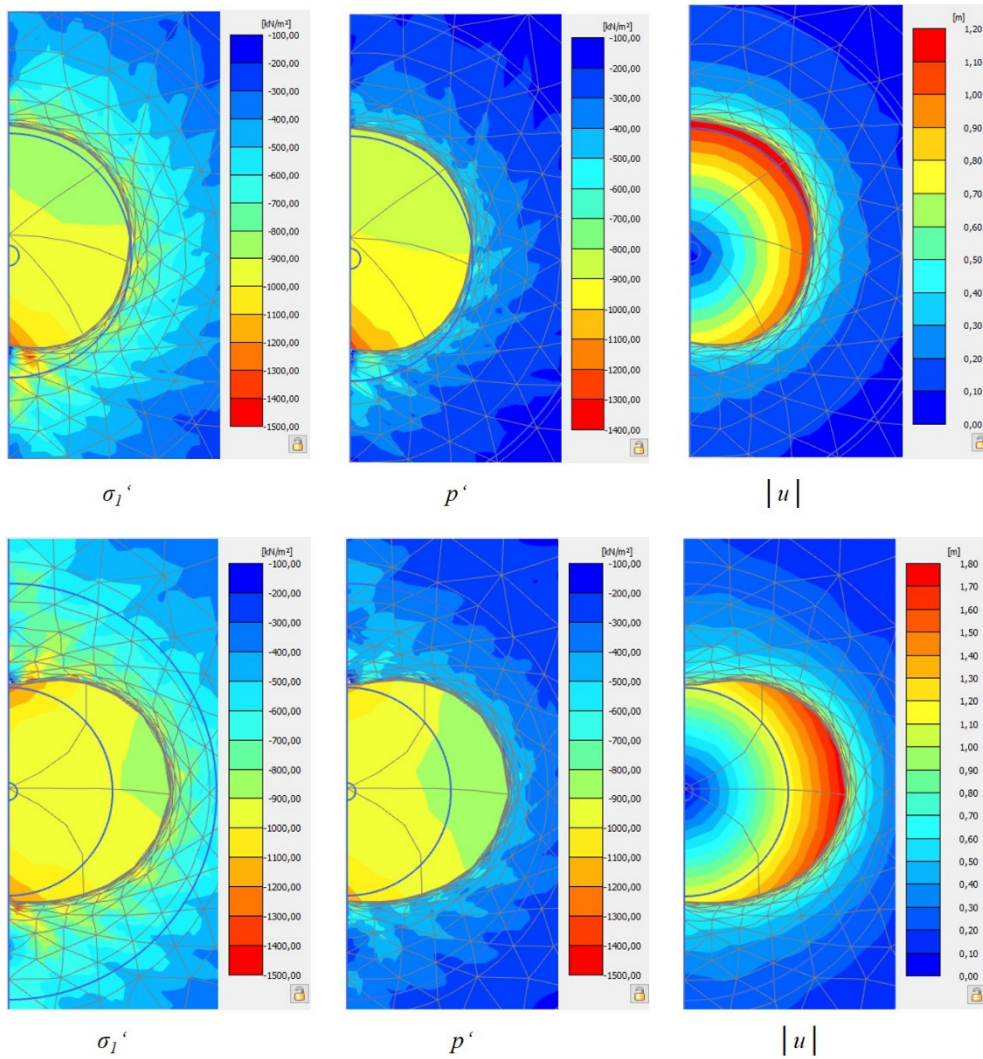
A. Fig 15: MATLAB-code for the closed-form solution by Yu and Houlsby [44] of the SCE within an infinite continuum



A. Fig 16: Distribution of σ'_l , p' and $|u|$ across the cavity – CavityE250 model

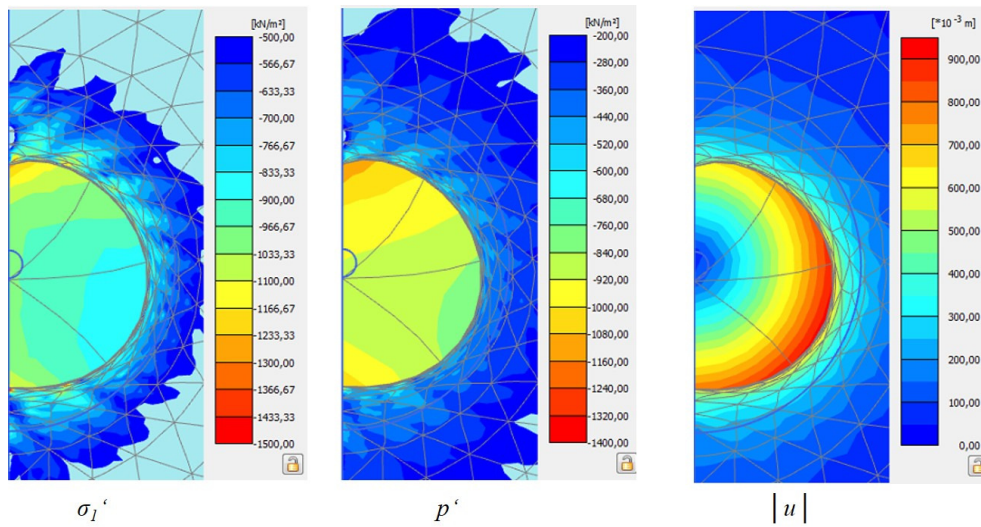


A. Fig 17: Distribution of σ_1' , p' and $|u|$ across the cavity – CavityE250_ny0 model

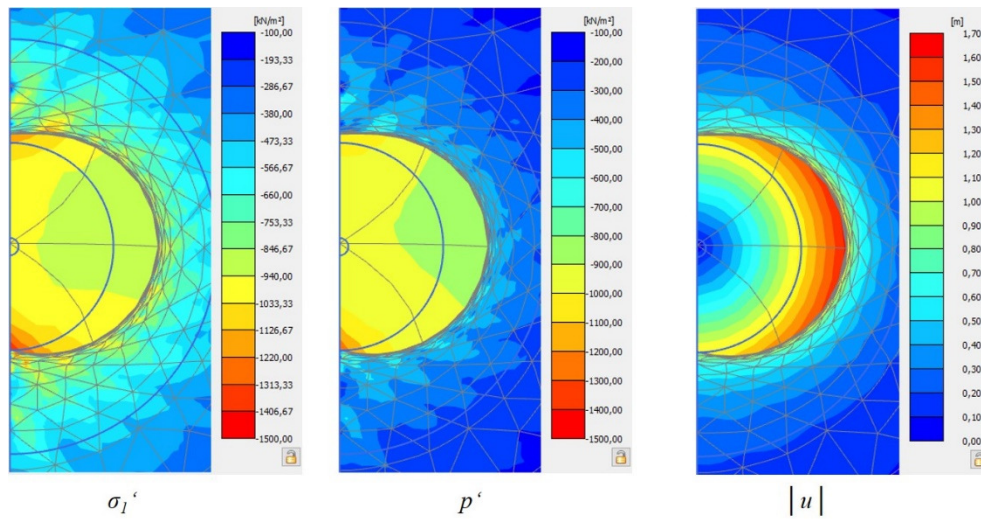


A. Fig 18: Distribution of σ_1' , p' and $|u|$ across the cavity – CavityE1000 model

A. Fig 19: Distribution of σ_1' , p' and $|u|$ across the cavity – CavityE1000_ny0 model



A. Fig 20: Distribution of σ_I' , p' and $|u|$ across the cavity – CavityE2000 model



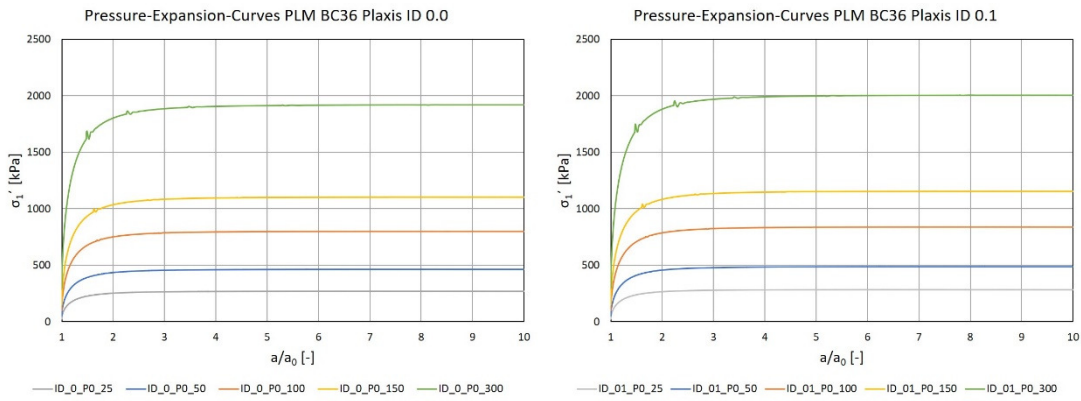
A. Fig 21: Distribution of σ_I' , p' and $|u|$ across the cavity – CavityE2000_ny0 model

```

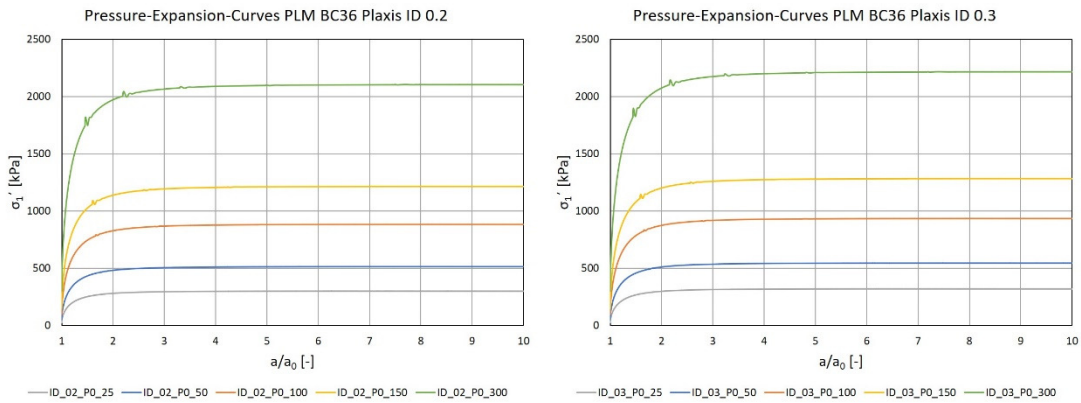
1  from plxscripting.easy import *
2  from numpy import *
3  s_i, g_i = new_server('localhost', 10000, password='AH=f^9y@r5?/LuSc')
4
5
6  ID = [0.0, 0.1, 0.2, 0.3, 0.4, 0.5, 0.6, 0.7, 0.8, 0.9]
7  p0 = [0.025, 0.050, 0.100, 0.150, 0.300]
8  e0 = []
9  ec0 = 1.261
10 ed0 = 0.74
11 hs = 39
12 n = 0.525
13 title="AZ28_PortdelaMer"
14 PhaseNum=11
15
16 for k in range (0, len(ID)):
17     zP = 0
18     e0.append(ec0-ID[k]*(ec0-ed0))
19
20
21 print(e0)
22
23 #+++++++Creation of the 50 different
24 Models+++++++
25
26 for j in range (0, len(p0)):
27     for i in range(0, len(ID)):
28         einit = ec0*exp(-((3*p0[j]/hs)**n))-ID[i]*exp(-((3*p0[j]/hs)**n))*(ec0-ed0)
29         #print(einit)
30         g_i.Materials[1].setproperties("einit", einit)
31         g_i.Materials[1].setproperties("User16", e0[i])
32         g_i.Materials[0].setproperties("gammaUnsat", p0[j]*1000,"gammaSat", p0[j]*1000)
33         IDstring = str(ID[i])
34         p0stringNoZeros = str(p0[j])
35         p0string = p0stringNoZeros[::-1].zfill(5)[::-1]
36         print(p0string)
37         name = "\ID_0" + IDstring[2] + "_p0_" + p0string[2:] + ".p2dx"
38
39
40         g_i.save("C:\\Users\\manuel_winkler\\Documents\\ManuelWinkler_Thesis\\Python\\50
41 Models"+name)
42
43 #+++++++Calculation of the 50 different
44 Models+++++++
45
46 for j in range (0, len(p0)):
47     for i in range(0, len(ID)):
48
49         IDstring = str(ID[i])
50         p0stringNoZeros = str(p0[j])
51         p0string=p0stringNoZeros[::-1].zfill(5)[::-1]
52         print(p0string)
53         name = "\ID_0" + IDstring[2] + "_p0_" + p0string[2:] + ".p2dx"
54
55
56         s_i.open("C:\\Users\\manuel_winkler\\Documents\\ManuelWinkler_Thesis\\Python\\50
57 Models"+name)
58         g_i.calculate()
59         g_i.save()

```

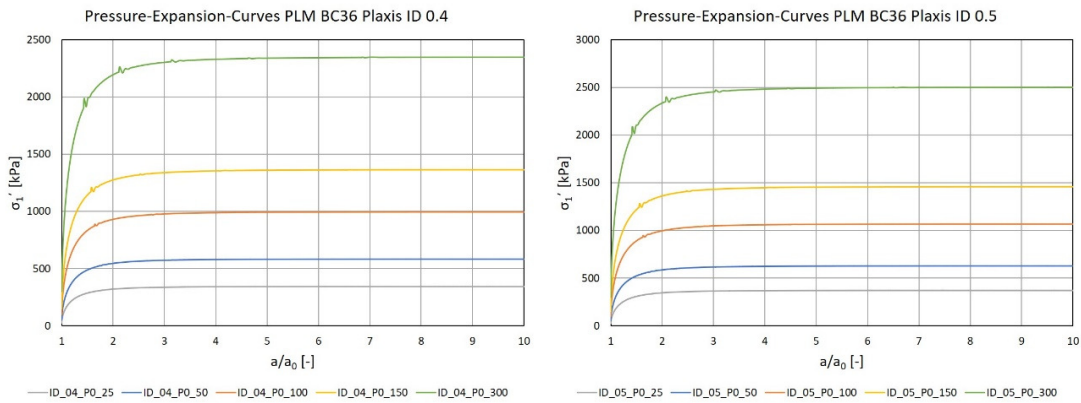
A. Fig 22: Python script - Automatic model generation - KIM-analysis



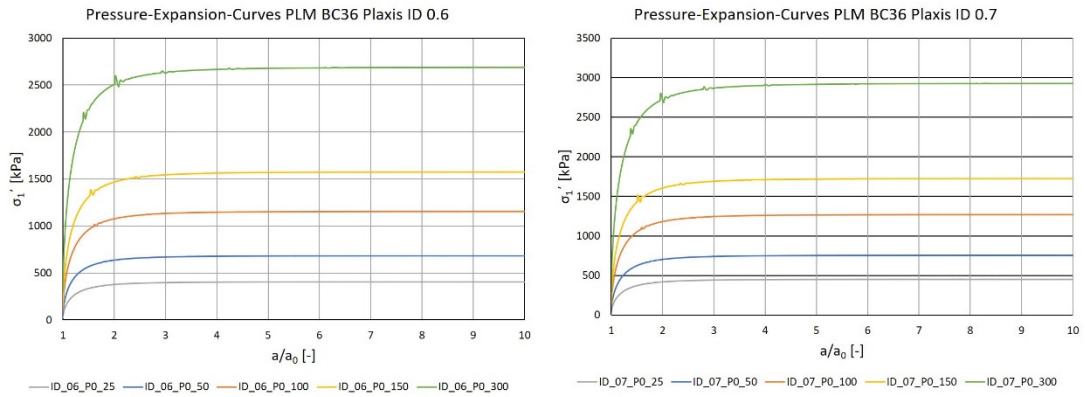
A. Fig 23: Pressure-expansion-curves PLM BC36 for I_D 0.0 and 0.1 (PLAXIS)



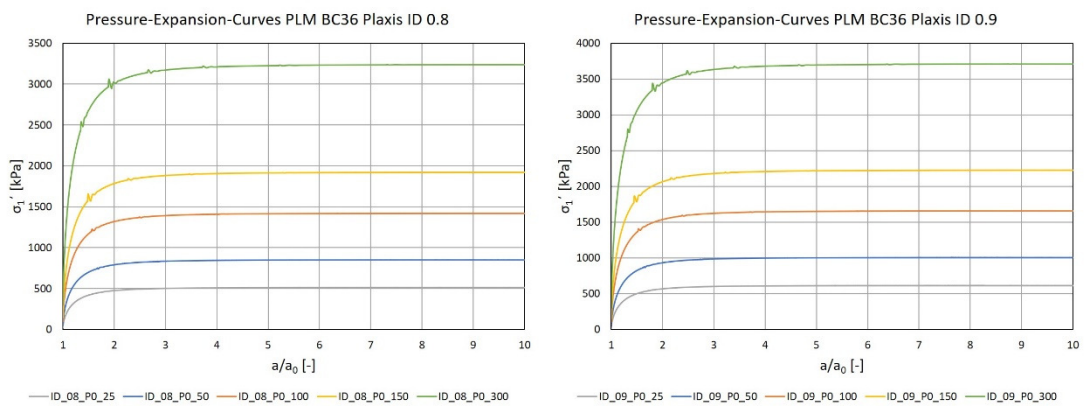
A. Fig 24: Pressure-expansion-curves PLM BC36 for I_D 0.2 and 0.3 (PLAXIS)



A. Fig 25: Pressure-expansion-curves PLM BC36 for I_D 0.4 and 0.5 (PLAXIS)



A. Fig 26: Pressure-expansion-curves PLM BC36 for I_D 0.6 and 0.7 (PLAXIS)



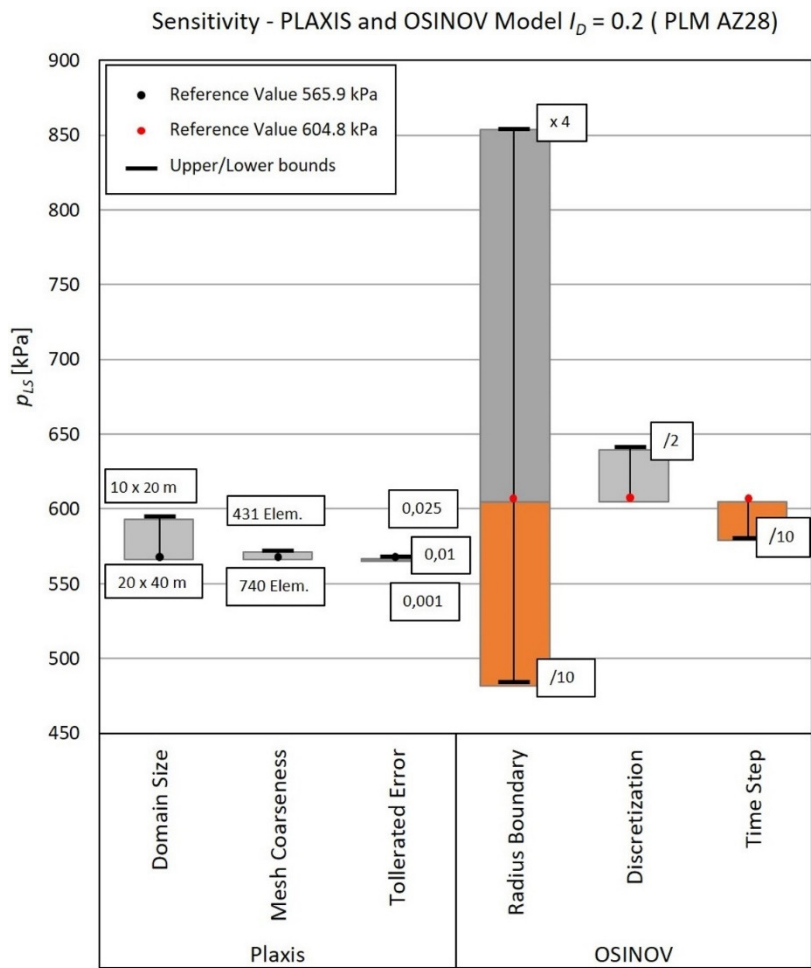
A. Fig 27: Pressure-expansion-curves PLM BC36 for I_D 0.8 and 0.9 (PLAXIS)

A. Tab. 7: Limit Pressures – PLAXIS vs. OSINOV (PLM BC36)

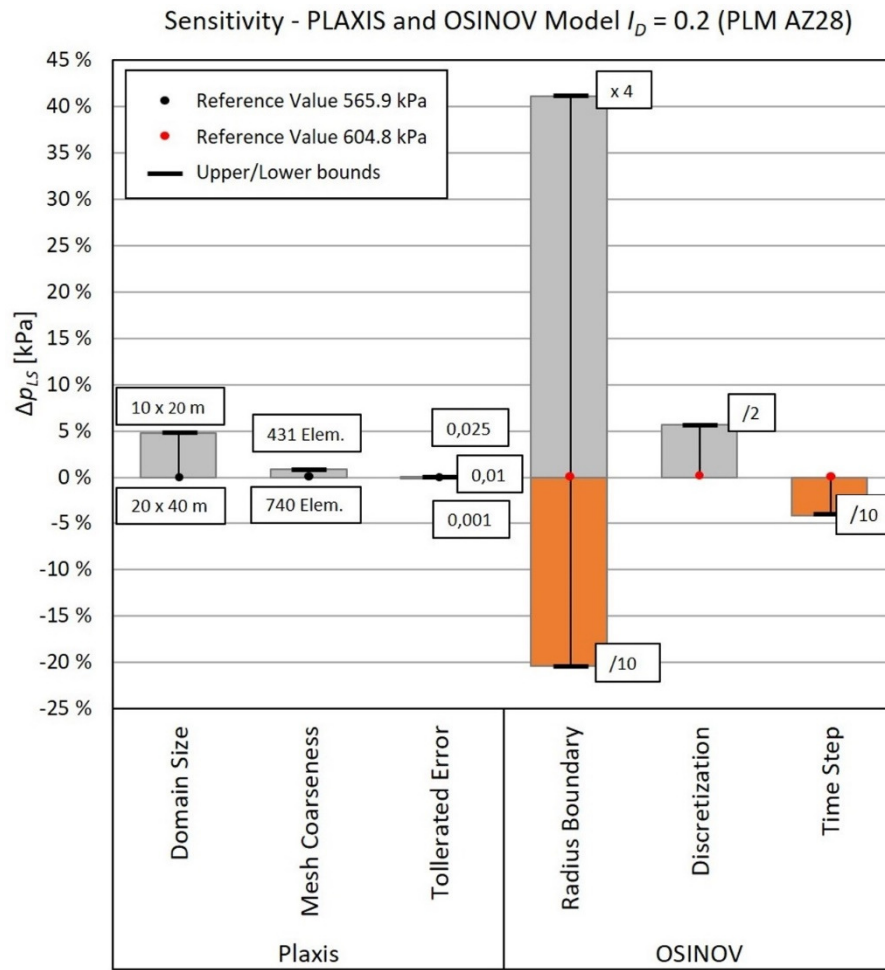
Limit Pressures - Material PLM BC36							
I_D	p_0	p_{LS} (PLAXIS)	p_{LS} (OSINOV)	I_D	p_0	p_{LS} (PLAXIS)	p_{LS} (OSINOV)
[-]	[kPa]	[kPa]	[kPa]	[-]	[kPa]	[kPa]	[kPa]
0.0	25	269	287	0.5	25	371	393
	50	463	493		50	627	670
	100	799	857		100	1067	1136
	150	1103	1185		150	1459	1561
	300	1919	2070		300	2502	2685
0.1	25	284	302	0.6	25	405	429
	50	487	517		50	682	729
	100	838	898		100	1155	1228
	150	1154	1241		150	1575	1682
	300	2005	2161		300	2689	2885

Continuation on next page

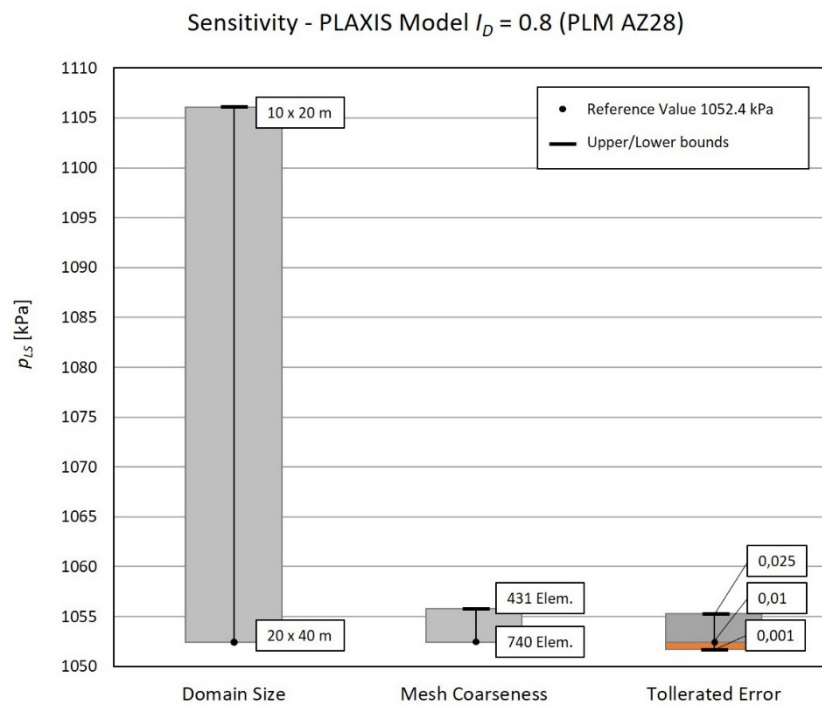
I_D [-]	p_0 [kPa]	p_{LS} (PLAXIS) [kPa]	p_{LS} (OSINOV) [kPa]	I_D [-]	p_0 [kPa]	p_{LS} (PLAXIS) [kPa]	p_{LS} (OSINOV) [kPa]
0.2	25	301	320	0.7	25	450	477
	50	514	545		50	754	804
	100	883	945		100	1269	1343
	150	1214	1303		150	1724	1837
	300	2104	2266		300	2927	3132
0.3	25	320	340	0.8	25	513	543
	50	546	581		50	852	905
	100	934	998		100	1420	1504
	150	1283	1376		150	1922	2042
	300	2216	2385		300	3239	3456
0.4	25	343	364	0.9	25	614	649
	50	583	622		50	1006	1064
	100	995	1062		100	1657	1756
	150	1364	1460		150	2226	2346
	300	2348	2522		300	3711	3896



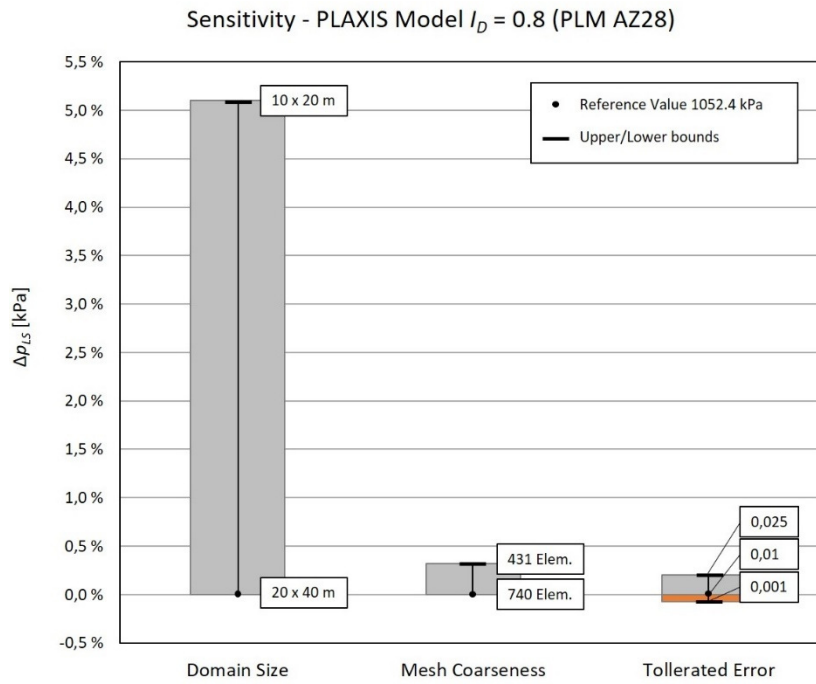
A. Fig 28: Sensitivity diagram p_{LS} -range – PLAXIS and OSINOV $I_D = 0.2$ (PLM AZ28)



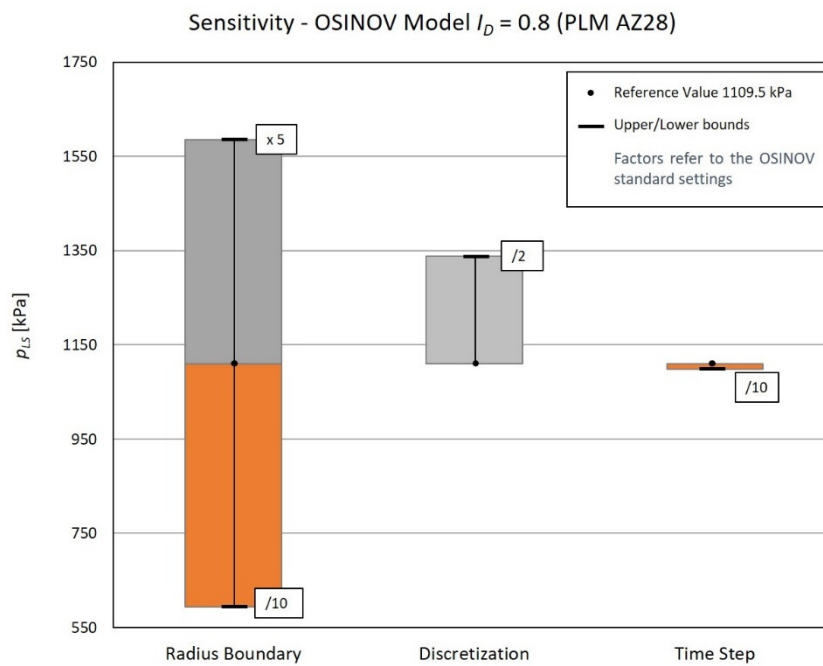
A. Fig 29: Sensitivity diagram Δp_{LS} -range – PLAXIS and OSINOV $I_D = 0.2$ (PLM AZ28)



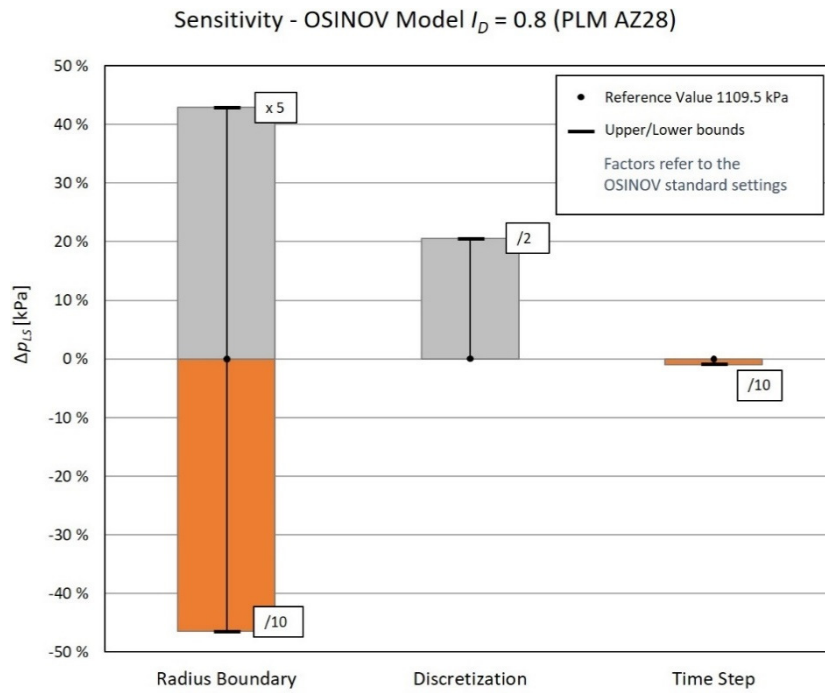
A. Fig 30: Sensitivity diagram p_{LS} -range – PLAXIS $I_D = 0.8$ (PLM AZ28)



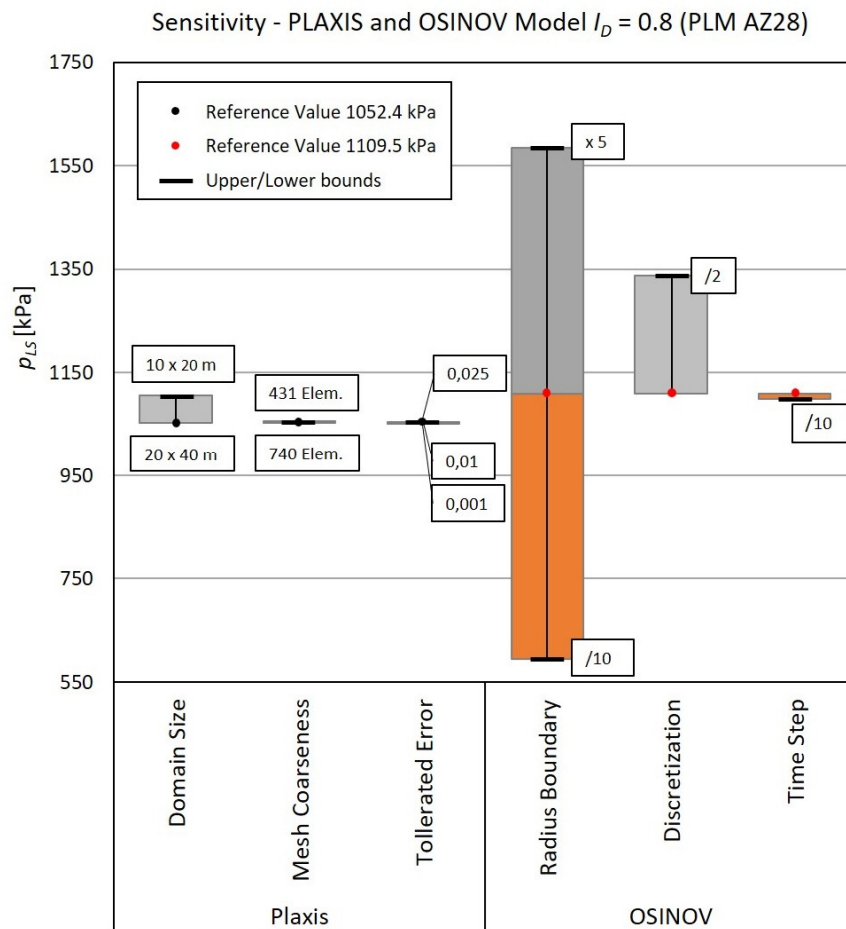
A. Fig 31: Sensitivity diagram Δp_{LS} -range – PLAXIS $I_D = 0.8$ (PLM AZ28)



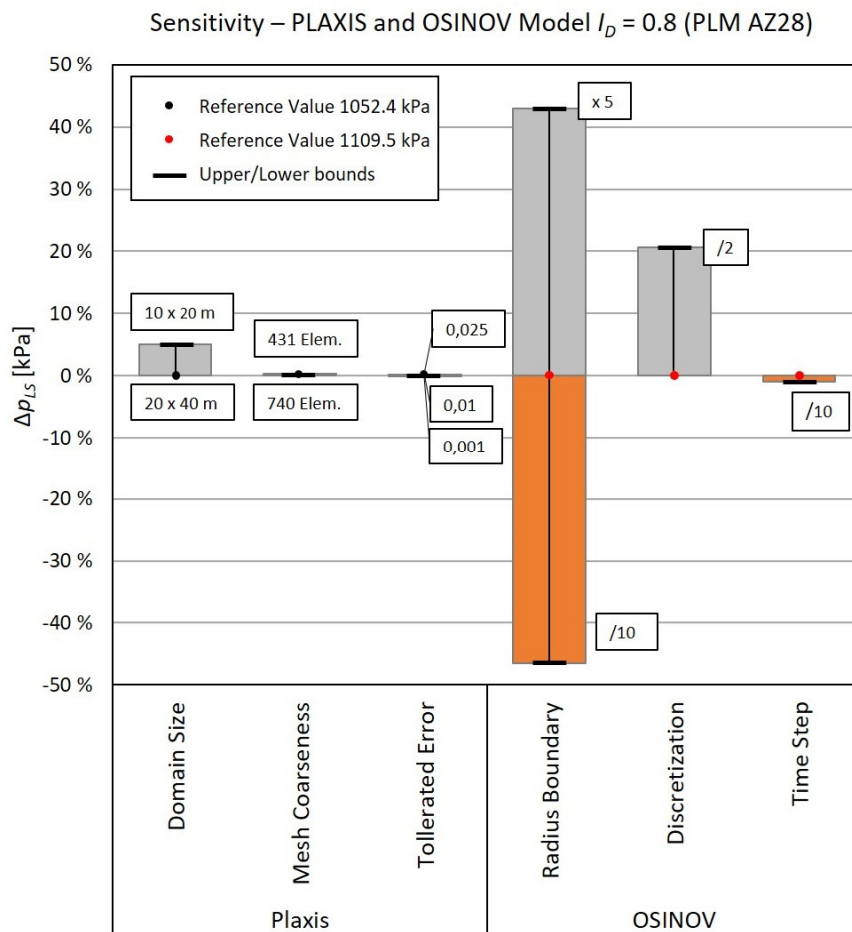
A. Fig 32: Sensitivity diagram p_{LS} -range – OSINOV $I_D = 0.8$ (PLM AZ28)



A. Fig 33: Sensitivity diagram Δp_{LS} -range – OSINOV $I_D = 0.8$ (PLM AZ28)



A. Fig 34: Sensitivity diagram p_{LS} -range – PLAXIS and OSINOV $I_D = 0.8$ (PLM AZ28)



A. Fig 35: Sensitivity diagram Δp_{LS} -range – PLAXIS and OSINOV $I_D = 0.8$ (PLM AZ28)

```

%*****
%GENERATION OF QC-CURVES from different Curve Fit approaches for 1 Material
%and 3 different ID's with changing Unit weight over depth following Bauers
%compression law
%*****

clc
clear
close all
Materialname=strcat('PLM AZ28');

%Initialize all Soil paramters and hypoplastic parameters for the material
hs = 39000; %[kPa]
n = 0.525; %[-]
ed0 = 0.74; %[-]
ec0 = 1.261; %[-]
phi_c = 36.3; %[°]
roh_s = 2.791; %[g/cm³]

%Initialize the 3 desired values for ID

ID = [0.3 0.6 0.9];

```

```

ID_String1 = strcat('ID ',{ ' },string(ID(1)));
ID_String2 = strcat('ID ',{ ' },string(ID(2)));
ID_String3 = strcat('ID ',{ ' },string(ID(3)));

%Initialize the KIM Parameters of the different Curvefits

KIM_params={[]};

%report
KIM_params{1}(1)=1.666;      %a1 - report
KIM_params{1}(2)=-6.152;    %a2 - report
KIM_params{1}(3)=-1.597;    %a3 - report
KIM_params{1}(4)=0.835;     %b1 - report
KIM_params{1}(5)=0.073;     %b2 - report
KIM_params{1}(6)=-1.395;    %b3 - report

%Plaxis Excel Fit
KIM_params{2}(1)=1.94957949677086;    %a1
KIM_params{2}(2)=-4.79544908482518;    %a2
KIM_params{2}(3)=-1.49210659649755;    %a3
KIM_params{2}(4)=0.812079090646639;    %b1
KIM_params{2}(5)=0.0519274491595657;    %b2
KIM_params{2}(6)=-1.32345939802458;    %b3

%Plaxis GnuPlot Fit
KIM_params{3}(1)=1.95417018403748;    %a1
KIM_params{3}(2)=-4.78704334456454;    %a2
KIM_params{3}(3)=-1.49135143335749;    %a3
KIM_params{3}(4)=0.812153149695471;    %b1
KIM_params{3}(5)=0.0520319617570925;    %b2
KIM_params{3}(6)=-1.32413250652236;    %b3

%Osinov Excel Fit
KIM_params{4}(1)=1.70488013159653;    %a1
KIM_params{4}(2)=-6.08282864255751;    %a2
KIM_params{4}(3)=-1.59258258640936;    %a3
KIM_params{4}(4)=0.84231233023794;    %b1
KIM_params{4}(5)=0.0841205388236344;    %b2
KIM_params{4}(6)=-1.43971888295734;    %b3

%Osinov GnuPlot Fit
KIM_params{5}(1)=1.70536149344721;    %a1
KIM_params{5}(2)=-6.081743966418;    %a2
KIM_params{5}(3)=-1.59248003389682;    %a3
KIM_params{5}(4)=0.842417628960368;    %b1
KIM_params{5}(5)=0.0842978067881274;    %b2
KIM_params{5}(6)=-1.44054632981235;    %b3

KIM_Title_String={[]};
KIM_Title_String{1}='Report';
KIM_Title_String{2}='Plaxis Curve Fit Excel';
KIM_Title_String{3}='Plaxis Curve Fit GnuPlot';
KIM_Title_String{4}='Osinov Curve Fit Excel';
KIM_Title_String{5}='Osinov Curve Fit GnuPlot';

%Inizialize Groundwaterdepth below surface and estimated watercontent
GW_depth = 2; %[m]
w_content = 20; %[%]

```

```

%Specify the Linestyles of the plotted lines
plotstyle={'-r','--g',':g','--b',':b','--b',':b','-.b','-r','--r'};

%)+++++
%+++++Computation of K0 and unit weight for pressure 0+++++
%+++++

K0 = 1-sin(phi_c*pi()/180);

e_target_0=zeros(length(ID),1);
for i = 1:length(ID)
    e_target_0(i)=ec0-ID(i)*(ec0-ed0);
end

roh_target_0=zeros(length(ID),1);
for i = 1:length(ID)
    roh_target_0(i)=roh_s/(e_target_0(i)+1);
end

gamma_target_0=zeros(length(ID),1);
for i = 1:length(ID)
    gamma_target_0(i)=(1+w_content/100)*10*roh_target_0(i); %[kN/m³]
end

gamma_uplift_target_0=zeros(length(ID),1);
for i = 1:length(ID)
    gamma_uplift_target_0(i)=(roh_s+e_target_0(i)*1)/(1+e_target_0(i))*10-10; %[kN/m³]
end

%)+++++
%+++++Computation of the qc-values+++++
%+++++

z_vec=linspace(0,10,1000);

sigv={[]};
e_z={[]};
roh_z={[]};
gamma_z={[]};

for i = 1:length(ID)
    sigv{i}(1)= 0;
    e_z{i}(1)=e_target_0(i);
    roh_z{i}(1)=roh_target_0(i);

    if GW_depth == 0
        sigv{i}(2)=z_vec(2)*gamma_uplift_target_0(i);
        gamma_z{i}(1)=gamma_uplift_target_0(i);
    else
        sigv{i}(2)=z_vec(2)*gamma_target_0(i);
        gamma_z{i}(1)=gamma_target_0(i);
    end
end

sigvCurrent=zeros(length(ID),1);           %initialize current sigma v for
subsequent loop
for i=1:length(ID)

```

```

    SigvCurrent(i)=Sigv{i}(2);
end

for i=1:length(ID)
for j = 3:length(z_vec)

    e_z{i}(j-1)= ec0*exp(-(3*(1/3)*SigvCurrent(i)*(1+2*k0)/(hs)^n)...
                -ID(i)*exp(-(3*(1/3)*SigvCurrent(i)*(1+2*k0)/(hs)^n)*(ec0-ed0);

    if GW_depth > z_vec(j-1)
        roh_z{i}(j-1)=roh_s/(e_z{i}(j-1)+1);
        gamma_z{i}(j-1)=(1+w_content/100)*10*roh_z{i}(j-1); %[kN/m³]
    else
        gamma_z{i}(j-1)=(roh_s+e_z{i}(j-1)*1)/(1+e_z{i}(j-1))*10-10; %[kN/m³]
    end

    Sigv{i}(j)=Sigv{i}(j-1)+gamma_z{i}(j-1)*(z_vec(j)-z_vec(j-1));
    SigvCurrent(i)=Sigv{i}(j);
end
end

p0_values={ [] };
qc_ID1_values={ [] };
qc_ID2_values={ [] };
qc_ID3_values={ [] };
%qc values for ID(1)
for i=1:size(KIM_params,2)
for j=1:length(z_vec)
    p0_values{i}(j)=Sigv{1}(j)/3*(1+2*k0);

qc_ID1_values{i}(j)=(1.5+5.8*ID(1)^2/(ID(1)^2+0.11))*(KIM_params{i}(1)+KIM_params{i}(2)/
(ID(1)+KIM_params{i}(3)))*(p0_values{i}(j)/1000)^(KIM_params{i}(4)+KIM_params{i}(5)/(ID(
1)+KIM_params{i}(6)));
end
end

%qc values for ID(2)
for i=1:size(KIM_params,2)
for j=1:length(z_vec)
    p0_values{i}(j)=Sigv{2}(j)/3*(1+2*k0);

qc_ID2_values{i}(j)=(1.5+5.8*ID(2)^2/(ID(2)^2+0.11))*(KIM_params{i}(1)+KIM_params{i}(2)/
(ID(2)+KIM_params{i}(3)))*(p0_values{i}(j)/1000)^(KIM_params{i}(4)+KIM_params{i}(5)/(ID(
2)+KIM_params{i}(6)));
end
end

%qc values for ID(3)
for i=1:size(KIM_params,2)
for j=1:length(z_vec)
    p0_values{i}(j)=Sigv{3}(j)/3*(1+2*k0);

qc_ID3_values{i}(j)=(1.5+5.8*ID(3)^2/(ID(3)^2+0.11))*(KIM_params{i}(1)+KIM_params{i}(2)/
(ID(3)+KIM_params{i}(3)))*(p0_values{i}(j)/1000)^(KIM_params{i}(4)+KIM_params{i}(5)/(ID(
3)+KIM_params{i}(6)));
end
end

```

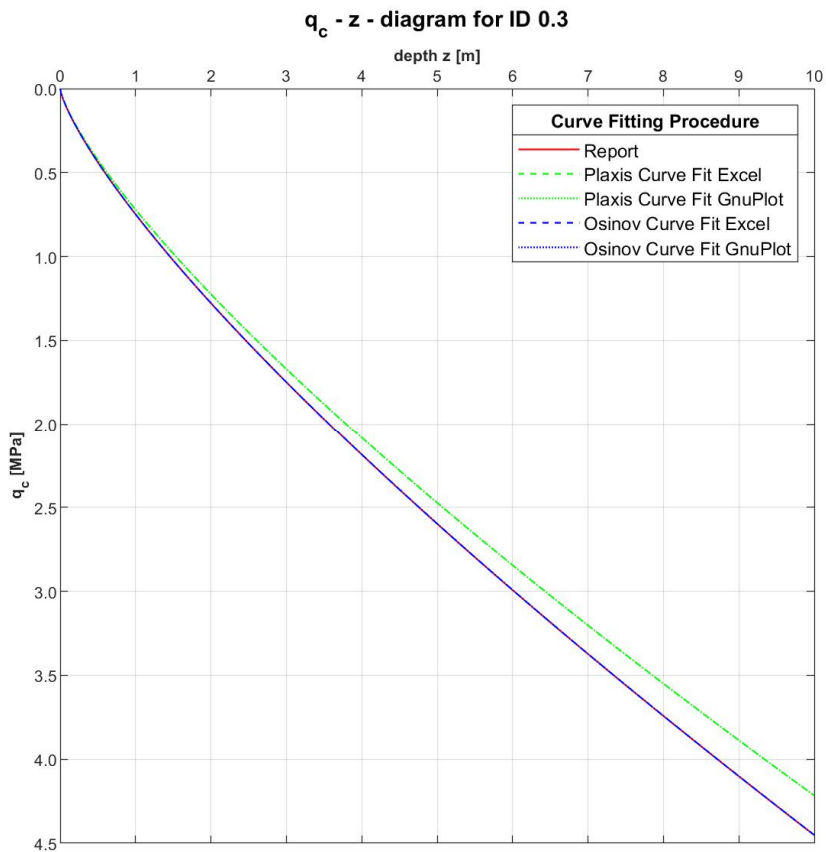
```

%+-----+
%+-----+PLOTTING THE RESULTS+-----+
%+-----+

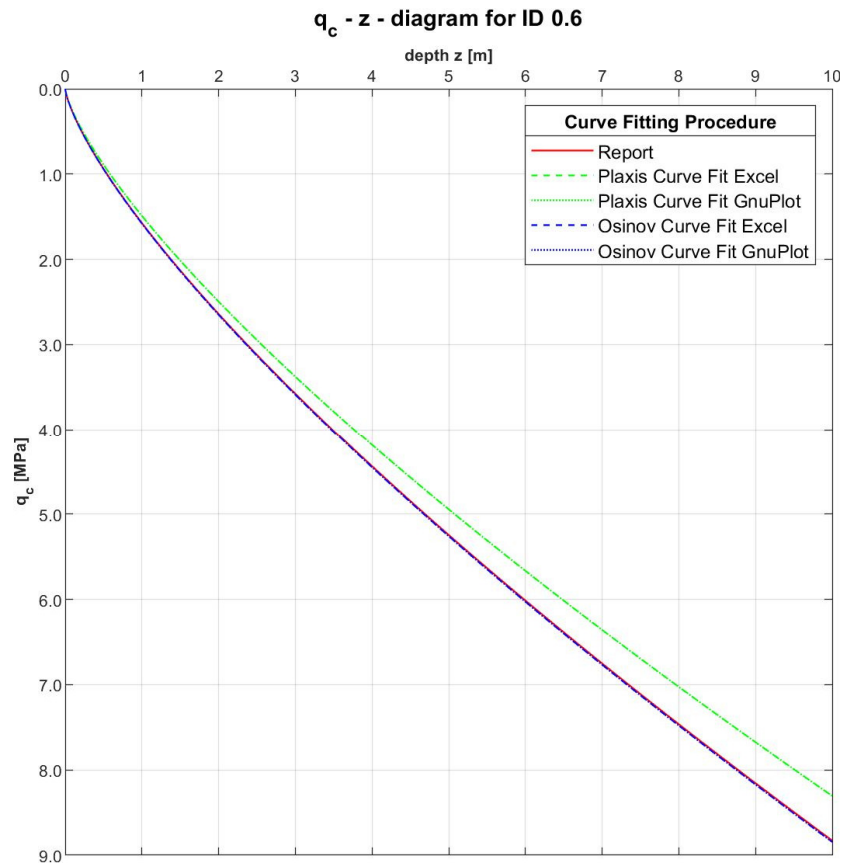
Plot_qcVSdepth_ID(ID_String1,z_vec,qc_ID1_values,KIM_Title_String,plotstyle)
Plot_qcVSdepth_ID(ID_String2,z_vec,qc_ID2_values,KIM_Title_String,plotstyle)
Plot_qcVSdepth_ID(ID_String3,z_vec,qc_ID3_values,KIM_Title_String,plotstyle)

```

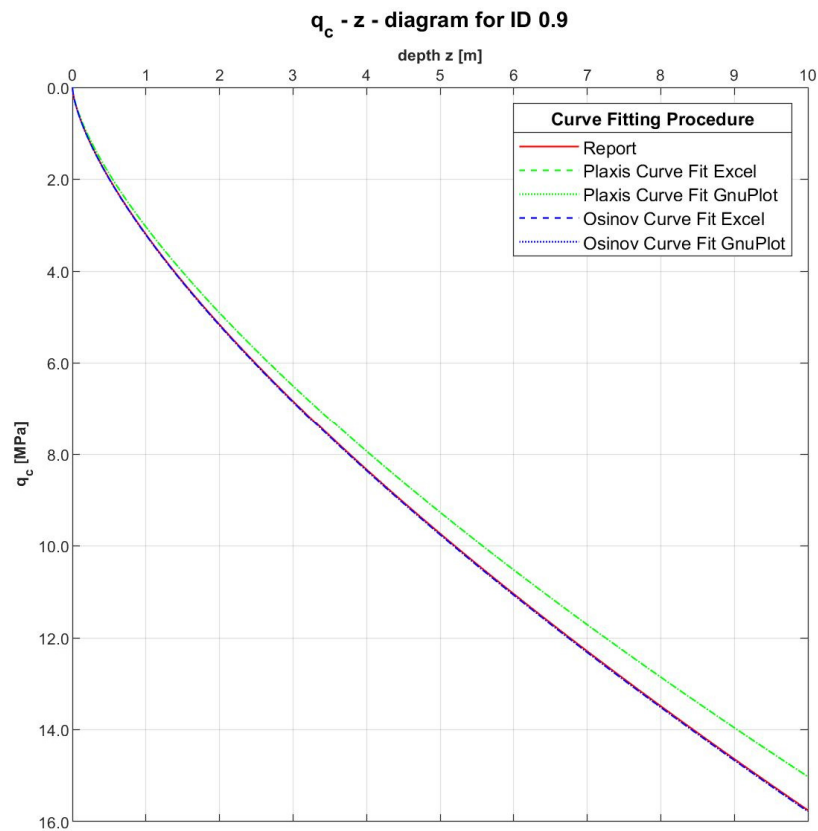
A. Fig 36: MATLAB code – Calculation of q_c over depth z



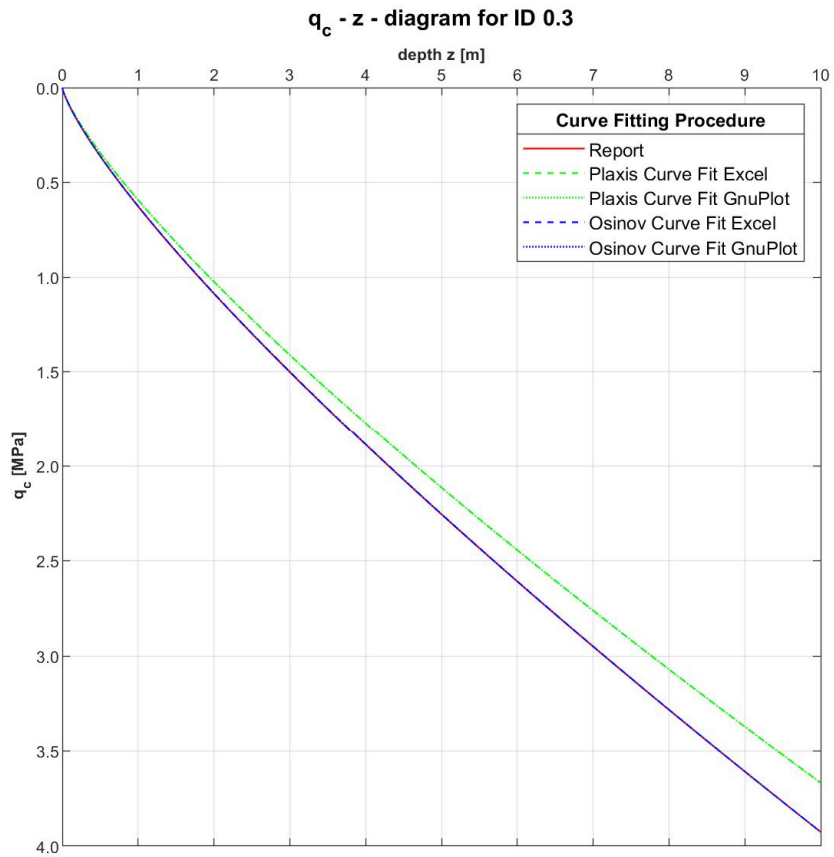
A. Fig 37: q_c vs. z for $I_D = 0.3$, $z_{GW} = 10$ m and $w = 20$ % (PLM AZ28)



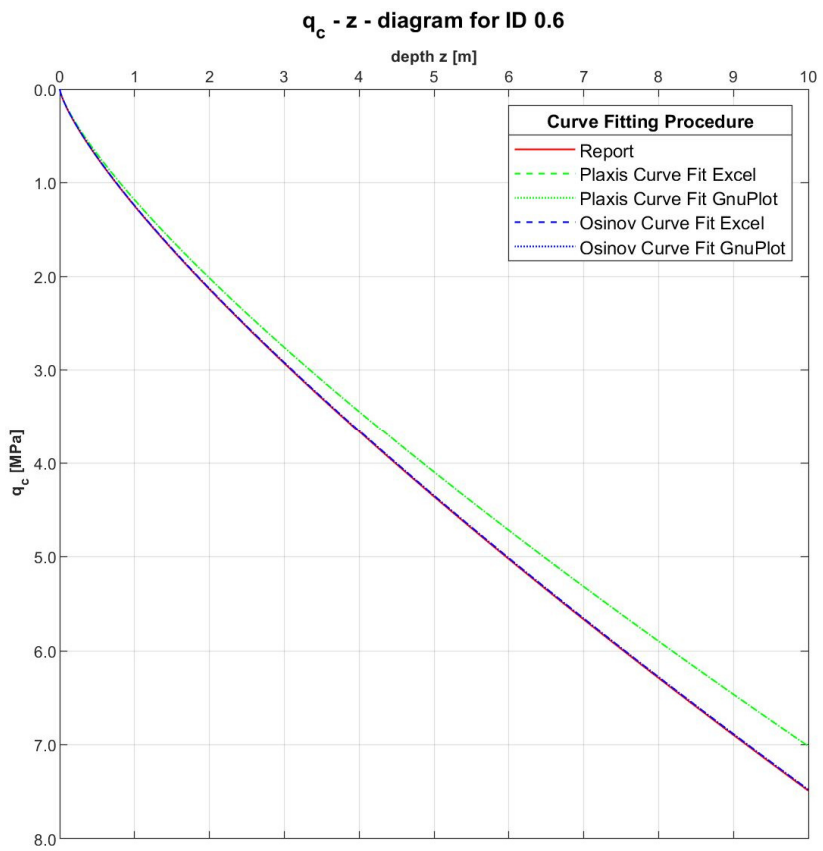
A. Fig 38: q_c vs. z for $I_D = 0.6$, $z_{GW} = 10$ m and $w = 20$ % (PLM AZ28)



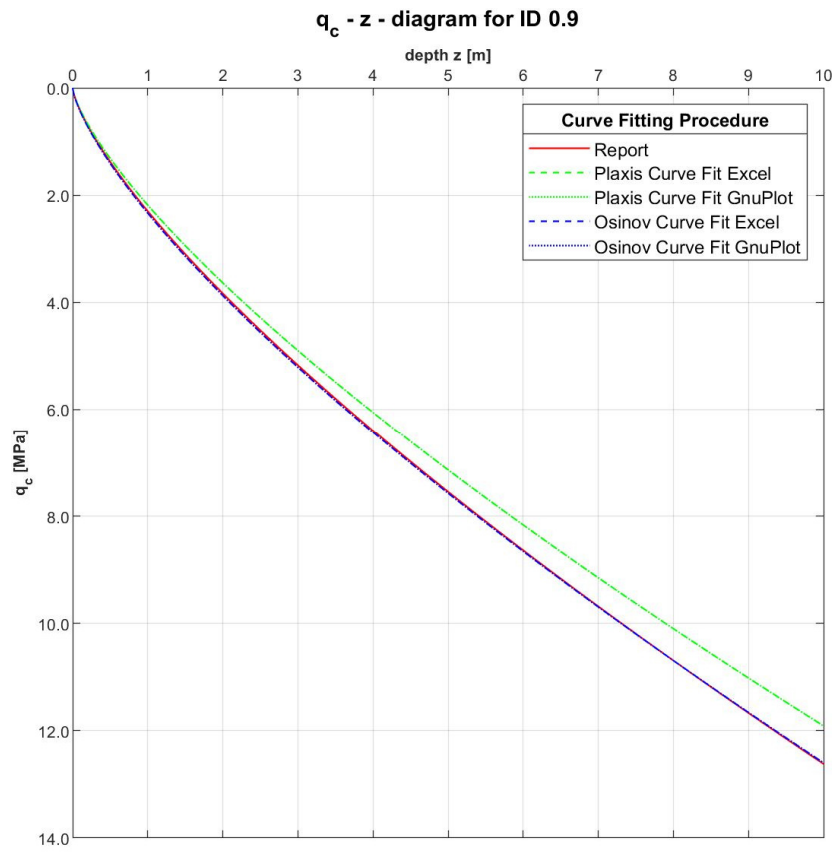
A. Fig 39: q_c vs. z for $I_D = 0.9$, $z_{GW} = 10$ m and $w = 20$ % (PLM AZ28)



A. Fig 40: q_c vs. z for $I_D = 0.3$, $z_{GW} = 10$ m and $w = 20$ % (PLM BC36)

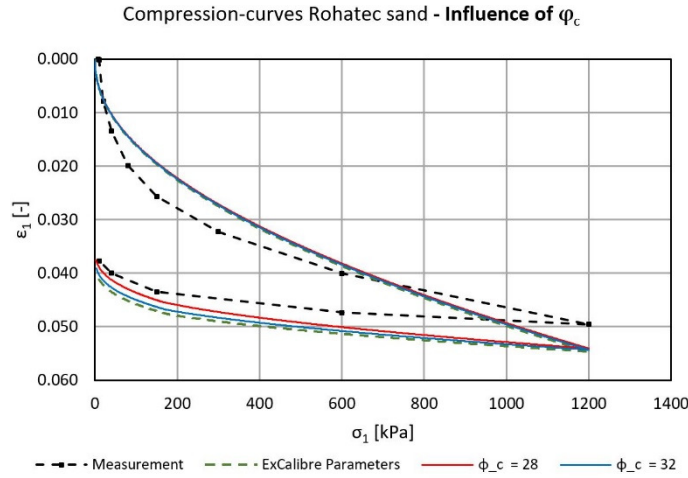


A. Fig 41: q_c vs. z for $I_D = 0.6$, $z_{GW} = 10$ m and $w = 20$ % (PLM BC36)

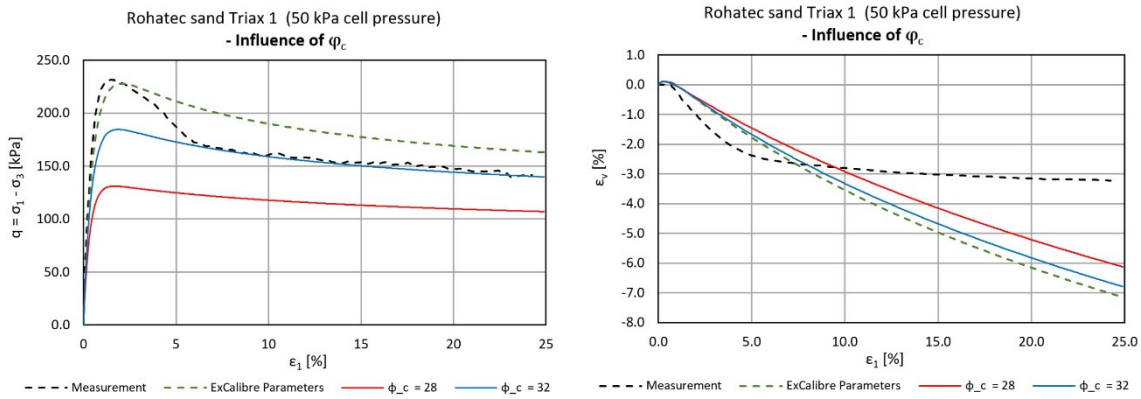


A. Fig 42: q_c vs. z for $I_D = 0.9$, $z_{GW} = 10$ m and $w = 20$ % (PLM BC36)

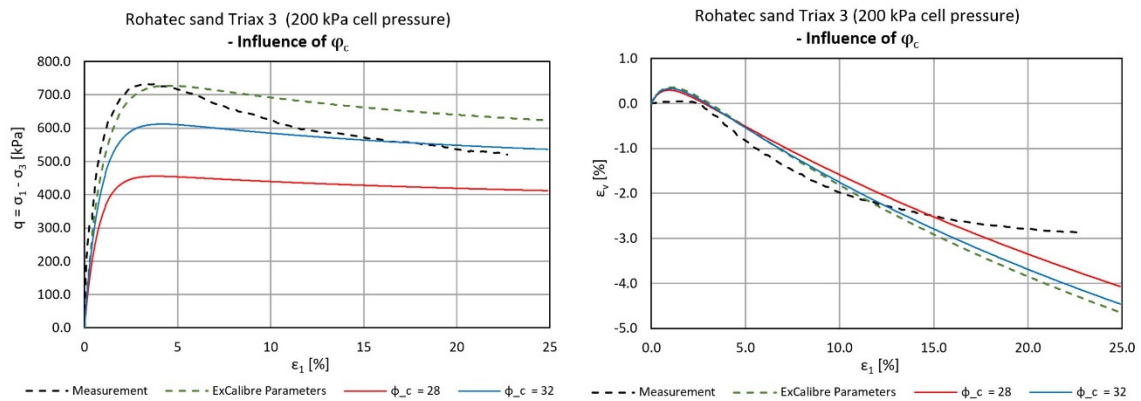
Appendix F for Chapter 7



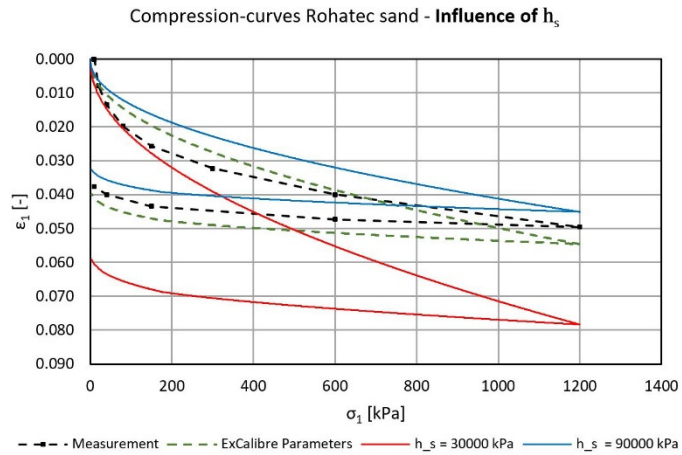
A. Fig 43: Influence of φ_c on compression curve – Rohatec sand



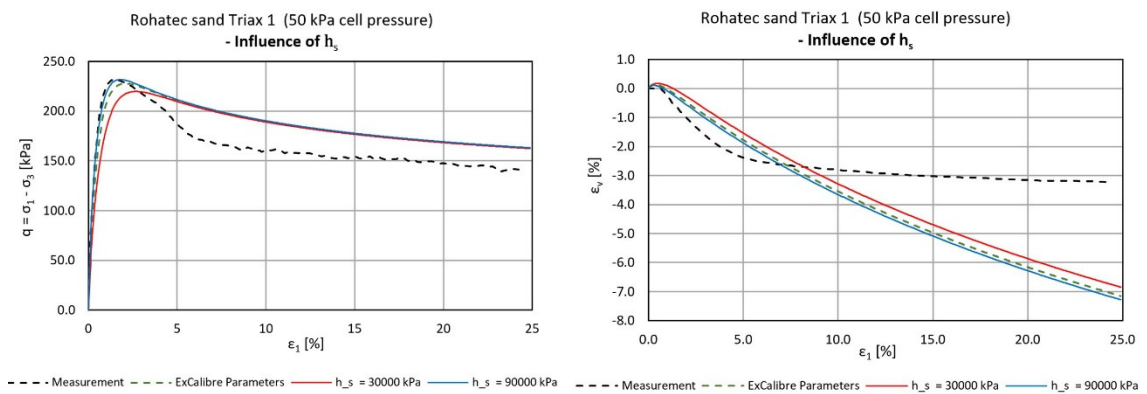
A. Fig 44: Influence of φ_c on triaxial curves (50 kPa cell pressure) – Rohatec sand



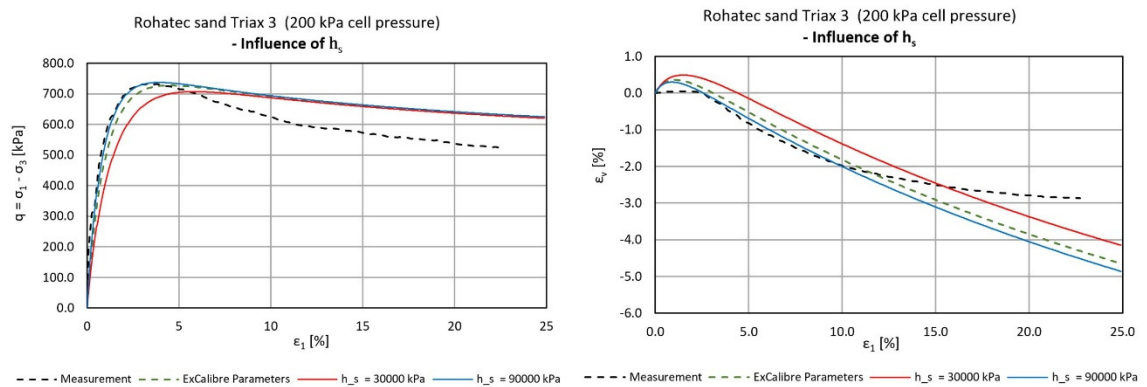
A. Fig 45: Influence of φ_c on triaxial curves (200 kPa cell pressure) – Rohatec sand



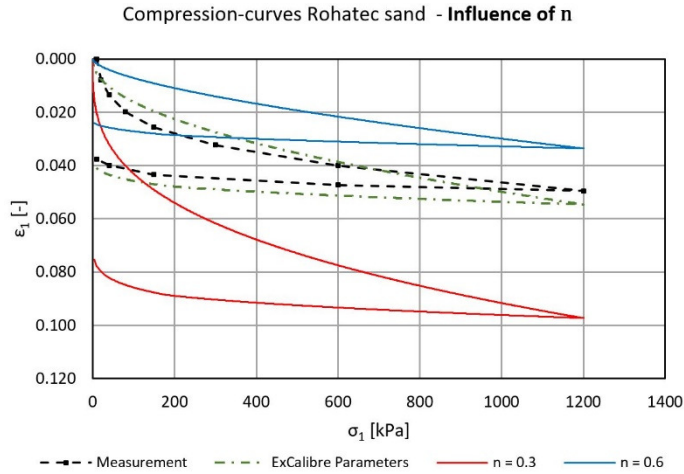
A. Fig 46: Influence of h_s on compression curve – Rohatec sand



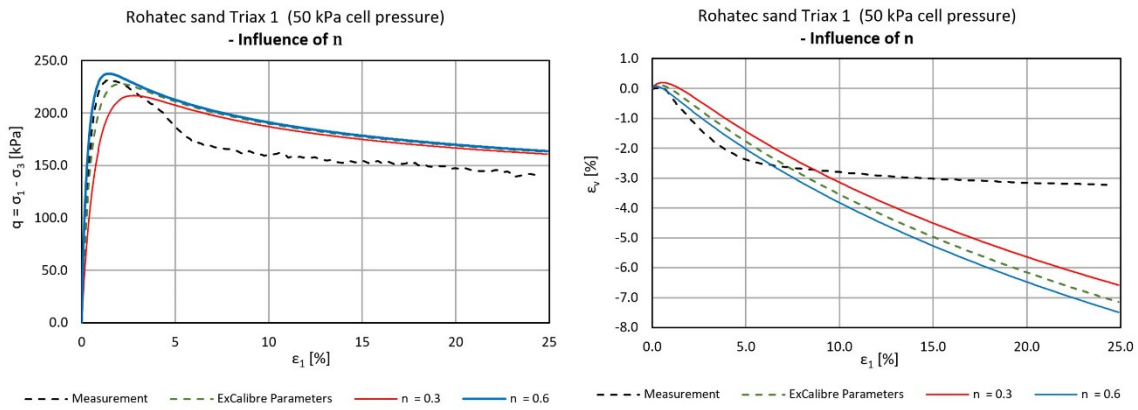
A. Fig 47: Influence of h_s on triaxial curves (50 kPa cell pressure) – Rohatec sand



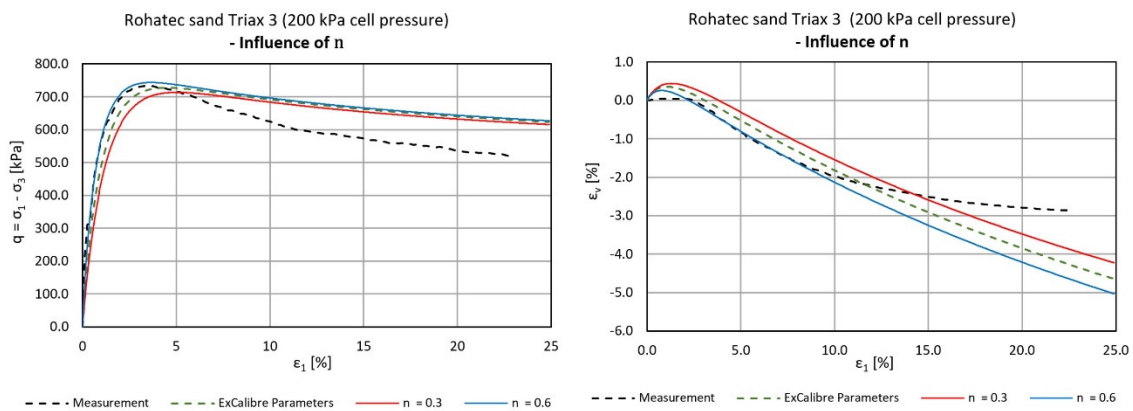
A. Fig 48: Influence of h_s on triaxial curves (200 kPa cell pressure) – Rohatec sand



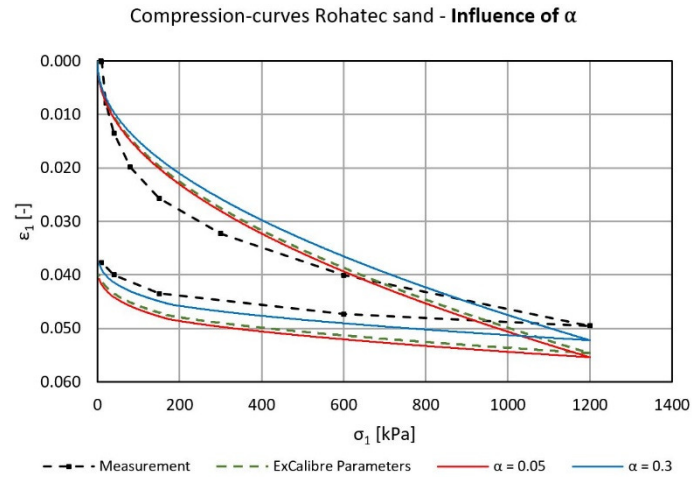
A. Fig 49: Influence of n on compression curve – Rohatec sand



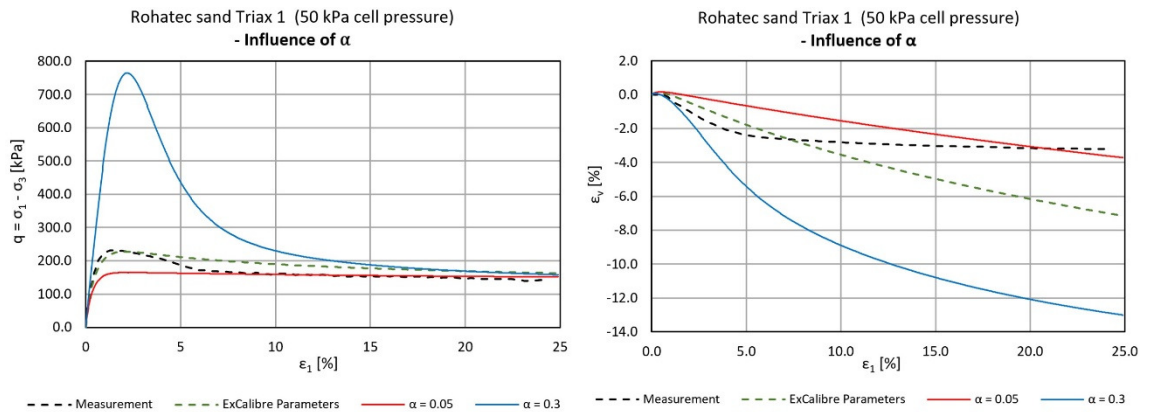
A. Fig 50: Influence of n on triaxial curves (50 kPa cell pressure) – Rohatec sand



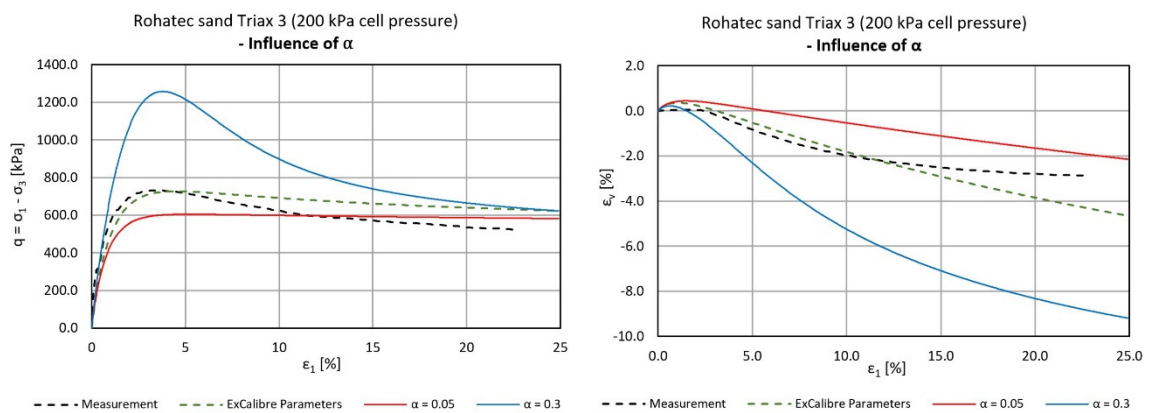
A. Fig 51: Influence of n on triaxial curves (200 kPa cell pressure) – Rohatec sand



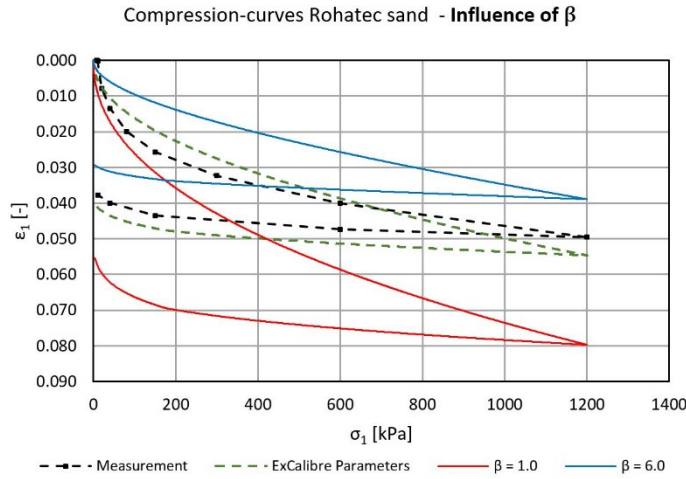
A. Fig 52: Influence of α on compression curve – Rohatec sand



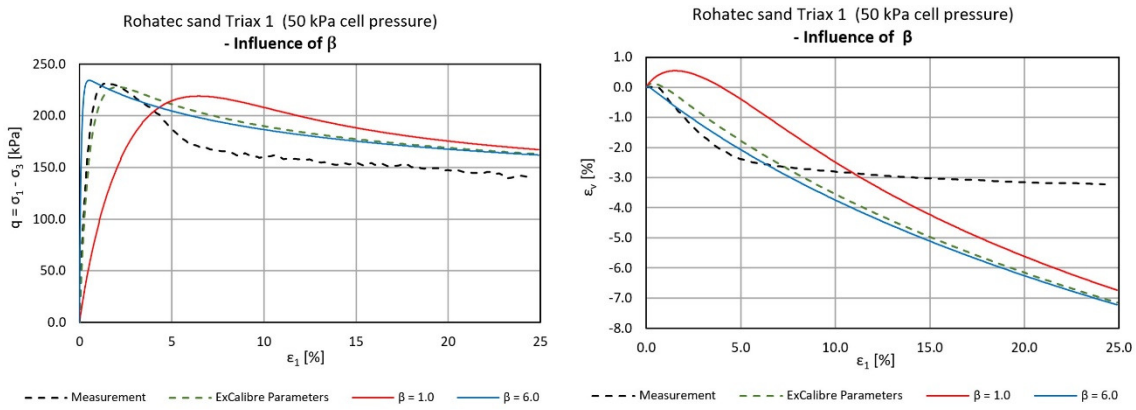
A. Fig 53: Influence of α on triaxial curves (50 kPa cell pressure) – Rohatec sand



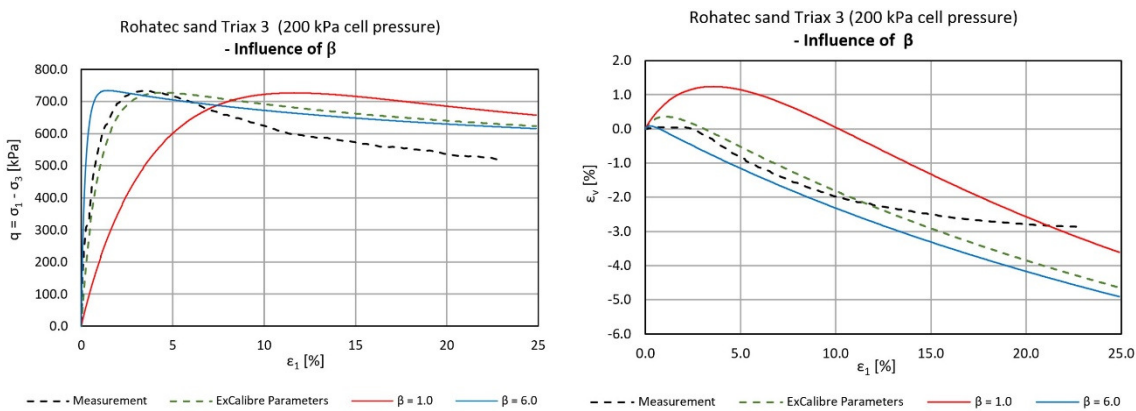
A. Fig 54: Influence of α on triaxial curves (200 kPa cell pressure) – Rohatec sand



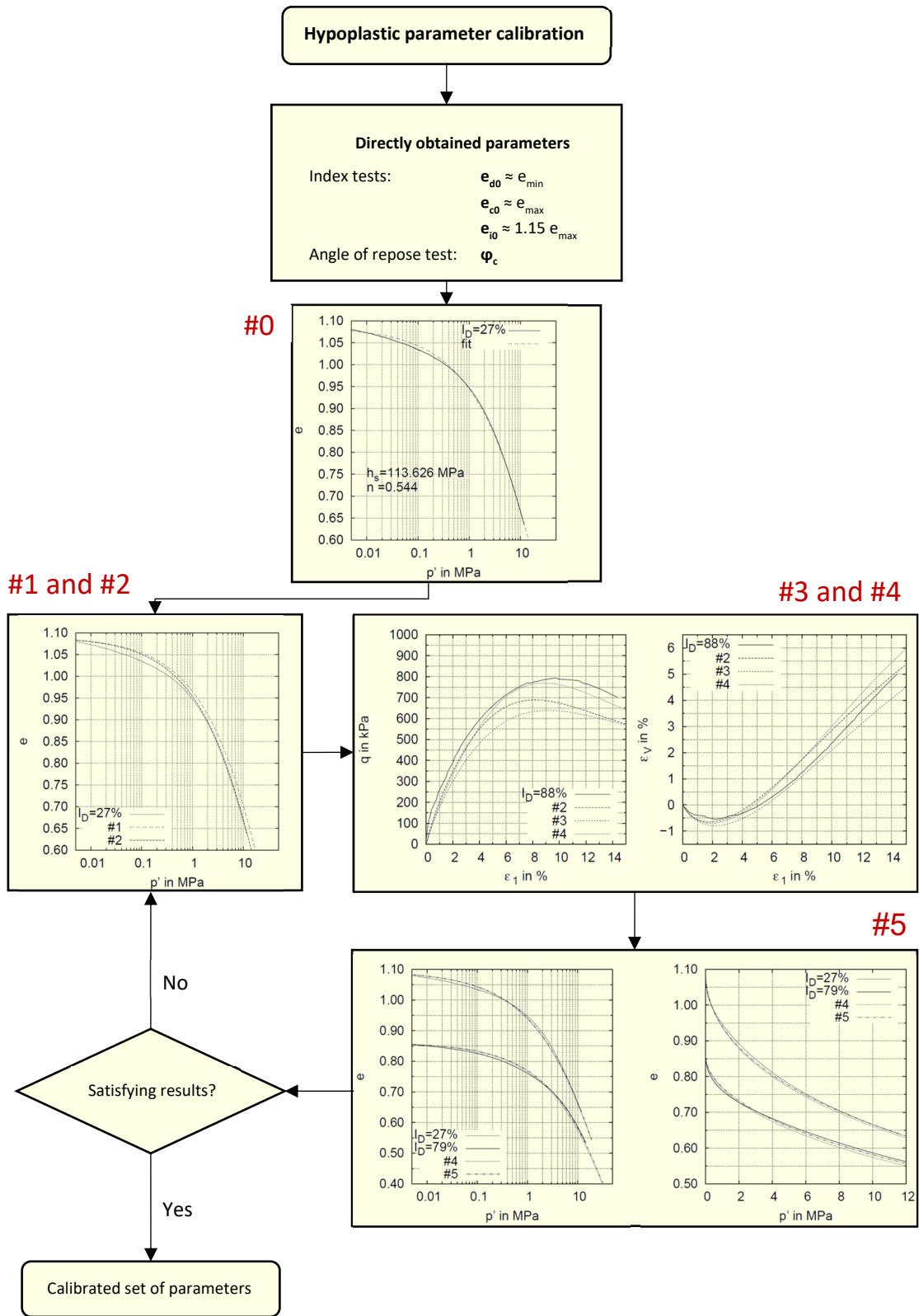
A. Fig 55: Influence of β on compression curve – Rohatec sand



A. Fig 56: Influence of β on triaxial curves (50 kPa cell pressure) – Rohatec sand



A. Fig 57: Influence of β on triaxial curves (200 kPa cell pressure) – Rohatec sand



A. Fig 58: Flow chart of the calibration procedure acc. to Meier [6] – Influence of different parameter sets on the simulation results